Chair of Theoretical Solid-State Physics
Department of Physics
Technical University of Munich

Quantum Many-Body Systems Far Out of Equilibrium — Simulations with Tensor Networks

Dissertation

Johannes Michael Hauschild

Chair of Theoretical Solid-State Physics
Department of Physics
Technical University of Munich

Fakultät für Physik
Lehrstuhl für Theoretische Festkörperphysik

Quantum Many-Body Systems Far Out of Equilibrium — Simulations with Tensor Networks

Johannes Michael Hauschild

Vollständiger Abdruck der von der Fakultät für Physik der Technischen Universität München zur Erlangung des akademischen Grades eines
Doktors der Naturwissenschaften (Dr. rer. nat.)
genehmigten Dissertation.

Vorsitzender: Prof. Dr. Christian Pfleiderer
Prüfer der Dissertation:
1. Prof. Dr. Frank Pollmann
2. Prof. Dr. Michael Knap

Die Dissertation wurde am 03.09.2019 bei der Technischen Universität München eingereicht und durch die Fakultät für Physik am 15.10.2019 angenommen.

Abstract

Quantum many-body systems far out of equilibrium can lead to rich physics and are challenging to understand due to the exponentially large Hilbert space. We employ large scale tensor network techniques in numerical simulations and investigate the dynamics of different model systems, where we focus on the dimensional crossover in two-dimensional systems and on many-body localization. Moreover, we introduce a new method to efficiently simulate the dynamics of mixed states using minimally entangled purified states. The developed codes are made available as an open-source library.

Kurzfassung

Quantenvielteilchensysteme im Nichtgleichgewicht bieten reichhaltige Physik, der exponentiell große Hilbertraum stellt jedoch eine Herausforderung für deren Verständnis dar. Wir verwenden umfangreiche numerische Simulationen mit Tensor-Netzwerk-Methoden und erforschen die Dynamik in verschiedenen Modellsystemen, wobei wir uns auf auf den dimensionalen Übergang in zwei-dimensionalen Systemen und auf Vielteilchenlokalisierung konzentrieren. Außerdem präsentieren wir eine neue Methode, um effizient die Dynamik von gemischten Zuständen mit minimal verschränkten reduzierten Zuständen zu simulieren. Die entwickelten Programme sind als Open-Source-Code verfügbar.

Contents

List of Publications

Parts of the content of this thesis have been published in the following Refs. [1–5]. The author of this thesis has made significant and substantial contributions to these publications, ranging from the development of ideas, literature research, analytical calculations, design, development and implementation of numerical codes, to the interpretation of results, and writing of the papers.

[1] J. Hauschild and F. Pollmann. "Efficient numerical simulations with Tensor Networks: Tensor Network Python (TeNPy)." *SciPost Phys. Lect. Notes* p. 5, 2018. doi:10.21468/SciPostPhysLectNotes.5. arXiv:1805.00055.

[2] J. Hauschild, F. Pollmann, and Others. "Tensor Network Python (TeNPy).", 2018. The code is available online at `https://github.com/tenpy/tenpy/`, documentation at `https://tenpy.github.io/`.

[3] J. Hauschild, F. Pollmann, and F. Heidrich-Meisner. "Sudden expansion and domain-wall melting of strongly interacting bosons in two-dimensional optical lattices and on multileg ladders." *Phys. Rev. A* **92**, p. 053629, 2015. doi:10.1103/PhysRevA.92.053629. arXiv:1509.00696.

[4] J. Hauschild, F. Heidrich-Meisner, and F. Pollmann. "Domain-wall melting as a probe of many-body localization." *Phys. Rev. B* **94**, p. 161109, 2016. doi:10.1103/PhysRevB.94.161109. arXiv:1605.05574.

[5] J. Hauschild, E. Leviatan, J. H. Bardarson, E. Altman, M. P. Zaletel, and F. Pollmann. "Finding purifications with minimal entanglement." *Phys. Rev. B* **98**, p. 235163, 2018. doi:10.1103/PhysRevB.98.235163. arXiv:1711.01288.

Specifically, most of the pedagogical review of tensor network algorithms given in chapter 2 was published as lecture notes in Ref. [1]. Along with these notes, an open source library called *Tensor Network Python* (TeNPy) developed mainly by the author of this thesis was introduced to the scientific community. This library is described in Sec. 2.6; the code, extensive documentation and further examples can be found in Ref. [2]. The results on the sudden expansion of hard-core bosons presented in Ch. 3 have appeared in Ref. [3]. The results on the domain wall melting in disordered systems presented in chapter 4 have been published in Ref. [4]. Finally, the algorithm for the disentangling of purification states described in Ch. 5 has been published in Ref. [5].

1 Introduction

Quantum many-body systems display a rich phenomenology. One of the most celebrated examples is high-temperature superconductivity [6], which created an interest in strongly correlated systems lasting since the discovery to date. The Hubbard model is believed to describe the physics of those compounds [7], but despite the simplicity of the Hamiltonian, the problem remains unsolved due to the complexity in the interplay of charge and spins interactions. Anderson proposed a description in terms of quantum spin liquids as disordered spin states [7, 8]. Another candidate material for the realization of quantum spin liquids is Herbertsmithite, theoretically represented by a Heisenberg model on a two dimensional (2D) kagome lattice [9, 10]. A quantum spin liquid is an exotic state of matter without any magnetic long-range order, but with long-range entanglement and emergent fractionalized excitations at low temperatures [11, 12]. Hence, the description of quantum spin liquids goes beyond Landau's paradigm of characterizing phases by symmetry breaking, but shows topological order. Other well-known examples of topological phases of matter include the Haldane phase in quantum spin chains with integer spin [13, 14] and the fractional quantum Hall effect [15, 16]. The Nobel prize in physics 2016 was awarded to Thouless, Haldane, and Kosterlitz for their pioneering work on that topic and reflects the unbroken interest of the community in strongly correlated systems.

Common to the above examples is that the studied systems are in or close to equilibrium. The study of non-equilibrium systems is a much larger and mostly unexplored area with exciting physics waiting to be discovered. The focus on equilibrium (categorizing everything else as "non-equilibrium"!) is hardly surprising, given that our everyday experience teaches us that many systems quickly thermalize, i.e., drive towards thermal equilibrium. The theory of classical statistical mechanics explains thermalization with the increase of entropy manifested in the second law of thermodynamics. Yet, the unitary time evolution in quantum mechanics preserves the total entropy of an isolated system, making it less obvious how the time average of a pure state evolution can match a thermal distribution. The eigenstate thermalization hypothesis (ETH) resoves this apparent contradiction by proposing that the *individual* eigenstates have the same expectation values for local operators with fluctuations becoming negligible for large systems [17–20]. However, ETH fails if a system has an extensive number of conserved quantities. This occurs not only in fine-tuned models [21], but also robustly if a sufficiently strong disorder is introduced, giving rise to many body localization (MBL) [22–27]. Recent research on MBL ranges from the exact characterization of the MBL phase [28–33], questions about the existence of a mobility edge and the stability of MBL against thermal inclusions or in higher dimensions [34–36], to the exact nature of the transition between the ergodic and localized phase [37–42]. Moreover, experimental evidence for many-body localization was found [43–45].

Besides MBL, where the whole concept of equilibrium is questionable, there are two main ways how a quantum many-body system can be out of equilibrium. On one hand, open systems are coupled to an environment, often allowing for an exchange of particles. Mathematically, they need to be described by a density matrix instead of a pure state. In the case of Markovian dynamics, the dynamics follows a Lindblad master equation. Remarkably, open systems can still have steady states, even if there is a non-zero current through the system induced by the coupling to the environment. On the other hand, there can be an explicit time dependence

in the Hamiltonian even for closed systems, usually induced by an external force. Obviously, there is an endless number of possibilities in the exact form of the time dependence, and open systems can have an explicit time dependence as well. To keep the problem tractable, some kind of simplification is often considered. In Floquet systems, a (usually closed) system is driven periodically. This allows to engineer effective Floquet Hamiltonians, which can host new phases of matter [46–50] like discrete time crystals [46, 47, 51, 52].

However, in this thesis we will focus on so-called quantum quenches, see Ref. [53–55] for some reviews. Here, the system is prepared in an eigenstate of an initial Hamiltonian $\hat{H}_i$ and then some parameters of the Hamiltonian are tuned, such that a different, final Hamiltonian $\hat{H}_f$ governs the evolution of the state. In general, the change of the parameters can follow a certain ramping or sweeping protocol. In sudden quenches, however, the switch from $\hat{H}_i$ to $\hat{H}_f$ happens instantaneously (or experimentally on a much faster time scale than existent in the system), hence providing a very clean setup. In our theoretical work, we will usually specify the initial state $|\psi(t = 0)\rangle$ directly and leave the definition of the initial Hamiltonian $\hat{H}_i$ at time $t < 0$ implicit. Yet, in experiments, the quench protocol is often more relevant.

Ultracold quantum gases in optical lattices provide an excellent platform for the experimental study of quantum many-body systems both in and out of equilibrium [53, 56]. Almost all parameters in the (effective) Hamiltonian, including interaction and hopping strength, can be tuned by changing the intensities and frequencies of the lasers. Different lattices can be realized by an adjustment of the geometry of the laser setup, and choosing the hopping anisotropically allows to study the crossover from a one dimensional (1D) to a 2D system. Moreover, single-site resolution has been reached in the readout of the state [45, 57–59]. This flexibility makes a theorist's dreams come true and has lead to a very fruitful interplay between experiment and theory. For example, shortly after a growing theoretical interest in the MBL phase, signatures of it have been seen in experiments [43–45], which in turn motivated further theoretical studies — including our work on the domain wall melting as a probe of MBL presented in Ch. 4.

In fact, ultracold atoms in optical lattices can be viewed as (analog) quantum simulators. The idea to use quantum devices for computations goes back to Feynman [60, 61]. He proposed universal quantum computers, arguing that any classical simulation of a generic quantum many-body system is doomed due to the complexity caused by to the exponential growth of the Hilbert space. Since then, first universal quantum computers have been build by various groups [62–64]. Yet, the coherence of the involved q-bits seems not yet good enough for an accurate simulation of quantum many-body systems [65].

The exponential growth of the Hilbert space indeed poses a severe challenge to the numerical simulations of quantum many-body systems on classical computers. An exact diagonalization (ED) to obtain all eigenstates is limited to only about 20 spin-$\frac{1}{2}$ degrees of freedom, or up to 48 sites when focusing exclusively on the ground state with state-of-the-art high-performance computations exploiting all symmetries of the system [66]. Yet, there has been made significant process to overcome this limitation at least partially. Quantum Monte Carlo methods stochastically sample only a fraction of terms contributing to expectation values. In cases where the infamous sign problem can be cured, they arguably provide the best results in two or more dimensions. However, they cannot be applied efficiently to a large class of quantum many-body systems, most notably ones that involve fermionic degrees of freedom or geometric frustration [67]. Moreover, they are not suited for a real-time evolution, which is necessary for a study of non-equilibrium phenomena.

Tensor networks can be used to variationally represent quantum states and provide an alternative approach and powerful tool for efficient simulations of quantum many-body systems. Their

first application to condensed matter systems was the invention of the density matrix renormalization group (DMRG) algorithm by S. White, with which he immediately solved the spin $S = 1$ Heisenberg chain, demonstrated that it has a finite gap in the thermodynamic limit, and studied the effect of edge modes [68, 69]. Later on, DMRG has been reformulated in the language of matrix product state (MPS) [70–73] and established itself to be the best method to numerically obtain ground state properties of strongly correlated quantum many-body systems in 1D. The reason for the success of DMRG was shown to be based on the fact that ground states of physical systems have a low (area law) entanglement [74, 75], and that tensor product states represent exactly this class. Ultimately, one can view the tensors of a tensor network as successive basis transformations and truncations to a much smaller subspace relevant for the problem at hand.

In this thesis, we employ large-scale numerical simulations with tensor networks to investigate quench dynamics of different model systems. We focus on the dimensional crossover in the sudden expansion of interacting bosons in a 2D optical lattice, on domain-wall melting in systems which display MBL, and on the entanglement of mixed states represented by purification states.

We begin with a review of simulations with tensor networks in Chapter 2. After we motivated tensor networks as an Ansatz class with a short discussion of the area law in Sec. 2.1, we will introduce the conceptually simple time evolving block decimation (TEBD) algorithm [76] in Sec. 2.2.3 exemplary as a method to perform a real-time evolution of an MPS. While TEBD can be used to obtain ground states by means of an imaginary time evolution, the DMRG algorithm explained in Sec. 2.2.5 is much more efficient for this task. For both algorithms, we discuss the necessary steps to use them on infinite systems in Sec. 2.3, allowing to directly work in the thermodynamic limit. In Sec. 2.4, we will give a practical guide how to implement abelian symmetries (e.g., a particle number conservation) to accelerate tensor operations. In the modern formulation, DMRG requires to express the Hamiltonian in terms of a so-called matrix product operator (MPO). We explain a technique to efficiently generate this MPO representation for generic models in Sec. 2.5. For this, we have in mind that the use of MPS based methods requires to map a 2D system to be considered onto a 1D chain, as discussed in Sec. 2.5.2.

The implementation of of codes based on tensor networks can be quite cumbersome compared to for example an ED code. In fact, DMRG requires linear algebra subroutines like the singular value decomposition (SVD) and the Lanczos algorithm (which does ED) to be available for use. If symmetries are to be used, all of these functions need to be re-implemented or adjusted. Thus, sharing code between researches can save human resources by reducing the time required to set up a simulation (at least, if the code is well documented). Moreover, open source code enhances the transparency and reproducibility of the results. For these reasons, a program library called Tensor Network Python (TeNPy) was published as open source software [1, 2]. This library was developed mainly by the author during the preparation of this thesis, and has already found a significant number of users. We present this library in more detail in Sec. 2.6 to wrap up the review of tensor network based algorithms.

In Chapter 3, we use simulations with MPS to study the 1D-to-2D crossover in the sudden expansion of a cloud of strongly interacting bosons. This particular problem is of physical interest due to predictions for the emergence of non-equilibrium condensates at finite quasimomenta [77–79]. In the sudden expansion of hard-core bosons in a purely 1D chain, there appear quasi-condensates at finite momenta on an intermediate, yet long time scale before the quasimomentum distribution function ultimately approaches the one of the underlying free fermions [80–89]. After a formal definition of some quantities, we study the expansion in a fully 2D system in Sec. 3.4. The fast buildup of entanglement limits our simulations of this system to comparably

short times. Hence, we move on to analyze the 1D-to-2D crossover in Sec. 3.5 in quite some detail on cylinder and ladder geometries, where longer times can be reached.

In Chapter 4, we consider the effects of disorder on the expansion from a domain-wall like initial state. In a 1D chain, even a tiny amount of uncorrelated disorder leads to a full localization of the wave function of a single electron, a phenomenon known as Anderson localization [90–92]. We first study how this localization is manifested in the domain-wall melting of non-interacting electrons in Sec. 4.2, and show that the localization length can be read out from the density profile at long times. Interactions induce a delocalization at small disorder strength, such that there appears a transition from a delocalized phase into the MBL phase when the disorder strength is increased [22–24]. In Sec. 4.3, we show that this transition can be located by analyzing the domain-wall melting. As a first step into the direction of 2D, we consider a ladder in Sec. 4.4. Our work justifies the setup of an experiment with ultra-cold atoms [45].

In Chapter 5, we consider the entanglement dynamics of mixed states after local quenches. Purifications provide a way to represent density matrices, for example thermal ensembles, with MPS [93, 94], which we recapitulate in Sec. 5.1 to fix the notation. In Sec. 5.2, we then present a general method to use a freedom in the choice of the purification to obtain states with minimal entanglement entropy. The entanglement entropy at this minimum is called the entanglement of purification and of interest from a quantum information point of view, because it is linked to how efficent a purification state can be represented [95]. We benchmark our method in Sec. 5.3 both during imaginary and real-time evolution.

Finally, we summarize our work in Chapter 6 and give a short outlook.

2 Tensor networks

Most of the content of this chapter can also be found in a previous publication of the author [1]. Text and figures have been adjusted to fit into the context of the thesis.

The most prominent algorithm based on tensor networks is the DMRG method [68] which was originally conceived as an algorithm to study ground state properties of 1D systems. Since the invention in 1992, the DMRG algorithm has been successively improved and made more efficient. For example, the inclusion of abelian and non-abelian symmetries, [96–100], the introduction of single-site optimization with density matrix perturbation [101, 102], hybrid real-momentum space representation [103, 104], and the development of real-space parallelization [105] have increased the convergence speed and decreased the requirements of computational resources. An infinite version of the algorithm [106] has facilitated the investigation of translation invariant systems. The success of DMRG was extended to also simulate real-time evolution allowing to study transport and non-equilibrium phenomena [76, 107–111]. However, the bipartite entanglement of pure states after a global quench generically grows linearly with time [112], leading to a rapid exponential growth of the computational cost. This limits time evolution to rather short times. Projected entangled pair states (PEPS), or equivalently tensor product states (TPS), are a generalization of MPS to higher dimensions [113, 114]. This class of states is believed to efficiently describe a wide range of ground states of two-dimensional local Hamiltonians. PEPS serve as variational wave functions that can approximate ground states of model Hamiltonians. A number of algorithms have been proposed for PEPS, including the Corner Transfer Matrix Renormalization Group Method [115], Tensor Renormalization Group (TRG) [116], Tensor Network Renormalization (TNR) [117], and loop optimizations [118].

A number of very useful review articles on different tensor network related topics appeared over the past couple of years. Here we mention a few: Ref. [73] provides an extensive, pedagogical introduction to MPS and DMRG algorithms with detailed discussions regarding their implementation. In Ref. [119], a practical introduction to tensor networks including MPS and PEPS is given. Applications of DMRG in quantum chemistry are discussed in Ref. [120]. The early developments of the DMRG algorithm are summarized in Ref. [121]. A comparison of time-evolution methods based on MPS was recently made in Ref. [122].

In this chapter, we combine a pedagogical review of basic MPS based algorithms for both finite and infinite systems with the presentation of a versatile tensor library for Python called TeNPy. First, we motivate the ansatz of tensor product states with the area law of entanglement entropy in the following section 2.1. In Sec. 2.2 we introduce the MPS ansatz for finite systems and explain the TEBD [76] and the DMRG method [68] as prominent examples for algorithms working with MPS. In Sec. 2.3 we explain the generalization of these algorithms to the thermodynamic limit. Further, we provide a practical guide on how to implement abelian symmetries (e.g., a particle number conservation) to accelerate tensor operations in Sec. 2.4. Morover, we explain a generic way to construct the MPO representation of the Hamiltonian required for MPS based algorithms in Sec. 2.5. Finally, we present the TeNPy library and give short example codes demonstrating how to call each of the presented algorithms.

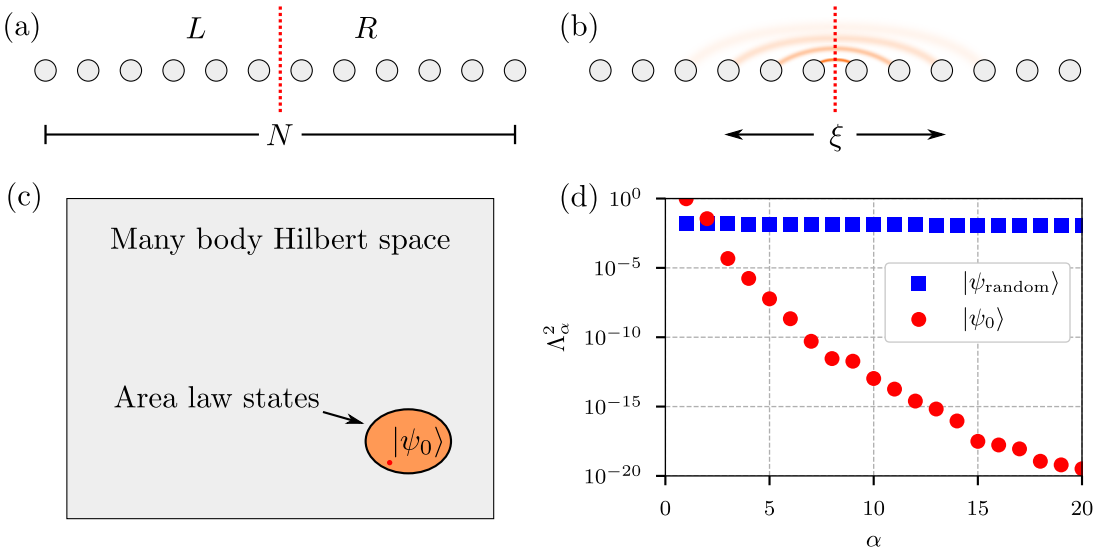

Figure 2.1 (a) Bipartition of a 1D system into two half chains. (b) Significant quantum fluctuations in gapped ground states occur only on short length scales. (c) 1D area law states make up a very small fraction of the many-body Hilbert space but contain all gapped ground states. (d) Comparison of the largest Schmidt values of the ground state of the transverse field Ising model ($g = 1.5$) and a random state for a system consisting of $N = 16$ spins. The index α labels different Schmidt values.

2.1 Entanglement in quantum many-body systems

Entanglement is one of the fundamental phenomena in quantum mechanics and implies that different degrees of freedom of a quantum system cannot be described independently. Over the past decades it was realized that the entanglement in quantum many-body systems can give access to a lot of useful information about quantum states. First, entanglement related quantities provide powerful tools to extract universal properties of quantum states. For example, scaling properties of the entanglement entropy help to characterize critical systems [123–126], and entanglement is the basis for the classification of topological orders [127, 128]. Second, the understanding of entanglement helped to develop new numerical methods to efficiently simulate quantum many-body systems [73, 129]. In the following, we give a short introduction to entanglement in 1D systems and then focus on the MPS representation.

Let us consider the bipartition of the Hilbert space $\mathcal{H} = \mathcal{H}_L \otimes \mathcal{H}_R$ of a 1D system as illustrated in Fig. 2.1(a), where $\mathcal{H}_L$ ($\mathcal{H}_R$) describes all the states defined on the left (right) of a given bond. In the so called *Schmidt decomposition*, a (pure) state $|\Psi\rangle \in \mathcal{H}$ is decomposed as

$$|\Psi\rangle = \sum_\alpha \Lambda_\alpha |\alpha\rangle_L \otimes |\alpha\rangle_R, \quad |\alpha\rangle_{L(R)} \in \mathcal{H}_{L(R)}, \tag{2.1}$$

where the states $\{|\alpha\rangle_{L(R)}\}$ form an orthonormal basis of (the relevant subspace of) $\mathcal{H}_L$ ($\mathcal{H}_R$) and $\Lambda_\alpha \geq 0$. The Schmidt decomposition is unique up to degeneracies and for a normalized state $|\Psi\rangle$ we find that $\sum_\alpha \Lambda_\alpha^2 = 1$.

An important aspect of the Schmidt decomposition is that it gives direct insight into the *bipartite entanglement* (i.e., the entanglement between degrees of freedom in $\mathcal{H}_L$ and $\mathcal{H}_R$) of a state, as we explain in the following. The amount of entanglement is measured by the *entanglement entropy*, which is defined as the von-Neumann entropy $S = -\operatorname{Tr}\left(\varrho^R \log(\varrho^R)\right)$ of

the reduced density matrix ϱ^R. The *reduced density matrix* of an entangled (pure) quantum state $|\psi\rangle$ is the density matrix of a mixed state defined on the subsystem,

$$\varrho^R \equiv \mathrm{Tr}_L \left(|\psi\rangle \langle\psi| \right). \tag{2.2}$$

A short calculation shows that it has the Schmidt states $|\alpha\rangle_R$ as eigenstates and the Schmidt coefficients are the square roots of the corresponding eigenvalues, i.e., $\varrho^R = \sum_\alpha \Lambda_\alpha^2 |\alpha\rangle_R \langle\alpha|_R$ (equivalently for ϱ^L). Hence, the entanglement entropy can be expressed in terms of the Schmidt values Λ_α,

$$S \equiv -\mathrm{Tr}\left(\varrho^R \log(\varrho^R) \right) = -\sum_\alpha \Lambda_\alpha^2 \log \Lambda_\alpha^2. \tag{2.3}$$

If there is no entanglement between the two subsystems, $S = 0$, the Schmidt decompositions consists only of a single term with $\Lambda_1 = 1$. The *entanglement spectrum* $\{\epsilon_\alpha\}$ [130] is defined in terms of the spectrum $\{\Lambda_\alpha^2\}$ of the reduced density matrix by $\Lambda_\alpha^2 = \exp(-\epsilon_\alpha)$ for each α.

2.1.1 Area law

A "typical" state in the Hilbert space shows a *volume law*, i.e., the entanglement entropy grows proportionally with the volume of the partitions. In particular, it has been shown in Ref. [131] that in a system of N sites with on-site Hilbert space dimension d, a randomly drawn state $|\psi_{\mathrm{random}}\rangle$ has an entanglement entropy of $S \approx N/2 \log d - 1/2$ for a bipartition into two parts of $N/2$ sites.

In contrast, ground states $|\psi_0\rangle$ of gapped and local Hamiltonians follow an *area law*, i.e., the entanglement entropy grows proportionally with the area of the cut [132]. For a cut of an N-site chain as shown in Fig. 2.1(a) this implies that $S(N)$ is constant for $N \gtrsim \xi$ (with ξ being the correlation length). This can be intuitively understood from the fact that a gapped ground state contains only fluctuations within the correlation length ξ and thus only degrees of freedom near the cut are entangled, as schematically indicated in Fig. 2.1(b). A rigorous proof of the area law in 1D is given in Ref. [75]. In this respect, ground states are very special states and can be found within a very small corner of the Hilbert space, as illustrated in Fig. 2.1(c).

In slightly entangled states, only a relatively small number of Schmidt states contribute significantly. This is demonstrated in Fig. 2.1(d) by comparing the largest 20 Schmidt values of an area law and a volume law state for a bipartition of an $N = 16$ chain into two half chains.

As an example of an area law state, we considered here the ground state of the transverse field Ising model

$$\hat{H} = -\sum_n \hat{\sigma}_n^z \hat{\sigma}_{n+1}^z + g\hat{\sigma}_n^x, \tag{2.4}$$

with $\hat{\sigma}_n^x$ and $\hat{\sigma}_n^z$ being the Pauli operators and $g > 0$. This $\mathbb{Z}_2$ symmetric model with a quantum phase transition at $g_c = 1$ has two very simple limits. For $g = 0$, the ground state is twofold degenerate and given by the ferromagnetic product state (symmetry broken), and at $g \to \infty$ the ground state is a product state in which all spins are polarized by the transverse field in x-direction (symmetric). For intermediate values of g, the ground states are area law type entangled states (except at the critical point). As shown in Fig. 2.1(d) for a representative example of $g = 1.5$, the ground state has essentially the entire weight contained in a few Schmidt states. Generic states fulfilling the area law show a similar behavior and thus the above observation provides an extremely useful approach to compress quantum states by truncating the Schmidt

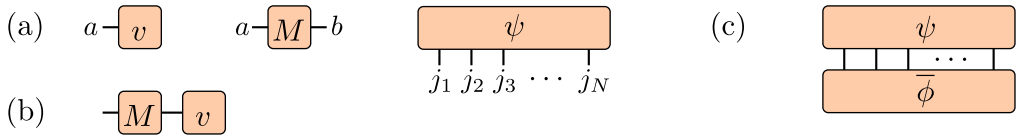

Figure 2.2 (a) Diagrammatic representations for a vector v, a matrix M, and the coefficients of a general wave function $|\psi\rangle = \sum_{j_1,j_2\ldots j_N} \psi_{j_1 j_2\ldots j_N} |j_1, j_2, \ldots, j_N\rangle$. (b) The connection of two legs symbolizes a tensor contraction, here $(Mv)_a = \sum_b M_{ab} v_b$. (c) Diagram for the overlap $\langle\phi|\psi\rangle = \sum_{j_1,j_2\ldots j_N} \overline{\phi_{j_1 j_2\ldots j_N}} \psi_{j_1 j_2\ldots j_N}$ of two wave functions.

decomposition. In particular, for all $\epsilon > 0$ we can truncate the Schmidt decomposition at some *finite* χ (independent of the system size) such that

$$\Big\| |\psi\rangle - \underbrace{\sum_{\alpha=1}^{\chi} \Lambda_\alpha |\alpha\rangle_L \otimes |\alpha\rangle_R}_{|\psi^{\text{trunc}}\rangle} \Big\| < \epsilon \tag{2.5}$$

This particular property of area law states is intimately related to the MPS representation of 1D quantum states, as we will discuss in the next chapter.

The situation is very different for a highly entangled (volume law) random state: All the Schmidt values are roughly constant for all $2^{N/2}$ states and thus only little weight is contained in the 20 dominant states (assuming an equal weight, we find $\Lambda_\alpha^2 \approx 1/2^{N/2}$ per Schmidt state).

2.2 Finite systems in one dimension

In this chapter, we consider a chain with N sites. We label the local basis on site n by $|j_n\rangle$ with $j_n = 1, \ldots, d$, e.g., for the transverse field Ising model we have spin-1/2 sites with the ($d = 2$) local states $|\uparrow\rangle, |\downarrow\rangle$. A generic (pure) quantum state can then be expanded as $|\psi\rangle = \sum_{j_1,j_2,\ldots j_N} \psi_{j_1 j_2 \cdots j_N} |j_1, j_2, \ldots, j_N\rangle$.

Before we proceed with the definition of MPS, we introduce a diagrammatic notation, which is very useful for representing tensor networks and related algorithms and has been established in the community. In this notation, a tensor with n indices is represented by a symbol with n legs. Connecting two legs among tensors symbolizes a tensor contraction, i.e., summing over the relevant indices. This is illustrated in Fig. 2.2.

2.2.1 Matrix Product States (MPS)

The class of MPS is an ansatz class where the coefficients $\psi_{j_1,\ldots,j_N}$ of a pure quantum state are decomposed into products of matrices [70, 71, 133]:

$$|\psi\rangle = \sum_{j_1,\ldots,j_N} \sum_{\alpha_2,\ldots\alpha_N} M^{[1]j_1}_{\alpha_1\alpha_2} M^{[2]j_2}_{\alpha_2\alpha_3} \ldots M^{[N]j_N}_{\alpha_N\alpha_{N+1}} |j_1, j_2, \ldots, j_N\rangle \tag{2.6}$$

$$\equiv \sum_{j_1,\ldots,j_N} M^{[1]j_1} M^{[2]j_2} \ldots M^{[N]j_N} |j_1, j_2, \ldots, j_N\rangle\,. \tag{2.7}$$

Here, each $M^{[n]j_n}$ is a $\chi_n \times \chi_{n+1}$ dimensional matrix, i.e., we have a set of d matrices for each site, which we usually group into a tensor of order 3 as shown in Fig. 2.3(a). The superscript

$[n]$ denotes the fact that for a generic state we have a different set of matrices on each site. The indices α_n of the matrices are called "bond", "virtual", or "auxiliary" indices, to distinguish them from the "physical" indices j_n. The matrices at the boundary are vectors, that is $\chi_1 = \chi_{N+1} = 1$, such that the matrix product in Eq. (2.7) produces a 1×1 matrix, i.e., a single number $\psi_{j_1,\ldots,j_n}$. In that sense, the indices α_1 and α_{N+1} are trivial and always 1; yet, introducing them leads to a uniform layout of the MPS such that we do not need to take special care about the boundaries in the algorithms. To become more familiar with the MPS notation, let us consider a few examples.

A **product state** $|\psi\rangle = |\phi^{[1]}\rangle \otimes |\phi^{[2]}\rangle \otimes \cdots \otimes |\phi^{[n]}\rangle$ can easily be written in the form of Eq. (2.7): Since it has no entanglement, the bond dimension is simply $\chi_n = 1$ on each bond and the 1×1 "matrices" are given by (see Fig. 2.3(b))

$$M^{[n]j_n} = \left(\phi^{[n]}_{j_n}\right). \tag{2.8}$$

Concretely, the ground state of the transverse field Ising model given in Eq. (2.4) at large field $g \gg 1$ is close to a product state $|\leftarrow \cdots \leftarrow\rangle \equiv \left(\frac{1}{\sqrt{2}}|\uparrow\rangle - \frac{1}{\sqrt{2}}|\downarrow\rangle\right) \otimes \cdots \otimes \left(\frac{1}{\sqrt{2}}|\uparrow\rangle - \frac{1}{\sqrt{2}}|\downarrow\rangle\right)$, which we write as an MPS using the same set of matrices on each site n,

$$M^{[n]\uparrow} = \left(\tfrac{1}{\sqrt{2}}\right) \text{ and } \qquad M^{[n]\downarrow} = \left(\tfrac{-1}{\sqrt{2}}\right). \tag{2.9}$$

For the Neel state $|\uparrow\downarrow\uparrow\downarrow \ldots\rangle$, we need different sets of matrices on odd and even sites,

$$M^{[2n-1]\uparrow} = M^{[2n]\downarrow} = \left(1\right) \text{ and } \qquad M^{[2n-1]\downarrow} = M^{[2n]\uparrow} = \left(0\right) \tag{2.10}$$

for $n = 1, \ldots, N/2$.

As a first example of a state with entanglement, we consider a dimerized **product of singlets** $\left(\frac{1}{\sqrt{2}}|\uparrow\downarrow\rangle - \frac{1}{\sqrt{2}}|\downarrow\uparrow\rangle\right) \otimes \cdots \otimes \left(\frac{1}{\sqrt{2}}|\uparrow\downarrow\rangle - \frac{1}{\sqrt{2}}|\downarrow\uparrow\rangle\right)$ on neighboring sites. This state can be written with 1×2 matrices on odd sites and 2×1 matrices on even sites given by

$$M^{[2n-1]\uparrow} = \begin{pmatrix} \frac{1}{\sqrt{2}} & 0 \end{pmatrix}, \quad M^{[2n-1]\downarrow} = \begin{pmatrix} 0 & \frac{-1}{\sqrt{2}} \end{pmatrix}, \quad M^{[2n]\uparrow} = \begin{pmatrix} 0 \\ 1 \end{pmatrix}, \quad M^{[2n]\downarrow} = \begin{pmatrix} 1 \\ 0 \end{pmatrix}. \tag{2.11}$$

Spin-1 AKLT state. Affleck, Kennedy, Lieb, and Tasaki (AKLT) constructed an exactly solvable Hamiltonian which reads

$$\hat{H} = \sum_n \hat{\vec{S}}_n \hat{\vec{S}}_{n+1} + \frac{1}{3}(\hat{\vec{S}}_n \hat{\vec{S}}_{n+1})^2 = 2 \sum_j \left(\hat{P}^{S=2}_{n,n+1} - \frac{1}{3}\right) \tag{2.12}$$

where $\hat{\vec{S}}$ are spin $S = 1$ operators and $\hat{P}^{S=2}_{n,n+1}$ is a projector onto the $S = 2$ sector of the spins on sites j and $j+1$ [134]. This model is in a topologically nontrivial phase with remarkable properties of the ground state. To construct the ground state, we note that the projector $\hat{P}^{S=2}_{n,n+1}$ does not give a contribution if we decompose the $S = 1$ spins on each site into two $S = \frac{1}{2}$ spins and form singlets between spins on neighboring sites, as illustrated in Fig. 2.3(d). While the ground state is unique on a ring with periodic boundary conditions, in a chain with open boundary conditions the $S = \frac{1}{2}$ spins on the edges do not contribute to the energy and thus lead to a 4-fold degeneracy of the ground state. Given the structure of the ground state, we can construct the corresponding MPS as shown in Fig. 2.3(e): We start by writing the product of singlets with the matrices of eq. 2.11 and add arbitrary spin-$\frac{1}{2}$ states ϕ^L and ϕ^R on the left and right. We apply

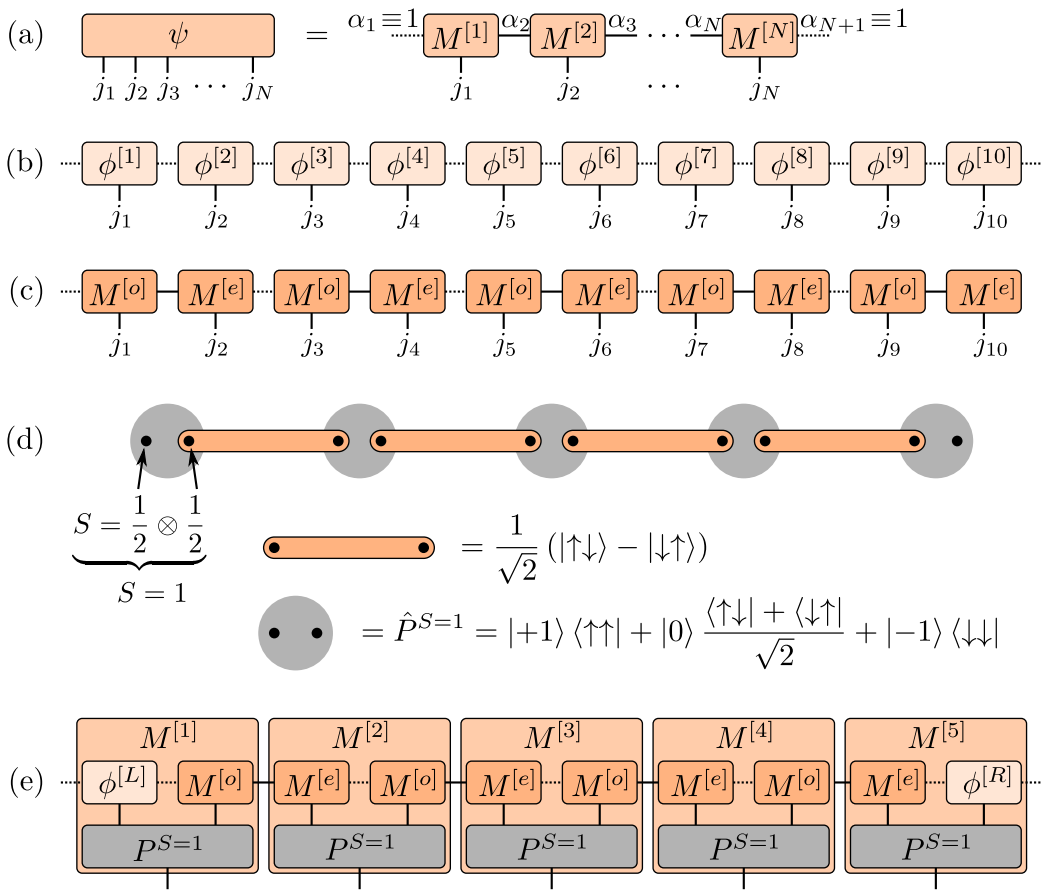

Figure 2.3 (a) In an MPS, the amplitude of the wave function is decomposed into a product of matrices $M^{[n]j_n}$. The indices α_1 and α_{N+1} are trivial, which we indicate by dashed lines. (b) A product state can be written as a trivial MPS with bond dimensions $\chi = 1$. (c) The MPS for a product of singlets on neighboring sites, with $M^{[1]}, M^{[2]}$ given in Eq. (2.11). (d) Diagrammatic representation of the AKLT state. The $S = 1$ sites (gray circles) are decomposed into two $S = \frac{1}{2}$ that form singlets between neighboring sites. With open boundary conditions, the $S = \frac{1}{2}$ spins on the left and right are free edge modes leading to a four-fold degeneracy of the ground state. (e) The AKLT state can be represented by an MPS with bond dimension $\chi = 2$.

the projectors $\hat{P}^{S=1}$ to map the two spin-$\frac{1}{2}$ onto the physical spin-1 site, and contract the three tensors on each site to obtain the MPS structure. For sites $1 < n < N$ in the bulk, we obtain

$$M^{[n]+1} = \sqrt{\frac{4}{3}} \begin{pmatrix} 0 & 0 \\ \frac{1}{\sqrt{2}} & 0 \end{pmatrix} \qquad M^{[n]0} = \sqrt{\frac{4}{3}} \begin{pmatrix} \frac{1}{2} & 0 \\ 0 & -\frac{1}{2} \end{pmatrix} \qquad M^{[n]-1} = \sqrt{\frac{4}{3}} \begin{pmatrix} 0 & -\frac{1}{\sqrt{2}} \\ 0 & 0 \end{pmatrix}. \tag{2.13}$$

Here, we included the factor $\sqrt{\frac{4}{3}}$ to normalize the MPS.

In general, any state in a finite system can be decomposed *exactly* into the MPS form of Eq. (2.7). The caveat is that for a generic state (with a volume law entanglement) the required bond dimension $\chi_{\max} := \max_n \chi_n$ increases exponentially with the number of sites N. However, by linking the MPS representation with the Schmidt decomposition (2.1), we will see that we can approximate area law states very well (in the sense of Eq. (2.5)) by MPS with a finite bond

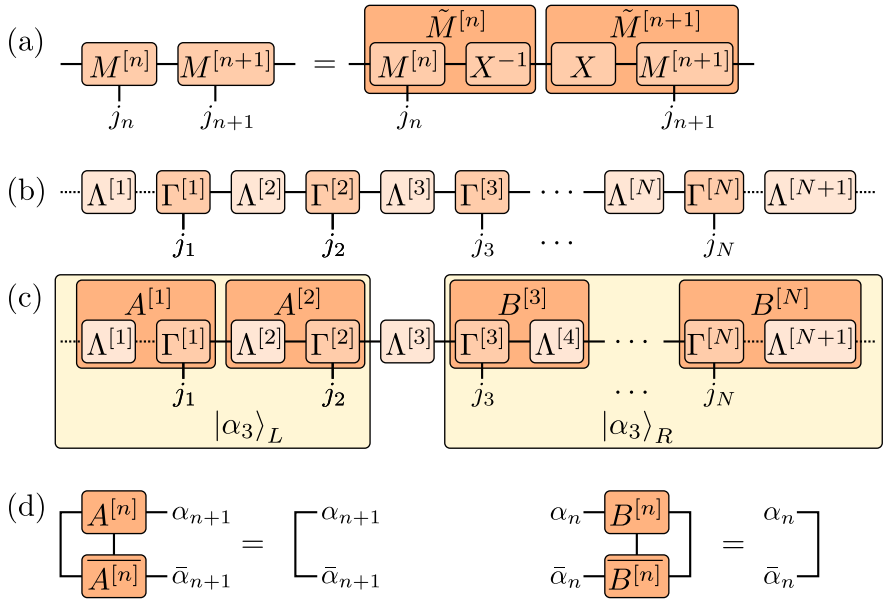

Figure 2.4 (a) The representation of an MPS is not unique. (b) This freedom is used to define the canonical form, where the $\Lambda^{[n]}$ are diagonal matrices containing the Schmidt values. (c) The canonical form allows to easily read off the Schmidt decomposition Eq. (2.1) on each bond, here exemplary on bond $n = 3$. (d) Orthonormality conditions for the Schmidt states.

dimension $\chi_{\max}$ [135, 136]. This link is given by the so-called canonical form of an MPS, which we introduce now.

2.2.2 Canonical form

The MPS representation in Eq. (2.7) is not unique. Consider the bond between sites n and $n+1$, which defines a bipartition into $L = \{1, \ldots, n\}$ and $R = \{n+1, \ldots, N\}$. Given an invertible $\chi_{n+1} \times \chi_{n+1}$ matrix X, we can replace

$$M^{[n]j_n} \to \tilde{M}^{[n]j_n} := M^{[n]j_n} X^{-1}, \qquad M^{[n+1]j_{n+1}} \to \tilde{M}^{[n+1]j_{n+1}} := X M^{[n+1]j_{n+1}} \tag{2.14}$$

and still represent the same state $|\psi\rangle$, see Fig. 2.4(a). This freedom can be used to define a convenient "canonical form" of the MPS, following Ref. [137, 138]. Without loss of generality, we can decompose the matrices $\tilde{M}^{[n]j_n} = \tilde{\Gamma}^{[n]j_n} \tilde{\Lambda}^{[n+1]}$, where $\tilde{\Lambda}^{[n+1]}$ is a square, diagonal matrix with positive entries $\tilde{\Lambda}^{[n+1]}_{\alpha_{n+1}\alpha_{n+1}}$ on the diagonal. Performing partial contractions gives a representation looking very similar to the Schmidt decomposition (2.1):

$$\begin{aligned} |\psi\rangle &= \sum_{j_1,\ldots,j_N} M^{[1]j_1} \ldots M^{[n-1]j_{n-1}} \tilde{\Gamma}^{[n]j_n} \tilde{\Lambda}^{[n+1]} \tilde{M}^{[n+1]j_{n+1}} M^{[n+2]j_{n+2}} \ldots M^{[N]j_N} |j_1, \ldots, j_N\rangle \\ &= \sum_{\tilde{\alpha}_{n+1}} \tilde{\Lambda}^{[n+1]}_{\tilde{\alpha}_{n+1},\tilde{\alpha}_{n+1}} |\tilde{\alpha}_{n+1}\rangle_L \otimes |\tilde{\alpha}_{n+1}\rangle_R , \text{ where} \end{aligned} \tag{2.15}$$

$$|\tilde{\alpha}_{n+1}\rangle_L = \sum_{j_1,\ldots,j_n} \left(M^{[1]j_1} \ldots M^{[n-1]j_{n-1}} \tilde{\Gamma}^{[n]j_n} \right)_{1,\tilde{\alpha}_{n+1}} |j_1, \ldots, j_n\rangle , \tag{2.16}$$

$$|\tilde{\alpha}_{n+1}\rangle_R = \sum_{j_{n+1},\ldots,j_N} \left(\tilde{M}^{[n+1]j_{n+1}} M^{[n+2]j_{n+2}} \ldots M^{[N]j_N} \right)_{\tilde{\alpha}_{n+1},1} |j_{n+1}, \ldots, j_N\rangle . \tag{2.17}$$

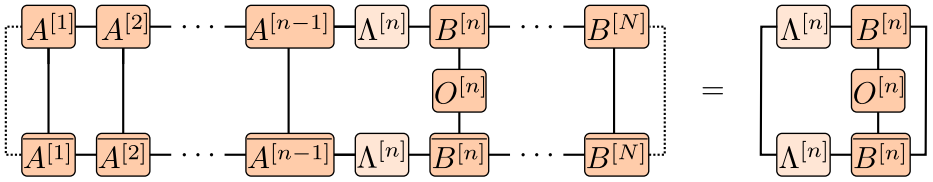

Figure 2.5 Due to the orthogonality conditions depicted in Fig. 2.4(d), evaluating the expectation value $\langle\psi|O^{[n]}|\psi\rangle$ of a local operator $O^{[n]}$ requires only a contraction of local tensors.

However, for general M and $\tilde{\Gamma}^{[n]}$, the states $|\tilde{\alpha}_{n+1}\rangle_{L/R}$ will not be orthonormal. Note that we can interpret the X in Eq. (2.14) as a basis transformation of the states $|\tilde{\alpha}_{n+1}\rangle_R$ in Eq. (2.17). The idea of the canonical form is to choose the X in Eq. (2.14) such that it maps $|\tilde{\alpha}_{n+1}\rangle_R$ to the Schmidt states $|\alpha_{n+1}\rangle_R$. Using the Schmidt values $\Lambda^{[n+1]}_{\alpha_{n+1}\alpha_{n+1}}$ on the diagonal of $\tilde{\Lambda}^{[n+1]} \to \Lambda^{[n+1]}$, we find that Eq. (2.15) indeed gives the Schmidt decomposition. Repeating this on each bond yields the canonical form depicted in Fig. 2.4(b),

$$|\Psi\rangle = \sum_{j_1,\ldots,j_N} \Lambda^{[1]}\Gamma^{[1]j_1}\Lambda^{[2]}\Gamma^{[2]j_2}\Lambda^{[3]}\cdots\Lambda^{[N]}\Gamma^{[N]j_N}\Lambda^{[N+1]}\,|j_1,\ldots,j_N\rangle\,. \tag{2.18}$$

Here, we have introduced trivial 1×1 matrices $\Lambda^{[1]} \equiv \Lambda^{[N+1]} \equiv \begin{pmatrix}1\end{pmatrix}$ multiplied to the trivial legs of the first and last tensor, again with the goal to achieve a uniform bulk. While the canonical form is useful as it allows to quickly read off the Schmidt decomposition on any bond, in practice we usually group each Γ with one of the Λ matrices and define

$$A^{[n]j_n} \equiv \Lambda^{[n]}\Gamma^{[n]j_n}, \qquad\qquad B^{[n]j_n} \equiv \Gamma^{[n]j_n}\Lambda^{[n+1]}. \tag{2.19}$$

If we write an MPS entirely with A tensors (B tensors), it is said to be in left (right) canonical form. In fact, all the examples given in Eq. (2.8)-(2.13) are in right-canonical form. If we consider the bond between sites n and $n+1$, we can write the MPS in a "mixed" canonical form with A tensors up to site n and B tensors starting from site $n+1$, as depicted in Fig. 2.4(c) for $n = 2$. The A and B tensors transform the Schmidt basis from one bond to the next:

$$|\alpha_{n+1}\rangle_L = \sum_{\alpha_n, j_n} A^{[n]j_n}_{\alpha_n\alpha_{n+1}}\,|\alpha_n\rangle_L \otimes |j_n\rangle\,, \qquad |\alpha_n\rangle_R = \sum_{j_n,\alpha_{n+1}} B^{[n]j_n}_{\alpha_n\alpha_{n+1}}\,|j_n\rangle \otimes |\alpha_{n+1}\rangle_R\,. \tag{2.20}$$

Therefore, the orthonormality conditions $\langle\alpha_n|_L\,|\bar{\alpha}_n\rangle_L = \delta_{\alpha_n\bar{\alpha}_n} = \langle\alpha_n|_R\,|\bar{\alpha}_n\rangle_R$ translate into the very useful relations shown in Fig. 2.4(d).

One great advantage of the canonical form is that these relations allow to evaluate expectation values of local operators very easily. As shown in Fig. 2.5, this requires only the contraction of a few *local* tensors. If needed, we can easily convert the left and right canonical forms into each other, e.g., $A^{[n]} = \Lambda^{[n]}B^{[n]}\left(\Lambda^{[n+1]}\right)^{-1}$; since the $\Lambda^{[n]}$ are diagonal matrices, their inverses are simply given by diagonal matrices with the inverse Schmidt values[1].

As mentioned above, we can represent any state in a finite system if we allow an arbitrary bond dimension $\chi_{\max}$; but to avoid a blowup of the computational cost (exponentially in N), we need to *truncate* the matrices to a moderate bond dimension $\chi_{\max}$. Consider the bond between sites n and $n+1$. It turns out that the simple truncation of the Schmidt decomposition is optimal in the sense of minimizing the error ϵ in Eq. (2.5). In the (mixed) canonical form, we can therefore simply

[1] If $\Lambda^{[n+1]}_{\alpha_{n+1}\alpha_{n+1}} = 0$ for some α_{n+1}, we can remove the corresponding columns of $B^{[n]}$ and rows of $B^{[n+1]}$ before taking the inverse, as they do not contribute to the wave function.

discard[2] some rows of $A^{[n]j_n}$, diagonal entries of $\Lambda^{[n+1]}$ and columns of $B^{[n+1]j_{n+1}}$ (namely the ones corresponding to the smallest Schmidt values). To preserve the norm of the wave function, we renormalize the Schmidt values on the diagonal of $\Lambda^{[n+1]}$ such that $\sum_{\alpha_{n+1}} \left(\Lambda^{[n+1]}_{\alpha_{n+1}\alpha_{n+1}}\right)^2 = 1$.

2.2.3 Time Evolving Block Decimation (TEBD)

In the TEBD algorithm [76], we are interested in evaluating the time evolution of a quantum state:

$$|\psi(t)\rangle = \hat{U}(t)\,|\psi(0)\rangle\,. \tag{2.21}$$

The time evolution operator $\hat{U}$ can either be $\hat{U}(t) = \exp(-it\hat{H})$ yielding a real time evolution, or an imaginary time evolution $\hat{U}(\tau) = \exp(-\tau\hat{H})$. The latter can be used to evaluate (finite temperature) Green's functions or as a first, conceptually simple way to find the ground state[3] of the Hamiltonian $\hat{H}$ through the relation

$$|\psi_{\mathrm{GS}}\rangle = \lim_{\tau\to\infty} \frac{e^{-\tau\hat{H}}\,|\psi_0\rangle}{\left\| e^{-\tau\hat{H}}\,|\psi_0\rangle \right\|}. \tag{2.22}$$

The TEBD algorithm makes use of the Suzuki-Trotter decomposition [139], which approximates the exponent of a sum of operators with a product of exponents of the same operators. For example, the first and second order expansions read

$$e^{(X+Y)\delta} = e^{X\delta}e^{Y\delta} + O(\delta^2), \tag{2.23}$$

$$e^{(X+Y)\delta} = e^{X\delta/2}e^{Y\delta}e^{X\delta/2} + O(\delta^3). \tag{2.24}$$

Here X and Y are operators, and δ is a small parameter. To make use of these expressions, we assume that the Hamiltonian is a sum of two-site operators of the form $\hat{H} = \sum_n \hat{h}^{[n,n+1]}$, where $\hat{h}^{[n,n+1]}$ acts only on sites n and $n+1$, and decompose it as a sum[4]

$$\hat{H} = \underbrace{\sum_{n \text{ odd}} \hat{h}^{[n,n+1]}}_{\hat{H}_{\mathrm{odd}}} + \underbrace{\sum_{n \text{ even}} \hat{h}^{[n,n+1]}}_{\hat{H}_{\mathrm{even}}}. \tag{2.25}$$

Each term $\hat{H}_{\mathrm{odd}}$ and $\hat{H}_{\mathrm{even}}$ consists of a sum of commuting operators, therefore $e^{\hat{H}_{\mathrm{odd}}\delta} = \prod_{n \text{ odd}} e^{\hat{h}^{[n,n+1]}\delta}$ and similar for $\hat{H}_{\mathrm{even}}$.

We now divide the time into small time slices $\delta t \ll 1$ (the relevant time scale is in fact the inverse gap) and consider a time evolution operator $\hat{U}(\delta t)$. Using, as an example, the first order decomposition in Eq. (2.23), the operator $\hat{U}(\delta t)$ can be expanded into products of two-site unitary operators

$$\hat{U}(\delta t) \approx \left[\prod_{n \text{ odd}} \hat{U}^{[n,n+1]}(\delta t)\right]\left[\prod_{n \text{ even}} \hat{U}^{[n,n+1]}(\delta t)\right], \tag{2.26}$$

[2] Strictly speaking, this changes the Schmidt values and vectors on *other* bonds and thus destroys the canonical form! However, if the discarded weight $\sum_{\alpha>\chi}\left(\Lambda^{[n]}_{\alpha\alpha}\right)^2$ is small, this error might be ignored.

[3] As explained later on, the DMRG algorithm is a better alternative for this task.

[4] One can extend TEBD for Hamiltonians with (limited) long-range couplings (e.g., next-to-nearest-neighbor couplings) by introducing so-called swap gates [140].

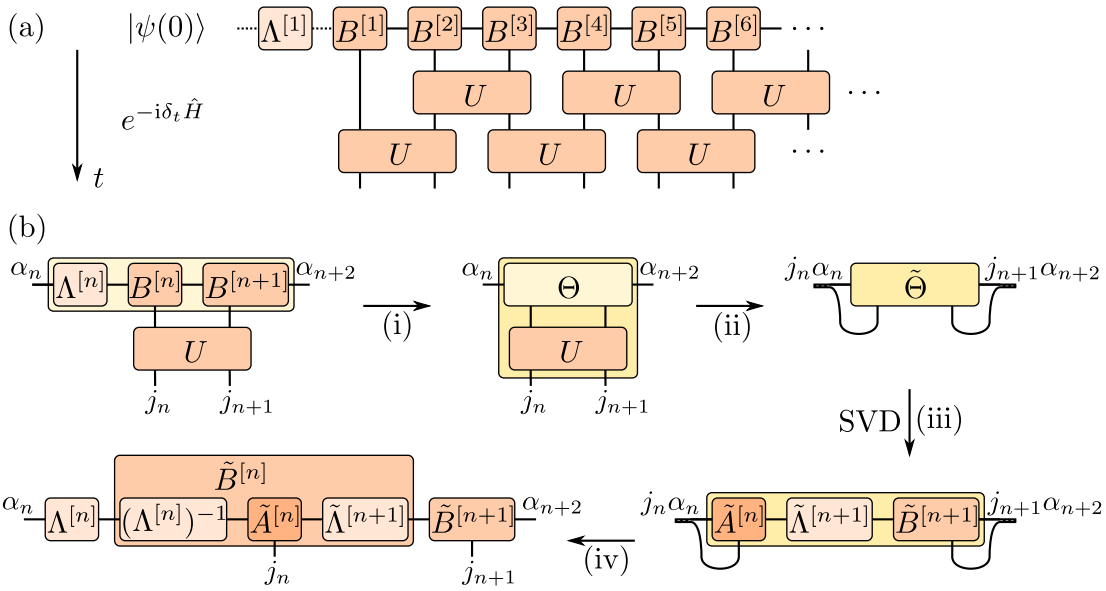

Figure 2.6 (a) In TEBD each time step δt of a time evolution is approximated using a Suzuki-Trotter decomposition, i.e., the time evolution operator is expressed as a product of two-site operators. (b) Update to apply a two-site unitary $\hat{U}$ and recover the MPS form, see main text for details.

where $\hat{U}^{[n,n+1]}(\delta t) = e^{-i\,\delta t\,\hat{h}^{[n,n+1]}}$. This decomposition of the time evolution operator is shown pictorially in Fig. 2.6(a). The successive application of these two-site unitary operators to an MPS is the main part of the algorithm and explained in the following.

Local unitary updates of an MPS. One of the advantages of the MPS representation is that local transformations can be performed efficiently. Moreover, the canonical form discussed above is preserved if the transformations are unitary [137].

A one-site unitary $\hat{U}$ simply transforms the tensors Γ of the MPS

$$\tilde{\Gamma}^{[n]j_n}_{\alpha_n\alpha_{n+1}} = \sum_{j'_n} \hat{U}^{j_n}_{j'_n} \Gamma^{[n]j'_n}_{\alpha_n\alpha_{n+1}}. \tag{2.27}$$

In such a case the entanglement of the wave-function is not affected and thus the values of Λ do not change.

The update procedure for a two-site unitary transformation acting on two neighboring sites n and $n+1$ is shown in Fig. 2.6(b). We first find the wave function in the basis spanned by the left Schmidt states $|\alpha_n\rangle_L$, the local basis $|j_n\rangle$ and $|j_{n+1}\rangle$ on sites n and $n+1$, and the right Schmidt states $|\alpha_{n+2}\rangle_R$, which together form an orthonormal basis $\{|\alpha_n\rangle_L \otimes |j_n\rangle \otimes |j_{n+1}\rangle \otimes |\alpha_{n+2}\rangle_R\}$. Calling the wave function coefficients Θ, the state is expressed as

$$|\psi\rangle = \sum_{\alpha_n, j_n, j_{n+1}, \alpha_{n+2}} \Theta^{j_n j_{n+1}}_{\alpha_n\alpha_{n+2}} |\alpha_n\rangle_L |j_n\rangle |j_{n+1}\rangle |\alpha_{n+2}\rangle_R . \tag{2.28}$$

Using the definitions of $|\alpha\rangle_{L/R}$ shown in Fig. 2.4(c), Θ is given by

$$\Theta^{j_n j_{n+1}}_{\alpha_n\alpha_{n+2}} = \sum_{\alpha_{n+1}} \Lambda^{[n]}_{\alpha_n\alpha_n} B^{[n],j_n}_{\alpha_n\alpha_{n+1}} B^{[n+1],j_{n+1}}_{\alpha_{n+1}\alpha_{n+2}} . \tag{2.29}$$

Writing the wave function in this basis is useful because it is easy to apply the two-site unitary in step (ii) of the algorithm:

$$\tilde{\Theta}^{j_n j_{n+1}}_{\alpha_n \alpha_{n+2}} = \sum_{j'_n j'_{n+1}} \hat{U}^{j_n j_{n+1}}_{j'_n j'_{n+1}} \Theta^{j'_n j'_{n+1}}_{\alpha_n \alpha_{n+2}}. \tag{2.30}$$

Next we have to extract the new tensors $\tilde{B}^{[n]}$, $\tilde{B}^{[n+1]}$ and $\tilde{\Lambda}^{[n+1]}$ from the transformed tensor $\tilde{\Theta}$ in a manner that preserves the canonical form. We first "reshape" the tensor $\tilde{\Theta}$ by combining indices to obtain a $d\chi_n \times d\chi_{n+2}$ dimensional matrix $\tilde{\Theta}_{j_n \alpha_n ; j_{n+1} \alpha_{n+2}}$. Because the basis $\{|\alpha_n\rangle_L \otimes |j_n\rangle\}$ is orthonormal, as for the right, it is natural to decompose the matrix using the SVD in step (iii) into

$$\tilde{\Theta}_{j_n \alpha_n ; j_{n+1} \alpha_{n+2}} = \sum_{\alpha_{n+1}} \tilde{A}^{[n]}_{j_n \alpha_n ; \alpha_{n+1}} \tilde{\Lambda}^{[n+1]}_{\alpha_{n+1} \alpha_{n+1}} \tilde{B}^{[n+1]}_{\alpha_{n+1} ; j_{n+1} \alpha_{n+2}}, \tag{2.31}$$

where $\tilde{A}^{[n]}$, $\tilde{B}^{[n+1]}$ are isometries and $\tilde{\Lambda}^{[n+1]}$ is a diagonal matrix. Indeed, the suggestive notation that the new tensors are in mixed canonical form is justified, since the SVD yields a Schmidt decomposition of the wave function for a bipartition at the bond between sites n and $n+1$. The isometry $\tilde{A}^{[n]}$ relates the new Schmidt states $|\alpha_{n+1}\rangle_L$ to the combined bases $|\alpha_n\rangle_L \otimes |j_n\rangle$. Analogously, the Schmidt states for the right site are obtained from the matrix $B^{[n+1]}$. Thus the diagonal matrix $\tilde{\Lambda}^{[n+1]}$ contains precisely the Schmidt values of the transformed state. In a last step (iv), we reshape the obtained matrices $\tilde{A}^{[n]}$, $\tilde{B}^{[n+1]}$ back to tensors with 3 indices and recover the right canonical form by

$$\tilde{B}^{[n] j_n}_{\alpha_n \alpha_{n+1}} = (\Lambda^{[n]})^{-1}_{\alpha_n \alpha_n} \tilde{A}^{[n]}_{j_n \alpha_n ; \alpha_{n+1}} \tilde{\Lambda}^{[n+1]}_{\alpha_{n+1} \alpha_{n+1}} \text{ and } \qquad \tilde{B}^{[n+1] j_{n+1}}_{\alpha_{n+1} \alpha_{n+2}} = \tilde{B}^{[n+1]}_{\alpha_{n+1} ; j_{n+1} \alpha_{n+2}}. \tag{2.32}$$

After the update, the new MPS is still in the canonical form. The entanglement at the bond $n, n+1$ has changed and the bond dimension increased to $d\chi$. Thus the amount of information in the wave function grows exponentially if we successively apply unitaries to the state. To overcome this problem, we perform an approximation by fixing the maximal number of Schmidt terms to $\chi_{\max}$. In each update, only the $\chi_{\max}$ most important states are kept in step (iii), i.e., if we order the Schmidt states according to their size we simply truncate the range of the index α_{n+1} in Eq. (2.31) to be $1 \ldots \chi_{\max}$. This approximation limits the dimension of the MPS and the tensors B have at most a dimension of $\chi_{\max} \times d \times \chi_{\max}$. Given that the truncated weight is small, the normalization conditions for the canonical form will be fulfilled to a good approximation. In order to keep the wave function normalized, one should divide by the norm after the truncation, i.e., divide by $\mathcal{N} = \sqrt{\sum_{j_n, j_{n+1}, \alpha_n, \alpha_{n+2}} \left|\Theta^{j_n j_{n+1}}_{\alpha_n \alpha_{n+2}}\right|^2}$.

Generically, the entanglement entropy increases with time and hence would require exponentially growing bond dimensions for an accurate description. With a finite $\chi_{\max}$ limited by computational resources, the truncation errors become more severe at intermediate to large times, and the approximations made in TEBD are no longer controlled: the simulation "breaks down". For example, TEBD does not even preserve the energy when the truncation is large. An improved algorithm based on the time dependent variational principle (TDVP) was introduced in Refs. [110, 111] which performs a unitary evolution in the space of MPS with given bond dimension $\chi_{\max}$.

If we perform an imaginary time evolution of the state, the operator $\hat{U}$ is not unitary and thus TEBD does not conserve the canonical form. It turns out, however, that the successive Schmidt decompositions assure a good approximation as long as the time steps are chosen small enough. One way to obtain very accurate results is to decrease the size of the time steps successively [138].

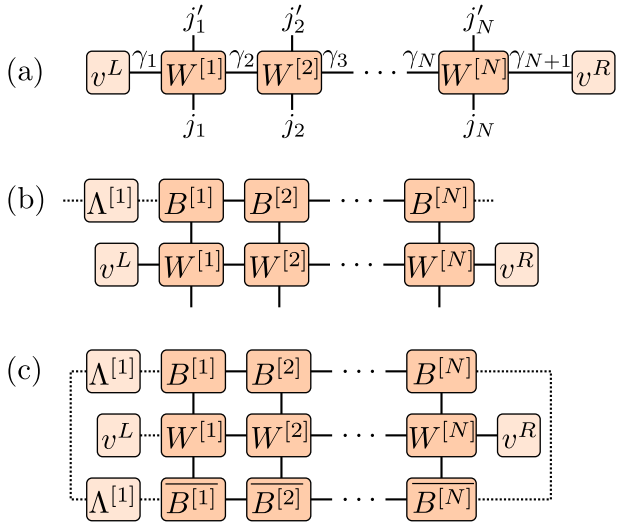

Figure 2.7 (a) An operator O acting on the entire chain expressed as an MPO. (b) An MPO acting on an MPS in right canonical form, $O|\psi\rangle$. (c) The expectation value $\langle\psi|O|\psi\rangle$.

The simulation cost of the TEBD algorithm scales as $O(d^3\chi_{\max}^3)$ and the most time consuming part of the algorithm is the SVD in step (iii). Numerically, the algorithm can become unstable when the values of Λ become very small since the matrix has to be inverted in order to extract the new tensors in step (iv) of the algorithm. This problem can be avoided by applying a slightly modified version of this algorithm as introduced by Hastings in Ref. [141].

2.2.4 Matrix Product Operators (MPO)

The DMRG algorithms explained in the next section relies on expressing the Hamiltonian in the form of a MPO. An MPO is a natural generalization of an MPS to the space of operators, given by

$$\hat{O} = \sum_{\substack{j_1,\ldots,j_N \\ j'_1,\ldots,j'_N}} v^L W^{[1]j_1 j'_1} W^{[2]j_2 j'_2} \ldots W^{[N]j_N j'_N} v^R \, |j_1,\ldots,j_N\rangle \langle j'_1,\ldots,j'_N|, \tag{2.33}$$

where $W^{[n]j_n j'_n}$ are $D \times D$ matrices, and $|j_n\rangle$, $|j'_n\rangle$ represent the local basis states at site n, as before. At the boundaries we initiate and terminate the MPO by the left and right vectors v^L, v^R. A diagrammatic representation of an MPO is given in Fig. 2.7(a). The advantage of the MPO is that it can be applied efficiently to a matrix product state as shown in Fig. 2.7(b).

All local Hamiltonians with only short range interactions can be represented *exactly* using an MPO of a small dimension D. Let us consider, for example, the MPO of the anisotropic Heisenberg (XXZ) model in the presence of a field h_n which can vary from site to site. The Hamiltonian is

$$\hat{H}^{\mathrm{XXZ}} = J \sum_n \left(\hat{S}^x_n \hat{S}^x_{n+1} + \hat{S}^y_n \hat{S}^y_{n+1} + \Delta \hat{S}^z_n \hat{S}^z_{n+1} \right) - \sum_n h_n \hat{S}^z_n, \tag{2.34}$$

where $\hat{S}_n^\gamma$, with $\gamma = x, y, z$, is the γ-component of the spin-S operator at site n, Δ is the XXZ anisotropic interaction parameter. Expressed as a tensor product, the Hamiltonian takes the following form:

$$\begin{aligned}\hat{H}^{\mathrm{XXZ}} = J\big(\quad & \hat{S}^x \otimes \hat{S}^x \otimes \hat{\mathbb{1}} \otimes \cdots \otimes \hat{\mathbb{1}} + \hat{\mathbb{1}} \otimes \hat{S}^x \otimes \hat{S}^x \otimes \cdots \otimes \hat{\mathbb{1}} + \ldots \\ + \ & \hat{S}^y \otimes \hat{S}^y \otimes \hat{\mathbb{1}} \otimes \cdots \otimes \hat{\mathbb{1}} + \hat{\mathbb{1}} \otimes \hat{S}^y \otimes \hat{S}^y \otimes \cdots \otimes \hat{\mathbb{1}} + \ldots \\ & + \Delta \hat{S}^z \otimes \hat{S}^z \otimes \hat{\mathbb{1}} \otimes \cdots \otimes \hat{\mathbb{1}} + \ldots \big) \\ & - h_1 \hat{S}^z \otimes \hat{\mathbb{1}} \otimes \hat{\mathbb{1}} \otimes \cdots \otimes \hat{\mathbb{1}} - \hat{\mathbb{1}} \otimes h_2 \hat{S}^z \otimes \hat{\mathbb{1}} \otimes \cdots \otimes \hat{\mathbb{1}} - \ldots\end{aligned} \tag{2.35}$$

The corresponding MPO has a dimension $D = 5$ and can be given by

$$W^{[n]} = \begin{pmatrix} \hat{\mathbb{1}} & \hat{S}^x & \hat{S}^y & \hat{S}^z & -h_n \hat{S}^z \\ 0 & 0 & 0 & 0 & J\hat{S}^x \\ 0 & 0 & 0 & 0 & J\hat{S}^y \\ 0 & 0 & 0 & 0 & J\Delta\hat{S}^z \\ 0 & 0 & 0 & 0 & \hat{\mathbb{1}} \end{pmatrix}, \tag{2.36}$$

where the entries of this matrix are operators acting on site n, corresponding to the indices j_n, j_n', and

$$v^L = \begin{pmatrix} 1, & 0, & 0, & 0, & 0 \end{pmatrix}, \qquad v^R = \begin{pmatrix} 0, & 0, & 0, & 0, & 1 \end{pmatrix}^T. \tag{2.37}$$

One can easily check that the product of the given matrices does indeed yield the Hamiltonian of Eq. (2.35). When we want to run simulations, we have typically the inverse problem: how do we have to chose $W^{[n]}$ to obtain a given Hamiltonian? We will discuss this in Sec. 2.5.1. Further details on the MPO form of operators can be found in Refs. [73, 142].

2.2.5 Density Matrix Renormalization Group (DMRG)

We now discuss the Density Matrix Renormalization Group (DMRG) algorithm [68]. Unlike TEBD, the DMRG is a variational approach to optimize the MPS, but the algorithms have many steps in common. One advantage of the DMRG is that it does not rely on a Suzuki-Trotter decomposition of the Hamiltonian and thus applies to systems with longer range interactions. We assume only that the Hamiltonian has been written as an MPO. Secondly, the convergence of the DMRG method to the ground state is in practice much faster. This is particularly the case if the gap above the ground state is small and the correlation length is long.

The schematic idea for the DMRG algorithm is as follows (see Fig. 2.8). Like in TEBD, the state at each step is represented by an MPS. We variationally optimize the tensors of two neighboring sites (say n and $n+1$) to minimize the ground state energy $\langle\psi|\hat{H}|\psi\rangle$, while keeping the rest of the chain fixed. To do so, at each step we represent the initial wave function $|\psi\rangle$ using the two site tensor $\Theta^{j_n j_{n+1}}_{\alpha_n \alpha_{n+2}}$ (as previously defined in Eq. (2.29) the TEBD section), project the Hamiltonian into the space spanned by the basis set $\{|\alpha_n\rangle_L \otimes |j_n\rangle \otimes |j_{n+1}\rangle \otimes |\alpha_{n+2}\rangle_R\}$, and use an iterative algorithm (e.g., Lanczos) to lower the energy. Repeating this two-site update for each pair of neighboring sites, the wave function converges to the ground state. While the Trotter decomposition requires to update first all even bonds and then odd bonds, see Eq. (2.26), in the DMRG we perform the two-site updates in a sequential order[5], starting from the left

[5] The two-site update is non-unitary and hence destroys the canonical form on *other* bonds. However, the sequential order (together with the properties of the SVD used in the update) ensures that the basis $\{|\alpha_n\rangle_L \otimes |j_n\rangle \otimes |j_{n+1}\rangle \otimes |\alpha_{n+2}\rangle_R\}$ is still orthonormal.

and proceeding to the right, $n = 1, 2, 3, \ldots, L-2, L-1$, and then back from right to left, $n = L-1, L-2, \ldots, 3, 2, 1$. This sequence is called a "sweep" from left to right and back.

Two-site update. We start by describing the update of the tensors on two neighboring sites n and $n+1$. Let us assume that we have the MPS in mixed canonical form as depicted in Fig. 2.8(a). We now want to find new $A^{[n]}, \Lambda^{[n]}, B^{[n+1]} \to \tilde{A}^{[n]}, \tilde{\Lambda}^{[n]}, \tilde{B}^{[n+1]}$ while keeping all other tensors fixed. Step (i) of the update is identical to the first step in the TEBD method: We contract the tensors for two neighboring sites to obtain the initial two-site wave function $\Theta^{j_n j_{n+1}}_{\alpha_n \alpha_{n+2}}$. The orthonormal basis $\{|\alpha_n\rangle_L \otimes |j_n\rangle \otimes |j_{n+1}\rangle \otimes |\alpha_{n+2}\rangle_R\}$ spans the variational space $|\tilde{\psi}\rangle = \sum_{\alpha_n, j_n, j_{n+1}, \alpha_{n+2}} \tilde{\Theta}^{j_n j_{n+1}}_{\alpha_n \alpha_{n+2}} |\alpha_n j_n j_{n+1} \alpha_{n+2}\rangle$ of the update, in which we must minimize the energy $E = \langle\tilde{\psi}|\hat{H}^{\text{eff}}|\tilde{\psi}\rangle$ in order to determine the new optimal $\tilde{\Theta}$. Here, $\hat{H}^{\text{eff}}$ is the Hamiltonian projected onto the variational space. Recall from Fig. 2.4(c) that the product $A^{[1]}A^{[2]} \cdots A^{[n-1]}$ gives exactly the projection from $|i_1 i_2 \ldots i_{n-1}\rangle$ to $|\alpha_n\rangle_L$, and similarly $B^{[n+2]} \cdots B^{[L]}$ maps $|i_{n+2} \ldots i_N\rangle$ to $|\alpha_{n+1}\rangle_R$. Hence, $\hat{H}^{\text{eff}}$ is given by the network shown in Fig. 2.8(b). For convenience, we have contracted the tensors strictly left of site n to form $L^{[n]}$, and the ones to the right of site $n+1$ into $R^{[n+1]}$, respectively. We call these partial contractions $L^{[n]}$ and $R^{[n+1]}$ the left and right "environments". Each environment has three open legs, e.g., $L^{[n]}$ has an MPO bond index γ_n and the two bond indices $\alpha_n, \overline{\alpha}_n$ of the ket and bra MPS. For now let us assume that we already performed these contractions; we will later come back to the initialization of them.

Grouping the indices on the top and bottom, we can view $\hat{H}^{\text{eff}}$ as a matrix with dimensions up to $\chi_{\max}^2 d^2 \times \chi_{\max}^2 d^2$. Minimizing the energy $E = \langle\tilde{\psi}|\hat{H}^{\text{eff}}|\tilde{\psi}\rangle$ thus means to find the the $\chi_{\max}^2 d^2$ dimensional ground-state vector $\tilde{\Theta}$ of the effective Hamiltonian. Since this is the computationally most expensive part of the DMRG algorithm, it is advisable to use an iterative procedure like the Lanczos algorithm instead of a full diagonalization of $\hat{H}^{\text{eff}}$. If the previous two-site wave function Θ obtained in step (i) is already a good approximation of the ground state, the Lanczos algorithm typically converges after a few steps and thus requires only a few "matrix-vector" multiplications, i.e., contractions of $\hat{H}^{\text{eff}}$ with Θ. Note that the scaling of such a matrix-vector multiplication is better (namely $O(\chi_{\max}^3 D d^2 + \chi_{\max}^2 D^2 d^3)$) if we contract the tensors $L^{[j]}, W^{[n]}, W^{[n+1]}, R^{[n+2]}$ one after another to Θ, instead of contracting them into a single tensor and applying it to Θ at once (which would scale as $O(\chi_{\max}^4 d^4)$).

This update step can be compared to the TEBD update where we obtain a new wave-function $\tilde{\Theta}$ after applying an time-evolution operator. As with TEBD, we split the new $\tilde{\Theta}$ using an SVD in step (iii), and must truncate the new index α_{n+1} to avoid a growth $\chi \to d\chi$ of the bond dimension. It is important that the left and right Schmidt basis $|\alpha_n\rangle_L, |\alpha_{n+2}\rangle_R$ are orthonormal, on one hand to ensure that the eigenstate of $\hat{H}^{\text{eff}}$ (seen as a matrix) with the lowest eigenvalue indeed minimizes $E = \langle\tilde{\psi}|\hat{H}^{\text{eff}}|\tilde{\psi}\rangle$ and on the other hand to ensure an optimal truncation at the given bond. Assuming that this is the case, the isometry properties of the SVD matrices imply that the orthonormality conditions also hold for the updated Schmidt states $|\alpha_n\rangle_{L/R}$ defined about the central bond.

At this point, we have improved guesses for the tensors $\tilde{A}^{[n]}, \tilde{\Lambda}^{[n+1]}, \tilde{B}^{[n]}$ (after a reshaping into the desired form) and can move on to the next bond. Note that we moved the center of the mixed canonical form to the central bond $n : n+1$. If we move to the right, the next two-site wave function Θ for step (i) is thus again given by $\tilde{\Lambda}^{[n+1]}\tilde{B}^{[n+1]}B^{[n+2]}$, while if we move to the left, we need to use $A^{[n-1]}\tilde{A}^{[n]}\tilde{\Lambda}^{[n+1]}$. Moreover, we need to find the next environments.

The starting environments on the very left and right are simply given by (see Fig. 2.8(a))

$$L^{[1]}_{\alpha_1 \overline{\alpha}_1 \gamma_1} = \delta_{\alpha_1 \overline{\alpha}_1} v^L_{\gamma_1}, \qquad R^{[N]}_{\alpha_{N+1} \overline{\alpha}_{N+1} \gamma_{N+1}} = \delta_{\alpha_{N+1} \overline{\alpha}_{N+1}} v^R_{\gamma_{N+1}}. \tag{2.38}$$

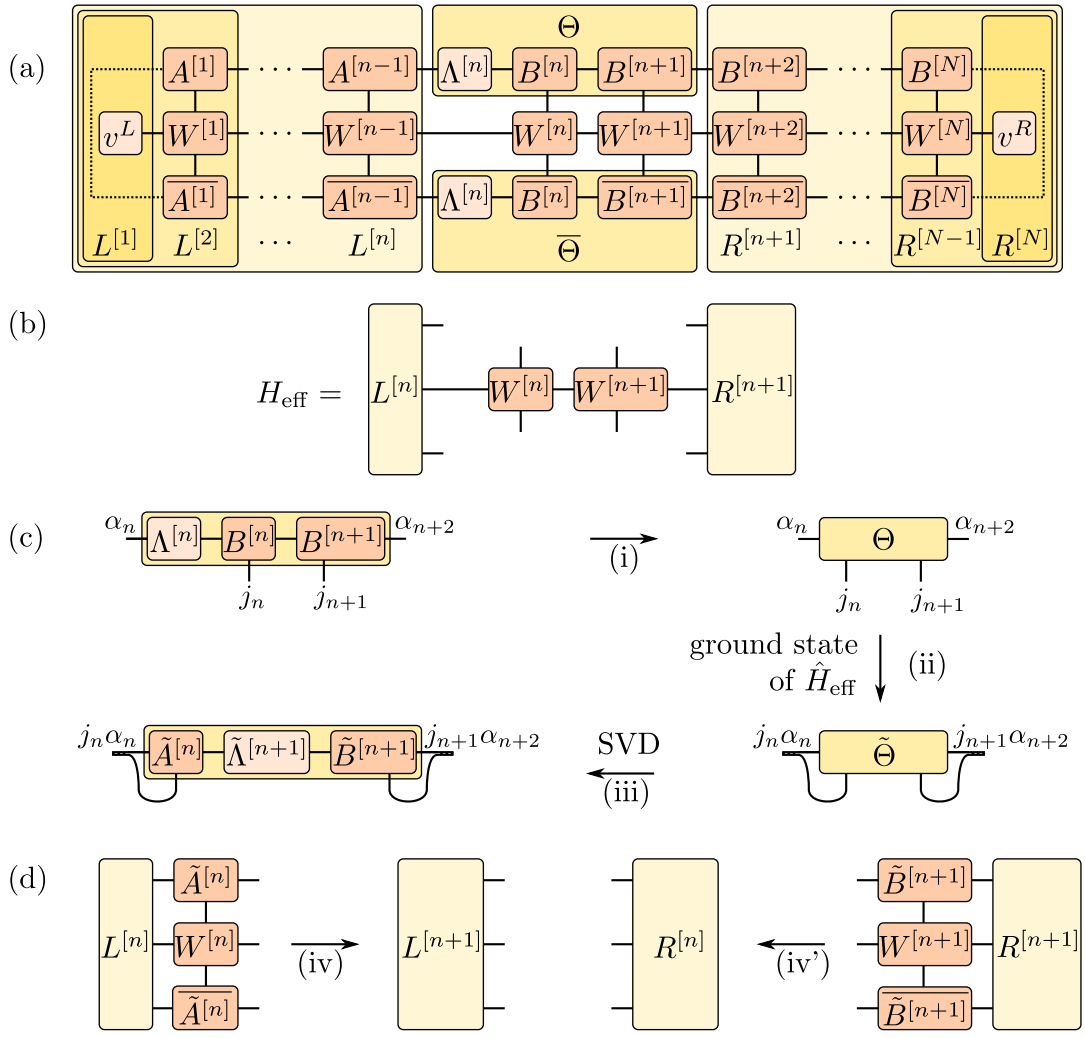

Figure 2.8 (a) The energy $E = \langle\psi|\hat{H}|\psi\rangle$ with the MPS $|\psi\rangle$ in mixed canonical form and $\hat{H}$ given by an MPO. We contract the parts to the left of site n (right of site $n+1$) into the left (right) environment $L^{[n]}$ ($R^{[n+1]}$). (b) The effective Hamiltonian $\hat{H}^{\text{eff}}$ to update sites $n, n+1$ is the MPO projected onto the basis $\{|\alpha_n\rangle_L \otimes |j_n\rangle \otimes |j_{n+1}\rangle \otimes |\alpha_{n+2}\rangle_R\}$. (c) Update steps for the sites $n, n+1$, see main text. (d) The update rules for the environment follow from the definition in (a).

Here, the $\delta_{\alpha_1\overline{\alpha}_1}$ and $\delta_{\alpha_{N+1}\overline{\alpha}_{N+1}}$ are trivial since α_1 and α_{N+1} are dummy indices which take only a single value. The other environments can be obtained from a simple recursion rule shown as step (iv) of Fig. 2.8(d). Using this recursion rule, $R^{[2]}$ required for the first update of the sweep can be obtained by an iteration starting from the right-most $R^{[N]}$. Note that the update on sites $n, n+1$ does not change the right environments R^k for $k > n+1$. Thus it is advisable to keep the environments in memory, such that we only need to recalculate the left environments when sweeping from left to right, and vice versa in the other direction.

The procedure described above optimizes always two sites at once. Ref. [101] introduced a way to perturb the density matrices during the algorithm. This allows to perform DMRG while optimizing only a single site at once, called "single-site DMRG" or "1DMRG" in the literature, and helps to avoid getting stuck in local minima. A detailed discussion of two-site vs. single-site DMRG and a improved version of the density matrix perturbation can be found in Ref. [102]. Especially for models with long-range interactions (which appear for example when mapping a quasi-2D cylinder to a 1D chain) or models with topological phases, this density matrix perturbation can be necessary to converge towards the correct ground state.

2.3 Infinite systems in one dimension

For translation invariant systems, we can take the thermodynamic limit in which the number of sites $N \to \infty$, generalizing (2.7) to

$$|\psi\rangle = \sum_{\ldots j_{n-1}, j_n, j_{n+1}, \ldots} \cdots M^{[n-1]j_{n-1}} M^{[n]j_n} M^{[n+1]j_{n+1}} \cdots |\ldots, j_{n-1}, j_n, j_{n+1}, \ldots\rangle \,. \tag{2.39}$$

We can ensure the translation invariance of this infinite matrix product state (iMPS) by construction if we simply take all the tensors $M^{[n]} \to M$ in Eq. (2.39) to be the same [also called uniform MPS (uMPS) in the literature]. The paramagnetic product state $|\cdots \leftarrow\leftarrow \cdots\rangle$ with the tensors of Eq. (2.9) is a trivial example for such a translation invariant state; another example is the AKLT state given in Eq. (2.13). In general, we might only have a translation invariance by shifts of (multiples of) L sites. In this case we introduce a repeating unit cell of L sites with L different tensors, $M^{[n]} = M^{[n+L]}$ in Eq. (2.39). For example, the Néel state $|\cdots \uparrow\downarrow\uparrow\downarrow \cdots\rangle$ is only invariant under a translation by (multiples of) $L = 2$ sites, with the tensors on even and odd sites as given in Eq. (2.10) for the finite case, illustrated in Fig. 2.9(a). The length L of the unit cell should be chosen compatible with the translation symmetry of the state to be represented, e.g., for the Néel state L should be a multiple of 2. Choosing L larger than strictly necessary allows to check the translation invariance explicitly.

At first sight, it might seem that we need to contract an infinite number of tensors to evaluate expectation values of local operators, as the corresponding network consists of an infinite number of tensors. However, as shown in Fig. 2.9(b) for a unit cell of $L = 2$ sites, the network has a repeating structure consisting of the so-called *transfer matrix* T defined as

$$T_{\alpha\overline{\alpha},\gamma\overline{\gamma}} = \sum_{j_1, j_2, \beta, \overline{\beta}} M^{[1]j_1}_{\alpha\beta} \overline{M^{[1]j_1}_{\overline{\alpha}\overline{\beta}}} M^{[2]j_2}_{\beta\gamma} \overline{M^{[2]j_2}_{\overline{\beta}\overline{\gamma}}} . \tag{2.40}$$

A state is called *pure* if the largest (in terms of absolute value) eigenvalue of T is unique and *mixed* if it is degenerate. In the following, we will always assume that the state is pure (in fact every mixed state can be uniquely decomposed into a sum of pure ones). We renormalize the iMPS such that the largest eigenvalue of T is 1. The eigenvector depends on the gauge freedom of

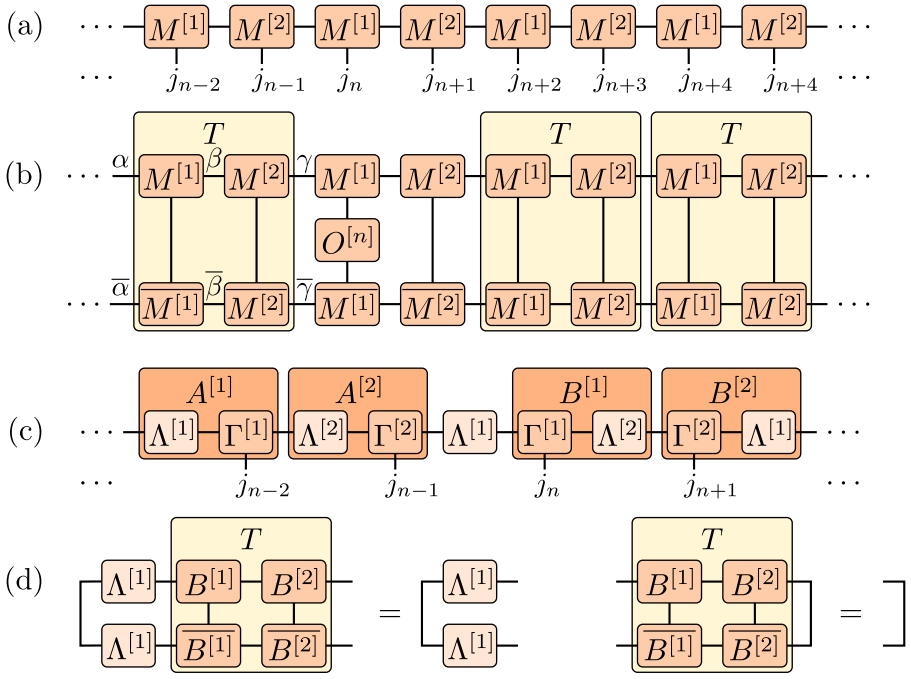

Figure 2.9 (a) An infinite MPS with a unit cell of $L = 2$ sites. (b) The expectation value $\langle\psi|O_n|\psi\rangle$ contains the transfer matrix T as a repetitive structure. (c) The canonical form is defined as in the finite case. (d) The orthonormality conditions of the Schmidt states yield eigenvector equations for the transfer matrix.

Eq. (2.14), which we can use to bring the iMPS into the convenient canonical form defined by the Schmidt decomposition on each bond, see Fig. 2.9(c). An algorithm to achieve this is described in Ref. [143]. For an iMPS in right-canonical form, i.e., $M^{[n]j_n} \to B^{[n]j_n} \equiv \Gamma^{[n]j_n}\Lambda^{[n+1]}$, the orthonormality condition of the Schmidt vectors depicted in Fig. 2.4(d) applied to the whole unit cell implies that $\delta_{\gamma\bar{\gamma}}$ is a right eigenvector of T with eigenvalue 1, as depicted in Fig. 2.9(d). Note that T is not symmetric and hence left and right eigenvectors differ; the left eigenvector to the eigenvalue 1 is $(\Lambda^{[1]}_\alpha)^2\delta_{\alpha\bar{\alpha}}$. All other eigenvalues of the transfer matrix have magnitude smaller than 1. Therefore, the repeated application of the transfer matrix in the network of the expectation value projects onto these dominant left and right eigenvectors, and the infinite network of the expectation value $\langle\psi|O_n|\psi\rangle$ simplifies to a local network as in the finite case, see Fig. 2.5.

A similar reasoning can be used for the correlation function $\langle\psi|O_nO_m|\psi\rangle$. Projecting onto the dominant eigenvectors left of O_n and right O_m, we arrive at the network of Fig. 2.10(a). In between the operators O_n and O_m, the transfer matrix T appears $N = \lfloor\frac{|m-n|}{L}\rfloor - 1$ times, where $\lfloor\cdot\rfloor$ denotes rounding down to the next integer. Formally diagonalizing the transfer matrix to take the N^{th} power shows that the correlation function is a sum of exponentials,

$$\langle\psi|O_nO_m|\psi\rangle = \langle\psi|O_n|\psi\rangle\,\langle\psi|O_m|\psi\rangle + (\eta_2)^N C_2 + (\eta_3)^N C_3 + \cdots . \tag{2.41}$$

Here, η_i labels the i-largest eigenvalue corresponding to the left and right eigenvectors $\eta_i^{[L/R]}$, $C_i = (O_n^{[L]}\eta_i^{[R]})(\eta_i^{[L]}O_n^{[R]})$ denotes the remaining parts of the network shown in Fig. 2.10, and we identified the $C_1 = \langle\psi|O_n|\psi\rangle\,\langle\psi|O_m|\psi\rangle$ in the term of the dominant eigenvalue $\eta_1 = 1$. The

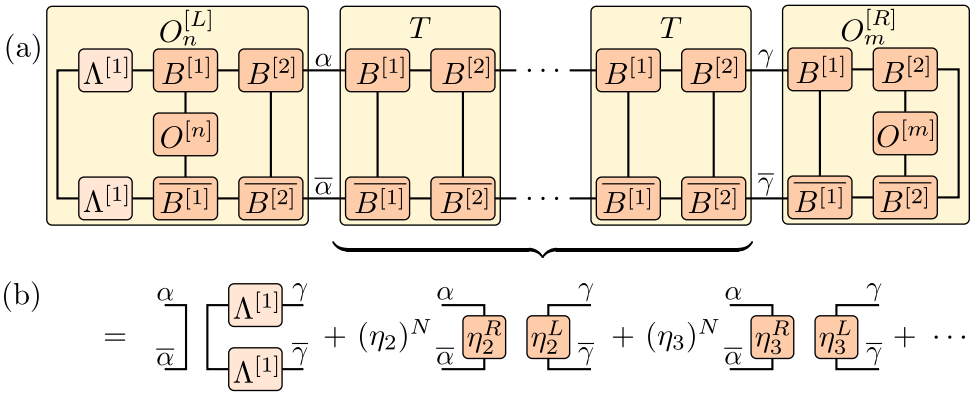

Figure 2.10 (a) Correlation function $\langle\psi|O_n O_m|\psi\rangle$. (b) Expansion of T^N in terms of dominant eigenvectors and eigenvalues of T for large N. The second largest eigenvalue η_2 of T determines the correlation length via eq. 2.42.

decay of the correlations is thus determined by the second largest eigenvalue η_2, which yields the correlation length

$$\xi = -\frac{L}{\log|\eta_2|}. \tag{2.42}$$

Numerically, it is readily obtained from a sparse algorithm finding extremal eigenvalues of T.

2.3.1 Infinite Time Evolving Block Decimation (iTEBD)

Generalizing TEBD to infinite time evolving block decimation (iTEBD) is very simple and requires only minor modifications in the code [138]. Without loss of generality we assume that the Hamiltonian is translation invariant by L sites as the iMPS; otherwise we enlarge the unit cells. As in the finite case, we use a Suzuki-Trotter decomposition to obtain the expression of the time evolution operator $\hat{U}(t)$ given in Eq. (2.26), but now the index n runs over all integer numbers, $n \in \mathbb{Z}$. If we apply the two-site unitary $\hat{U}^{[n,n+1]} = e^{i\hat{h}^{[n,n+1]}\delta t}$ on the iMPS to update the matrices $B^{[n]}$ and $B^{[n+1]}$ as illustrated in Fig. 2.6(b), this corresponds due to translation invariance to the action of $\hat{U}^{[n,n+1]}$ on the sites $(n+mL, n+1+mL)$ for any $m \in \mathbb{Z}$. Therefore, we can use the same two-site update as in the finite case; the only difference is that the matrices of the iMPS represent only the unit cell with nontrivial left and right bonds, and compared to a finite system with L sites we have an additional term $\hat{h}^{[L,L+1]} \equiv \hat{h}^{[L,1]}$ across the boundary of the unit cell.

Note that the iTEBD algorithm is different from a time evolution in a finite system of $N = L$ sites with periodic boundary conditions. For analytical calculations with MPS in systems with periodic boundary conditions, it can be useful to change the definition of an MPS from Eq. (2.7) to

$$|\psi\rangle = \sum_{j_1,\ldots,j_N} \mathrm{Tr}\left(M^{[1]j_1} M^{[2]j_2} \ldots M^{[N]j_N}\right) |j_1, j_2, \ldots, j_N\rangle, \tag{2.43}$$

which has at first sight the same tensor network structure as an iMPS. However, cutting a single bond of such a finite MPS with periodic boundary conditions does not split it into two parts. Therefore, the canonical form (which relies on the Schmidt decomposition) is not well defined for an MPS with periodic boundary conditions (or in general for any tensor network state in

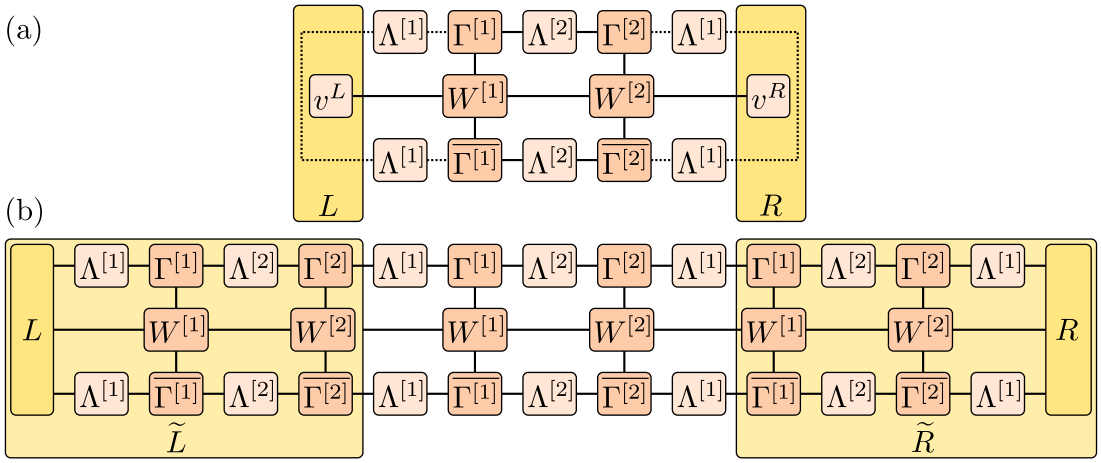

Figure 2.11 (a) For iDMRG (here with a unit cell of $L = 2$ sites), we initialize the environments and perform updates like in DMRG of a finite system with L sites. (b) Between the sweeps, we increase the system size by inserting a unit-cell of L sites into each of the environments (assuming translation invariance of the iMPS).

which the bonds form loops)[6]. Since the two-site update scheme of iTEBD implicitly uses the canonical form, it implements the time evolution in the infinite system with open boundary conditions. This also becomes evident by the fact that the bond dimension $\chi_{\max}$ – in other words the number of Schmidt states taken into account – can get larger than the Hilbert space dimension d^L inside one unit cell.

2.3.2 Infinite Density Matrix Renormalization Group (iDMRG)

While iTEBD works directly in the thermodynamic limit $N \to \infty$ by employing translation invariance, for the infinite density matrix renormalization group (iDMRG) one should think of a finite system with a growing number of sites - the "renormalization group" in the name refers to this. Let us assume that the Hamiltonian is given as an MPO with a translation invariant unit cell consisting of $W^{[n]}$, $n = 1, \cdots, L$, which we can terminate with the boundary vectors v^L, v^R to obtain the Hamiltonian of a finite system with a multiple of L sites. We initialize the environments and perform two-site updates during a sweep exactly like in finite DMRG. The crucial difference is that we increase the system size between the sweeps as illustrated in Fig. 2.11(b): assuming translation invariance, we redefine the left and right environments $\widetilde{L} \to L$ and $\widetilde{R} \to R$ to include additional unit cells. Moreover, we need to extend the sweep to include an update on the sites $(L, L+1) \equiv (L, 1)$. With each unit cell inserted, the described finite system grows by L sites, where we focus only only on the central L sites. Full translation invariance is only recovered when the iDMRG iteration of sweeps and growing environments converges to a fix point, at which the environments describe infinite half-chains.

One subtlety of the above prescription lies in the interpretation of the energy E obtained during the diagonalization step. Is it the (infinite) energy of the infinite system? Keeping track of the number of sites $\ell_{R/L}$ included into each of the environments, we see that the energy E corresponds to a system of size $N = \ell_L + L + \ell_R$. By monitoring the change in E with increased N, we can extract the energy per site. This is convenient for problems in which there is no few-site Hamiltonian with which to evaluate the energy.

[6] A generalization of the canonical form to networks with closed loops was recently given in Ref. [144].

When symmetry breaking is expected, it is helpful to initialize the environments by repeatedly performing the iDMRG update *without* performing the Lanczos optimization, which builds up environments using an initial symmetry broken MPS.

To close this section, we mention the variational uniform Matrix Product State algorithm (VUMPS) as a new alternative to iDMRG, see Ref. [145] and references therein. In short, the method can preserve a strict uniform structure of the infinite MPS in a very clever way by summing up geometric series appearing in the effective Hamiltonian.

2.4 Charge conservation

If there is a unitary $\hat{U}$ which commutes with the Hamiltonian, $\hat{U}$ and $\hat{H}$ can be diagonalized simultaneously, in other words the Hamiltonian has a block-diagonal structure when written in the eigenbasis of $\hat{U}$. This can be exploited to speed up simulations: for example, diagonalizing a full $N \times N$ matrix requires $O\left(N^3\right)$ FLOPs, whereas the diagonalization of m blocks of size $\frac{N}{m}$ requires $O\left(m\left(\frac{N}{m}\right)^3\right)$ FLOPs. A similar reasoning holds for the SVD and matrix or tensor products. While exploiting the block structure does not change the scaling of the considered algorithm with the total dimension of the tensors, the gained speedup is often significant and allows more precise simulations with larger bond dimensions at the same computational cost.

For tensor networks, the basic idea is that we can ensure a block structure of *each* tensor individually. One can argue based on representation theory of groups that the tensors can be decomposed in such a block structure [97, 98]. However, here we present a bottom-up approach which is closer to the implementation. Motivated by an example, we will state a simple "charge rule" which fixes the block structure of a tensor by selecting entries which have to vanish. We explain how to define and read off the required charge values. Then we argue that tensor network algorithms (like TEBD or DMRG) require only a few basic operations on tensors, and that these operations can be implemented to preserve the charge rule (and to exploit the block structure for the speedup).

Here, we focus exclusively on global, abelian symmetries which act locally in the computational basis, and refer to Refs. [96, 97, 99, 100, 146] for the non-abelian case, which requires a change of the computational basis and is much more difficult to implement.

2.4.1 Definition of charges

For concreteness, let us now consider two spin-$\frac{1}{2}$ sites coupled by

$$\hat{H} = \vec{S}_1 \cdot \vec{S}_2 = \sum_{ab} H_{ab} \left|a\right\rangle \left\langle b\right| \text{ with } H_{ab} = \frac{1}{4}\begin{pmatrix} 1 & & & \\ & -1 & 1 & \\ & 1 & -1 & \\ & & & 1 \end{pmatrix}, \tag{2.44}$$

where we have represented $\hat{H}$ in the basis $\{|a\rangle\} \equiv \{|\uparrow\uparrow\rangle, |\uparrow\downarrow\rangle, |\downarrow\uparrow\rangle, |\downarrow\downarrow\rangle\}$ and omitted zeros. Indeed, we clearly see a block-diagonal structure in this example, which stems from the conservation of the magnetization[7] $\hat{S}^z = \hat{S}^z_1 + \hat{S}^z_2$. We can identify the blocks if we note that the

[7] We call this a $U(1)$ symmetry since $\hat{H}$ commutes with $\hat{U} = \exp(\mathrm{i}\phi \sum_n \hat{S}^z_n) = \prod_n e^{\mathrm{i}\phi \hat{S}^z_n}$ which has a $U(1)$ group structure. If one thinks of particles (e.g., fermions after using a Jordan-Wigner transformation), this symmetry corresponds to the particle number conservation. In general, one could also exploit the non-abelian $SU(2) \cong SO(3)$ symmetry of spin rotations, but we focus on the simpler case of abelian symmetries.

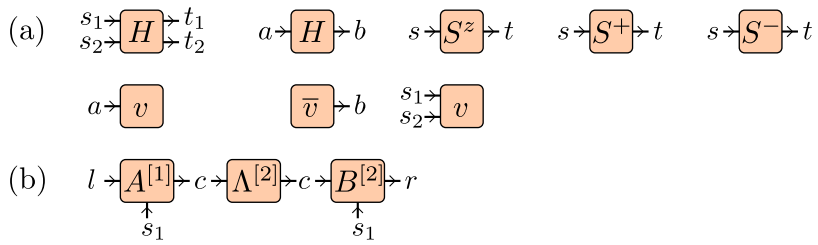

Figure 2.12 (a) Diagrammatic representation of the tensors in Tab. 2.1. We indicate the signs ζ by small arrows on the legs. (b) Sign convention for the MPS.

considered basis states are eigenstates of S^z and inspect their eigenvalues: $|\uparrow\uparrow\rangle$ corresponds to the eigenvalue $\hbar$, the two states $|\uparrow\downarrow\rangle, |\downarrow\uparrow\rangle$ form a block to the eigenvalue 0, and $|\downarrow\downarrow\rangle$ corresponds to $-\hbar$. To avoid floating point errors, we rescale the "charges" to take only integer values. Clearly, whenever S^z is conserved, so is $q := 2S^z/\hbar$, but the latter takes the simple values 2, 0 and -2 for the four basis states $|a\rangle$ considered above. We have thus associated one charge value to each index a, which we can summarize in a vector $q^{[a]} := (2, 0, 0, -2)$. Using this definition, we can formulate the conservation of S^z as a condition on the matrix elements:

$$H_{ab} = 0 \text{ if } q_a^{[a]} \neq q_b^{[a]}. \tag{2.45}$$

How does this generalize to tensors with a larger number of indices? To stay with the example, we can also write $\hat{H} = \sum_{s_1 s_2 t_1 t_2} H_{s_1 s_2 t_1 t_2} |s_1\rangle |s_2\rangle \langle t_1| \langle t_2|$ as a tensor with 4 indices s_1, s_2, t_1, t_2 corresponding to the single-site basis $\{|s\rangle\} \equiv \{|\uparrow\rangle, |\downarrow\rangle\}$. The charge values $q^{[s]} = (1, -1)$ for this basis are obvious from the definition $q = 2S^z/\hbar$ (and the reason why we included the factor 2 in the rescaling). Since S^z is additive, its conservation now implies that

$$H_{s_1 s_2 t_1 t_2} = 0 \text{ if } q_{s_1}^{[s]} + q_{s_2}^{[s]} \neq q_{t_1}^{[s]} + q_{t_2}^{[s]}. \tag{2.46}$$

Note that the indices corresponding to a ket appear on the left hand side of the inequality, while the ones corresponding to a bra appear on the right. For an arbitrary tensor, we therefore define one sign $\zeta = \pm 1$ for each leg, where we choose the convention $\zeta = +1$ ($\zeta = -1$) for a ket (bra); for the above example $\zeta^{[1]} = \zeta^{[2]} = +1$ for the first two indices s_1, s_2 and $\zeta^{[3]} = \zeta^{[4]} = -1$ for the legs of t_1, t_2. In diagrams, we can illustrate this sign by an arrow pointing into (for $\zeta = +1$) or out of (for $\zeta = -1$) the tensor, see Fig. 2.12.

Finally, we also introduce an offset Q, which we call the "total charge" of a tensor. The general **charge rule** for an arbitrary n-leg tensor M then reads

$$\boxed{\forall a_1, a_2 \cdots a_n : \ \zeta^{[1]} q_{a_1}^{[1]} + \zeta^{[2]} q_{a_2}^{[2]} + \zeta^{[3]} q_{a_3}^{[3]} + \cdots + \zeta^{[n]} q_{a_n}^{[n]} \neq Q \implies M_{a_1 a_2 \cdots a_n} = 0} \tag{2.47}$$

Note that the signs $\zeta^{[i]}$ and the total charge Q introduce some ambiguity: the charge rule (2.47) is still satisfied if we send $\zeta^{[j]} \to -\zeta^{[j]}$ and $q^{[j]} \to -q^{[j]}$ for some leg j, or if we send $\zeta^{[j]} q^{[j]} \to \zeta^{[j]} q^{[j]} + \delta Q$ and $Q \to Q + \delta Q$. However, introducing the signs and the total charge allows us to share the same q vector between legs representing the same basis, e.g., all four legs of $H_{s_1 s_2 t_1 t_2}$ shared the same $q^{[s]}$. We can therefore fix the charge vectors q of *physical* legs in the very beginning of the algorithm. Since also the signs ζ are fixed by conventions, for tensors with only physical legs one can solve the charge rule (2.47) for Q (by inspecting which entries of a tensor are non-zero). Examples of this kind are given in Tab. 2.1.

Example	$\zeta^{[1]}$	$q^{[1]}$	$\zeta^{[2]}$	$q^{[2]}$	$\zeta^{[3]}$	$q^{[3]}$	$\zeta^{[4]}$	$q^{[4]}$	Q
$\hat{H} = \sum H_{s_1 s_2 t_1 t_2} \lvert s_1\rangle \lvert s_2\rangle \langle t_1\rvert \langle t_2\rvert$	+1	$q^{[s]}$	+1	$q^{[s]}$	-1	$q^{[s]}$	-1	$q^{[s]}$	0
$\hat{H} = \sum H_{ab} \lvert a\rangle \langle b\rvert$	+1	$q^{[a]}$	-1	$q^{[a]}$					0
S^z	+1	$q^{[s]}$	-1	$q^{[s]}$					0
S^+	+1	$q^{[s]}$	-1	$q^{[s]}$					2
S^-	+1	$q^{[s]}$	-1	$q^{[s]}$					-2
$\lvert\uparrow\uparrow\rangle = \sum v_a \lvert a\rangle$	+1	$q^{[a]}$							2
$\langle\uparrow\uparrow\rvert = \sum v_a^* \langle a\rvert$	-1	$q^{[a]}$							-2
$\lvert\uparrow\uparrow\rangle = \sum v_{s_1 s_2} \lvert s_1\rangle \lvert s_2\rangle$	+1	$q^{[s]}$	+1	$q^{[s]}$					2

Table 2.1 Examples for charge definitions such that the tensors fulfill the charge rule (2.47). We consider spin-$\frac{1}{2}$ with $q = 2S^z/\hbar$, i.e., $q^{[s]} := (1, -1)$ for the single-site basis $\{\lvert s\rangle\} \equiv \{\lvert\uparrow\rangle, \lvert\downarrow\rangle\}$ and $q^{[a]} := (2, 0, 0, -2)$ for the two-site basis $\{\lvert a\rangle\} \equiv \{\lvert\uparrow\uparrow\rangle, \lvert\uparrow\downarrow\rangle, \lvert\downarrow\uparrow\rangle, \lvert\downarrow\downarrow\rangle\}$. The signs ζ are +1 (−1) for legs representing kets (bras). The total charge Q can then be determined from the charge rule (2.47).

On the other hand, if the total charge Q and the charges $q^{[i]}$ of all but one leg j of a tensor are fixed, one can also solve the charge rule (2.47) for the missing $q^{[j]}$:

$$\forall a_1, a_2 \cdots a_n : \; M_{a_1 a_2 \cdots a_n} \neq 0 \;\Rightarrow\; \zeta^{[j]} q^{[j]}_{a_j} = Q - \sum_{i \neq j} \zeta^{[i]} q^{[i]}_{a_i} \tag{2.48}$$

This allows to determine the charges on the *virtual* legs of an MPS. As an example, let us write the singlet $\lvert\psi\rangle = \frac{1}{\sqrt{2}}(\lvert\uparrow\downarrow\rangle - \lvert\downarrow\uparrow\rangle)$ as an MPS. The MPS in canonical form is given by

$$\lvert\psi\rangle = \sum_{s_1 s_2, c} \Gamma^{[1]s_1}_{lc} \Lambda^{[1]}_c \Gamma^{[2]s_2}_{cr} \lvert s_1\rangle \lvert s_2\rangle \;\text{ with }\; \Lambda^{[1]} = \frac{1}{\sqrt{2}} \begin{pmatrix} 1 \\ 1 \end{pmatrix},$$
$$\Gamma^{[1]\uparrow} = \begin{pmatrix} 1 & 0 \end{pmatrix}, \quad \Gamma^{[1]\downarrow} = \begin{pmatrix} 0 & 1 \end{pmatrix}, \quad \Gamma^{[2]\uparrow} = \begin{pmatrix} 0 \\ -1 \end{pmatrix}, \quad \Gamma^{[2]\downarrow} = \begin{pmatrix} 1 \\ 0 \end{pmatrix}. \tag{2.49}$$

Here, l and r are *trivial* indices $l \equiv r \equiv 1$, and only introduced to turn the $\Gamma^{[i]}$ into matrices instead of vectors. For trivial legs, we can (usually) choose trivial charges $q^{[\text{triv}]} := (0)$ which do not contribute to the charge rule. Moreover, we choose the convention that $\zeta = +1$ for left virtual legs, $\zeta = -1$ for right virtual legs and $Q = 0$, see Fig. 2.12(d). Then we can use the charge rule (2.48) of $\Gamma^{[1]}$ solved for $q^{[c]}$ and obtain:

$$\Gamma^{[1]\uparrow}_{11} \neq 0 \overset{(2.47)}{\Rightarrow} q^{[c]}_1 = 1, \qquad \Gamma^{[1]\downarrow}_{12} \neq 0 \overset{(2.47)}{\Rightarrow} q^{[c]}_2 = -1. \tag{2.50}$$

We use the *same* $q^{[c]} = (1, -1)$ for the left virtual leg of $\Gamma^{[2]}$; one can easily check that it also fulfills the charge rule (2.47) for $Q = 0$.

Strictly speaking, an operator with a non-zero total charge Q does not preserve the charge of the state it acts on. However, it still preserves the block structure, because it changes the charge by exactly Q, e.g., $\hat{S}^+$ increases it by 2. In contrast, $\hat{S}^x$ (and similarly $\hat{S}^y$) can both increases or decreases the charge, thus it can not be written as tensors satisfying Eq. (2.47); only the combination $\hat{S}^x_1 \hat{S}^x_2 + \hat{S}^y_1 \hat{S}^y_2 = \frac{1}{2}(\hat{S}^+_1 \hat{S}^-_2 + \hat{S}^-_1 \hat{S}^+_2)$ preserves the charge. When writing $\hat{H}$ as a charge conserving MPO, one can only use single-site operators with a well-defined Q.

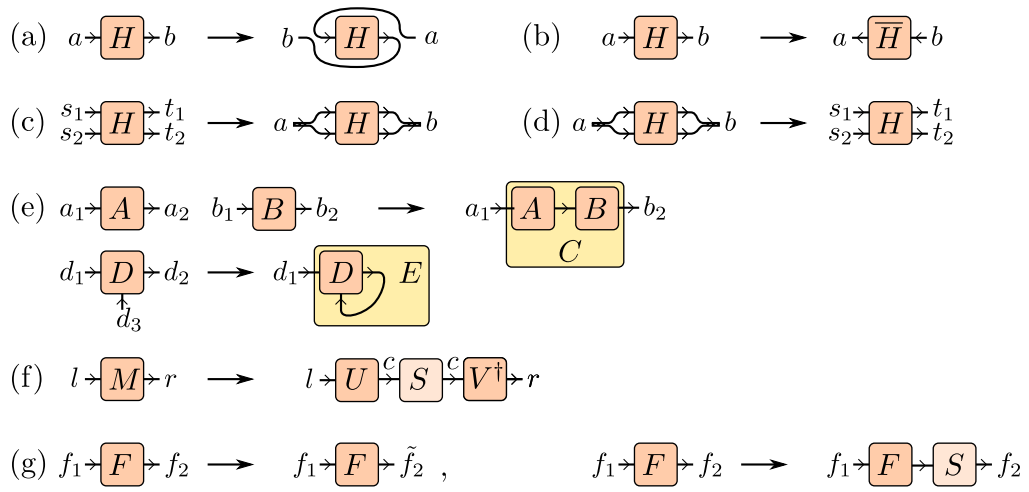

Figure 2.13 Basic operations required for tensor networks: (a) transposition, (b) conjugation, (c) combining two or more legs, (d) splitting previously combined legs (e) contraction of two legs, (f) matrix decompositions, and (g) operations on a single leg.

2.4.2 Basic operations on tensors

Above, we motivated the form of the charge rule (2.47) and explained how to define the charges for various tensors. Thus, we can write both the initial state and the Hamiltonian in terms of tensors satisfying Eq. (2.47). Now, we argue that tensor network algorithms require just a few basic operations on the tensors, namely (a) transposition, (b) conjugation, (c) combining two or more legs, (d) splitting previously combined legs (e) contraction of two legs, (f) matrix decompositions, and (g) operations on a single leg. These operations are depicted in Fig. 2.13. As we will show in the following, all of them can be implemented to preserve the charge rule (2.47) and thus the block structure of the tensors. Thus, *any* algorithm using (only) these basic operations preserves the charges.

Transposition is by definition just a reordering of the legs. Clearly, (2.47) is then still valid if we reorder the charge vectors q and signs ζ in the same way. Examples for the **conjugation** are already given in Tab. 2.1; beside the complex conjugation of the entries this includes exchanging bra and ket, i.e., a sign flip of all ζ. The charge rule is then preserved if we also flip the sign of the total charge Q. For hermitian operators like $\hat{H}$ the combination of complex conjugation and appropriate transposition changes neither the entries nor the charges of a tensor.

Another operation often needed is to **combine** two (or more) legs, e.g., before we can do an SVD, we need to view the tensor as a matrix with just two indices. In other words, we group some legs into a "pipe". The pipe looks like an ordinary leg, i.e., we define a sign ζ and charge vector q for it. However, it has the internal structure that it consists of multiple smaller legs. Thus, we can later **split** it, e.g., after we did an SVD. For concreteness, let us again consider the above example $H_{s_1 s_2 t_1 t_2} \to H_{ab}$, i.e., we want to combine the indices s_1, s_2 into a pipe a (and t_1, t_2 into a pipe b). In this case, we map the indices as $a(s_1, s_2) := 2s_1 + s_2$ and $b(t_1, t_2) := 2t_1 + t_2$. The charge rule is then preserved if we *define* the charge vectors q of the pipes as $\zeta^{[a]} q^{[a]}_{a(s_1,s_2)} := \zeta^{[1]} q^{[s]}_{s_1} + \zeta^{[2]} q^{[s]}_{s_2}$ and $\zeta^{[b]} q^{[b]}_{b(t_1,t_2)} := \zeta^{[3]} q^{[s]}_{t_1} + \zeta^{[4]} q^{[s]}_{t_2}$, where $\zeta^{[1]} = \zeta^{[2]} = 1$, $\zeta^{[3]} = \zeta^{[4]} = +1$ are the signs of the indices s_1, s_2, t_1, t_2, and $\zeta^{[a]} = 1$, $\zeta^{[b]} = -1$ are the desired signs of the pipes. One can easily check that these definitions coincide with the previous ones, $q^{[a]} = (2, 0, 0, -2) = q^{[b]}$. Since the mapping of indices is one to one, one can also split a pipe into the smaller legs it consists

of. However, note that this requires the q vectors and signs ζ of these legs; the pipe should thus store a copy of them internally.

One of the most important (and expensive) operations on tensors is the **contraction** of legs. Let us consider two tensors $A_{a_1 a_2}$ and $B_{b_1 b_2}$ with charges $Q^A, q^{[a_i]}, \zeta^{A[i]}$ and $Q^B, q^{[b_i]}, \zeta^{B[i]}$, $i = 1, 2$. A contraction means to identify two indices and sum over it. Two indices can be identified if they represent the same basis, thus we *require* them to have the same charge vector q and opposite signs ζ. For example for the usual matrix product $C_{a_1 b_2} \coloneqq \sum_c A_{a_1 c} B_{c b_2}$ we require $q^{[a_2]} = q^{[b_1]}$ and $\zeta^{A[2]} = -\zeta^{B[1]}$. The charge rule (2.47) for C then follows from the charge rules of A and B, if we define $Q^C \coloneqq Q^A + Q^B$ and just copy the signs ζ and charge vectors q for the free, remaining indices. Moreover, the cost of the contraction is reduced if we exploit the block structure of A and B, which becomes most evident if we have a block diagonal structure as in H_{ab}, Eq. (2.44). On the other hand, we can also contract two legs of the same tensor, i.e., take a (partial) trace. The contributions of these two indices to the charge rule (2.47) then simply drop out and the rule again stays the same for the remaining indices of the tensor.

We collect linear algebra methods that take a matrix as input and decompose it into a product of two or three matrices under the name **matrix decomposition**. Examples include the diagonalization of a matrix $H = U^\dagger E U$, QR-decomposition $M = QR$ and SVD $M = USV^\dagger$. Here, we focus exemplary on the SVD, other decompositions can be implemented analogously. Let us first recap the properties of the SVD: it decomposes an arbitrary $m \times n$ matrix into a product $M_{lc} = \sum_c U_{lc} S_c (V^\dagger)_{cr}$, where S_c are the $k = \min(m, n)$ positive singular values, and U and V are isometries, i.e., $U^\dagger U = \mathbb{1} = V^\dagger V$. The charge rule (2.47) for the matrix elements M_{lc} implies a block structure: assuming that the basis states of the index l are sorted by charge (which we discuss in the next paragraph), we can group indices with the same charge values together to form a block. Moreover, for each block of l with a charge value $q_l^{[l]}$, there is at most one block of the index r with compatible charges, i.e., we have some kind of pseudo block-diagonal form (even if the blocks are not strictly on the diagonal). Therefore, we can apply the SVD to each of the (non-zero) blocks separately and simply stack the results, which again yields a (pseudo) block-diagonal form for U and $V^\dagger$ with the required properties. To define the charges of the new matrices we can ignore S, since it is only a trivial rescaling of one leg. Similar as for the contraction, we keep the charge vectors q and signs ζ for the indices l and r. Further, we choose the total charges as $Q^U \coloneqq 0$ and $Q^V \coloneqq Q^M$, as well as the sign $\zeta^{[c]}$ of the new index c negative for U and positive for V. The charge vector $q^{[c]}$ can then easily be read off using Eq. (2.48), which yields $q^{[c]} \coloneqq \zeta^{[l]} q^{[l]}$ (for both U and $V^\dagger$).

Finally, the remaining operations needed for tensor networks are **operations on a single leg** of a tensor. One example is a permutation of the indices of the leg, for example required to sort a leg by q as mentioned above. Clearly, this preserves the charge rule if we apply the same permutation to the corresponding charge vector q. Similarly, if we discard some of the indices of the leg, i.e., if we truncate the leg, we just apply the same truncation to the charge vector q. Lastly, we might also want to slice a tensor by plugging in a certain index of a leg, e.g., taking a column vector of a matrix. This requires to update the total charge Q to preserve the charge rule, as one can show by viewing it as a contraction with a unit vector.

Above we explained how to define the charges for the $U(1)$ symmetry of charge conservation. In general, one can have multiple different symmetries, e.g., for spin-full fermions we might have a conservation of both the particle numbers and the magnetization. The generalization is straight-forward: just define one q for each of the symmetries. Another simple generalization is

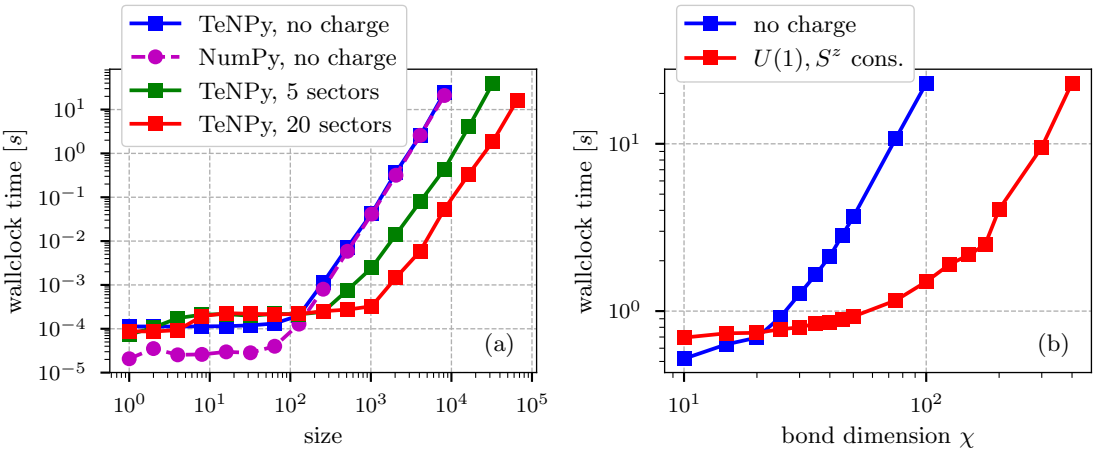

Figure 2.14 (a) Benchmark of a matrix multiplication without charge conservation ("NumPy, no charge") or with a $U(1)$ charge ("TeNPy") with each leg having 5 or 20 charge sectors. (b) A similar benchmark for a few DMRG sweeps of an infinite spin-$S = 2$ chain. The number of tensordot operations per sweep was fixed. For both benchmarks, a single CPU core was used.

due to another type of symmetry, namely $\mathbb{Z}_n$, where all the (in)-equalities of the charge rules are taken modulo n. An example for such a case is the parity conservation of a superconductor.

The ability of the TeNPy library to exploit charge conservation for faster calculations is demonstrated in Fig. 2.14. The benchmark of matrix multiplications in Fig. 2.14(a) shows that using the `Array` class of TeNPy in the case of no charges introduces only a small overhead compared to NumPy [147]. Compared to pure NumPy arrays, the `Array` class of TeNPy offers many convenient advantages, for example the possiblity to label the array indices, methods to combine and split legs, and consistency checks whether contracting two legs is reasonable. Moreover, it makes the generalization of the code to charge conservation almost trivial. Both NumPy and TeNPy arrays have an constant overhead on the order of 10^{-4} seconds per matrix multiplication for small matrices of size $n \lesssim 100$. This overhead can be attributed to the interpreted nature of the Python programming language, as opposed to languages like C++ or Fortran, where the program code is compiled to machine code before execution. However, there is a quick crossover to a regime at larger sizes n with a scaling of (roughly) $O(n^3)$, where the computation time is dominated by the matrix multiplication of blocks berformed by the underlying BLAS/LAPACK libraries. In this regime, using a C++ or Fortran based library does not lead to a (significant) speed up of the simulations. In Fig. 2.14(b), we benchmark the advantage in computer time of using the $U(1)$ symmetry corresponding to the conservation of $\hat{S}^z$ in a DMRG simulation of the $S = 2$ Heisenberg chain. This shows that exploiting the charge conservation can give a significant speedup already at moderate bond dimensions.

2.5 Efficient representations of general models

2.5.1 From Hamiltonians to MPOs using finite state machines

Let us now come back to the problem of how to obtain the MPO tensor $W^{[n]}$ for a given Hamiltonian, which we postponed in Sec. 2.2.4. To this end, we view the MPO as a finite state machine, which can also be drawn as a graph [103, 148, 149]. This is especially useful for translation invariant Hamiltonians where we have only a single $W^{[n]}$ tensor for the MPO such as

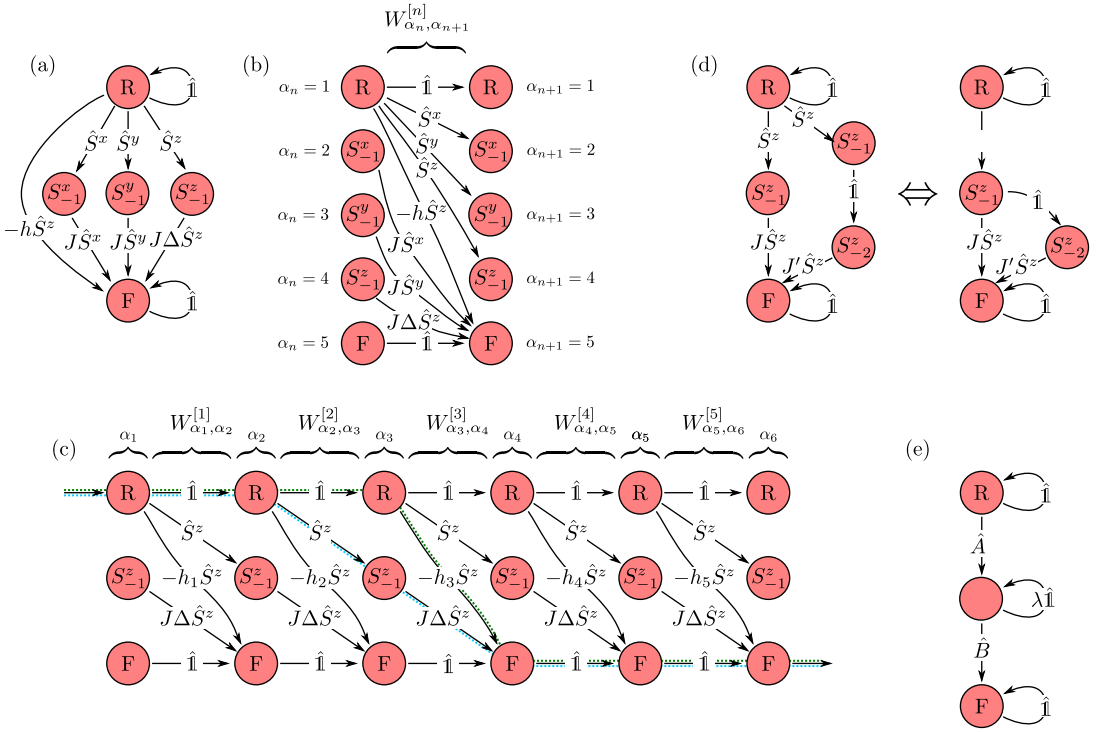

Figure 2.15 (a) Finite state machine generating the $W^{[n]}$ for the translation invariant Hamiltonian (2.34). (b) Labelling the indices on adjacent bonds as α_n and α_{n+1} allows to read off the entries $W^{[n]}_{\alpha_n,\alpha_{n+1}}$ from the edges. (c) Repeating the structure allows to identify the paths in the MPO graph corresponding to terms of the Hamiltonian, and to generalize to non-translation invariant settings, here for $H = \sum_n J\Delta\hat{S}^z_n\hat{S}^z_n - \sum_n h_n\hat{S}^z_n$. The R and F states are special states where the MPO is terminated on the left and right and correspond to having only identities on the left or right of the bond. Here, the green, dotted path corresponds to $\hat{\mathbb{1}}\otimes\hat{\mathbb{1}}\otimes(-h_3\hat{S}^z)\otimes\hat{\mathbb{1}}\otimes\hat{\mathbb{1}}$, while the blue path corresponds to $\hat{\mathbb{1}}\otimes\hat{S}^z\otimes(J\Delta S^z)\otimes\hat{\mathbb{1}}\otimes\hat{\mathbb{1}}$. (d) Adding a next-to-nearest neighbor coupling $J'\sum_n S^z_nS^z_{n+2}$ requires a path with two intermediate states. The first, intermediate state can be shared with the nearest neighbor coupling. (e) Exponentially decaying interactions $\sum_n\sum_{m>0}A_n\lambda^{m-1}B_{n+m}$ can be achieved by a loop in the intermediate states.

in Eq. (2.36). A sequence of actions of the finite state machine can be thought of to generate a term in the Hamiltonian, such that the total Hamiltonian is generated by *all* possible actions of the finite state machine. To explain the mapping between the MPO and the finite state machine in more detail, let us discuss all the elements individually. We identify the set of indices α_n on the virtual bonds of an MPO as possible states of a finite state machine and draw them as nodes of a graph as shown in Fig. 2.15. For a translation invariant Hamiltonian, the indices α_n on the bond to the left of site n are equivalent to the ones on the right, α_{n+1}, so the number of states of the finite state machine is just the MPO bond dimension. The (directed) edges of the drawn graph are transitions between different states, or equivalently actions or inputs of the finite state machine. They correspond to entries of the matrix $W^{[n]}_{\alpha_n,\alpha_{n+1}}$ as written in Eq. (2.36). These entries are onsite operators acting on the local Hilbert space of site n (corresponding to the indices j_n, j'_n in Eq. (2.33)). To read off the entries of the $W^{[n]}$ tensor from a given finite state machine or graph as in Fig. 2.15(a), we can enumerate and distinguish the left and right indices α_n, α_{n+1} as shown in Fig. 2.15(b), such that the entries $W^{[n]}_{\alpha_n,\alpha_{n+1}}$ of Eq. (2.36) become apparent. We can also distinguish between different sites n to generalize the finite state machine to Hamiltonians which are not translation invariant, as illustrated in Fig. 2.15(c) for a system with $N = 5$ sites. While we have just adjusted the prefactors h_n to be site-dependent in this example, the necessary intermediate states α_n may in general also depend on n.

To find the transitions and states of the finite state machine for a given Hamiltonian, we need to read each term of the Hamiltonian as a product of onsite operators from left to right to ensure that the required actions are included in the finite state machine. As a first example, let us consider the onsite field terms

$$-h\sum_n \hat{S}^z_n = \sum_n \hat{\mathbb{1}} \otimes \cdots \otimes \hat{\mathbb{1}} \otimes (-h\hat{S}^z) \otimes \hat{\mathbb{1}} \otimes \cdots \otimes \hat{\mathbb{1}}. \tag{2.51}$$

The finite state machine starts in the special state R (for "ready") on the very left of the product, which correspond to the index where the left boundary vector v^L of the MPO definition in Eq. (2.7) is non-zero. We illustrate this with an incoming arrow from the left in Fig. 2.15(c). Each onsite operator in the tensor product of Eq. (2.51) needs to be in one W matrix and is hence a transition between states of the finite state machine, until we terminate in another special state F (for "finish"), where v^R is non-zero, indicated by the outgoing arrow to the right in Fig. 2.15(c). By adding an $\hat{\mathbb{1}}$ edge from R to itself and from F to itself, we can identify the R and F states on bonds in the bulk as the states where we have only identities on the left or right of the bond, respectively. In the translation invariant case of Fig. 2.15(a), a single edge from R to F with the operator $-h\hat{S}^z$ then yields the full translation invariant sum $-h\sum_n \hat{S}^z_n$, since the transition from R to F can happen on any site n. This becomes evident in Fig. 2.15(c), where the green path indicates the case where the transition happens on site $n = 3$ as an example.

General two-site couplings of the form $J\sum_n \hat{A}_n\hat{B}_{n+m}$ with a range $m > 0$ require m extra intermediate states, since $m + 1$ onsite operators (counting $\hat{\mathbb{1}}$ as well) appear between the trivial products of $\hat{\mathbb{1}}$ on the left and right represented by the R and F state. For example, for the nearest-neighbor coupling $J\Delta\sum_n \hat{S}^z_n\hat{S}^z_{n+1}$ we need to add a transition with $\hat{S}^z$ from R to a new state and from there to F with the operator $J\Delta\hat{S}^z$. We label the new state by $\hat{S}^z_{-1}$ to indicate that $\hat{S}^z$ acted on the next site on the left of the bond. The blue path in Fig. 2.15(c) illustrates the case where the finite state machines produces the term $J\Delta\hat{S}^z_2\hat{S}^z_3$. Including similar transitions and extra states for the $\hat{S}^x$ and $\hat{S}^y$ coupling completes the finite state machine for the Heisenberg model (2.34), which is shown in Fig. 2.15(a,b).

For a next-to-nearest neighbor coupling with terms of the form $J'\hat{S}^z_n\hat{S}^z_{n+2} = J'\hat{\mathbb{1}} \otimes \cdots \otimes \hat{\mathbb{1}} \otimes \hat{S}^z \otimes \hat{\mathbb{1}} \otimes \hat{S}^z \otimes \hat{\mathbb{1}} \otimes \cdots \otimes \hat{\mathbb{1}}$, we need a transition from R to the state $\hat{S}^z_{-1}$, from there to a new state

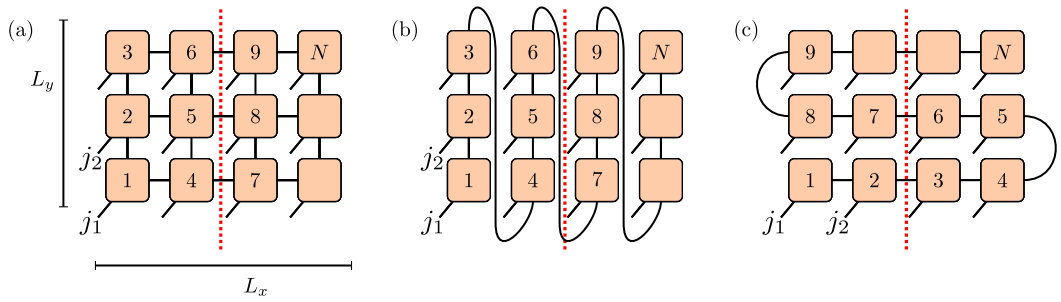

Figure 2.16 (a) PEPS are generalizations of MPS to higher dimensions, here for a square lattice. The open, diagonal legs correspond to the physical degrees of freedom. (b) Alternatively, one can map the 2D system to a 1D chain and use an MPS, which winds through the 2D plane. (c) The MPS "snake" can wind in different ways, which also affects the efficiency of the representation depending on the entanglement structure of the state to be represented, in particular if $L_x \gg L_y$ or if the coupling is strongly anisotropic.

(labeled S^z_{-2}) with an $\hat{\mathbb{1}}$, and a final transition with $J'\hat{S}^z$ to the F state. However, as suggested by the identical labels and shown in Fig. 2.15(d), we can reuse the state S^z_{-1} from the nearest-neighbor coupling in the longer-range coupling. Effectively, this groups $J\Delta\hat{S}^z_n\hat{S}^z_{n+1} + J'\hat{S}^z_n\hat{S}^z_{n+2} = \hat{S}^z_n(J\Delta\hat{S}^z_{n+1} + J'\hat{S}^z_{n+2})$. Since this reduces the number of states in the finite state machine, it reduces the bond dimension of the MPO and ultimately leads to a higher efficiency.

An extreme case of such a grouping of terms is achieved when we add a transition from a state to itself as shown in Fig. 2.15(d). Such a finite state machine naturally encodes exponentially decaying interactions of the form

$$\sum_n \sum_{m>0} \hat{A}_n \lambda^{m-1} \hat{B}_{n+m} = \sum_{n<m} \hat{A}_n e^{-|m-n|/\xi} \hat{B}_m \qquad \text{with} \quad \lambda = e^{-1/\xi}, \tag{2.52}$$

similar as exponentially decaying correlations are naturally encoded in an MPS. In fact, if any other long-range interaction, for example with a power-law decay, should be included into the model, it is often more effective to approximate it by as sum of exponentials up to a desired precision, rather than to represent it exactly with a much higher bond dimension of the MPO [150, 151].

2.5.2 Towards two-dimensional systems: cylinders and ladders

There are two fundamentally different approaches for the simulation of 2D systems with tensor networks. One approach is to generalize the concept of MPS to the higher-dimensional analog of PEPS, as illustrated in Fig. 2.16 for the example of a square lattice [113, 114, 152]. In this case, each tensor has four virtual bonds in addition to the physical leg. Like MPS, a PEPS can serve as variational wave function to approximate ground states. There have already been impressive and promising applications of PEPS, e.g., for the t-J model [153]. The big advantage of the PEPS class is that it can represent states with an entanglement entropy satisfying an area law — which we expect for the ground states of gapped, local Hamiltonians, see Sec. 2.1. This can be seen from the fact that a bipartition into a left and right part requires to cut L_y virtual bonds of the PEPS, as illustrated by the red dashed line in Fig. 2.16. However, using PEPS in practice also comes with a big challenge: even the evaluation of expectation values $\langle\psi|\hat{A}|\psi\rangle$ requires a full contraction of the tensor network, which is in the #P complexity class and thus very hard [154]. In contrast to MPS, cutting a single virtual bond does not divide the PEPS into two halves, such that we can not directly associate the indices of a virtual bond

to Schmidt states, as we did for the definition of the canonical form of an MPS in Eq. (2.15). A generalization of the canonical form to PEPS was introduced in Ref. [144], but in this case it does not simplify the evaluation of expectation values. Over the years, several algorithms have been proposed to find PEPS representations of ground states and approximate, efficient schemes for the evaluation of expectation values have been presented. The most common used algorithms include the Corner Transfer Matrix Renormalization Group Method [115], Tensor Renormalization Group (TRG) [116], Tensor Network Renormalization (TNR) [117], and loop optimizations [118]. More recently, Ref. [155] suggested to restrict to a subset of the PEPS class defined by certain isometry conditions; this provides a promising, new alternative to the more established contraction schemes.

However, in this work we will focus on the second way to simulate a 2D system with tensor networks: we simply map it to a 1D chain and use the well established techniques we have at hand for 1D systems [156, 157]. In particular, we can cover the 2D system with a 1D MPS, as illustrated in Fig. 2.16(b). The biggest challenge of this approach is that we are limited to systems with a small width L_y in y-direction (although the length L_x in x-direction can be made very large or even infinite). All the entanglement between the left and right part indicated by the red dashed line in Fig. 2.16(b) needs to go through the virtual bond between sites 8 and 9. From the area law, we expect an entanglement entropy $S \propto L_y$, so we need to increase the MPS bond dimension $\chi_{\max} \geq e^S$ exponentially with L_y to keep the error at a given precision. Depending on the entanglement structure, choosing a different way how the MPS winds through the 2D system can have a severe impact on the precision and computational cost. For example, if the system is much more strongly coupled in x direction than in y direction, the winding shown in Fig. 2.16(c) might be preferable [158]. Note that the MPO representing the Hamiltonian needs to wind through the system in the same way as the MPS. Even just nearest neighbor couplings then become long-range in the 1D chain of the MPS, consider for example the coupling from site 1 to site $4 = 1 + L_y$ in Fig. 2.16(b), or even from 1 to $8 = 1 + (2L_x - 1)$ in Fig. 2.16(c). In the former case, we can hence scale up the lenght L_x in x-direction for fixed, small L_y and even take the thermodynamic limit $L_x \to \infty$, whereas the increasing MPO bond dimensions due to the additional long range couplings hinders us to do so in the latter case.

In many cases, periodic boundaries in y-direction reduce the finite size effects of the small L_y, as we will for example see in Sec. 3.5. In this work, we refer to this case as "cylinders", while "ladders" refer to the case of open boundaries with $L_x \gg L_y$. Another advantage of cylinder boundary conditions is that one can observe the response of the ground state when an external flux is inserted to the cylinder, which can reveal the fractionalized nature of excitations, see e.g., [159–161]. An important aspect to keep in mind both for ladders and cylinders with $L_x \gg L_y$ is the fact that the orientation of the lattice (i.e., in which direction the lattice is infinite) can have a severe impact on the physics. This becomes most obvious if we consider the Brillouin zone of infinite cylinders. Depending on the orientation of the lattice relative to the cylinder axis, we get different lines of compatible momenta through the Brillouin zone. If we have gapless points in the Brillouin zone, depending on whether those are covered by the lines of compatible momenta, the effective 1D model can be critical or not, as for example seen in Ref. [162].

Finally, let us note that it is straightforward to implement fermionic models for MPS: we simply use a Jordan-Wigner transformation, which maps the fermionic operators to spins [163],

$$\hat{n}_j \leftrightarrow (\hat{\sigma}_j^z + 1)/2, \qquad \hat{c}_j \leftrightarrow (-1)^{\sum_{l<j} \hat{n}_l} \hat{\sigma}_j^-, \qquad \hat{c}_j^\dagger \leftrightarrow (-1)^{\sum_{l<j} \hat{n}_l} \hat{\sigma}_j^+. \tag{2.53}$$

The Jordan-Wigner strings are easiest chosen along the MPS, however it winds through a 2D system, if desired. If we want to consider spin-full fermions, we can simply split the local Hilbert

space into a product of spin-less fermionic degrees of freedom, one for each spin state of the fermion, and perform the Jordan-Wigner transformation with Eq. (2.53) as before.

2.6 The Tensor Network Python (TeNPy) library

We now present the TeNPy program library [2]. The library aims for a good balance between its two main design goals: On one hand, TeNPy should be accessible and easy to use for students and researchers who have not yet performed simulations with tensor networks. On the other hand, the provided algorithms should be highly efficient to allow an economic use of available computational resources. Moreover, the library should be versatile and flexible enough such that experts in the field of tensor network algorithms can quickly implement new variants of existing algorithms, test out ideas for new algorithms, and share them with other researchers.

To support those goals, the library is mostly implemented in the Python programming language, which is easy to learn for novices, and yet a very powerful high-level language with many available tools to simplify and speed up the development [147]. The library is published as open source code under the GNU General Public License (version 3) to encourage the sharing of algorithms between researchers[8]. For the goal of accessibility, we distribute small "toy codes" along with the source code. Those toy codes are not meant to be used for the day-to-day research, but to illustrate the very basic and necessary steps of the algorithms in just[9] around 200 lines of code per file. They accompany an extensive documentation, both directly inside the code on the level of documentation strings for (almost) each function and class, as well as in the form of examples and user guides explaining the interface of the various algorithms. While the documentation is contained inside the source code, it is also made available online[10]. Moreover, we have set up a question-and-answer forum[11], which has already been accepted well by the community. One can never guarantee that a software works as intended for all cases. Nevertheless, we can get some confidence in that direction by employing automated tests with typical test cases comparing to known results. In the case of TeNPy, those tests can be run with the pytest tool[12]. Any serious bugs get reported as GitHub issues[13], which are also used to streamline the further development. Git is used as version control system[14].

There are several layers of abstraction implemented in the TeNPy library, illustrated in Fig. 2.17. While there is a certain hierarchy of how the concepts build up on each other, the user can decide to utilize only some of them. A maximal flexibility is provided by an object oriented style based on classes, which can be inherited and adjusted to individual demands.

The most basic layer is given by in the `linalg` module, which provides basic features of linear algebra. In particular, the `np_conserved` submodule implements an `Array` class which is used to represent the tensors. The basic interface of `np_conserved` is very similar to that of the NumPy and SciPy libraries [147]. However, the `Array` class implements charge conservation as outlined in Sec. 2.4. If no charges are to be used, one can use "trivial" arrays, as shown in the following example code.

```
import tenpy.linalg.np_conserved as npc
```

[8] https://github.com/tenpy/tenpy
[9] This should be compared to the core files of TeNPy, which have more than 25000 lines (version 0.4.1).
[10] https://tenpy.github.io
[11] https://tenpy.johannes-hauschild.de
[12] https://pytest.org
[13] https://github.com/tenpy/tenpy/issues
[14] https://git-scm.org

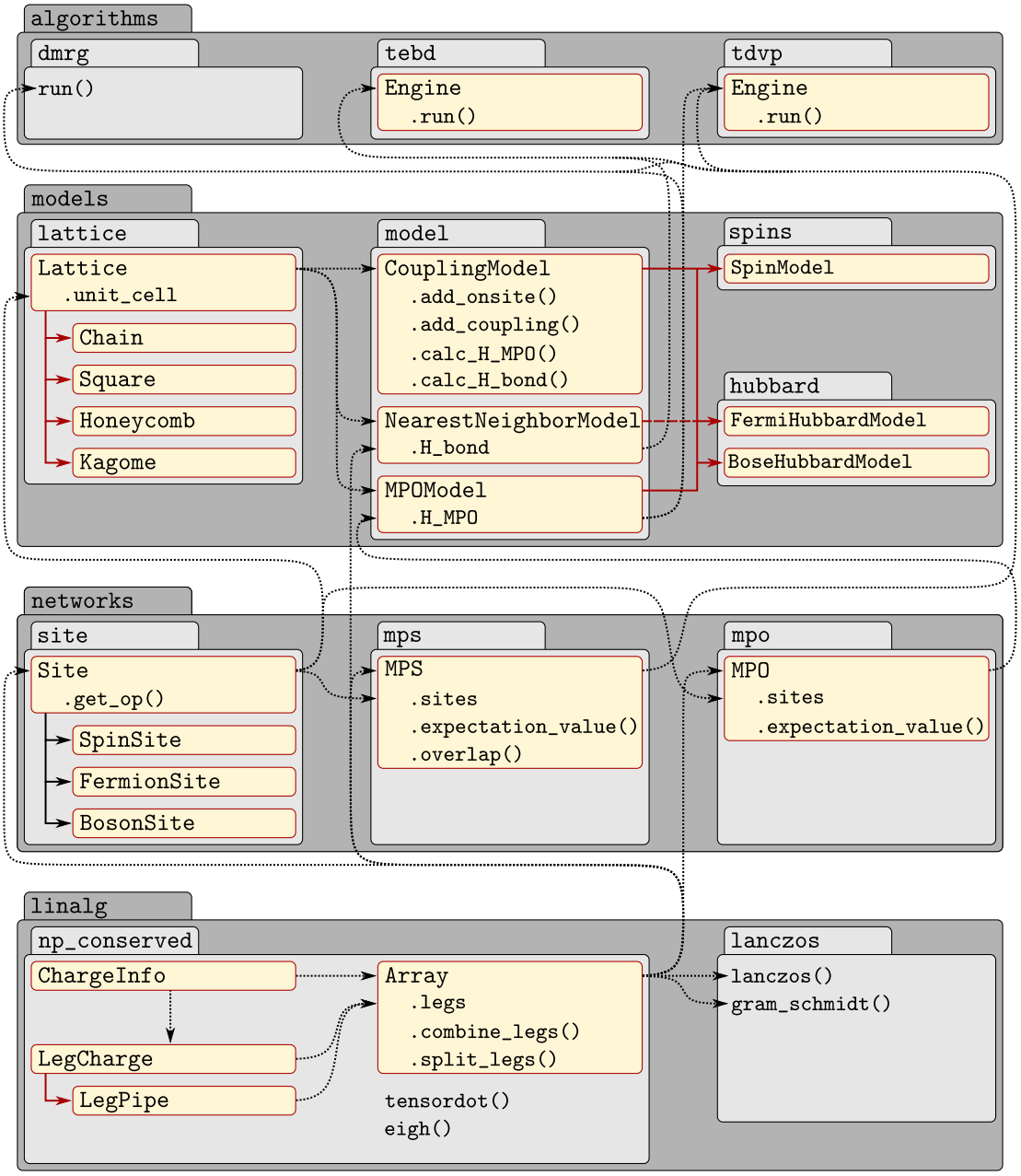

Figure 2.17 Overview of the most important modules, classes and functions in TeNPy. Gray backgrounds indicate (sub)modules, yellow backgrounds indicate classes. Red arrows indicate inheritance relations, dashed black arrows indicate a direct use. (The individual models might be derived from the `NearestNeighborModel` depending on the geometry of the lattice.) There is a clear hierarchy from high-level algorithms in the `algorithms` module down to basic operations from linear algebra in the `linalg` module.

```
M = npc.Array.from_ndarray_trivial([[0., 1.],
                                    [1., 0.]])
v = npc.Array.from_ndarray_trivial([2., 4. + 1.j])
v[0] = 3. # set indiviual entries like in numpy
print("|v> =", v.to_ndarray())
# |v> = [ 3.+0.j  4.+1.j]

M_v = npc.tensordot(M, v, axes=[1, 0])
print("M|v> =", M_v.to_ndarray())
# M|v> = [ 4.+1.j  3.+0.j]
print("<v|M|v> =", npc.inner(v.conj(), M_v))
# <v|M|v> = (24+0j)
```

Algorithm 2.1 Basic use of the `Array` class.

The number and types of symmetries are specified in a `ChargeInfo` class. An `Array` instance represents a tensor satisfying the charge rule of Eq. (2.47) and internally stores only the non-zero blocks of the tensor, along with one `LegCharge` instance for each leg, which contains the charge values q and sign ζ (called `qconj`) for the leg. If we combine multiple legs into a single larger "pipe" as explained in Sec. 2.4, the resulting leg will have be `LegPipe`, which is derived from the `LegCharge` and stores all the information necessary to later split the pipe. The following code explicitly defines the spin-1/2 $\hat{S}^+$, $\hat{S}^-$ and $\hat{S}^z$ operators and uses them to generate and diagonalize the two-site Hamiltonian of Eq. (2.44); it prints the charge vector $q^{[a]}$ (by default sorted ascending) and the eigenvalues of H.

```
import tenpy.linalg.np_conserved as npc

# consider spin-1/2 with Sz-conservation
chinfo = npc.ChargeInfo([1])  # just a U(1) charge
# charges for up, down state
p_leg = npc.LegCharge.from_qflat(chinfo, [[1], [-1]])
Sz = npc.Array.from_ndarray([[0.5, 0.], [0., -0.5]],
                            [p_leg, p_leg.conj()])
Sp = npc.Array.from_ndarray([[0., 1.], [0., 0.]],
                            [p_leg, p_leg.conj()])
Sm = npc.Array.from_ndarray([[0., 0.], [1., 0.]],
                            [p_leg, p_leg.conj()])

Hxy = 0.5*(npc.outer(Sp, Sm) + npc.outer(Sm, Sp))
Hz = npc.outer(Sz, Sz)
H = Hxy + Hz
# here, H has 4 legs
H.iset_leg_labels(["s1", "t1", "s2", "t2"])
H = H.combine_legs([["s1", "s2"], ["t1", "t2"]], qconj=[+1, -1])
# here, H has 2 legs
print(H.legs[0].to_qflat().flatten())
# prints [-2  0  0  2]
E, U = npc.eigh(H)  # diagonalize blocks individually
print(E)
# [ 0.25 -0.75  0.25  0.25]
```

Algorithm 2.2 Explicit definition of charges and spin-1/2 operators

The next basic concept is that of a local Hilbert space, which is represented by a `Site` in TeNPy. This class does not only label the local states and define the charge values q, but also provides onsite operators. For example, the `SpinHalfSite` provides the $\hat{S}^+, \hat{S}^-, \hat{S}^z$ operators under the names `'Sp'`, `'Sm'`, `'Sz'`, defined as `Array` instances similarly as in Alg. 2.2. Since the most common sites like for example the `SpinSite` (for general spin s), `BosonSite` and `FermionSite` are predefined, a user of TeNPy usually does not need to define the local charges and operators explicitly. The total Hilbert space, i.e, the tensor product of the local Hilbert spaces, is then just given by a list of `Site` instances. If desired, different kinds of `Site` can be combined in that list. This list is then given to classes representing tensor networks like the `MPS` and `MPO`. The tensor network classes also use `Array` instances for the tensors of the represented network. The following example illustrates the initialization of a spin-1/2 site, and MPS representing the Neél state Eq. (2.10), and an MPO representing the Heisenberg model of Eq. (2.34) by explicitly defining the $W^{[n]}$ tensor of Eq. (2.36).

```
from tenpy.networks.site import SpinHalfSite
from tenpy.networks.mps import MPS
from tenpy.networks.mpo import MPO

spin = SpinHalfSite(conserve="Sz")
print(spin.Sz.to_ndarray())
# [[ 0.5  0. ]
#  [ 0.  -0.5]]

N = 6  # number of sites
sites = [spin] * N  # repeat entry of list N times
pstate = ["up", "down"] * (N // 2)  # Neel state
psi = MPS.from_product_state(sites, pstate, bc="finite")
print("<Sz> =", psi.expectation_value("Sz"))
# <Sz> = [ 0.5 -0.5  0.5 -0.5]
print("<Sp_i Sm_j> =", psi.correlation_function("Sp", "Sm"),
      sep="\n")
# <Sp_i Sm_j> =
# [[1. 0. 0. 0. 0. 0.]
#  [0. 0. 0. 0. 0. 0.]
#  [0. 0. 1. 0. 0. 0.]
#  [0. 0. 0. 0. 0. 0.]
#  [0. 0. 0. 0. 1. 0.]
#  [0. 0. 0. 0. 0. 0.]]


# define an MPO
Id, Sp, Sm, Sz = spin.Id, spin.Sp, spin.Sm, spin.Sz
J, Delta, hz = 1., 1., 0.2
W_bulk = [[Id,   Sp,   Sm,   Sz,   -hz*Sz    ],
          [None, None, None, None, 0.5*J*Sm  ],
          [None, None, None, None, 0.5*J*Sp  ],
          [None, None, None, None, J*Delta*Sz],
          [None, None, None, None, Id        ]]
W_first = [W_bulk[0]]  # first row
W_last =  [[row[-1]] for row in W_bulk] # last column
Ws = [W_first] + [W_bulk] * (N-2) + [W_last]
H = MPO.from_grids([spin] * N, Ws, bc='finite', IdL=0, IdR=-1)
```

```
print("<psi|H|psi> =", H.expectation_value(psi))
# <psi|H|psi> = -1.25
```

Algorithm 2.3 Initialization of sites, MPS, and MPO.

Technically, the explicit definition of an MPO is already enough to call an algorithm like DMRG. However, writing down the $W^{[n]}$ tensors is cumbersome especially for more complicated models. Hence, TeNPy provides another layer of abstraction for the definition of models, which we discuss first. Different kinds of algorithms require different representations of the Hamiltonian. Therefore, the library offers to specify the model abstractly by the individual onsite terms and coupling terms of the Hamiltonian. The following example illustrates this.

```
from tenpy.networks.site import SpinSite
from tenpy.models.lattice import Chain
from tenpy.models.model import CouplingModel,
    NearestNeighborModel, MPOModel

class XXZChain(CouplingModel, NearestNeighborModel, MPOModel):
  def __init__(self, L=2, S=0.5, J=1., Delta=1., hz=0.):
    spin = SpinSite(S=S, conserve="Sz")
    # the lattice defines the geometry
    lattice = Chain(L, spin, bc="open", bc_MPS="finite")
    CouplingModel.__init__(self, lattice)
    # add terms of the Hamiltonian
    self.add_coupling(J*0.5, 0, "Sp", 0, "Sm", 1)   # Sp_i Sm_{i+1}
    self.add_coupling(J*0.5, 0, "Sp", 0, "Sm", -1)  # Sp_i Sm_{i-1}
    self.add_coupling(J*Delta, 0, "Sz", 0, "Sz", 1)
    # (for site dependent prefactors, the strength can be an array)
    self.add_onsite(-hz, 0, "Sz")

    # finish initialization
    # generate MPO for DMRG
    MPOModel.__init__(self, lat, self.calc_H_MPO())
    # generate H_bond for TEBD
    NearestNeighborModel.__init__(self, lat, self.calc_H_bond())
```

Algorithm 2.4 Definition of a model: the XXZ chain of Eq. (2.34).

While this generates the same MPO as in Alg. 2.3, this example can easily adjusted and generalized. Internally, the MPO is generated using the finite state machine picture discussed in Sec. 2.5.1. This allows not only to translate more complicated Hamiltonians into their corresponding MPOs, but also to automate the mapping from a higher dimensional lattice to the 1D chain along which the MPS winds, as explained in Sec. 2.5.2. Recall that this mapping introduces longer-range couplings, so the model can no longer be defined to be a `NearestNeighborModel` suited for TEBD if another lattice than the `Chain` is to be used. Of course, many commonly studied models are also predefined. For example, the following code initializes the Heisenberg model on a kagome lattice; the spin liquid nature of the ground state of this model is highly debated in the current literature [66, 162, 164–166].

```
from tenpy.models.spins import SpinModel

model_params = {
    "S": 0.5, # Spin 1/2
    "lattice": "Kagome",
```

```
    "bc_MPS": "infinite",
    "bc_y": "cylinder",
    "Ly": 2,  # defines cylinder circumference
    "conserve": "Sz", # use Sz conservation
    "Jx": 1., "Jy": 1., "Jz": 1.  # Heisenberg coupling
}
model = SpinModel(model_params)
```

Algorithm 2.5 Initialization of the Heisenberg model on a kagome lattice.

The highest level in TeNPy is given by algorithms like DMRG and TEBD. Using the previous concepts, setting up a simulation running those algorithms is a matter of just a few lines of code. The following example runs a DMRG simulation as explained in Sec. 2.2.5, exemplary for the transverse field Ising model at the critical point. The `"mixer"` parameter enables the density matrix perturbation of Ref. [101]; for a further description of (optional) parameters we refer to the documentation [2].

```
from tenpy.networks.mps import MPS
from tenpy.models.tf_ising import TFIChain
from tenpy.algorithms import dmrg

N = 16 # number of sites
model = TFIChain({"L": N, "J": 1., "g": 1., "bc_MPS": "finite"})
sites = model.lat.mps_sites()
psi = MPS.from_product_state(sites, ['up'] * N, "finite")
dmrg_params = {"trunc_params": {"chi_max": 100, "svd_min": 1.e-10},
               "mixer": True}
info = dmrg.run(psi, model, dmrg_params)
print("E =", info['E'])
# E = -20.01638790048513
print("max. bond dimension =", max(psi.chi))
# max. bond dimension = 27
```

Algorithm 2.6 Call of DMRG.

The switch from DMRG to iDMRG in TeNPy is simply accomplished by a change of the parameter `"bc_MPS"` from `"finite"` to `"infinite"`, both for the model and the state. The returned E is then the energy density per site. Due to the translation invariance, one can also evaluate the correlation length as definined in Eq. (2.42), here slightly away from the critical point.

```
from tenpy.networks.mps import MPS
from tenpy.models.tf_ising import TFIChain
from tenpy.algorithms import dmrg

N = 2 # number of sites in unit cell
model = TFIChain({"L": N, "J": 1., "g": 1.1, "bc_MPS": "infinite"})
sites = model.lat.mps_sites()
psi = MPS.from_product_state(sites, ['up'] * N, "infinite")
dmrg_params = {"trunc_params": {"chi_max": 100, "svd_min": 1.e-10},
               "mixer": True}
info = dmrg.run(psi, model, dmrg_params)
print("E =", info['E'])
# E = -1.342864022725017
print("max. bond dimension =", max(psi.chi))
```

```
# max. bond dimension = 56
print("corr. length =", psi.correlation_length())
# corr. length = 4.915809146764157
```

Algorithm 2.7 Call of iDMRG.

Running TEBD requires an additional loop, during which the desired observables have to be measured. The following code shows this directly for the infinite version of TEBD.

```
from tenpy.networks.mps import MPS
from tenpy.models.tf_ising import TFIChain
from tenpy.algorithms import tebd

model = TFIChain({"L": 2, "J": 1., "g": 1.0, "bc_MPS": "infinite"})
sites = model.lat.mps_sites()  # list of sites => Hilbert space
psi = MPS.from_product_state(sites, ["up"] * 2, bc="infinite")
tebd_params = {"order": 4, # fourth order in dt
               "dt": 0.05, # time step
               "N_steps": 10, # repeat 10 steps by dt in each `run()`
               "trunc_params": {"chi_max": 100, "svd_min": 1.e-10}}
eng = tebd.Engine(psi, model, tebd_params)
for i in range(6):
    t = eng.evolved_time
    xi = psi.correlation_length()
    print("t = {0:.2f}, corr. length = {1:.2f}".format(t, xi))
    eng.run()
    # t = 0.00, corr. length = 0.00
    # t = 0.50, corr. length = 0.20
    # t = 1.00, corr. length = 0.29
    # t = 1.50, corr. length = 0.38
    # t = 2.00, corr. length = 0.47
    # t = 2.50, corr. length = 0.56
```

Algorithm 2.8 Call of TEBD.

2.7 Conclusion

In this chapter we combined a pedagogical review of MPS based algorithms for both finite and infinite systems with the presentation of the open-source library TeNPy. While there exists by now a huge arsenal of tensor-product state based algorithms, we focused here on the time evolving block decimation (TEBD) [76] and the density-matrix renormalization group (DMRG) method [68]. For both algorithms, we provided a basic introduction and showed how to call them using the TeNPy package. While we did not cover PEPS-based methods for the simulation of 2D systems, we discussed how the latter can be mapped to 1D systems in Sec. 2.5, such that MPS based algorithms can be used. Moreover, we note that the tensor class implemented in TeNPy allows for a fairly simple implementation of general tensor networks in higher dimensions as well. In particular, the method of conserving abelian symmetries discussed in Sec. 2.4 directly carries over to genuine 2D PEPS.

3 Sudden expansion and domain-wall melting of strongly interacting bosons in two-dimensional optical lattices and on multileg ladders

Most of the content of this chapter can also be found in a previous publication of the author [3]. Text and figures have been adjusted to fit into the context of the thesis.

Ultracold quantum gases are famous for the possibility of realizing many-body Hamiltonians such as the Hubbard model, the tunability of interaction strength, and, effectively, also dimensionality [56]. This provides access to genuine 1D and 2D physics as well as to the crossover physics between these limiting cases. Moreover, time-dependent changes of various model parameters can be used to explore the nonequilibrium dynamics of many-body systems (see [53–55] for recent reviews). Timely topics that are investigated in experiments include the relaxation and thermalization dynamics in quantum quenches [167–176], the realization of metastable states [87, 177], and nonequilibrium mass transport [178–180] and spin transport [181]. Due to the availability of powerful analytical and numerical methods such as bosonization [182], exact solutions for integrable systems [183], or the density matrix renormalization group method [68, 73, 121], a direct comparison between theoretical and experimental results is often possible in the case of 1D systems [170, 172, 175, 180].

Strongly interacting many-body systems in two spatial dimensions, however, pose many of the open problems in condensed matter theory and many-body physics, concerning both equilibrium and nonequilibrium properties. The reason is related to the lack of reliable numerical approaches. Exact diagonalization, while supremely flexible, is inherently restricted to small system sizes [19]. Nevertheless, smart constructions of truncated basis sets by selecting only states from subspaces that are relevant for a given time-evolution problem have given access to a number of 2D nonequilibrium problems (see, e.g., Ref. [184, 185]). The truncation of equation of motions for operators provides an alternative approach [186], which has also been applied to quantum quench problems in the 2D Fermi-Hubbard model [187]. Quantum Monte Carlo methods can be applied to systems in arbitrary dimensions including nonequilibrium problems (see, e.g., [188–190]), but suffer, for certain systems and parameter ranges, from the sign problem [191]. Dynamical mean-field methods become accurate in higher dimensions, yet do not necessarily yield quantitatively correct results in 2D [192].

Regarding analytical approaches, we mention just a few examples, including solutions of the Boltzmann equation [178], flow equations [193], expansions in terms of the inverse coordination number [194], semiclassical approaches [195, 196], or time-dependent mean-field approaches [197–199] such as the time-dependent Gutzwiller ansatz (see, e.g., Ref. [78, 79]). All these methods have provided valuable insights into aspects of the nonequilibrium dynamics in two (or three) dimensions, yet often involve approximations. Recently, the application of a

nonequilibrium Green's function approach to the dynamics in the sudden expansion in the 2D Fermi-Hubbard model has been explored [200].

As we discussed in Sec. 2.5.2, MPS-based methods face, in general, a disadvantageous scaling with system size in 2D, yet there have been very impressive recent applications [157, 164, 165] of the DMRG method to 2D systems. A relatively little-explored area of research is the time evolution of 2D many-body systems in quantum quench problems using MPS-based algorithms [109, 110, 201–203].

In this chapter, we present the application of a recently introduced algorithm [109] for the time evolution of MPS, that is specifically tailored to deal with long-range interactions. As discussed in Sec. 2.5.2, such long-range interactions arise by mapping even a short-range Hamiltonian on a 2D lattice to a 1D chain.

Recent experiments have started to study the nonequilibrium dynamics of interacting quantum gases in 2D lattices or in the 1D-to-2D crossover [178, 180, 204]. Motivated by Refs. [87, 180], we study the sudden expansion of hard-core bosons which is the release of a trapped gas into a homogeneous optical lattice after quenching the trapping potential to zero. The results of Ref. [180] show that strongly interacting bosons in 2D exhibit a much slower expansion than their 1D counterpart. In the latter case, the integrability of hard core bosons leads to a strictly ballistic and (for the specific initial conditions of Ref. [180]) fast expansion that is indistinguishable from the one of noninteracting fermions and bosons. In the 2D case, it is believed that diffusive dynamics sets in and virtually inhibits the expansion in the high-density region, leading to a stable high-density core surrounded by ballistically expanding wings [180], similar to the behavior of interacting fermions in 2D [178]. The characteristic feature of these diffusive-like expansions in contrast to the ballistic case is the emergence of a spherically symmetric high-density core, while the ballistic expansion unveils the topology of the underlying reciprocal lattice.

In our work, we investigate this problem for both 2D clusters that can expand symmetrically in the x and y directions [see Fig. 3.1(a)] and wide cylinders and ladders [see Fig. 3.1(b)]. We use the ratio of hopping matrix elements J_x and J_y along the x and y directions as a parameter to study the 1D-to-2D crossover. For the 2D expansion in the isotropic case $J_x = J_y$, we clearly observe the emergence of a spherically symmetric core, while for small values of $J_y < J_x$ and on the accessible time scales, the expansion is essentially 1D-like. We further compute the expansion velocities derived from the time dependence of the radius as a function of J_y/J_x.

Since we are, in general, able to reach both longer times and larger particle numbers in the case of ladders than in 2D, we present an extensive analysis of multi-leg ladders and cylinders [i.e., ladders with periodic boundary conditions in the (narrow) y direction] with $L_y = 2, 3, 4$ legs [see the sketch in Fig. 3.1(b)]. From the analysis of the expansion in 1D systems [87], we expect that the short-time dynamics is identical to the melting of so-called domain-wall states [82, 205, 206], in which half of the system is empty while the other half contains one particle per site in the initial state [see the sketch in Fig. 3.1(c)]. The domain-wall melting has been attracting considerable attention as a nonequilibrium problem in 1D spin-$\frac{1}{2}$ systems (see, e.g., [82, 205–211]). Our results show that this similarity between the expansion of clusters and the domain-wall melting carries over to the transient dynamics on L_y-leg ladder systems, irrespective of boundary conditions.

A considerable portion of the discussion in both theoretical and experimental papers has focused on the question of whether there are signatures of diffusive dynamics in the sudden expansion in 2D, in the dimensional crossover [178, 180], or on coupled chains [86]. The analysis of the expansion of fermions in the 2D square lattice starting from an initial state with two particles per site (i.e., a fermionic band insulator) suggests that diffusive dynamics

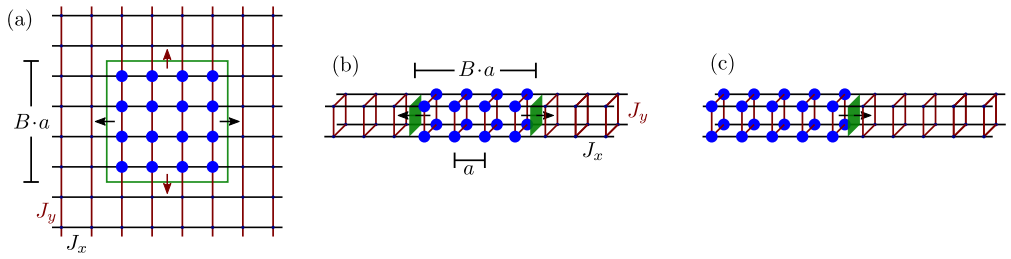

Figure 3.1 Illustration of initial states and geometries: (a) central block for the 2D expansion; (b) central block of size $B \times L_y$; and (c) domain wall on a cylinder with $L_y = 4$ legs.

is responsible for the slow expansion in the high-density regions [178]. This is expected to carry over to the bosonic case, yet there only two-leg ladders have been thoroughly studied. In linear response, hard-core bosons on a two-leg ladder realize a textbook diffusive conductor at high temperatures [212, 213], thus suggesting that diffusion may also play a role in the sudden expansion [86]. Curiously, the expansion velocities measured numerically for hard-core bosons on a two-leg ladder exhibit a dependence on J_y/J_x that resembles the experimental observations for the true 2D case [86, 180]. Here we are able to provide a more refined picture. Our analysis unveils that the sudden expansion becomes faster by going from two-leg to three- or four-leg ladders. We trace this back to the existence of heavy excitations on the two-leg ladder that are defined on a rung of the ladder and are inherited from the $J_x \ll J_y$ limit, which cannot propagate in first-order tunneling processes in J_x/J_y. Conversely, the three- and four-leg ladders possess single-particle-like excitations, which we dub propagating modes, that have a sufficiently low mass to become propagating. This picture provides an intuitive understanding of the emergence of slow mass transport in the sudden expansion in the initial stages of the time evolution, complementary to the discussion of diffusive versus ballistic dynamics. The reasoning is similar to the role that doublons play for slowing down mass transport in the 1D Bose-Hubbard model [86, 180, 214–216], which has also been emphasized in the case of the Fermi-Hubbard model [217, 218]. Our results raise the question as to whether the expansion in both directions in 2D and the one-directional expansion on wide ladders and cylinders will result in the same dependence of expansion velocities on J_y/J_x for large L_y. It appears that the ladders and cylinders, at least for small L_y, preserve some degree of one-dimensionality. A possible scenario is that the expansion velocities in the x direction will depend non-monotonically on L_y for a fixed value of J_y/J_x if ever they become identical to the behavior on the 2D systems. As a caution, we stress that long expansion times may be necessary to fully probe the effect of a 2D expansion at small $J_y \ll J_x$ since the bare time scale for charge dynamics in the y direction is set by $1/J_y$, as pointed out in [219].

Apart from the nonequilibrium mass transport of strongly interacting bosons, there are also predictions for the emergence of nonequilibrium condensates at finite quasimomenta in the sudden expansion in a 2D square lattice. These predictions are based on exact diagonalization for narrow stripes [77], as well as on the time-dependent Gutzwiller method [78, 79]. The dynamical condensation phenomenon has first been discussed for 1D systems (where it actually is a quasicondensation [80]), where it was firmly established from exact numerical results [80, 81] and analytical solutions [82] (see also [83–86]) and has recently been observed in an experiment [87]. In the sudden expansion of hard-core bosons in 1D, the dynamical quasicondensation is a transient, yet long-lived phenomenon [80, 86] as ultimately the quasimomentum distribution

function of the physical particles approaches the one of the underlying noninteracting fermions via the dynamical fermionization mechanism [88, 89].

It is therefore an exciting question whether a true nonequilibrium condensate can be generated in 2D. Our results cannot fully clarify this point, yet we do observe a bunching of particles at certain nonzero momenta in the quasimomentum distribution after releasing the particles whenever propagating modes as discussed above are present. For the melting of domain walls, the occupation of most of these modes, at which a nonequilibrium condensation is allowed by energy conservation and at which a bunching occurs, saturates at long expansion times. The notable exception are certain modes on the $L_y = 4$ cylinder. This behavior, i.e., the saturation is markedly different from the 1D case of hard-core bosons in the domain-wall melting, where the occupation continuously increases. The reason for this increase is that the semi-infinite, initially filled half of the system will indefinitely feed the quasicondensates [82, 87]. As such an increase is a necessary condition for condensation, we interpret the saturation of occupations as an indication that either breaking the integrability of strictly 1D hard-core bosons or the larger phase space for scattering in 2D inhibits the dynamical condensation of expanding clouds. However, even in those cases on the ladder, in which we do not see a saturation, the increase is slower than the true 1D case, suggesting that coupling chains, in general, disfavors condensation. Yet a decisive analysis of this problem will require access to larger particle numbers and times in numerical simulations or future experiments. Note that multi-leg ladder systems can be readily realized with optical lattices, using either superlattices [220] or the more recent approach of using a synthetic lattice dimension [221–223]. Using a synthetic lattice dimension [221], it is in principle possible to obtain cylinders, i.e., periodic boundary conditions along the (narrow) y-direction.

The plan of this chapter is the following. In Sec. 3.1, we introduce the model and definitions. Section 3.2 provides a discussion and definitions for various measures of expansion velocities employed throughout our work, while Sec. 3.3 provides details on our numerical method. We present our results for the 2D case in Sec. 3.4, while the results for multi-leg ladders and cylinders are contained in Sec. 3.5. We conclude with a summary presented in Sec. 3.6

3.1 Model and initial conditions

We consider hard-core bosons on a square lattice and on multi-leg ladders. The Hamiltonian reads

$$H = -\sum_{r_x,r_y} [J_x(\hat{a}^\dagger_{r_x,r_y}\hat{a}_{r_x+a,r_y} + h.c.) + J_y(\hat{a}^\dagger_{r_x,r_y}\hat{a}_{r_x,r_y+a} + h.c.)]\,. \tag{3.1}$$

Here $\hat{a}^\dagger_{r_x,r_y}$ denotes the creation operator on site $\vec{r} = (r_x, r_y) = (x\,a, y\,a)$, and $J_x(J_y)$ are the hopping matrix elements in the $x(y)$ direction. We choose the hopping matrix element J_x in the x direction and the lattice constant a as units and set $\hbar$ to unity; the ratio J_y/J_x is dimensionless. Note that the Hamiltonian is equivalent to the spin-$\frac{1}{2}$ XX model. In 1D ($J_y = 0$), the Jordan-Wigner transformation maps the bosons to free fermions [224]. L_x and L_y denote the number of sites in the x and y direction, respectively.

We consider different geometries, namely (i) a small square-shaped cluster of $L_x = L_y = 12$ sites with open boundary conditions (OBC) in both directions, (ii) ladders with $L_x = 60$, $L_y \in \{2, 3, 4\}$ with OBC in both the x- and y-direction, and (iii) cylinders with $L_x = 60$, $L_y \in \{2, 3, 4\}$ with periodic boundary conditions (PBC) in the y direction and OBC in the x direction. For two-leg ladders, the only difference between the Hamiltonian with OBC and PBC

along the y direction is thus a factor of two in the tunneling matrix element J_y. In pratice, we obtain the behavior with PBC by just taking the OBC data with $J_y \to J_y/2$.

For all simulations, we start the expansion from a product state,

$$|\psi_0\rangle = \prod_{\vec{r}\in\mathcal{B}} \hat{a}^\dagger_{r_x,r_y} |\text{vac}\rangle\,, \tag{3.2}$$

in real space. To model the fully 2D expansion, we choose $\mathcal{B}$ to be a square-shaped block of $B \times B$ sites centered in the cluster; see Fig. 3.1(a). On cylinders and ladders, we study two different types of $\mathcal{B}$: (i) a block of $B \times L_y$ bosons, centered in the x direction and filling all the sites in the y direction as shown in Fig. 3.1(b), and (ii) a domain wall, where the left half of the lattice is occupied by a block of $L_x/2 \times L_y$ bosons while the right half is empty; see Fig. 3.1(c).

3.2 Definitions of expansion velocities

There are several possible ways of defining the spatial extension of an expanding cloud and thus also several different velocities.

3.2.1 Position of the fastest wave front

One can define the cloud size from its maximum extension, i.e., from the position of the (fastest) wave front. The velocity derived from this approach will typically simply be the fastest possible group velocity (provided the corresponding quasimomentum is occupied in the initial state). Thus, this velocity will not contain information about the slower-moving particles and any emergent slow and possibly diffusive dynamics in the core region. We do not study the wave front in this work.

3.2.2 Radial velocity

Theoretically, it is natural to define the radius R as the square root of the second moment of the particle distribution $n_{r_x,r_y}(t) = \langle \hat{n}_{r_x,r_y}(t)\rangle$. Suppose we are interested in the expansion in x direction: We average the density profile over the y direction to calculate the radius

$$R_x^2(t) = \frac{1}{N} \sum_{r_x,r_y} n_{r_x,r_y}(t)(r_x - r_x^0)^2, \tag{3.3}$$

where r_x^0 is the center of mass in the x direction and N is the total number of bosons. An analogous expression is used to define $R_y^2(t)$. To get rid of an initial constant part, we use $\tilde{R}_\mu^2(t) = R_\mu^2(t) - R_\mu^2(t=0)$ to define the radial velocity

$$v_{R,\mu} = \frac{\partial \tilde{R}_\mu(t)}{\partial t} \tag{3.4}$$

with $\mu = x, y$. The corresponding velocity has contributions from all occupied quasimomenta. It will ultimately be dominated by the fastest expanding particles, and for the sudden expansion, R_μ will be linear in time in the limit in which the gas has become dilute and effectively noninteracting.

The radial expansion velocity of 1D systems was studied for the Fermi-Hubbard model [225], the Bose-Hubbard model [86, 180], and the Lieb-Liniger model [226]. For Bethe-integrable 1D systems, it can be related to distributions of rapidities [227]. For a recent study of the radial velocity in the 2D Fermi-Hubbard model, see [200].

3.2.3 Core expansion velocity

In the related experiments with ultracold atoms [178, 180], the focus was on the core expansion velocity that is derived from the time evolution of the half width at half maximum $R_c(t)$. The reason is that in these experiments, an average over many 1D or 2D systems is measured. Moreover, the core expansion velocity is primarily sensitive to the dynamics in the high-density core (but insensitive to the ballistic tails) and thus yields slightly different information. In case of multiple local maxima, the two outermost points are taken. Since in our simulations we have smaller particle numbers compared to the experiments [178, 180], we use linear splines to interpolate the density profile between the lattice sites in order to get values for $R_c(t)$ to a better accuracy than just a single lattice constant. The core expansion velocity is defined as the time derivative

$$v_c = \frac{\partial R_c(t)}{\partial t} \,. \tag{3.5}$$

The full time dependence of R_c and the extraction of v_c will be discussed in Sec. 3.5.4.

3.3 Numerical method

Although the Hamiltonian Eq. (3.1) itself is short ranged, long-range interactions arise by mapping the 2D lattice to a 1D chain along which the MPS can wind, see Sec. 2.5.2. The presence of such long-range interactions renders most of the existing MPS-based algorithms for the time evolution like TEBD [73, 76, 107, 108] inefficient because a direct Trotter decomposition of the exponential is not possible. In our work, we use a recently developed extension [109], which provides a direct way to exponentiate an MPO. The actual time evolution can then be performed using standard algorithms that apply an MPO to a given MPS [73]. An advantage of the method is that it can be easily implemented into an existing MPS based DMRG code and has a constant error per site.

For our simulations, we choose the MPS to wind first along the y direction in order to keep the range of the interactions as small as possible (namely L_y). Sources of errors are the discretization in time and the discarded weight per truncation of the MPSs after each time step. The time steps are chosen small enough to make the error resulting from the second-order expansion negligible. We furthermore choose the truncation error at each step to be smaller than 10^{-10}, which is sufficient to obtain all measured observables accurately. The growth of the entanglement entropy following the quench requires increasing the bond dimension χ with time. Conversely, since we restrict the number of states to $\chi \lesssim 2000$, we are naturally limited to a finite maximum time t_m at which the truncation error becomes significant. Note that the bond dimension χ required for the simulations grows exponentially with time. Increasing the particle numbers and L_y leads to a faster growth of the entanglement entropy and thus to a shorter maximal time t_m. However, we stress that we clearly reach longer times and larger systems than is accessible with exact diagonalization (i.e., pure state propagation using, e.g., Krylov subspace methods).

3.4 Two-dimensional expansion

3.4.1 Density profiles

We first characterize the expansion by analyzing the time- and position-resolved density profile $n_{r_x,r_y}(t) = \langle \hat{n}_{r_x,r_y}(t) \rangle$, where $\hat{n}_{r_x,r_y} = \hat{a}^\dagger_{r_x,r_y} \hat{a}_{r_x,r_y}$ is the number operator. We present exemplary

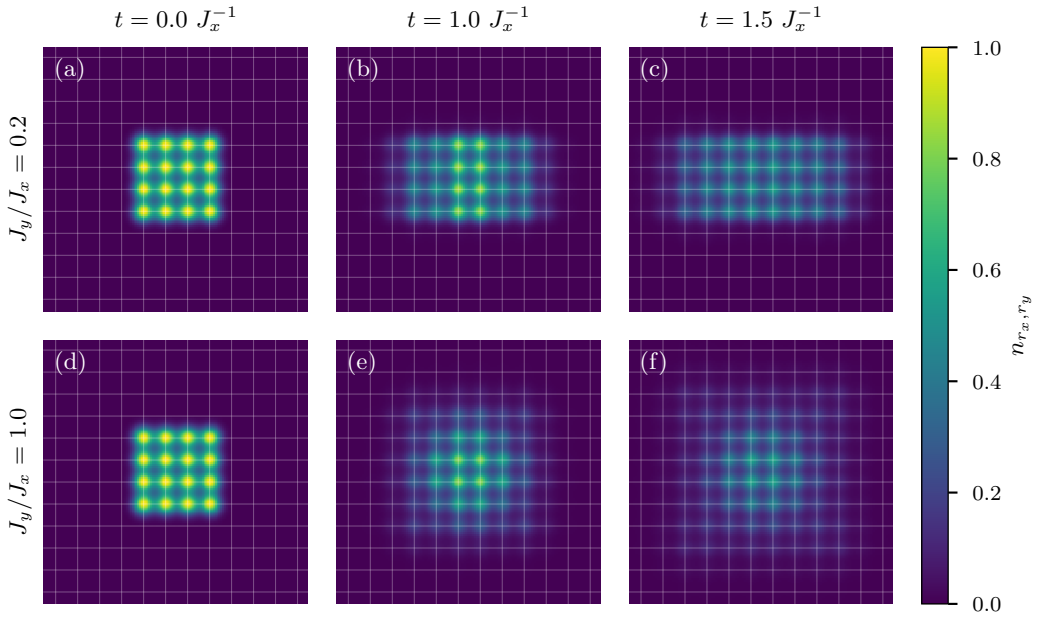

Figure 3.2 Density profiles for the 2D expansion from a 4×4 cluster with (a)–(c) $J_y/J_x = 0.2$ and (d)–(f) $J_y/J_x = 1.0$ at times $tJ_x = 0.0, 1.0, 1.5$.

density profiles for three different times and two anisotropies $J_y/J_x \in \{0.2, 1\}$ in Fig. 3.2. For small $J_y/J_x = 0.2$ [Figs. 3.2(a)–(c)], there is a fast expansion in the x direction and nearly no expansion in the y direction. This is expected since the bare timescale for the expansion in the y direction set by $1/J_y$ is here much larger than the one in the x direction [219]. On the other hand, for $J_y = J_x$, we find four "beams" of faster expanding particles going out along the diagonals. These beams are even more pronounced for initial states with smaller clusters of 2×2 and 3×3 bosons (not shown here).

The most important qualitative difference between the density profiles at $J_y/J_x = 0.2$ and $J_y/J_x = 1$ is the *shape*. In the former case, the profiles retain a rectangular form, reflecting the underlying reciprocal lattice and the different bare tunneling times in the x versus the y direction. For the isotropic case, the initial square shape of the cluster changes into a spherically symmetrical form in the high-density region. This observation is consistent with the experimental results of [180].

3.4.2 Radial velocity

In order to compare the expansion for different values of J_y/J_x more quantitatively, we extract certain integrated quantities from the profiles, which contain relevant information. One such quantity is the radial velocity $v_{r,x/y}$ derived from the reduced radius $\tilde{R}_{x/y}$, see Eq. (3.3). We extract the velocity with a linear fit $\tilde{R}(t) = v_R \cdot t + \text{const}$ in the regime $1.0\, J_x^{-1} \leq t \leq 1.5\, J_x^{-1}$. The full time dependence of $\tilde{R}$ (and hence v_R) will be discussed in Sec. 3.5.4 for the example of the cylinders and ladders.

The radial velocities $v_{R,x}$ and $v_{R,y}$ for the 2D expansion are shown in Fig. 3.3. Unfortunately, our simulations for the 2D lattice are restricted to both very short times and small numbers of bosons with block sizes $B \in \{2, 3, 4\}$. For instance, for 4×4 bosons we reach only times

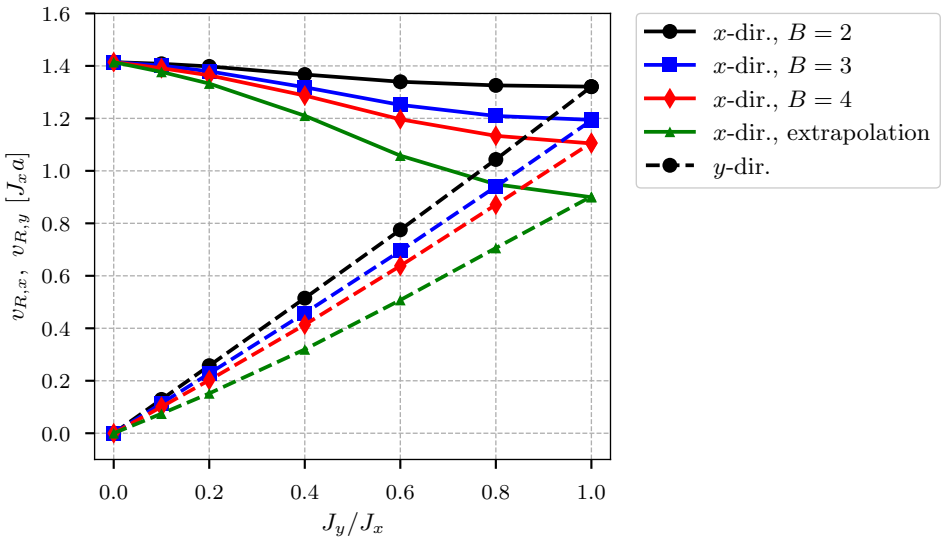

Figure 3.3 Radial velocity in the x direction $v_{R,x/y}$ (top three solid lines) and the y direction $v_{R,y}$ (dashed lines) for the 2D expansion from $B \times B$ clusters. The small green triangles show the result of an extrapolation to $B = \infty$ using Eq. (3.6).

$t_m \approx 1.5\, J_x^{-1}$. The short times prevent us from a reliable extraction of the core expansion velocity, which would allow for a direct comparison to the experiment [178, 180]. The experimental results [180] suggest that, for increasing J_y, the core expansion velocity in the x direction decreases dramatically (see Fig. 3.9), which has been attributed to the breaking of integrability of 1D hard-core bosons [86, 180].

Our results for the radial velocity show that for the smallest block size $B = 2$, tuning J_y/J_x from 0 to 1 changes the velocity $v_{R,x}$ only gradually while the velocity in the y direction scales almost linearly with J_y. A previous study of the expansion of two-leg ladders also indicated that the core expansion velocity exhibits a much stronger dependence on J_y/J_x than the radial expansion velocity [86]. We suspect that this weak dependence may additionally result from the small number of bosons considered in our simulations: Increasing J_y allows a hopping in the y direction, which reduces the density and thus the effective interaction. In other words, tuning J_y/J_x from 0 to 1 increases the effective surface of the initial block to include the upper and lower boundaries. From the surface, there is always a fraction of the bosons that escape and which effectively do not experience the hard-core interaction. This effect becomes more relevant for smaller boson numbers, where the bosons are almost immediately dilute, feel no effective interaction, and, thus, expand (nearly) ballistically in both directions. For larger block sizes $B = 3, 4$, the ratio of surface to bulk is smaller and, therefore, interaction effects become more relevant. Indeed, we find for $B = 3, 4$ that tuning J_y/J_x from 0 to 1 leads to a significant reduction of $v_{r,x}$, most pronounced for $B = 4$.

Even though we have access to only three values of B, it is noteworthy that for all values of J_y/J_x, $v_{R,\mu}$ decreases monotonically with B and thus with total particle number. This tendency is compatible with the behavior of the experiments [180] performed with much larger boson numbers, which motivates us to perform an extrapolation to $B = \infty$ despite the small number of bosons. We assume that the finite-size dependence is dominated by the surface effects of the

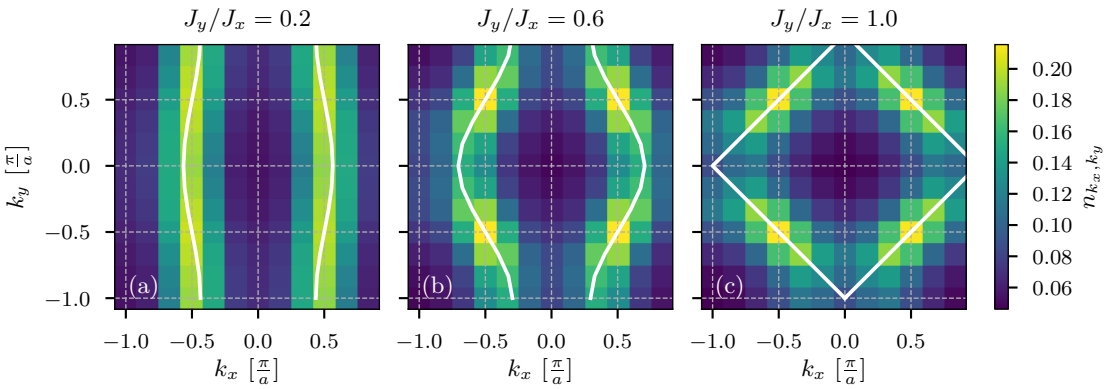

Figure 3.4 Momentum distribution function n_{k_x,k_y} (dimensionless) for the 2D expanding cloud of 4×4 bosons at time $t = 1.5\, J_x^{-1}$. The solid white lines show the solutions to Eq. (3.8).

initial boundary, which scales with B. Therefore, we extract the velocity for $B = \infty$ from a fit to the form

$$v_{r,x/y}(B) = v_{r,x/y}(B = \infty) + \frac{\text{const}}{B} \tag{3.6}$$

at fixed J_y/J_x. The resulting values, which are indicated by the small green symbols in Fig. 3.3, should only be considered as rough estimates.

3.4.3 Momentum distribution function

Figure 3.4 shows the momentum distribution function

$$n_{k_x,k_y} = \frac{1}{L_x L_y} \sum_{r_x,r_y,r_x',r_y'} e^{-\mathrm{i}\left(k_x(r_x-r_x')+k_y(r_y-r_y')\right)} \langle \hat{a}^\dagger_{r_x,r_y} \hat{a}_{r_x',r_y'} \rangle \tag{3.7}$$

for the 2D expansion. For a purely 1D expansion ($J_y = 0$), dynamical quasicondensation occurs at $k_x = \pm\frac{\pi}{2a}$ [80, 81, 87]. As discussed in Refs. [77, 78], energy conservation restricts the (quasi)condensation to momenta at which the single-particle dispersion relation $\epsilon(k_x, k_y)$ vanishes since the initial state has zero energy, resulting in the emission of bosons with, on average, zero energy per particle. For a 2D system, this leads to

$$\epsilon(k_x, k_y) = -2J_x \cos(k_x a) - 2J_y \cos(k_y a) = 0. \tag{3.8}$$

The solutions of this equation are indicated by the solid green lines in Fig. 3.4. We indeed observe an accumulation of particles at momenta compatible with Eq. (3.8). For $J_y/J_x = 0.2$ [Fig. 3.4(a)], there is almost the same weight at any momentum k_y compatible with Eq. (3.8). We suspect that this is a relict of the short time $t = 1.5\, J_x^{-1} = 0.3\, J_y^{-1}$ reached in the simulations: Up to this time there was almost no expansion in the y direction; thus, we have roughly $\langle \hat{a}^\dagger_{r_x,r_y} \hat{a}_{j_x,j_y} \rangle \approx \delta_{r_y,j_y}$ such that n_{k_x,k_y} is initially independent of k_y. Nevertheless, closer inspection shows slightly more weight at compatible momenta with $k_y = \pm\frac{\pi}{2a}$ than at those with $k_y = 0$ even for small J_y [see Fig. 3.4(a)]. This becomes much more pronounced for $J_y = J_x$ [see Fig. 3.4(c)]. In this case, the strongest peaks are at $(k_x, k_y) = (\pm\frac{\pi}{2a}, \pm\frac{\pi}{2a}), (\pm\frac{\pi}{2a}, \mp\frac{\pi}{2a})$. These four points correspond to the maximum group velocities $v(k_x, k_y) = (2J_x a \sin(k_x a), 2J_y a \sin(k_y a))$ and, in real space, manifest themselves via the four "beams" in the density profile shown in Fig. 3.2(f).

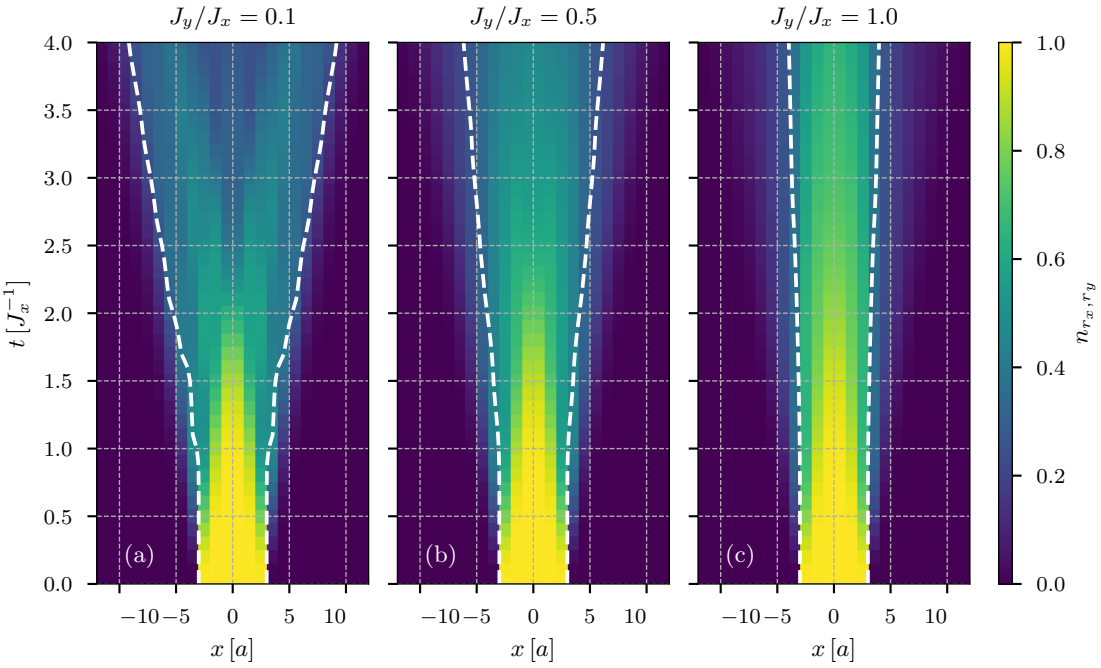

Figure 3.5 Integrated density profiles $\frac{1}{L_y}\sum_{r_y} n_{r_x,r_y}(t)$ (dimensionless) for the expansion from a 6×3 cluster on a cylinder with $L_y = 3$. The white dashed lines show the location of the half maximum on the left and right.

Our results do not serve to clarify whether there actually is a dynamical condensation at finite momenta in 2D or not since our initial clusters have too few particles in the bulk compared to their surface. The fast ballistic propagation of the particles melting away from the surface will only be suppressed once the majority of particles is in the bulk initially. If we attribute the outermost particles to the surface, this would require us to be able to simulate at least 7×7 clusters. We believe that the accumulation at finite momenta seen in the quasimomentum distribution function is due to these fast particles melting away from the boundary during the first tunneling time. Moreover, we would need to be able to study the particle-number dependence of the height of the maxima in the quasimomentum distribution function or the decay of single-particle correlations over sufficiently long distances [80].

3.5 Cylinders and ladders

In contrast to the 2D lattice, the ratio of surface to bulk is much lower for cylinders and ladders, as we initialize the system uniformly in the y direction. Moreover, if we tune J_y from 0 to 1, the additional hopping in the y direction does not lower the density (and with it the effective interaction), as it is the case for the fully 2D expansion. We thus expect a weaker dependence of the results on the number of bosons. Additionally, we can reach larger times than for the fully 2D expansion since the range of hopping terms after mapping to the MPS chain is smaller. While we can reach times up to $t_m \approx 6\,J_x^{-1}$ for $L_y = 2$, we are restricted to times up to $t_m \approx 4\,J_x^{-1}$ for $L_y = 3$ and $t_m \approx 3\,J_x^{-1}$ for $L_y = 4$.

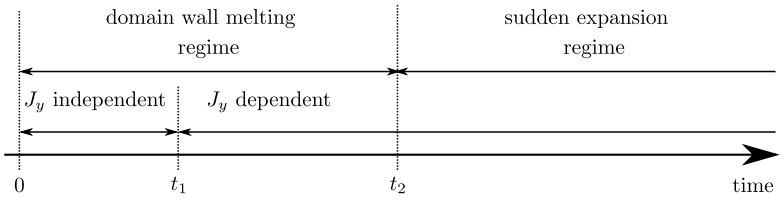

Figure 3.6 Illustration of the time regimes for the expansion of blocks (see the text in Sec. 3.5.1 for details).

3.5.1 Density profile

Figure 3.5 shows some typical results for the column density for the expansion of a block on a cylinder with $L_y = 3$. We identify three different time regimes for the expansion of blocks, schematically depicted in Fig. 3.6. First, the evolution during the first tunneling time $t_1 \propto 1/J_x$ is independent of J_y: Since we initialize our system uniformly in y direction, in the initial longitudinal hopping, there cannot be any dependence on J_y and a finite amount of time is required before correlations in the y direction can build up.

Then, in a transient regime $0 < t_2$ (where $t_2 > t_1$), the melting of the block from either side is equivalent to the domain-wall melting [87, 206] (compare the sketch in Fig. 3.1). From the two boundaries, two "light cones" emerge, consisting of particles outside and holes inside the block. Both particles and holes have a maximum speed of $v_m = 2\,J_x a$. Consequently, the time $t_2 \coloneqq B/4J_x$ is the earliest possible time at which the melting arrives at the center, such that the density drops below one on all sites. Thus, t_2 marks the point in time at which density profiles obtained from blocks start to differ quantitatively from those of domain walls, defining the third time regime. In the case of a ballistic expansion realized for $J_y \ll J_x$, the density in the center drops strongly at t_2 and we can clearly identify two outgoing "jets" as two separating maxima in the density profiles; see Fig. 3.5(a). To be clear, the expectation for the nature of mass transport in a nonintegrable model such as coupled systems of 1D hard-core bosons is diffusion, sustained by numerical studies [212]. However, in the sudden expansion, the whole cloud expands and it is conceivable that the expansion appears to be ballistic because the cloud becomes dilute too fast, resulting in mean-free paths being on the order of or larger than the cloud size at any time [86].

On the other hand, for larger J_y the block in the center does not split at t_2, but a region with a high density ("core") remains in the center. The high-density core is clearly established already at intermediate $J_y/J_x = 0.5$, where it still expands slowly. For larger J_y, the spreading of this core is continuously suppressed.

3.5.2 Integrated current

In order to investigate the different time regimes further, we consider the number of bosons $\Delta N(t)$ that at a time t have left the block $\mathcal{B}$ where they were initialized. This is equivalent to the particle current $\mathcal{J}^x_{r_x} = \mathrm{i}J_x \sum_{r_y} \langle \hat{a}^\dagger_{r_x+a,r_y} \hat{a}_{r_x,r_y} - \hat{a}^\dagger_{r_x,r_y} \hat{a}_{r_x+a,r_y} \rangle$ integrated over time and along the boundary $\partial\mathcal{B}$ of the block,

$$\Delta N(t) = \sum_{i \notin \mathcal{B}} n_{r_x,r_y}(t) = \int_0^t \mathrm{d}s \, \left[\mathcal{J}^x_{b_r}(s) - \mathcal{J}^x_{b_l}(s) \right]. \tag{3.9}$$

Here b_r and b_l denote the right and left indices r_x of the boundary of the initially centered block $\mathcal{B}$. We compare ΔN for the expansion on a two-leg ladder starting from either central blocks or

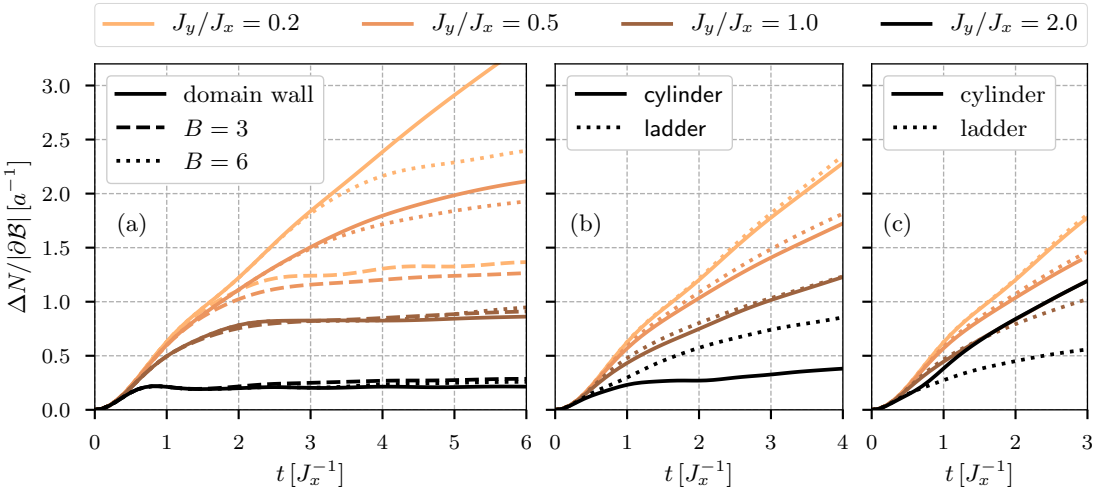

Figure 3.7 Comparison of $\Delta N/|\partial\mathcal{B}|$ (a) on a two-leg ladder for the expansion from central blocks (dashed/dotted lines, $B \times 2$ bosons) versus the melting of a domain wall (solid lines). The lower panels compare domain walls on ladders (dashed lines) to domain walls on cylinders (solid lines) for (b) $L_y = 3$ and (c) $L_y = 4$. The curves for the $L_y = 4$ cylinder in (c) with $J_y/J_x = 1, 2$ are nearly on top of each other for $t \gtrsim 1.5\, J_x^{-1}$.

domain walls in Fig. 3.7(a). To this end we normalize ΔN by the boundary length $|\partial\mathcal{B}|$, which is simply $2L_y\, a$ for the central blocks and $L_y\, a$ for the domain walls.

For short times $t \lesssim 0.5\, J_x^{-1}$ (i.e., $t \lesssim t_1$, see the above), all curves in Fig. 3.7 are independent of J_y. For the quantity ΔN, the first deviations between domain walls and cylinders do not occur at t_2 but at $2t_2 = B/2J_x$, which is exactly the time the fastest holes need to travel once completely through the block: By definition, ΔN is not sensitive to the density inside the initial block. For the expansion of central blocks, particle conservation gives a strict bound $\Delta N/|\partial\mathcal{B}| \leq B/2a$, in which case all the bosons have left the initial block. These bounds (equal to $1.5\, a^{-1}$ and $3\, a^{-1}$ for $B = 3$ and $B = 6$, respectively) are approached in the long-time limit of the ballistic expansion for small $J_y/J_x = 0.2$, which for $B = 6$, however, happens beyond the times reached in our simulations. For the domain walls, ΔN is not bounded (as long as the melting does not reach the boundary of the system) and grows for small J_y/J_x as $\Delta N \propto t$ linearly in time, which, via Eq. (3.9), corresponds to a nondecaying current j^x. On the other hand, ΔN gets almost constant for large J_y/J_x for both the domain walls and the blocks. This indicates that the expansion is strongly suppressed on the two-leg ladder, with a high-density core remaining in the center. We speculate that the regime in which ΔN increases only very slowly is indicative of diffusive dynamics, by similarity with [178].

3.5.3 Propagating modes: Limit of large $J_y \gg J_x$

In order to qualitatively understand the suppression of the expansion for certain geometries and specific values of L_y, it is very instructive to consider the limit of large $J_y \gg J_x$. The Hamiltonian in Eq. (3.1) can be split up into two parts according to $H = H^y + H^x = \sum_{r_x}(H^y_{r_x} + H^x_{r_x, r_x+a})$, where

$$H^y_{r_x} = -J_y \sum_{r_y} (\hat{a}^\dagger_{r_x, r_y}\, \hat{a}_{r_x, r_y+a} + h.c.) \tag{3.10}$$

collects the hopping terms within the rung r_x (we denote sites with the same index r_x as a "rung" for both ladders and cylinders), and $H^x_{r_x,r_x+a}$ is proportional to J_x and collects the hopping terms in the x direction between neighboring rungs.

The following analysis is based on a diagonalization of $H^y = \sum_{r_x} H^y_{r_x}$, which is a block-diagonal product of terms operating on single rungs. We view the eigenstates of single rungs as "modes," which can be delocalized by H^x. Since a coherent movement of multiple bosons is a higher-order process of H^x and thus generally suppressed for large J_y/J_x, we focus on modes with a single particle on a rung. We then look for modes which are candidates for a propagation at finite k_x. Importantly, the kinetic energy $E_x \propto J_x$ cannot compensate for a finite $E_y \propto J_y$ for $J_y \gg J_x$. Since we initialize the system in states with zero total energy, energy conservation allows only modes with $E_y = 0$ to contribute to the expansion in first-order processes in J_x/J_y in time. In general, one could also imagine to create pairs of two separate bosons with exactly opposite E_y, summing up to 0. Yet, as we will see, H^x cannot create such pairs.

For smaller J_y, the scaling argument of the energy conservation does not hold and additional modes (beginning with those of small energy E_y) can be used for the propagation in the x direction; ultimately, for $J_y \ll J_x$ any mode contributes to the expansion already at short times. We note that modes with strictly $E_y = 0$ are either present or absent at any value of J_y/J_x. Whether propagating modes with $E_y = 0$ exist or not depends not only on L_y but also on the boundary conditions in the y direction. This can serve as a test for our reasoning.

Two-leg ladder

In the following we give an explicit expression for $H^x_{r_x,r_x+a}$ on a two-leg ladder in terms of the eigenstates of $H^y_{r_x}$ and $H^y_{r_x+a}$. We denote the four eigenstates of $H^y_{r_x}$ on rung r_x as

$$
\begin{aligned}
|0\rangle &= |\mathrm{vac}\rangle\,, & |1^+\rangle &= \frac{\hat{a}^\dagger_{r_x,1} + \hat{a}^\dagger_{r_x,2}}{\sqrt{2}}\,|\mathrm{vac}\rangle\,,\\
|2\rangle &= \hat{a}^\dagger_{r_x,2}\hat{a}^\dagger_{r_x,1}\,|\mathrm{vac}\rangle\,, & |1^-\rangle &= \frac{\hat{a}^\dagger_{r_x,1} - \hat{a}^\dagger_{r_x,2}}{\sqrt{2}}\,|\mathrm{vac}\rangle\,,
\end{aligned}
\tag{3.11}
$$

where $|\mathrm{vac}\rangle$ denotes the vacuum on rung r_x. The corresponding eigenenergies E_y of $H^y_{r_x}$ are listed in Tab. 3.1. We then express $\hat{a}_{r_x,r_y}$ and $\hat{a}^\dagger_{r_x,r_y}$ in terms of these eigenstates, plug them into $H^x_{r_x,r_x+a}$ and obtain:

$$
\begin{aligned}
-H^x_{r_x,r_x+a}/J_x = &\left(|0;1^+\rangle\langle 1^+;0| + |0;1^-\rangle\langle 1^-;0| + h.c.\right)\\
&+ \left(|2;1^+\rangle\langle 1^+;2| + |2;1^-\rangle\langle 1^-;2| + h.c.\right)\\
&+ \left(|1^+;1^+\rangle\langle 0;2| - |1^-;1^-\rangle\langle 0;2| + h.c.\right)\\
&+ \left(|1^+;1^+\rangle\langle 2;0| - |1^-;1^-\rangle\langle 2;0| + h.c.\right).
\end{aligned}
\tag{3.12}
$$

Here, $|\alpha;\beta\rangle \equiv |\alpha\rangle \otimes |\beta\rangle$ with $\alpha, \beta \in \{0, 1^+, 1^-, 2\}$ denotes the tensorproduct of the eigenstates on rungs r_x and $r_x + a$. The terms in the first two lines of Eq. (3.12) correspond to just an exchange of the eigenstates $\alpha \leftrightarrow \beta$ between the neighboring sites. Thus we can identify the terms of the first line to drive the propagation of single bosons on top of the vacuum. The second line can be seen as the propagation of a particle on top of a one-particle background, or alternatively, a single hole in the background of filled rungs.

In contrast to the terms of the first two lines, the terms in the third and fourth row of Eq. (3.12) mix different eigenstates. If we imagine to start from a domain wall $|\ldots;2;2;0;0;\ldots\rangle$, those

$L_y = 2$ ladder			
N	$k_y\,[\frac{\pi}{a}]$	$E_y\,[J_y]$	state
0	0	0	$\|0\rangle$
1	0	-1	$\|1^+\rangle$
	1	1	$\|1^-\rangle$
2	0	0	$\|2\rangle$

$L_y = 4$ cylinder		
N	$k_y\,[\frac{\pi}{a}]$	$E_y\,[J_y]$
0; 4	0	0
1; 3	0	-2
	0.5	0
	-0.5	0
	1	2
2	0	-2.828
	0.5	0
	-0.5	0
	1	0
	1	0
	0	2.828

$L_y = 4$ ladder	
N	$E_y\,[J_y]$
0; 4	0
1; 3	-1.618
	-0.618
	0.618
	1.618
2	-2.236
	-1
	0
	0
	1
	2.236

Table 3.1 Eigenenergies of a single rung. For a given particle number, degenerate levels are listed by their multiplicity.

are the terms which "create" the single particle modes $|1^\pm\rangle$ at the border of the domain wall. Subsequently, we would imagine these modes to propagate away to the left as single-hole modes and to the right as single-boson modes. Yet, for the two-leg ladder all these mixing terms change the total energy E_y from 0 to either $+2J_y$ or $-2J_y$. Thus, the creation is only possible via higher-order processes, which are suppressed with increasing J_y/J_x. A term such as $|1^+;1^-\rangle\langle 2;0|$ would not change the total energy E_y, but such a term is not present in Eq. (3.12) due to the conservation of total momentum k_y: it would change from $k_y = 0+0$ to $k_y = 0+\frac{\pi}{a}$.

To summarize, we argue that the $L_y = 2$ ladder is special as it possesses the two extremal modes $k_y = 0$ and π with large energies $E_y = \pm J_y$ for one particle on a rung. Precisely this lack of modes with $E_y = 0$ leads to the suppression of the expansion with increasing J_y/J_x due to energy conservation. It is manifest in Fig. 3.7(a) by the fact that ΔN gets almost constant. Note that energy conservation for large $J_y \gg J_x$ does not suppress the propagation of the modes $|1^\pm\rangle$ in the vacuum, but the creation of these modes at the edges of the initial blocks or a domain wall. We can view the expansion to be inhibited by the existence of heavy objects (particles of a large effective mass) that can propagate only via higher-order processes. This is similar to the reduction of expansion velocities due to doublons in the strongly interacting regime of the 1D Bose-Hubbard model [86, 177, 180, 215, 216]. Another effect with very similar physics is self-trapping (see, e.g., [79, 228, 229]).

Larger cylinders and ladders

We turn now to the cylinder and the ladder with $L_y = 4$. The eigenenergies of $H^y_{r_x}$ on a single rung are listed in Tab. 3.1. Giving an explicit expression for $H^x_{r_x,r_x+a}$ on an $L_y = 4$ cylinder or ladder is not possible here, since it contains too many terms. Nevertheless, we examine its structure. Similar to that for the two-leg ladder, we can distinguish between terms which just exchange the eigenstates of neighboring rungs and terms which mix them. As on the two-leg ladder, we associate the exchange terms with the propagation of modes. Since H^x contains only single-particle hopping, the exchange terms appear only between eigenstates with N and $N+1$ bosons on neighboring rungs. Thus, to first order in J_x/J_y, a mode of N bosons can propagate

"freely" only in a background of $N \pm 1$ bosons per rung. By definition, all these exchange terms do not change the total energy E_y.

For the mixing terms, there is no restriction on the initial particle numbers on the neighboring rungs. However, $H^x_{r_x,r_x+a}$ obviously preserves the total number of particles, thus there are only mixing terms for $|\ldots N, N' \ldots\rangle \leftrightarrow |\ldots N \pm 1; N' \mp 1 \ldots\rangle$. The initial melting of the edge thus happens via a cascade of subsequent mixing processes. For example, consider

$$|\ldots 4;4;0;0\ldots\rangle \to |\ldots 4;3;1;0\ldots\rangle \to |\ldots 4;2;2;0\ldots\rangle \\ \to |\ldots 3;3;2;0\ldots\rangle \to |\ldots 3;3;1;1\ldots\rangle \,. \quad (3.13)$$

On the cylinder there are states with $E_y = 0$ for any number of bosons per rung (see Tab. 3.1). This makes it plausible that cascades like (3.13) are possible without changing E_y on the single rungs. Indeed, we find the corresponding terms in the expression for $H^x_{r_x,r_x+a}$ (not given here). The initial edge of a block or domain wall can thus gradually melt into states with one particle per rung while preserving the energy E_y. This will be confirmed later by a strong peak in the momentum distribution function depicted in Fig. 3.10(f). These additional $k_y = \pm\frac{\pi}{2a}$ modes with $E_y = 0$, which are not present in the two-leg ladder, explain thus the trend of a faster expansion.

On the other hand, on the four-leg ladder, there are no states with $E_y = 0$ for one or three bosons on a rung. It is thus immediately clear that there can be no mixing terms which preserve E_y on every rung separately. Moreover, we find that there are also no mixing terms which create modes with opposite energy starting from $E_y = 0$ on both rungs. As a consequence, the domain wall melting on the four-leg ladder requires higher-order processes, similar to the two-leg ladder. However, the necessary intermediate energies $E_y = \pm 0.613 \times 2J_y$ are smaller than for the two-leg ladder, such that these higher-order processes are more likely.

We compare ΔN for the cylinder and ladder geometry directly in Fig. 3.7(b,c). For small $J_y/J_x = 0.2$, the additional coupling of the cylinders compared to the ladders has (at least on the time scales accessible to us) nearly no influence. Yet, for large J_y/J_x, we find not only a quantitative but even a qualitative difference: For the $L_y = 4$ cylinders, ΔN increases linearly in time, irrespective of how large J_y/J_x is. Moreover, the slope is (at $t \gtrsim 1.5\, J_x^{-1}$) roughly the same for all $J_y/J_x \gtrsim 0.5$ and does almost not decrease with time. Using Eq. (3.9), we can relate this to the presence of a non-decaying current, which we explain in terms of an enhanced occupation at momenta compatible with $E_y = 0$. In contrast, on the four-leg ladder there are no propagating modes with $E_y = 0$; thus, we expect no linear increase of ΔN. Indeed, we find that the currents – i.e., the slopes of ΔN in Fig. 3.7(c) – on the four-leg ladder decay in time. Yet, the decay is not as extreme as for the two-leg ladder, which we explain by the existence of modes with lower energies $E_y > 0$ than on the two-leg ladder. For $L_y = 3$, it is exactly the other way around: There are modes with $E_y = 0$ on the ladder but not on the cylinder. In agreement with this, Fig. 3.7(b) shows that the expansion on a three-leg ladder is faster than on an $L_y = 3$ cylinder for large $J_y/J_x = 2$.

3.5.4 Radii and expansion velocities

Both velocities $v_R = \frac{\partial \tilde{R}(t)}{\partial t}$ and $v_c = \frac{\partial R_c(t)}{\partial t}$ are time derivatives of quantities which are not strictly linear in time. Thus, both v_R and v_c themselves are time dependent. Figure 3.8(a-c) shows the time dependence of the reduced radius $\tilde{R}(t)$, Fig. 3.8(d-f) the one of the core radius $R_c(t)$. In the ideal case we would expect the velocities to get constant in the long-time limit. However, our calculations are limited to finite times $t_m = 6\, J_x^{-1}$ for the two-leg ladder, $t_m \approx 4\, J_x^{-1}$

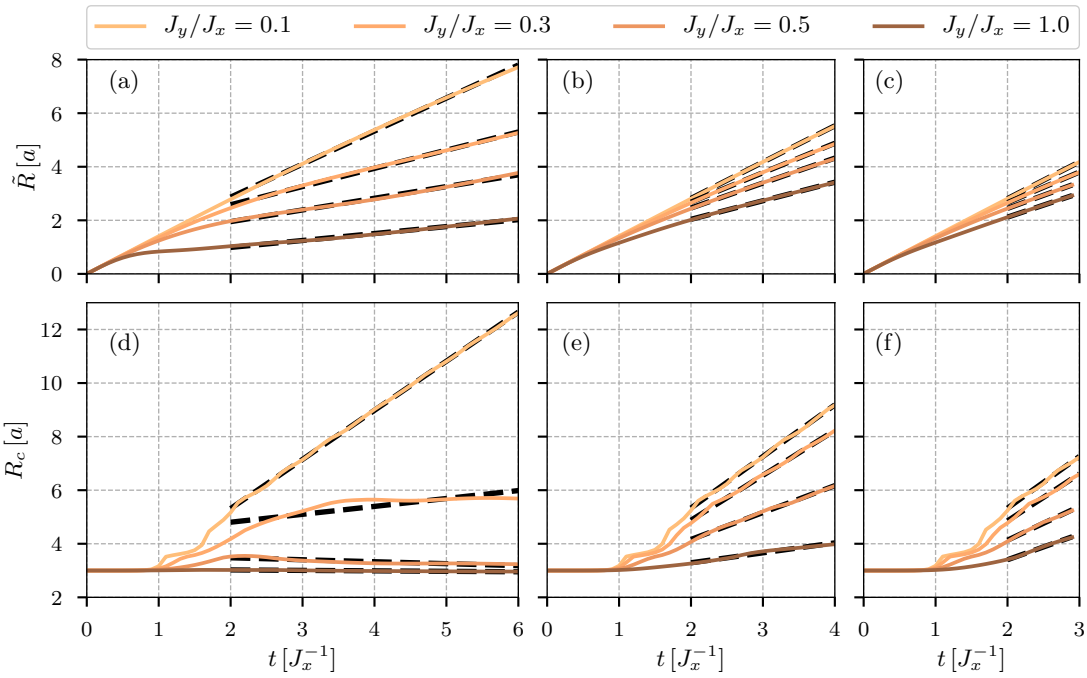

Figure 3.8 Reduced radius $\tilde{R}(t)$ (a-c) and core radius $R_c(t)$ (d-f) for cylinders with (a,d) $L_y = 2$, (b,e) $L_y = 3$, and (c,f) $L_y = 4$, starting from a $6 \times L_y$ cluster. The thick dashed lines show the linear fits used to extract the radial velocities v_R, shown in Fig. 3.9(b), and the core velocities v_c (d-f), shown in Fig. 3.9(a).

for $L_y = 3$ cylinders/ladders, $t_m \approx 3\,J_x^{-1}$ for $L_y = 4$ cylinders/ladders, and just $t_m \approx 1.5\,J_x^{-1}$ for the 2D lattice.

The reduced radii all start as $\tilde{R}(t) = \sqrt{2}tJ_x a$ on very short time scales $t \lesssim 0.5\,J_x^{-1}$. This is clear as we are initially confined to the hopping in the x direction, independently of J_y. For very small $J_y \ll J_x$, the reduced radius remains linear in time with the velocity $v_R = \sqrt{2}J_x a$ at all times, as expected for a ballistic expansion from an initial state with a flat quasimomentum distribution function [180, 225]. A J_y dependence may show up on a timescale $t \propto J_y^{-1}$. For larger J_y the slope v_R reduces at intermediate times (in the time range where we can observe it) but increases again for large tJ_x. The latter can be understood as follows: The outermost parts have the strongest contribution to the sum in Eq. (3.3), and naturally these outer parts have the highest velocity $2\,J_x a$ (and also reached a low density such that they are dilute and thus do not see each other any more). Assuming a fraction p of the particles to expand with v and the rest $(1 - p)$ to form an inert time-independent block in the center (see also the argument given in [216]), a straightforward calculation shows that $\tilde{R}(t) \approx \sqrt{p}\,v\,t$ at large times. This is also the reason why $\tilde{R}(t)$ does *not* settle to a constant value on the two-leg ladder even for large J_y, although the core in the center barely melts and ΔN becomes only weakly time dependent: There is always a nonzero fraction of particles which go out from the center.

We extract the time-independent expansion velocities v_R shown in Figs. 3.3 and 3.9 by a linear fit $\tilde{R}(t) = v_R \cdot t + \text{const}$ in the time interval $2.0\,J_x^{-1} \leq t \leq t_m$, where t_m is the maximum time reached in the simulations; see the above. For the 2D lattice, we reach only $t_m = 1.5\,J_x^{-1}$; thus, we fit only in the interval in this case. In Fig. 3.9 we show error bars resulting from similar fits but using only the first or the second half of the time interval.

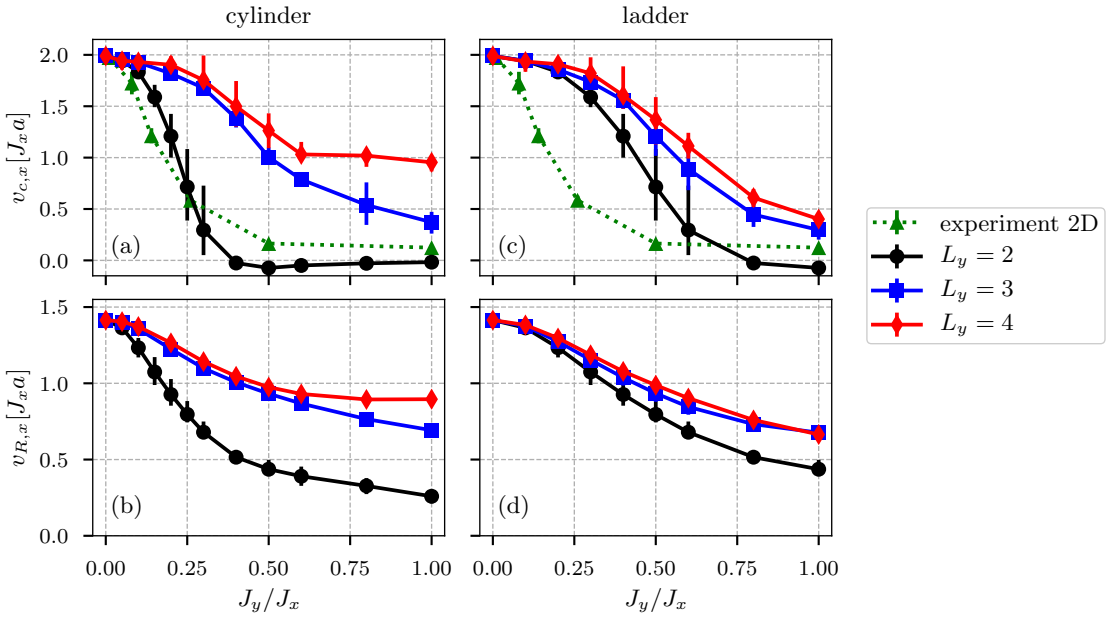

Figure 3.9 (a),(c) Core expansion velocities $v_{c,x}$ and (b),(d) radial velocities $v_{R,x}$ versus J_y for the expansion of a $6 \times L_y$ block. The left panels (a) and (b) are obtained on $L_y = 2, 3, 4$ cylinders; the right panels (c),(d) are obtained on $L_y = 2, 3, 4$ ladders. The green triangles taken from Ref. [180] show the results of the experiments for the fully 2D expansion corresponding to the setup of Sec. 3.4.

In the time regime $0 < t < t_2$, the core radius R_c is constant, although the cloud already expands: From both edges, the block melts, but the location of the half-maximum density does not move due to particle-hole symmetry. Just when the first holes arrive in the center of the block, the global maximum decreases and R_c, the half width at half maximum, begins to increase. It then exhibits strong initial oscillations. The latter stem, on the one hand, from the discreteness of the particles' coordinates on the lattice, which is only partly cured by the linear splines used to extract R_c. On the other hand, the melting of domain walls in 1D happens in quantized "charges," which lead to well-defined structures in the density profile [206, 230, 231]. Those oscillations prevent us from extracting the core velocity for the 2D lattice, where they are too strong at the times reached in the simulations. Yet it seems reasonable to extract v_c for the cylinders and ladders by linear fits $R_c(t) = v_c \cdot t + \text{const}$ in the same way as for v_R. While it works quite well for the ballistic expansion at $J_y \ll J_x$ and quite large $J_y \gtrsim J_x$, $R_c(t)$ still exhibits a stronger time dependence for intermediate J_y, e.g., $J_y \approx 0.3 J_x$ on the $L_y = 2$ cylinder. In the latter case, some of the bosons expand initially during the domain-wall melting and thus the block and R_c grow, yet then the expansion is slowed down and the extension of the high-density block measured by R_c becomes weakly time dependent.

Figure 3.9 shows the radial and core velocities for the expansion of blocks on cylinders and ladders. We note that, while v_c and v_R are nearly independent of J_y/J_x in the range $J_y/J_x = 0.6, \ldots, 1$ for the $L_y = 4$ cylinder [Figs. 3.9(a) and 3.9(b)], the values $R_c(t)$ and $\tilde{R}(t)$ themselves actually do decrease when J_y/J_x is tuned from 0.6 to 1 (see Fig. 3.8), due to different short-time dynamics. Further, for the accessible times ($t_m = 3\,J_x^{-1}$ for $L_y = 4$), the density profile outside the original block is still completely equivalent to the domain-wall melting. Nevertheless, $R_c(t)$, by definition, is also sensitive to the maximum value in the center of the

block, and $\tilde{R}(t)$ is sensitive to the densities at all positions. Thus, the velocities shown in Fig. 3.9 contain valuable and complementary information.

The two-leg ladder (for which the expansion velocity has been studied in Ref. [86]) shows a behavior similar to the experimental data for 2D expansions [180], namely that the core velocity v_c drops down to zero with increasing J_y/J_x. However, by comparing different L_y, we find a trend towards a faster expansion when L_y is increased at fixed J_y/J_x. This trend is in contrast to the naive expectation that wider cylinders should mimic the 1D-to-2D crossover better. In other words, it demonstrates that the two-leg ladder does not capture all the relevant physics of the expansion in all directions in the 1D-to-2D crossover, although it shows the same qualitative dependence of velocities on J_y/J_x as the 2D system studied experimentally [180]. However, we understand this from our considerations of the limit $J_y \gg J_x$ in Sec. 3.5.3: On the $L_y = 4$ cylinder and the $L_y = 3$ ladder, there exist $E_y = 0$ modes, and thus a preferred occupation of these propagating modes with nonzero k_y is possible. Moreover, in those other cases in which there are no modes with strictly $E_y = 0$, there are at least modes with lower $|E_y| < J_y$.

3.5.5 Momentum distribution function

The momentum distribution n_{k_x,k_y} on cylinders starting from $6 \times L_y$ blocks and at fixed time $t = 2.0\, J_x^{-1}$ is shown in Fig. 3.10. At small $J_y/J_x = 0.2$, we observe a bunching of particles at the $k_x = \pm\frac{\pi}{2a}$ modes independent of k_y, similar to the fully 2D expansion at the same value of J_y/J_x shown in Fig. 3.4.

For $J_y = J_x$ and on the $L_y = 3$ cylinder, the energy $E_y(k_y = \pm\frac{2\pi}{3a}) = J_y$ can be compensated by kinetic energy $E_x = -2J_x \cos(k_x a)$ in the x direction; compare Eq. (3.8). Indeed, we find a bunching of particles at those momenta in Fig. 3.10(e). The $E_y(k_y = 0) = -2J_y$ and $E_y(k_y = \frac{\pi}{a}) = 2J_y$ mode would yield $k_x = \frac{\pi}{a}$ and $k_y = 0$, yet we find a slightly higher weight at smaller k_x in Fig. 3.10(e). However, we note that all these peaks for $J_y = J_x$ in Figs. 3.10(d) and 3.10(e) are not as high as their counterparts for $J_y/J_x = 0.2$. As we have discussed in Sec. 3.5.3, there are no modes with $E_y = 0$ for $L_y = 2, 3$ on cylinders; hence, the maxima in n_{k_x,k_y} are generally suppressed as we go from small to large J_y/J_x for $L_y = 2, 3$.

On the $L_y = 4$ cylinder, we find a bunching of particles at $(k_x, k_y) = (\frac{\pi}{2a}, \frac{\pi}{2a})$ with roughly the same weight for all J_y; compare Figs. 3.10(c) and 3.10(f). This is in agreement with our considerations of Sec. 3.5.3, since the modes with $k_y = \frac{\pi}{2a}$ have $E_y = 0$. The $k_y = 0, \frac{\pi}{a}$ modes are suppressed, similar to the case of $L_y = 2, 3$.

The question of whether the bunching of particles at certain quasimomenta (that requires the existence of propagating modes with energies compatible with those quasimomenta) will lead to a true dynamical quasicondensation at finite momenta can best be addressed using the domain walls as initial stats. Here, we are guided by the behavior of 1D hard-core bosons: In the sudden expansion [80, 86], the dynamical quasicondensation is a transient phenomenon, hence the occupation at $k = \pm\frac{\pi}{2a}$ first increases and then slowly decreases as dynamical fermionization sets in [86, 88, 89]. The crossover between these two regimes—the formation and the decay of quasicondensates—is given by $t_2 \propto B$ (see also the discussion in [87]). For the domain-wall melting, the quasicondensates are continuously fed with particles with identical properties due to the presence of an infinite reservoir and thus the quasicondensation peaks in n_k never decay but keep increasing.

Figure 3.11 shows the time dependence of the occupation at the maximum of n_{k_x,k_y} for the domain-wall melting on $L_y = 2, 3, 4$ cylinders for (a)–(c) $J_y/J_x = 0.2$ and (d)–(f) $J_y/J_x = 1$. For $J_y/J_x = 0.2$ and the accessible time windows of the $L_y = 3, 4$ cylinders, the occupation indeed increases monotonically in time. On the $L_y = 2$ cylinder in Fig. 3.11(a), the maximum initially

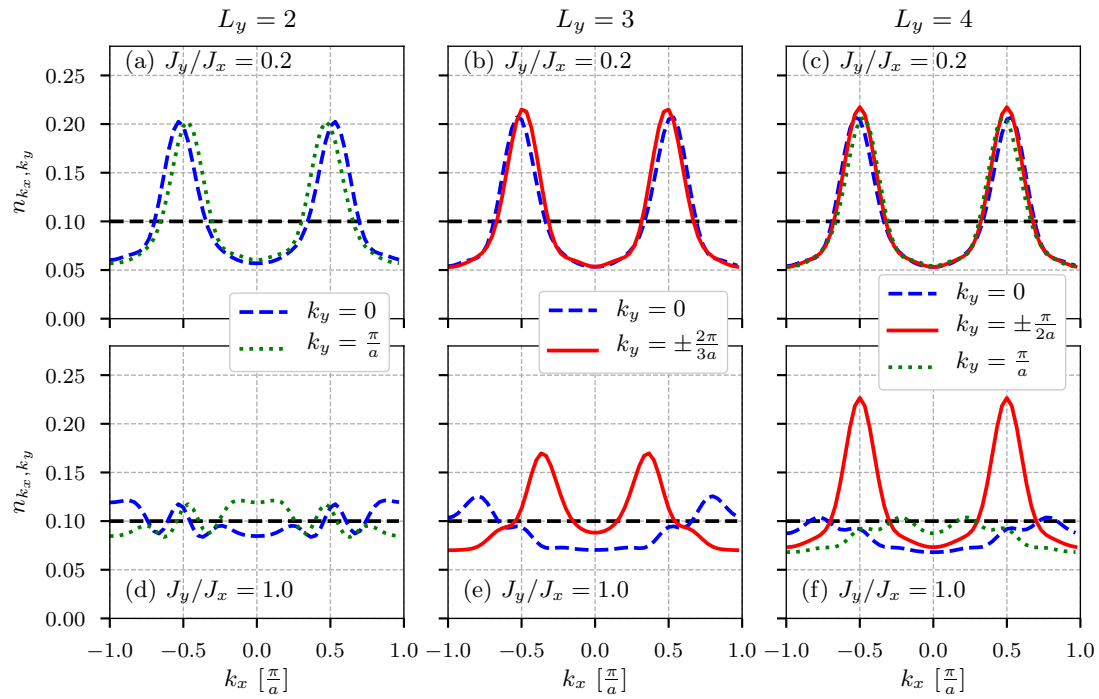

Figure 3.10 Momentum distribution function n_{k_x,k_y} (dimensionless) for cylinders with (a),(d) $L_y = 2$, (b),(e) $L_y = 3$ and (c),(f) $L_y = 4$, starting from a $6 \times L_y$ cluster. Data are shown for time $t = 2.0\, J_x^{-1}$ and (a)–(c) $J_y/J_x = 0.2$ and (d)–(f) $J_y/J_x = 1.0$ (Note that we have a symmetry $n_{-k_x,k_y} = n_{k_x,k_y} = n_{k_x,-k_y}$). The black dashed lines indicate the flat initial distribution at $t = 0$.

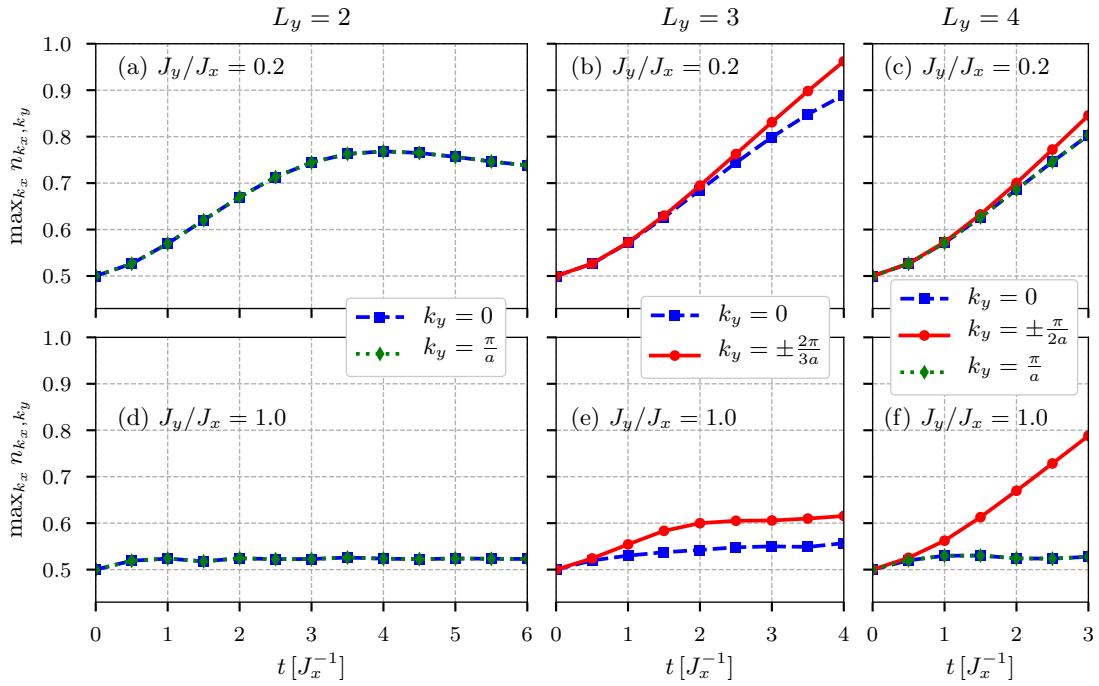

Figure 3.11 Time evolution of the peak heights in the momentum distribution function for cylinders with (a),(d) $L_y = 2$, (b),(e) $L_y = 3$, and (c),(f) $L_y = 4$, starting from a domain wall. Data are shown for (a)–(c) $J_y/J_x = 0.2$ and (d)–(f) $J_y/J_x = 1.0$.

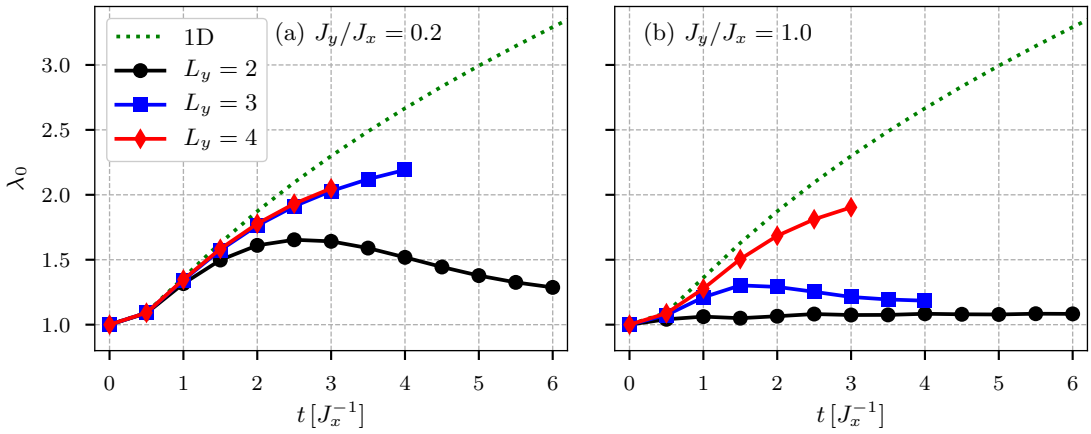

Figure 3.12 Time evolution of the occupation of the largest eigenvalue λ_0 (dimensionless) of the one particle density matrix for cylinders with (a) $J_y/J_x = 0.2$ and (b) $J_y/J_x = 1.0$, starting from a domain wall. The dotted green lines show the results of an 1D chain ($J_y = 0$) for comparison.

increases similar as for $L_y = 3, 4$, yet for times $t \gtrsim 3J_x^{-1}$ it saturates and even decreases, which suggests that no condensation sets in. Note that the time scale at which the saturation happens is quite large, as it is set by J_y^{-1}. This suggests that there is no condensation even for very small $J_y > 0$ on the $L_y = 2$ cylinder.

The behavior for $J_y/J_x = 1$ is quite different. In almost all cases, the occupation at the maximum quickly saturates, which suggests that no condensation sets in. This observation is consistent with the absence of fast propagating modes on the $L_y = 2, 3$ cylinders. Among the data sets shown in Fig. 3.11(d)–3.11(f), there is one exception, namely the peak at $(k_x, k_y) = (\frac{\pi}{2a}, \pm\frac{\pi}{2a})$ on the four-leg cylinder, which monotonically increases without a trend towards saturation. This case is thus the most promising candidate for a condensation at $J_y = J_x$.

3.5.6 Occupation of lowest natural orbital

To investigate the question of condensation in more detail, we look at the maximum occupation λ_0 of the natural orbitals [232]. The natural orbitals are effective single particle states defined as the eigenstates of the one particle density matrix $\langle \hat{a}^\dagger_{\vec{r}} \hat{a}_{\vec{r}'} \rangle$. The corresponding eigenvalues sum up to the number of particles and can be interpreted as the occupations of the natural orbitals. A true condensate requires that λ_0 becomes macroscopically large.

The largest occupation λ_0 for the domain-wall melting of cylinders is shown in Fig. 3.12. In the 1D case, indicated by the green dotted line, the occupation grows, for large times, as $\lambda_0 \approx 1.38\sqrt{t}$ [80]. For $L_y = 2$ we find two degenerate natural orbitals with occupation λ_0. For $J_y/J_x = 0.2$, we find an initial growth for all $L_y = 2, 3, 4$, but for $L_y = 2$, the occupation saturates and even decreases for large times $t \gtrsim 3J_x^{-1}$, similar as for the peaks in the momentum distribution function. In fact, the peaks in the momentum distribution are directly related to the natural orbitals with the largest occupation: For $L_y = 2$ there are two degenerate natural orbitals with maximal occupation with $k_y = 0$ and $k_y = \frac{\pi}{a}$, and their Fourier transformation is peaked slightly above (below) $k_x = \frac{\pi}{2a}$ for $k_y = 0$ ($k_y = \frac{\pi}{a}$). Similarly, for $L_y = 3$ ($L_y = 4$) there are two natural orbitals with maximal occupation with $k_y = \pm\frac{2\pi}{3a}$ ($k_y = \pm\frac{\pi}{2a}$) and one (two) with slightly lower occupation with $k_y = 0$ ($k_y = 0, \frac{\pi}{a}$), leading to the peak structure of Figs. 3.10(b) and 3.10(c) (with peaks only at $k_x > 0$ for domain-wall initial states).

For $J_y = J_x$, shown in Fig. 3.12(b), λ_0 saturates and even decreases for the cylinders of width $L_y = 2, 3$, but keeps growing monotonically for $L_y = 4$ (at least on the time scale accessible to us), in accordance with Figs. 3.10(f) and 3.11(f). For $L_y = 4$, we find only two (degenerate) natural orbitals with $k_y = \pm\frac{\pi}{2a}$ with peaks at $k_x = \frac{\pi}{2a}$. Yet the maximal occupation λ_0 is significantly smaller than in the 1D case and seems to saturate at larger times.

It is instructive to compare λ_0 to the number of particles in the expanding cloud ΔN shown in Fig. 3.7, defining a condensate fraction $\lambda_0/\Delta N$. ΔN increases linearly in time in 1D; hence, the condensate fraction goes to zero with $1/\sqrt{t}$, consistent with the absence of true long-range order. In the case of cylinders, we never observe a saturation of $\lambda_0/\Delta N$ to a constant nonzero value, but it keeps decreasing as a function of time. Therefore, a true condensation is not supported by the existing data on any cylinder. Yet the survival of a quasicondensation on the cylinders is consistent with our data.

3.6 Conclusion

Motivated by recent experiments with ultracold bosons in an optical lattice [87,180], we simulated the sudden expansion of up to 4×4 hard-core bosons in a 2D lattice. In the limit $J_x \gg J_y$, we find a fast expansion (at least on the time scale accessible to us), similar to the 1D case. When J_y is tuned to the isotropic limit $J_x = J_y$, some fraction of the particles remains as a high-density core in the center and a spherically symmetric shape emerges. This trend is compatible with the observations made in the experiment of Ref. [180]. Unfortunately, our results for the 2D expansion are dominated by surface effects due to the small boson numbers – in fact, we have more particles at the boundary of the initial block than in the bulk in our simulations. This prevents us from analyzing the core expansion velocity [180], yet the radial velocities $v_{r,x}$ decrease monotonically with the block size B at any fixed J_y/J_x. We observe a bunching in the momentum distribution function at quasimomenta compatible with energy conservation. This bunching could signal a dynamical condensation at finite quasimomenta as in the 1D case, where this dynamical quasicondensation [80] has recently been observed in an experiment [87]. Although we cannot ultimately clarify the question of dynamical condensation in 2D with our small clusters, we believe that the bunching of particles at certain finite momenta in the 2D expansion $J_y \approx J_x$ stems from surface effects.

In order to investigate the dimensional crossover further, we studied the expansion on long cylinders and ladders with up to $L_y = 4$ legs. Correlations between the particles in different legs, which lead to a J_y dependence, built up on a very short timescale of about one tunneling time in the longitudinal x direction. Up to a time t_2 that is proportional to the linear dimension of the initial block, the expansion of blocks, restricted to either the left or right half of the system, is identical to the domain-wall melting. On two-leg ladders, the density in the central region becomes very weakly time dependent and almost stationary for $J_y/J_x \gtrsim 1$, even for the domain walls. This is reflected by a vanishing or even slightly negative core velocity, similar to the observations made in experiments [178, 180]. By considering the limit $J_y \gg J_x$, we argue that this suppressed expansion on the two-leg ladder for large J_y/J_x stems from the fact that there are no modes with $E_y = 0$ on single rungs. For cylinders and ladders with larger $L_y \in \{3, 4\}$, we generically find a faster expansion with higher velocities than in the $L_y = 2$ case. Additionally, there is a dependence of expansion velocities on the boundary conditions in the y direction. For instance, the expansion on $L_y = 4$ cylinder is faster than on a four-leg ladder. In agreement with our considerations of the limit $J_y \gg J_x$, this is accompanied by a bunching at preferred

momenta $k_y = \pm\frac{\pi}{2a}$ and $k_x = \pm\frac{\pi}{2a}$ and an increasing occupation of natural orbitals. Yet our data does not support a true condensation on any cylinder.

Finally, we state the interesting question whether the expansion velocities on cylinders or ladders will ever show the same dependence on J_y/J_x as the width L_y increases compared to the expansion of a 2D block. The obvious difference is that we fill the cylinders and ladders completely in the y direction. Due to symmetry, the expansion on cylinders is restricted to be along the x direction and, as such, closer to the 1D case, at least for small L_y. There can thus be two scenarios: Either, even for $L_y \to \infty$, the velocities of the cylinders might well be above the experimental results or, as L_y increases beyond $L_y = 4$, the velocities at a fixed J_y/J_x will depend nonmonotonically on L_y.

Further insight into these questions, i.e., the dependence on L_y or the question of dynamical condensation at finite momenta in dimensions higher than one, could be gained from future experiments with access to measuring the radius. This could be accomplished using single-site resolution techniques; see [58, 59, 233] for work in this direction.

4 Domain-wall melting as a probe of many-body localization

Most of the content of this chapter can also be found in a previous publication of the author [4]. Text and figures have been adjusted to fit into the context of the thesis.

In pioneering works based on perturbation theory [22, 23], it was shown that Anderson localization, i.e., perfectly insulating behavior even at finite temperatures, can persist in the presence of interactions. Subsequent theoretical studies on mostly 1D model systems have unveiled many fascinating properties of such a MBL phase; we will summarize the most important results in Sec. 4.1. The phenomenology of the MBL phase has mostly been established for closed quantum systems. A sufficiently strong coupling of a disordered, interacting system to a bath is expected to lead to thermalization (see, e.g., [234, 235]). Thus, the most promising candidate systems for the experimental investigation of MBL physics are quantum simulators such as ultracold quantum gases in optical lattices or ion traps. So far, the cleanest evidence for MBL in an experiment has been reported for an interacting Fermi gas in an optical lattice with quasiperiodicity, realizing the Aubry-André model [43, 44]. Other quantum gas experiments used the same quasi-periodic lattices or laser speckles to investigate Anderson localization [236, 237] and the effect of interactions [238], however, at low energy densities. Experiments with ion traps provide an alternative route, yet there, at most a dozen of ions can currently be studied [239].

By using a novel experimental approach, a first demonstration and characterization of MBL in a 2D optical-lattice system of interacting bosons with disorder has been presented by Choi et al. [45]. They start from a state that contains particles in only one half of the system while the rest is empty. Once tunneling is allowed, the particles from the initially occupied region can spread out into the empty region (see Fig. 4.1). The evolution of the particle density is tracked using single-site resolution techniques [57, 240] and digital mirror devices allow one to tune the disorder. The relaxation dynamics provides evidence for the existence of an ergodic and an MBL regime as disorder strength is varied, characterized via several observables such as density profiles, particle-number imbalances and measures of the localization length [45]. This experiment serves as the main motivation for our theoretical work.

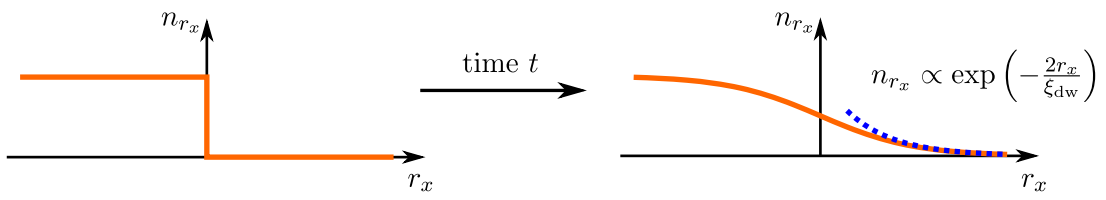

Figure 4.1 Sketch of the initial state (left) and density profile after a sufficiently long time (right) in the localized regime. The profile develops an exponential decay with distance $n_{r_x} \propto \exp(-\frac{2r_x}{\xi_{\mathrm{dw}}})$ in its tails away from the initial edge $r_x = 0$ of the domain wall.

The term domain-wall melting is inherited from the equivalent problem in quantum magnetism (see, e.g., [82, 206, 231, 241–243]), corresponding to coupling two ferromagnetic domains with opposite spin orientation. Furthermore, as discussed in Ch. 3, the domain-wall melting describes the transient dynamics [86, 87] of sudden-expansion experiments of interacting quantum gases in optical lattices (i.e., the release of initially trapped particles into an empty homogeneous lattice) [87, 177, 178, 180]. Theoretically, the sudden expansion of interacting bosons in the presence of disorder was studied in, e.g., [244, 245] for the expansion from the *correlated ground state* in the trap, while for MBL, higher energy densities are relevant.

In this chapter, we use ED and time-evolution methods with MPS [76, 109] to clarify some key questions of the domain-wall experiments. After a brief introduction to the phenomenons of MBL in Sec. 4.1, we first consider noninteracting fermions in a 1D tight-binding model with diagonal disorder in Sec. 4.2. We demonstrate that it is possible to extract the single-particle localization length $\xi_{\mathrm{loc}}^{(1)}$ as a function of disorder strength from such an experiment since the density profiles develop exponential tails with a length scale ξ_{dw} (see Fig. 4.1). This domain-wall decay length ξ_{dw} also captures the disorder driven metal-insulator transition in the Aubry-André model when approached from the localized regime, exhibiting a divergence. Second, we study the case of spinless fermions with nearest-neighbor repulsive interactions on chains and two-leg ladders, for which numerical estimates of the critical disorder strength W_c of the metal-insulator transition are available [24, 33, 246–250]. For both models, essential features of the noninteracting case carry over, namely, the steady-state profiles decay exponentially with distance in the localized regime $W > W_c$ (i.e., the expansion stops), while particles continue to spread in the ergodic regime $W < W_c$. Moreover, we discuss experimentally accessible measures to investigate the dynamics close to the transition for all models.

4.1 Phenomenology of Many Body Localization (MBL)

Text-books on quantum mechanics teach us that eigenstates of a Hamiltonian extend over the whole system [251]. The wave function of a particle can even leak into a region with a high potential energy, where the particle cannot be found in classical mechanics, causing the famous tunnel effect. However, even if the energy is much higher than the background potential, the single particle wave functions can be exponentially localized due to disorder in the potential, an effect known as Anderson localization [90–92]. As schematically illustrated in Fig. 4.2(a), spatially separated states can be very close in energy. Thus, one could think that any weak interaction immediately hybridizes the single particle states. However, seminal works showed that a localization in Fock space can persist, giving rise to MBL [22, 23, 252].

The MBL phase is a *dynamical* phase of matter in the sense that it is characterized by the properties of highly excited many-body eigenstates, which govern the dynamics of generic initial states (with little overlap to the ground state). Note that this is very different from the notion of a quantum phase transitions [253]. In an ergodic system, the ETH is expected to hold and dictates many of the properties of the (highly excited) eigenstates [17–20]. On the other side, MBL implies a failure of ETH [24] and therefore, memory of initial conditions [25, 26]. The phenomenology of MBL systems is connected to the existence of a complete set of commuting (quasi) local integrals of motion, so-called "l-bits", that are believed to exist in systems in which all many-body eigenstates are localized [30, 254–256]. These l-bits can be thought of as quasiparticles with an infinite lifetime, in close analogy to a zero-temperature Fermi liquid [22, 248]. Let us oppose the properties in the ergodic and the MBL phase, see Fig. 4.2(b).

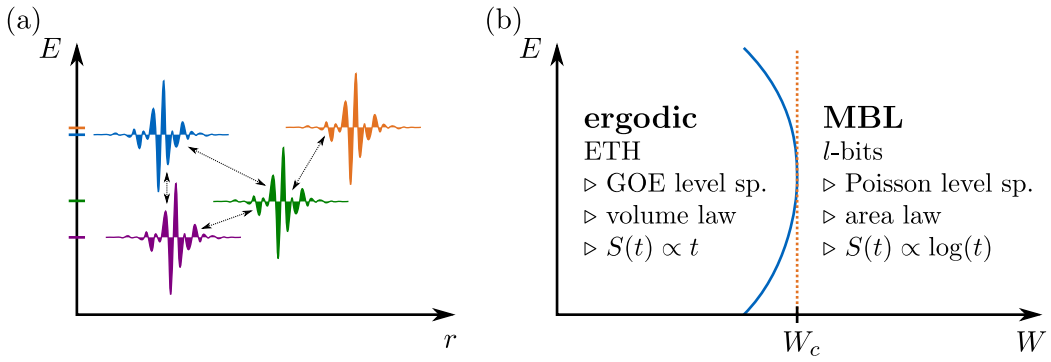

Figure 4.2 (a) In a non-interacting system with disorder, the single-particle wave functions are Anderson localized. Interactions can hybridize the different levels and induce delocalization, but seminal, perturbative works showed that localization can persist, forming the MBL phase [22, 23]. (b) Schematic phase diagram of a 1D system with disorder strength W and energy E. Numerical studies with ED indicate the presence of a mobility edge (blue, solid line) [32, 33], yet there are analytical arguments against it (orange, dashed line) [34].

Random matrix theory predicts for an ergodic system a certain statistical distribution for example from a Gaussian orthogonal ensemble (GOE)[1] with energy level repulsion. Since levels of spatially separated, localized states are independent, see Fig. 4.2(a), the level spacing in the MBL phase is Poisson distributed [246]. The ETH implies that the eigenstates in an ergodic phase obey a volume law. In contrast, the eigenstates in the localized phase are only little entangled: they obey an area law [31–33] — similar as the area law for the ground state discussed in Sec. 2.1, but here also for high excited states in the center of the spectrum. Hence, those eigenstates can also be represented by MPS; in fact, there have been given generalizations of DMRG targeting highly excited states deep in the MBL phase [46, 257, 258]. One might hope that this carries over to the dynamics. Indeed, compared to a linear growth $S(t) \propto t$ in an ergodic system [112], the (half-chain) entanglement entropy after a quench starting from an initial state grows in the MBL phase significantly slower, namely logarithmically, $S(t) \propto \log(t)$ [28, 29]. This characteristic feature of MBL distinguishes it from a simple Anderson insulator, where the entanglement is bounded by an area law at long times, and has been linked to dephasing [28, 30].

Note that disorder is not a crucial ingredient for MBL, it can also be induced effectively by other degrees of freedom [259].

Important open questions are the nature of the MBL transition and the existence of MBL in higher dimensions. The early, perturbative work [22] and numerical results with ED [32, 33] suggest the existence of a mobility edge, i.e., a separation of localized and delocalized states at different energy densities for a given disorder strength $W \lesssim W_c$, see the blue line in Fig. 4.2(b), known for example from Anderson localization in three dimensions [91]. However, De Roeck et al. argued that this is inconsistent, since rare regions with lower-than-average disorder, so called "hot bubbles", would thermalize their surroundings, making them larger and thus more powerful in delocalizing the whole system in an avalanche-like scheme [34]. This picuture and the transition in general were studied by several groups with renormalization-group (RG) schemes [36, 40, 260–262], some finding a very slow finite size scaling of a Kosterlizt-Thouless transition [41, 263]. Others identified the MBL transition with a percolation in Fock space [42, 264]. Whatever the exact nature of the phase transition is, the dynamics can be very slow

[1] The ensemble to be used depends on the symmetries present in the Hamiltonian.

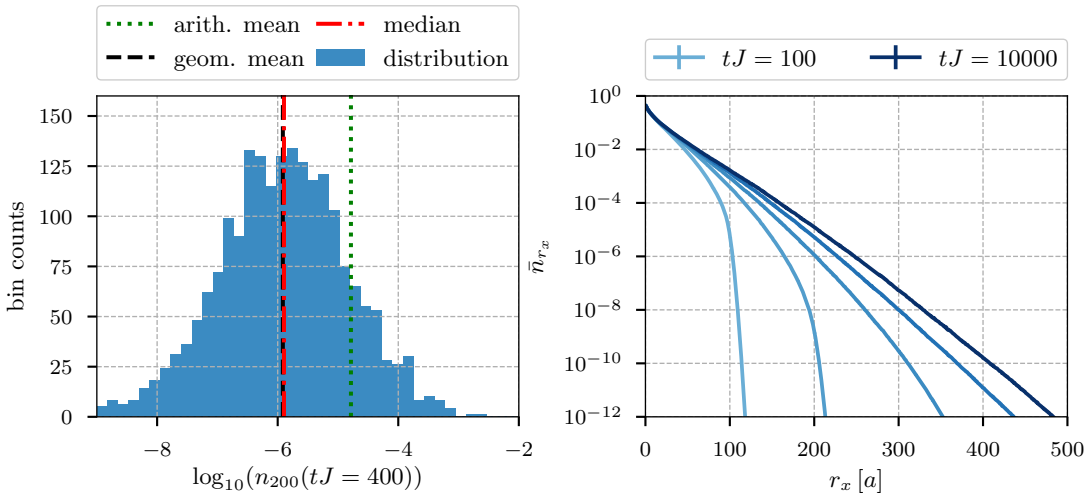

Figure 4.3 ED results ($L = 2000$) for 1D noninteracting fermions with uncorrelated diagonal disorder Eq. (4.1). (a) Exemplary distribution of n_{r_x} on a logarithmic scale for the free fermions at site $r_x = 200$, $tJ = 400$ and $W = 0.5J$. (b) Representative *typical* density profile for $W = 0.5J$ at times $tJ = 100, 200, 400, 1000, 10\,000$ (bottom to top). Error bars are smaller than the linewidth.

even on the ergodic side [38, 265, 266], questioning the common definition of MBL purely based on the properties of the eigenstates [35, 267].

4.2 Noninteracting cases

4.2.1 Anderson insulator

We will first consider noninteracting fermions in a 1D tight-binding chain with uncorrelated diagonal disorder. The Hamiltonian reads:

$$\hat{H}_0 = -\frac{J}{2}\sum_{r_x}\left(\hat{c}^\dagger_{r_x}\hat{c}_{r_x+a} + h.c.\right) - \sum_{r_x}\epsilon_{r_x}\hat{n}_{r_x}\,, \tag{4.1}$$

where $\hat{c}^\dagger_{r_x}$ denotes the fermionic creation operator on site r_x, $\hat{n}_{r_x} = \hat{c}^\dagger_{r_x}\hat{c}_{r_x}$ is the number operator, $n_{r_x} = \langle\hat{n}_{r_x}\rangle$ is density, and $\epsilon_{r_x} \in [-W, W]$ is a random onsite potential (L is the number of sites). We choose the lattice spacing a as unit and set $\hbar = 1$. All single-particle eigenstates are localized for any nonzero W and thus the system is an Anderson insulator at all energy densities [91, 92].

An exemplary distribution of n_{r_x} for the free fermion case is shown in Fig. 4.3(a). In a rough approximation, the probability for a particle to hop the r_x sites out of the domain wall can be seen as a product of the hopping probabilities to neighboring sites, which depend on the specific disorder realization. The geometric mean $\bar{n}_{r_x}$ (i.e., the arithmetic mean of $\log n_{r_x}$) is thus a natural choice for the average over different disorder realizations. As evident from Fig. 4.3 (a), it coincides with the median and represents the typical value. In contrast, the arithmetic mean is an order of magnitude larger as it puts a large weight in the upper tail of the distribution. Although the geometric mean is a good choice for n_{r_x}, we note that it is reasonable to use the arithmetic mean for other quantities such as VAR_n and ΔN, which we discuss later: these quantities are integrated over r_x for a given disorder realization. We checked that the arithmetic mean is close to typical values for these quantities.

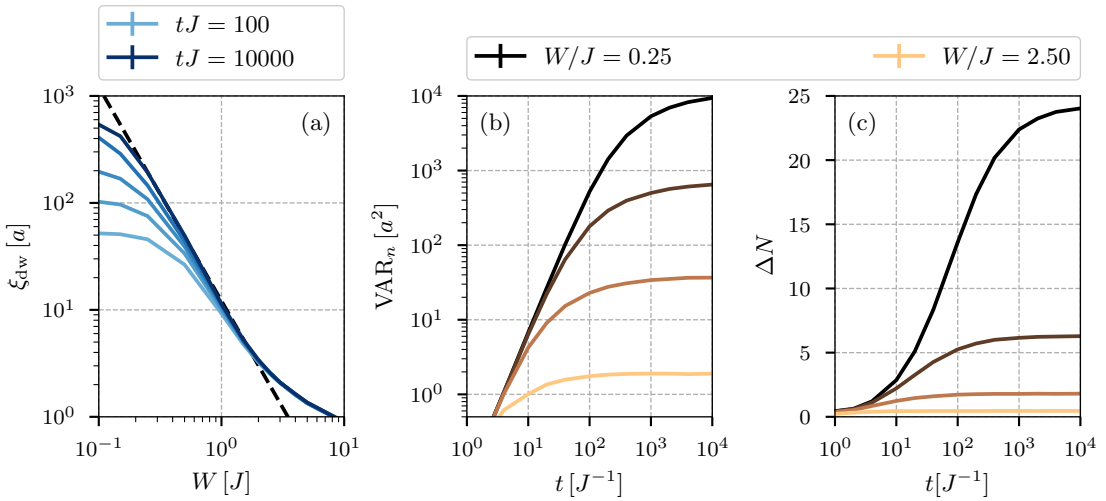

Figure 4.4 ED results ($L = 2000$) for 1D noninteracting fermions with uncorrelated diagonal disorder Eq. (4.1). (a) Domain-wall decay length ξ_{dw} (extracted from VAR_n) for times $tJ = 100, 200, 400, 1000, 10\,000$ (bottom to top), as a function of the disorder strength W. The dashed line shows a fit to the expected scaling $\xi_{\mathrm{dw}} \propto W^{-2}$ [91]. (b) Variance VAR_n of the distribution of expanded particles for $W/J = 0.25, 0.5, 1.0, 2.5$ (top to bottom). (c) Number of emitted particles $\Delta N(t)$. Error bars are smaller than the line width.

Typical density profiles for the dynamics starting from a domain-wall initial state are shown for different times in Fig. 4.3(b). Here, "typical" refers to the geometric mean $\bar{n}_{r_x}$ over disorder realizations.

The domain wall first melts slightly yet ultimately stops expanding. The profiles clearly develop an exponential tail $\bar{n}_{r_x} \propto \exp(-2r_x/\xi_{\mathrm{dw}})$ for $r_x \gg 0$. The crucial question is now whether the length scale ξ_{dw} is directly related to the single-particle localization length or not.

We compare two ways of extracting ξ_{dw}: First, a fit to the numerical data for $\bar{n}_{r_x}$ in the tails $r_x \gg 0$ and second, via computing the variance of the particles emitted into the originally empty region. For the latter, we view the density n_{r_x} in the initially empty region $r_x > 0$ as a spatial distribution $\langle\cdot\rangle_n \equiv \left(\sum_{r_x>0} n_{r_x}\,\cdot\right)/\Delta N$ where $\Delta N = \sum_{r_x>0} n_{r_x}$ is the number of emitted particles. The variance $\mathrm{VAR}_n = \langle r_x^2\rangle_n - \langle r_x\rangle_n^2$ of this particle distribution is shown in Fig. 4.4(b) and approaches a stationary regime on a timescale depending on W. For the time window plotted, only the curves with $W \geq J$ saturate, yet we checked that also the curves for $W < J$ saturate at sufficiently long times. At short times, $\mathrm{VAR}_n \propto t^2$ signals a ballistic expansion of the particles as long as $\mathrm{VAR}_n(t) \ll \xi_{\mathrm{loc}}^{(1)}$.

Assuming a strictly exponential distribution $n_{r_x} \propto \exp\left(-\frac{2r_x}{\xi_{\mathrm{dw}}}\right)$ for all $r_x > 0$ yields $\mathrm{VAR}_n \approx \frac{\xi_{\mathrm{dw}}^2}{4}$ for $\mathrm{VAR}_n \gg 1$. We use that relation to extract ξ_{dw} in the general case as well and in addition, we introduce an explicit time dependence of ξ_{dw} to illustrate the approach to the stationary state. In general, this gives only a lower bound to W_c since VAR_n can be finite for diverging ξ_{dw} if the distribution is not exponential. Yet we find that both methods give similar results for the final profile and show only ξ_{dw} extracted from VAR_n in Fig. 4.4(a).

The known result for the localization length in the 1D Anderson model is $\xi_{\mathrm{loc}}^{(1)} = \frac{8(J^2-E^2)}{W^2}$ [91] for $E = 0$ (our initial state leads to that average energy for sufficiently large systems). Our data for ξ_{dw} shown in Fig. 4.4(a) clearly exhibit the expected scaling $\xi_{\mathrm{dw}} \propto W^{-2}$ over a wide range of W as suggested by a fit of $\xi_{\mathrm{dw}} = a/W^{-2}$ to the data [dashed line in Fig. 4.4(a); the

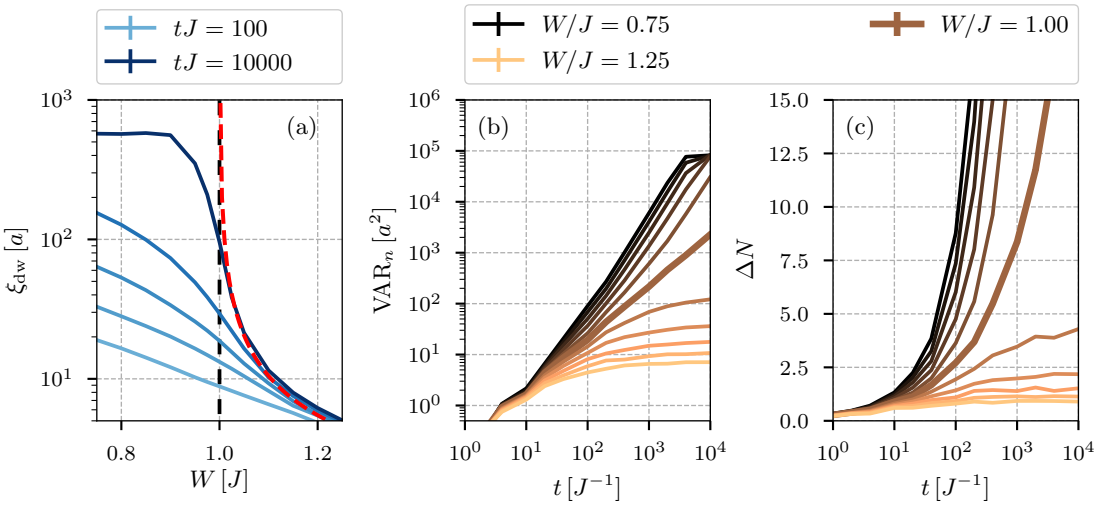

Figure 4.5 ED results ($L = 2000$) for the Aubry-André model with a localization transition at $W_c = J$ (indicated by the vertical dashed line in (a) and the thicker lines in panels (b,c)). (a) Domain-wall decay length ξ_{dw} (extracted from VAR_n) for times $tJ = 100, 200, 400, 1000, 10\,000$ (bottom to top), as a function of the disorder strength W. The red, dashed line shows the analytical result $\xi^{(1)}_{\mathrm{loc}} = 1/\log\left(\frac{W}{J}\right)$ [268]. (b) Variance VAR_n for $W/J = 0.75, 0.8, 0.85, \ldots, 1.25$ (top to bottom). (c) Number of emitted particles $\Delta N(t)$. Error bars are smaller than the line width.

prefactor is larger by about a factor of 1.5 than the typical localization length $\xi^{(1)}_{\mathrm{loc}}$]. Deviations from the W^{-2} dependence at small W, where $\xi^{(1)}_{\mathrm{loc}} \sim O(L)$, are due to the finite system size. At large W, the discreteness of the lattice makes it impossible to resolve ξ_{dw} that are much smaller than the lattice spacing. We stress that fairly long times need to be reached to observe a good quantitative agreement with the W^{-2} dependence. For instance, for the parameters of Fig. 4.4(a), $tJ \sim 1000$ is necessary to reach the asymptotic form. Nevertheless, even at shorter times, the density profiles are already approximately exponential. To summarize, our results demonstrate that the characteristic length scale ξ_{dw} is a measure of the single-particle localization length, most importantly exhibiting the same qualitative behavior.

In Fig. 4.4(c), we introduce an alternative indicator of localization, namely, the number of emitted particles $\Delta N(t)$ that have propagated across the edge $r_x = 0$ of the initial domain wall at a time t. Due to particle conservation, ΔN is directly related to the imbalance $\mathcal{I} = \frac{N-2\Delta N}{N}$ analyzed in the experiment [45]. We observe that ΔN shares qualitatively the same behavior with VAR_n [note the linear y scale in Fig. 4.4(c)], which will also apply to the models discussed in the following.

4.2.2 Aubry-André model

As a further test, we now focus on the dynamics in the Aubry-André model, where a quasiperiodic modulation is introduced in Eq. (4.1) via $\epsilon_{r_x} = W\cos(2\pi\varphi r_x + \phi_0)$ instead of the uncorrelated disorder. This model was studied in the MBL experiments of Ref. [43, 44]). We set the irrational ratio φ to $\varphi = (\sqrt{5}-1)/2 = 0.61803\ldots$ and perform the equivalent to disorder averages by sampling over the value of the phase $\phi_0 \in [0, 2\pi)$. This noninteracting model has a delocalization-localization transition at $W_c/J = 1$, where the single-particle localization length diverges as $\xi^{(1)}_{\mathrm{loc}} = \log\left(\frac{W}{J}\right)$ [268]. Similar to the previously considered Anderson model, the density profiles become stationary with an exponential tail in the localized phase for $W > W_c$.

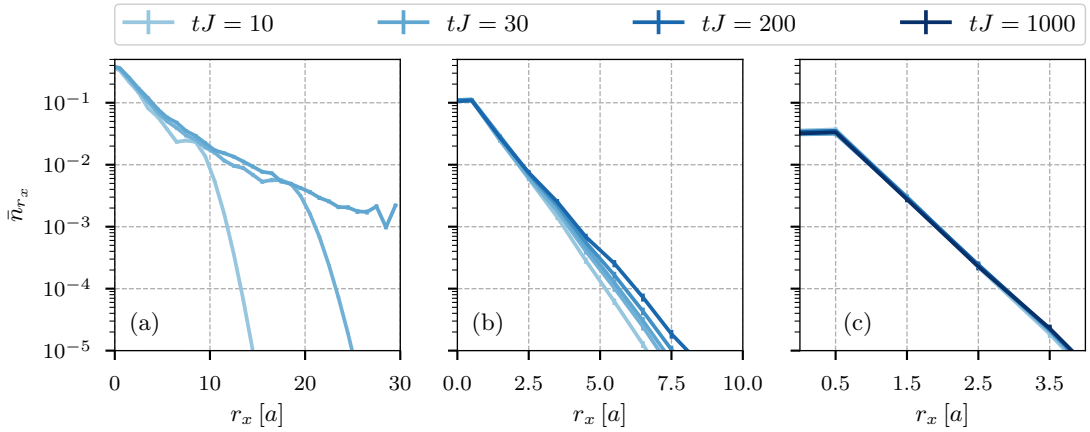

Figure 4.6 tDMRG results ($L = 60$) for a chain of interacting spinless fermions with $V = J$. Typical density profiles for (a) $W/J = 0.5$ at $tJ = 10, 20, 30$ (bottom to top), (b) $W/J = 3$ and additional data for $tJ = 60, 200$, and (c) $W/J = 6$, additional data for $tJ = 1000$ (on top of the data for shorter times).

As W is varied, a clear transition is visible in the time dependence of both VAR_n and ΔN shown in Figs. 4.5(b) and 4.5(c), respectively, which become stationary for $W > W_c$, while growing with a power law for $W < W_c$. The corresponding domain-wall decay length ξ_{dw} shown in Fig. 4.5(a) diverges as W_c is approached from above, in excellent agreement with the single-particle localization length of that model [268]. The maximum value of ξ_{dw} in the extended phase reached at long times diverges with L. This demonstrates that the domain-wall melting can resolve the delocalization-localization transition at $W = J$.

4.3 Interacting fermions on a chain

Given the encouraging results discussed above, we move on to studying the dynamics in a system with an MBL phase, namely to the model of spinless fermions with repulsive nearest-neighbor interactions $\hat{H}_{\mathrm{int}} = \hat{H}_0 + V \sum_{r_x} \hat{n}_{r_x} \hat{n}_{r_x+a}$, equivalent to the spin-1/2 XXZ chain. We focus on $SU(2)$ symmetric exchange, i.e., $V = J$, for which numerical studies predict a delocalization-localization transition from an ergodic to the MBL phase at $W_c/J = (3.5 \pm 1)$ [24,33,247,248] at energy densities in the middle of the many-body spectrum (corresponding to infinite temperature when approaching the transition from the ergodic side). Note, though, that even for this much studied model, some aspects of the phase diagram are still debated in the recent literature (see, e.g., [34,35]).

Typical time evolutions of density profiles in the ergodic and MBL phase are shown in Fig. 4.6(a-c), obtained from tDMRG simulations [76,107,108]. We use a time step of $dt = 0.04/J$ and a bond dimension of up to $\chi = 1000$ and keep the discarded weight in each time step under 10^{-10}. The disorder average is performed over about 500 realizations. These profiles show a crucial difference between the dynamics in the localized and the delocalized regime. Deep in the localized regime, Fig. 4.6(c), similar to the noninteracting models discussed before, the density profiles quickly become stationary with an exponential decay even close to $r_x = 0$. In the ergodic phase, however, the density profiles never become stationary on the simulated time scales and for the values of interactions considered here. For $W = 0.5J$ shown in Fig. 4.6(a), the particles spread over the whole considered system. Remarkably, we find a regime of slow dynamics [37, 38, 247, 266, 269] at intermediate disorder $W < W_c$ in Fig. 4.6(b), where there

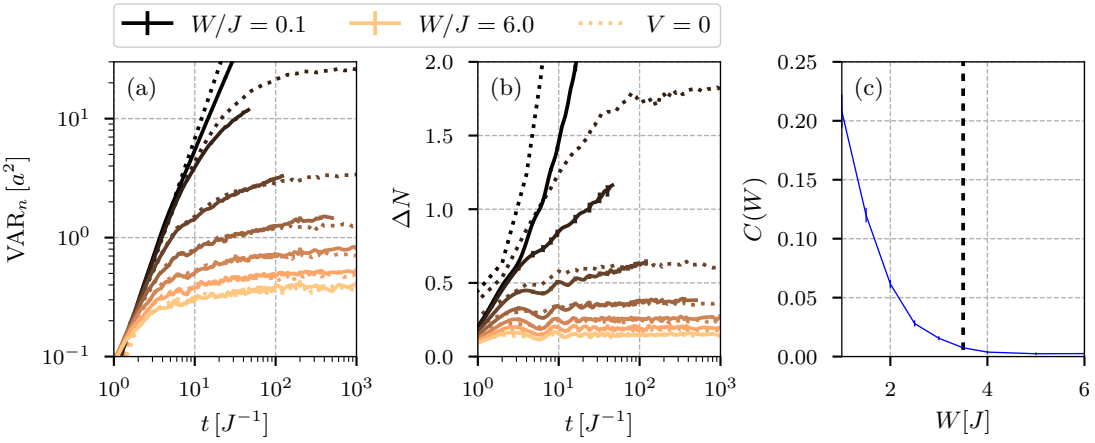

Figure 4.7 tDMRG results ($L = 60$) for a chain of interacting spinless fermions with $V = J$. (a) Variance VAR_n of the distribution of expanded particles for $W/J = 0.1, 1, 2, 3, 4, 5, 6$ (solid lines top to bottom). The dotted lines show equivalent data for the noninteracting case $V = 0$. (b) Number of emitted particles $\Delta N(t)$. (c) $C(W)$ from fit of $\Delta N(t)$ to Eq. (4.2) for $tJ > 10$. Error bars are mostly smaller than the linewidth.

seems to persist an exponential decay of n_{r_x} at finite times, but with a continuously growing $\xi_{\mathrm{dw}}(t)$. We note that $\xi_{\mathrm{dw}}(t)$ at the shortest time scales is on the order of the single-particle localization length. An explanation can thus be obtained in this picture: On short time scales, single particles can quickly expand into the right, empty side within the single-particle localization length, thus leading to the exponential form of n_{r_x}. The interaction comes into play by scattering events at larger times, ultimately allowing the expansion over the whole system for infinite times.

The slow regime is also reflected in the quantities VAR_n and ΔN in Fig. 4.7(a,b), which behave qualitatively in the same way. While both quantities saturate for $W > W_c$ and the results hardly differ from the noninteracting case shown by the dotted lines, the slow growth becomes evident for $W \lesssim W_c$ at the intermediate time scales accessible to us. The slow growth of both VAR_n and ΔN is, for $W \lesssim W_c$, the best described by (yet hard to distinguish from a power-law)

$$\Delta N(t), \mathrm{VAR}_n(t) = C(W) \log(tJ) + \mathrm{const}\,. \tag{4.2}$$

This growth is qualitatively different from the non-interacting case, where a saturation sets in after a faster initial increase. Figure 4.7(c) shows the prefactor $C(W)$ extracted from a fit to the data of $\Delta N(t)$ for $tJ > 10$. This allows us to extract W_c since $C(W > W_c) = 0$ for the stationary profiles in the localized phase. Our result for W_c is compatible with the literature value $W_c/J = 3.5 \pm 1$ [24, 33, 247, 248] (dashed line in Fig. 4.7(c)).

4.4 Interacting fermions on a ladder

As a first step towards 2D systems, we present results for the dynamics of interacting spinless fermions on a two-leg ladder in the presence of diagonal disorder. The simulations are done with a variant of tDMRG suitable for long-range interactions [109], with a time step $dt = 0.01/J$. Figures 4.8(a) and 4.8(b) show the variance VAR_n and ΔN for $V = J$, respectively. As for the chain, we observe that both the variance and ΔN have a tendency to saturate for large disorder strength, while they keep growing for small disorder. The data are best described by Eq. (4.2) and we extract $C(W)$ from fits of the data for $tJ > 10$ to Eq. (4.2). The results of these fits shown

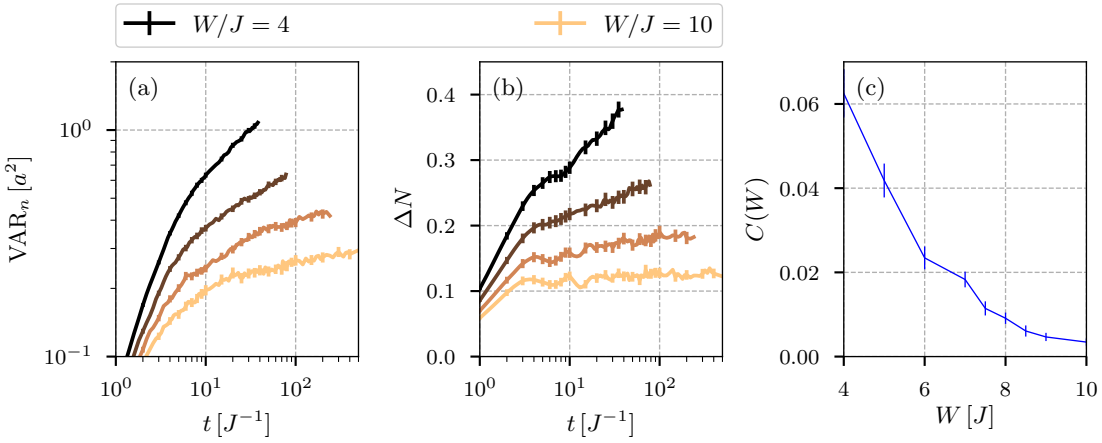

Figure 4.8 tDMRG results for a two-leg ladder ($L = 60$) of interacting spinless fermions with $V = J$. (a) Variance VAR_n at $W/J = 4, 6, 8, 10$ (top to bottom). (b) Number of emitted particles $\Delta N(t)$. (c) $C(W)$ from fit to Eq. (4.2) for $tJ > 10$.

in Fig. 4.8(c) suggest a critical disorder strength $8 \lesssim W_c/J \lesssim 10$, in good agreement with the value of $W_c/J = 8.5 \pm 0.5$ found in an ED study of the isotropic Heisenberg model on a two-leg ladder[2] [250].

4.5 Conclusion

We analyzed the domain-wall melting of fermions in the presence of diagonal disorder, motivated by a recent experiment [45] that was first in using this setup for interacting bosons in 2D. Our main result is that several quantities accessible in experiments (such as the number of propagating particles and the variance of their particle density) are sensitive to localization and can be used to locate the disorder-driven metal-insulator transition, based on our analysis of several models of noninteracting and interacting fermions for which the phase diagrams are known. Notably, this encompasses a two-leg ladder as a first step towards numerically simulating the dynamics of interacting systems with disorder in the 1D-2D crossover. Our work further indicates that care must be taken in extracting quantitative results from finite systems or finite times since the approach to the stationary regime can be slow. Interestingly, we observe a slow dynamics in the ergodic phase of interacting models as the transition to the MBL phase is approached, which deserves further investigation.

The domain-wall melting thus is a viable approach for theoretically and experimentally studying disordered interacting systems, and we hope that our work will influence future experiments on quasi-1D systems where a direct comparison with theory is feasible. Concerning 2D systems, where numerical simulations of real-time dynamics face severe limitations, our results for two-leg ladders provide confidence that the domain-wall melting is still a reliable detector of localization as well, as evidenced in the experiment of [45]. Even for clean systems, experimental studies of domain-wall melting in the presence of interactions could provide valuable insights into the nonequilibrium transport properties of interacting quantum gases [86,178,180,206,241]. For instance, even for the isotropic spin-1/2 chain ($V = 1$ in our case), the qualitative nature of

[2] The two models differ by correlated hopping terms which are not believed to be important for the locus of the transition.

transport is still an open issue [270–277]. Moreover, the measurement of diffusion constants would be desirable [278].

5 Finding purifications with minimal entanglement

Most of the content of this chapter can also be found in a previous publication of the author [5]. Text and figures have been adjusted to fit into the context of the thesis.

Simulating quantum many-body systems faces a fundamental difficulty due to the complexity required to represent highly entangled states. Significant progress has been made through the observation that quantum ground states of interest often have only limited (area-law) entanglement, and thus can be represented efficiently using MPS [70, 73–75] in 1D and PEPS [114] in higher dimensions. Such approaches have been particularly successful in the study of ground-state properties of 1D systems, where the DMRG method [68] revolutionized the efficiency of numerical methods.

To extend the success of DMRG to transport and non-equilibrium phenomena, it is necessary to simulate real-time evolution [76, 107, 108]. The bipartite entanglement of pure states generically grows linearly with time, which leads to a rapid exponential blow up in computational cost, limiting pure-state time evolution to rather short times. But, while the entanglement growth limits the ability to compute the real time evolution of pure quantum states, it need not impose the same restriction on the imaginary time evolution of mixed states [279, 280]. It is then natural to ask if the time evolution of mixed states can be represented efficiently using MPS and what sets the difficulty of such computations.

There are different techniques for simulating mixed states using MPS methods, including a direct representation of the density matrix as an MPO [281], using minimally entangled typical thermal states (METTS) [140, 282–284], and purification [93, 94]; in this work we focus on the latter. In purification, a density matrix $\hat{\varrho}$ acting on a *physical* Hilbert space $\mathcal{H}^P$ is represented as a pure state $|\psi\rangle$ in an enlarged space $\mathcal{H}^P \otimes \mathcal{H}^A$:

$$\hat{\varrho} = \mathrm{Tr}_A \, |\psi\rangle \langle\psi| \, . \tag{5.1}$$

It is always sufficient to choose $\mathcal{H}^A$ to be identical to $\mathcal{H}^P$, "doubling" each degree of freedom (DoF) as illustrated in Fig. 5.1(a). We note that the purification description can be a limitation for infinite systems [285, 286]. Yet on finite systems, a purification can be found formally by diagonalizing the density matrix. In equilibrium this gives the thermofield double (TFD) purification, $|\psi_\beta\rangle = \frac{1}{\sqrt{Z}} \sum_m e^{-\beta E_m/2} \, |m\rangle_P \, |m\rangle_A$, where $|m\rangle$ are the eigenvectors and E_m the eigenvalues of the Hamiltonian. It was recently argued that the TFD state can be efficiently represented with an MPS of bond dimension that grows at most polynomially with the inverse temperature [279]. The TFD is only one possible choice of purification, since Eq. (5.1) is left invariant under an arbitrary unitary transformation $\hat{U}_{\mathrm{anc}}$ which acts only on the ancilla space $\mathcal{H}^A$.

This gauge freedom may be used to reduce the entanglement in $|\psi\rangle$, rendering the MPS representation more efficient [287, 288]. Here, we propose a way to find the minimally entangled purification. This minimum defines the entanglement of purification E_p [95] [defined below in

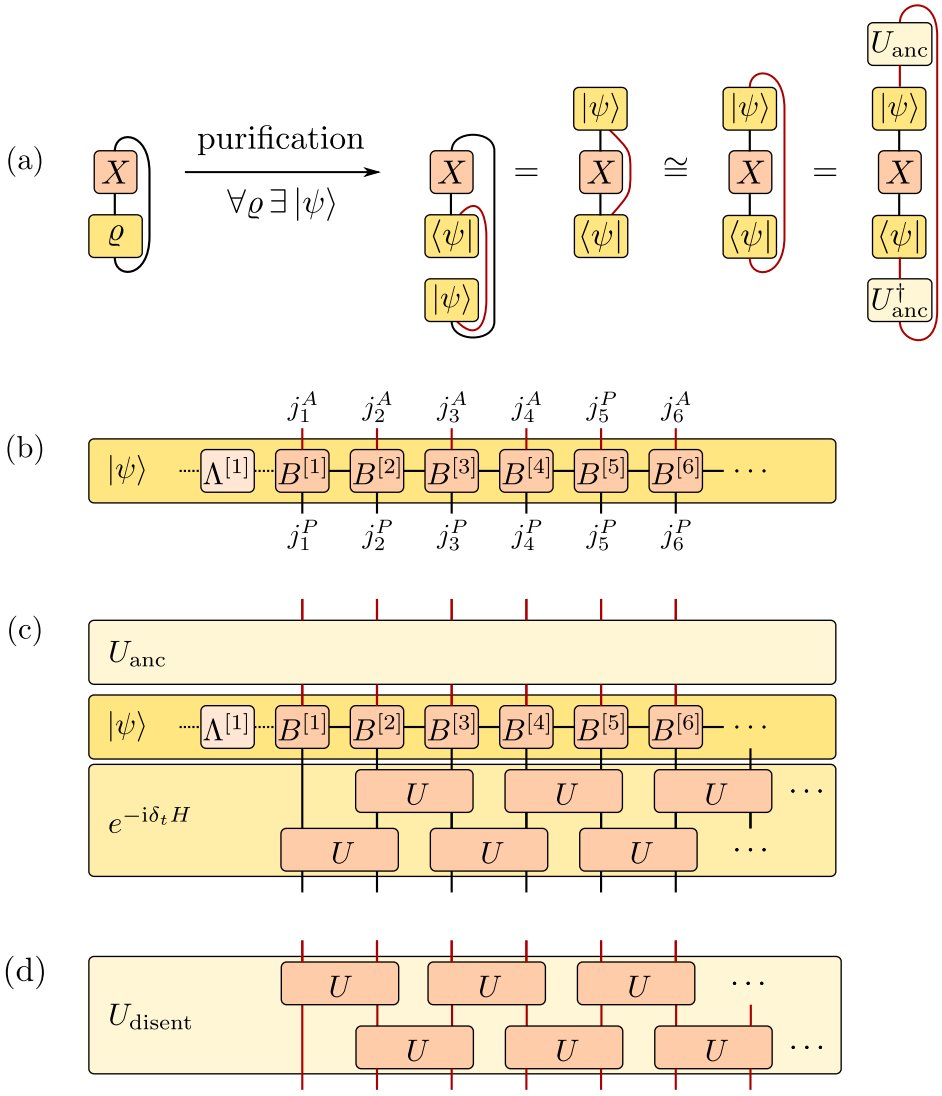

Figure 5.1 (a) Purification: any density matrix ϱ in a physical Hilbert space $\mathcal{H}^P$ can be represented by a pure state $|\psi\rangle$ in an enlarged Hilbert space $\mathcal{H}^P \otimes \mathcal{H}^A$. (b) Schematic representation of purified states using MPS. (c) A purified state is evolved in real or imaginary time by acting on the physical degrees of freedom (e.g., using a Trotter decomposition of the time-evolution operator). The auxiliary degrees of freedom are only defined up to a global unitary $\hat{U}_{\text{anc}}$ which can be chosen to minimize the entanglement on the bonds. (d) The global $\hat{U}_{\text{anc}}$ is decomposed into a network of two-site gates to produce a disentangler $\hat{U}_{\text{disent}}$.

Eq. (5.10)], which thus plays a role similar to the entanglement entropy in the pure case: it bounds the bond dimension $\chi \geq e^{E_P}$ [136]. However, this lower bound is irrelevant unless there is an efficient algorithm to *find* the minimally entangled purification at a cost comparable to DMRG [e.g., $O(\chi^3)$], which, since it constitutes a global optimization problem over the many-body Hilbert space, is not *a priori* obvious.

Below we introduce a method to find an approximately optimal purification by sequentially applying local disentangling operations to the ancilla DoF. The cost of the disentangling procedure is comparable to DMRG, and the resulting entanglement $\widetilde{E}_p$ reproduces the known properties of E_p in certain limits. We use the method to optimize both the equilibrium purification and that of a time-dependent state. We find that the method can significantly slow the entropy growth during real-time evolution down, as we demonstrate for both the transverse field Ising model and a disordered Heisenberg chain. For the latter, we find a slow spreading of $\widetilde{E}_p$ already for intermediate disorder strengths. In equilibrium, $\widetilde{E}_p$ approaches half of the entropy in the TFD state at low temperature.

Before proceeding, we comment on the difference between the method presented here and two other proposals to compute long-time dynamics efficiently using MPS. First, it was argued that the dynamics of local quantities in thermalizing systems can be captured accurately using the time-dependent variational principle (TDVP) [289], allowing to extract transport coefficients and even characteristics of chaos. Moreover, a new truncation method to approximate the time evolution of a density matrix, represented as an MPO, was proposed by Ref. [290], also allowing to reach long times. Both of these methods rely on the assumption that the increase of the non-local information encoded by the ever-growing entanglement entropy is irrelevant to the evolution of observable properties in thermalizing systems. These methods attempt to simulate the correct macro-state rather than the nearly exact microstate. Thus, the "truncation error" as usually defined in DMRG studies can be large as it is measured with respect to the exact state. In contrast, the approach presented here attempts, by optimizing the purification, to minimize the truncation error in order to compute the exact micro-state.

5.1 Purifications within the MPS formalism

Before we explain how we can use purifications within the MPS formalism, let us first recall a proof for the existence of the pure state $|\psi\rangle \in \mathcal{H}^P \otimes \mathcal{H}^A$. Since any density matrix ϱ is hermitian and positive, we can find an orthonormal eigenbasis $|m\rangle_P \in \mathcal{H}^P$ of $\hat{\varrho}$ with eigenvalues $p_m \geq 0$. We then take a copy $\mathcal{H}^Q \sim \mathcal{H}^P$ of the Hilbert space and construct the purified state as

$$|\psi\rangle = \sum_m \sqrt{p_m}\, |m\rangle_P\, |m\rangle_A \qquad \in \mathcal{H}^P \otimes \mathcal{H}^A. \tag{5.2}$$

Then we can easily check that Eq. (5.1) is fulfilled:

$$\mathrm{Tr}_A\left(|\psi\rangle\langle\psi|\right) = \sum_{m,m'} \sqrt{p_m}\sqrt{p_{m'}} \underbrace{\mathrm{Tr}_A\left(|m\rangle_P\, |m\rangle_A \langle m'|_P \langle m'|_A\right)}_{=\delta_{m,m'}|m\rangle_P\langle m'|_P} = \sum_m p_m\, |m\rangle_P \langle m|_P = \hat{\varrho}.$$

Hence, any density matrix $\hat{\varrho}$ can be represented by an MPS (which is a pure state) in the doubled Hilbert space $\mathcal{H}^P \otimes \mathcal{H}^A$. □

To double the DoFs on each site n, we simply add an ancilla index j_n^A to each $B^{[n]}$, as indicated by the red legs in Fig. 5.1(b). There is a striking similarity of Fig. 5.1(b) and Fig. 2.7(a). In fact, we can also view the purification state $|\psi\rangle$ as an MPO, and re-interpret Eq. (5.2) as

$$|\psi\rangle = \sum_m \sqrt{p_m}\, |m\rangle_P\, |m\rangle_A \cong \sum_m \sqrt{p_m}\, |m\rangle_P\, \langle m|_P = \sqrt{\hat{\varrho}}. \tag{5.3}$$

Whether $|\psi\rangle$ is viewed as a state or operator is indicated in Fig. 5.1(a) by bending the ancilla leg from top to bottom. Strictly speaking, we should draw the ancilla legs in Fig. 5.1(b) on the bottom as well, but we keep drawing it on the other side than the physical legs for a better visual distinction of the physical and ancilla legs. In fact, in the case that we want to preserve some charges following the ideas outlined in Sec. 2.4, viewing the purification as operator as outlined in Eq. (5.3) gives us a hint how we can choose the charge values of the new leg: the charge values for j_n^A should simply have be the negative charges of the j_n^P leg.

In the spirit of Eq. (5.3), purification consists just of two main steps: split the density matrix as

$$\hat{\varrho} = \sqrt{\hat{\varrho}}^\dagger \sqrt{\hat{\varrho}} \tag{5.4}$$

and view the (matrix) square root $\sqrt{\hat{\varrho}}$ as a state $|\psi\rangle$. The square structure in Eq. (5.4) makes it evident that $\hat{\varrho}$ is positive semi-definite by construction, independent of how much we truncate the MPS. This is an advantage of purification as opposed to naively representing $\hat{\varrho}$ as an MPO [291]. Further, the gauge freedom with $\hat{U}_{\text{anc}}$ becomes obvious from Eq. (5.4), as the square root is not unique, $\sqrt{\hat{\varrho}}^\dagger \sqrt{\hat{\varrho}} = \sqrt{\hat{\varrho}}^\dagger \hat{U}_{\text{anc}}^\dagger \hat{U}_{\text{anc}} \sqrt{\hat{\varrho}}$. In general, $\hat{U}_{\text{anc}}$ could also be an isometry to an ancilla Hilbert space $\mathcal{H}^A$ of a smaller size than $\mathcal{H}^P$; but clearly this can only work if $\hat{\varrho}$ does not have full rank. In the extreme case that only a single pure state contributes to the density matrix, e.g., at zero temperature $T \to 0$, we would be back to the usual MPS description. If $\hat{\varrho}$ has only a few eigenstates with significant contributions, it can be more effective to explicitly evaluate the sum over them — this is the basic idea behind METTS [282], where the sum is sampled with a Monte-Carlo scheme. However, in this work we focus on thermal density matrices $\hat{\varrho} = \frac{1}{Z} e^{-\beta \hat{H}}$ with full rank at finite temperatures.

While the proof for the existence of purifications is enlightening regarding the structure of $|\psi\rangle$, Eq. (5.2) is of little use for MPS simulations: diagonalizing $\hat{\varrho}$ requires to obtain the eigenstates of the Hamiltonian, which is prohibitively expensive. There is, however, one exception, which we can exploit: at infinite temperature ($\beta = 0$), $\hat{\varrho} = \frac{1}{Z}\hat{\mathbb{1}}$ is diagonal in any basis, and we can define the infinite temperature TFD purification as[1]

$$|\psi_0\rangle = \prod_n \left(\frac{1}{\sqrt{d}} \sum_{j_n} |j_n\rangle_P\, |j_n\rangle_A \right), \tag{5.5}$$

where j_n runs over the local Hilbert space, resulting in a $\chi_{\max} = 1$ MPS. In the standard purification approach, the finite-temperature TFD is obtained by cooling down $|\psi_0\rangle$ using imaginary-time evolution,

$$|\psi_\beta\rangle \propto e^{-\frac{\beta}{2}\hat{H}}\, |\psi_0\rangle, \tag{5.6}$$

which can be performed with any of the standard methods for MPS [76, 107–110], for example TEBD as outlined in Sec. 2.2.3. Here, $\hat{H}$ acts only on $\mathcal{H}^P$. Care needs to be taken due to the

[1] In the literature, a singlet state between j_n^A and j_n^P (equivalent to our choice by a local unitary transformation) is sometimes chosen to simplify the implementation of charges [73, 273]. With our choice to use the negative charge values for the ancilla leg, this is not necessary.

fact that the two-site gates are no longer unitary during the imaginary time evolution, which can destroy the canonical form if the usual even–odd brick-wall scheme as illustrated in Fig. 5.1(c) is used. As an alternative, one can perform left-right-left sweeps similar as in DMRG. From $|\psi_\beta\rangle$, thermal expectation values can get evaluated with

$$\langle \hat{X} \rangle_\beta \equiv \frac{1}{Z(\beta)} \operatorname{Tr}_P \left(e^{-\beta \hat{H}} \hat{X} \right) = \langle \psi_\beta | \hat{X} | \psi_\beta \rangle , \tag{5.7}$$

as shown in Fig. 5.1(a). Here, we have used that the normalization of $|\psi_\beta\rangle$, which is convenient to have for an MPS, corresponds to the required $\langle \hat{\mathbb{1}} \rangle_\beta = 1$. If one accumulates the renormalization factors during the imaginary time evolution, one can obtain the partition function $Z(\beta) = \operatorname{Tr} e^{-\beta \hat{H}}$ [73].

Similarly, we can compute dynamical properties with an additional real time evolution of the purification MPS after the application of an operator $\hat{B}$,

$$C(t,\beta) := \langle \hat{B}^\dagger \hat{X}(t) \hat{B} \rangle_\beta = \langle B(t,\beta) | \hat{X} | B(t,\beta) \rangle , \text{ where } |B(t,\beta)\rangle = e^{-\mathrm{i}t\hat{H}} \hat{B} \, |\psi_\beta\rangle . \tag{5.8}$$

By taking $\hat{B} = e^{\mathrm{i}\varepsilon \hat{Y}}$, this form is sufficient to find quantities of interest such as the spectral function

$$-\mathrm{i}\partial_\varepsilon C(t,\beta) = A_{XY}(t,\beta) = \langle [\hat{X}(t), \hat{Y}(0)] \rangle_\beta . \tag{5.9}$$

The computational complexity of such simulations is generically linked to the bipartite von-Neumann entanglement entropy $S_{LL'} = -\operatorname{Tr}(\hat{\varrho}_{LL'} \log(\hat{\varrho}_{LL'}))$, where $\hat{\varrho}_{LL'} = \operatorname{Tr}_{RR'}(|\psi\rangle \langle\psi|)$ is the reduced density matrix defined by a bipartition $\mathcal{H}^P = L \otimes R$ and $\mathcal{H}^A = L' \otimes R'$ at any of the bonds of the MPS; the bond dimension χ is bounded by $\chi \geq e^{S_{LL'}}$. Since other purifications can be obtained by acting with $\hat{U}_\text{anc}$ on the ancilla space, see Fig. 5.1(b), it is desirable to exploit this choice to reduce $S_{LL'}$. Karrasch et al. [287] noticed that a natural choice is the "backward time evolution," $\hat{U}_\text{anc} = e^{\mathrm{i}t\hat{H}}$, because if B is local, this choice leaves $|B(t,\beta)\rangle$ invariant outside the growing "light cone" of the perturbation. Barthel [288] improved this approach by evolving both X and Y in the spectral function $A_{XY}(t,\beta) = \langle [\hat{X}(t), \hat{Y}(0)] \rangle_\beta = \langle [\hat{X}(t/2), \hat{Y}(-t/2)] \rangle_\beta$ as Heisenberg operators, which allows reaching times twice as long with comparable numerical effort [273, 288]. However, these prescriptions need not be optimal; ideally, we would minimize $S_{LL'}$ over all possible purifications, which would result in the entanglement of purification E_p [95]:

$$E_p[\hat{\varrho}_{LR}] \equiv \min_{|\psi\rangle} S_{LL'}[|\psi\rangle] = \min_{\hat{U}_\text{anc}} S_{LL'} \left[\hat{U}_\text{anc} \, |\psi\rangle \right] . \tag{5.10}$$

Equivalently, given an ansatz purification $|\psi\rangle$, we search for $\hat{U}_\text{anc}$ such that $\hat{U}_\text{anc} \, |\psi\rangle$ has minimal entanglement; from this perspective, $\hat{U}_\text{anc}$ is a "disentangling" operation.

5.2 Disentangling algorithm

We propose an algorithm to approximately identify the optimal $\hat{U}_\text{anc}$ via a sequence of local disentangling operations, producing a circuit $\hat{U}_\text{anc} = \hat{U}_\text{disent}$ of the form shown in Fig. 5.1(d): The time evolution is applied to the purified state using the TEBD algorithm [76]. As illustrated in Fig. 5.1(c) and explained in Sec. 2.2.3, the TEBD algorithm is based on a Trotter decomposition of $e^{-\mathrm{i}t\hat{H}}$ into two-site unitaries $e^{-\mathrm{i}\delta_t H_{n,n+1}}$. These unitaries are applied to the physical indices of the effective two-site wave function [c.f. Eq. (2.29)]

$$|\Theta\rangle = \sum_{\substack{j_n^P, j_n^A, j_{n+1}^P, j_{n+1}^A \\ \alpha_n, \alpha_{n+2}}} \Theta^{j_n^P j_n^A, j_{n+1}^P j_{n+1}^A}_{\alpha_n, \alpha_{n+2}} \, |\alpha_n\rangle \, |j_n^P \, j_n^A\rangle \, |j_{n+1}^P j_{n+1}^A\rangle \, |\alpha_{n+2}\rangle ,$$

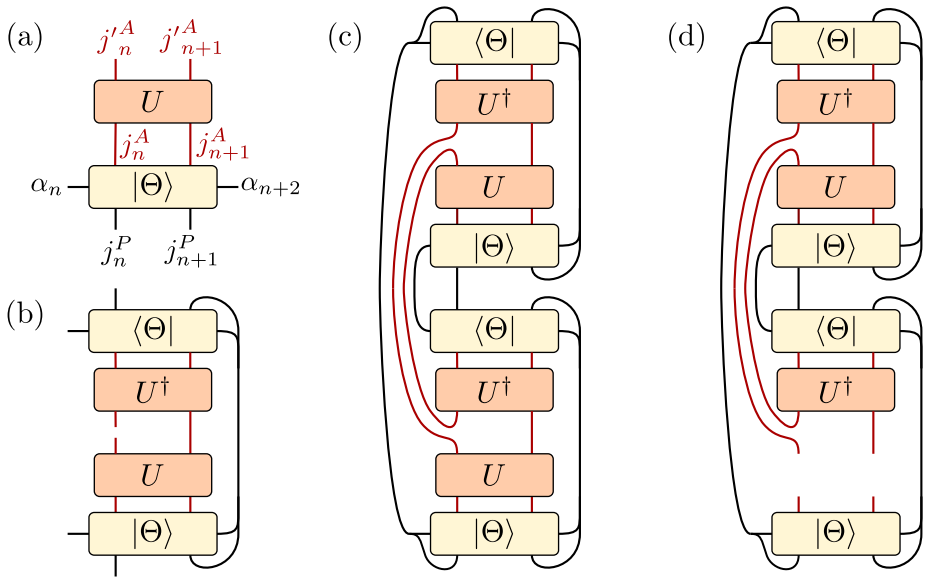

Figure 5.2 (a) Effective two-site wave function to be disentangled by $\hat{U}$. (b) Tensor network for the reduced density matrix $\hat{\varrho}_{LL'} = \mathrm{Tr}_{RR'}\left(\hat{U}\,|\Theta\rangle\,\langle\Theta|\,\hat{U}^\dagger\right)$. (c) Tensor network for $Z_2(\hat{U},\Theta) = \mathrm{Tr}(\hat{\varrho}^2_{LL'})$. (d) Effective environment $E_2(\hat{U},\Theta)$ such that $Z_2(\hat{U},\Theta) = \mathrm{Tr}\left(\hat{U}\,E_2(\hat{U},\Theta)\right)$.

where $|\alpha_n\rangle$ (and $|\alpha_{n+2}\rangle$) labels a basis consisting of Schmidt states to the left of site n (and right of site $n+1$, respectively). During a real-time evolution, we disentangle the two-site wave function right after each Trotter step using a unitary acting on the auxiliary space. These two-site disentanglers can be found using an iterative scheme based on minimizing the second Rényi entropy as a cost function as explained below, similar to the optimization of a multi-scale entanglement renormalization ansatz (MERA) [292]. As the time evolution proceeds, the disentangling unitary circuit $\hat{U}_{\mathrm{disent}}$ is then gradually built up by two-site unitaries, as depicted in Fig. 5.1(d). During an imaginary-time evolution we use a different scheme outlined in Sec. 5.2.3.

While the algorithm can suffer from numerical instabilities, we find empirically that it converges to a purification with significantly less entanglement compared to both backward time evolution and no disentangling at all, as shown in the Sec. 5.3. The method described above is particularly suitable for correlation functions which involve only a single purification, e.g., $C(t,\beta)$, as there is no need to keep track of $\hat{U}_{\mathrm{disent}}$. When two distinct purifications $|B(t)\rangle$ and $|A(t)\rangle$ are required, one would have to compress $\hat{U}^\dagger_{\mathrm{distent},A}\hat{U}_{\mathrm{distent},B}$ as a separate MPO.

5.2.1 Two-site disentangler minimizing the entropy

We explain now how to find a two-site unitary $\hat{U} = \hat{U}^{j'^A_n, j'^A_{n+1}}_{j^A_n, j^A_{n+1}}$ (i.e., acting in $\mathcal{H}^A$) which minimizes the entanglement of an effective two-site wave function $\hat{U}\,|\Theta\rangle$, similar as during the optimization of MERA [292]. We chose to minimize the second Rényi entropy $S_2(\hat{U}\,|\Theta\rangle) = -\log \mathrm{Tr}\left(\hat{\varrho}^2_{LL'}\right)$, where $\hat{\varrho}_{LL'}$ is the reduced density matrix $\hat{\varrho}_{LL'} = \mathrm{Tr}_{j^P_{n+1}, j^A_{n+1}, \alpha_{n+2}}\left(\hat{U}\,|\Theta\rangle\,\langle\Theta|\,\hat{U}^\dagger\right)$ [293]. In contrast to the von-Neumann entropy, the second Rényi entropy is readily expressed as $S_2(\hat{U}\,|\Theta\rangle) = -\log(Z_2)$ with the tensor network Z_2 depicted in Fig. 5.2(c); Z_2 is to be maximized. We solve this non-linear optimization problem iteratively: in the m-th iteration, we consider one $\hat{U}_{m+1}$

formally as independent of the other $\hat{U}_m$ and write $Z_2(\hat{U}_{m+1}, \hat{U}_m, \Theta) = \mathrm{Tr}\left(\hat{U}_{m+1}\, E_2(\hat{U}_m, \Theta)\right)$, where the network for the "environment" $E_2(\hat{U}_m, \Theta)$ is shown in Fig. 5.2(d). It is easy to see that the unitary $\hat{U}_{m+1}$ maximizing this expression is given by a polar decomposition of $E_2(\hat{U}_m, \Theta)$, in other words we set $\hat{U}_{m+1} \coloneqq YX^\dagger$ where X and Y are obtained from an SVD of $E_2(\hat{U}_m, \Theta) = X\Lambda Y^\dagger$. The unitary minimizing $Z_2(\hat{U}, \Theta)$ is then a fixed point $\hat{U}_*$ of this iteration procedure. As a starting point of the iteration, one can choose the identity $\hat{U}_1 \coloneqq \hat{\mathbb{1}}$. At later times, one can also use the result of $\hat{U}_m$ from previous iterations (for the same time step and at the same bond) as initial guess for the next disentangler, which reduces the number of necessary iterations in many cases.

Since this iteration is based on a descent, it tends to go into local minima within the optimization space. To find the global optimum, we can perform multiple iterations in parallel: one starting from the identity, and others starting from initially random unitaries (chosen according to the Haar measure, i.e., from the so-called circular unitary ensemble). From the unitaries obtained by the parallel iterations, we choose the one with the smallest final entropy.

The disentangler $\hat{U}_m$ obtained by the above procedure preserves the quantum numbers of symmetries in the Hamiltonian, at least if the initial guess $\hat{U}_0$ preserves them. In the presence of such a symmetry one should choose $\hat{U}_0$ accordingly from the Haar measure on unitaries preserving the symmetry to avoid an artificial build-up of entanglement. In our case, we exploited the S^z conservation in the Heisenberg chain (5.12) to reduce the computational cost in the tensor contractions and SVDs with the method explained in Sec. 2.4.

5.2.2 Two-site norm disentangler

In this subsection, we discuss an alternative way to obtain a two-site disentangler, which directly focuses on the required bond dimension. The procedure described below is equivalent to finding the "entanglement branching operator" introduced by Ref. [294]. In order to reduce the bond dimension, we look for a two-site unitary $\hat{U}$ (acting on the ancilla DoFs) for which the truncation of the effective two-site wave function $\hat{U}\,|\Theta\rangle$ has the smallest truncation error. To find this $\hat{U}$, we use a similar, iterative scheme as above: given $\hat{U}_m$, we calculate the truncated $\left(\hat{U}_m\,|\Theta\rangle\right)_{\mathrm{trunc}}$ and find the $\hat{U}_{m+1}$ maximizing the overlap $\left|\langle\Theta|\,\hat{U}_{m+1}^\dagger(\hat{U}_m\,|\Theta\rangle)_{\mathrm{trunc}}\right|$. Again, the new $\hat{U}_{m+1}$ can be found by a polar decomposition of the "environment" consisting of the corresponding tensor network for $\left|\langle\Theta|\,\hat{U}_{m+1}^\dagger(\hat{U}_m\,|\Theta\rangle)_{\mathrm{trunc}}\right|$, but excluding the $\hat{U}_{m+1}$. Since the optimal $\hat{U}$ depends on the final bond dimension χ after truncation, we need to gradually increase χ and repeat the iteration procedure until the truncation error for the given bond dimension is below a desired accuracy threshold. While we found that this gradual increase of χ also helps to find the optimal disentangler, it substantially increases the computational cost.

5.2.3 Global disentangling for imaginary-time evolution

In contrast to the real-time evolution, the Trotter gate $e^{-\delta_\beta H_{n,n+1}}$ in imaginary-time evolution is non-unitary. Thus, it can change the Schmidt values and thus generate entanglement on sites it does not even act on, which creates the necessity for a more global scheme of disentangling than the one presented above for the real-time evolution. Instead, we perform the imaginary time evolution as usual (with $\hat{U}_{\mathrm{anc}} = \hat{\mathbb{1}}$) and disentangle only after each l^{th} time step in a more global fashion: in this case, we find that generating the network of $\hat{U}_{\mathrm{disent}}$ by optimizing bonds with right and left sweeps similar as in DMRG is more effective than the Trotter-type scheme

of even and odd bonds depicted in Fig. 5.1(d). Moreover, it is straight-forward to generalize the two-site disentangling described above to multiple sites by grouping multiple sites. For example, we can disentangle the wave function of four sites $n, n+1, n+2, n+3$ by grouping each two sites as $(n, n+1)$ and $(n+2, n+3)$ and then using the above-described method. As the resulting disentangler can perform arbitrary "on-site" rotations within each group, it is necessary to disentangle the obtained wave function (recursively) within each group. While such a grouping provides additional freedom in the unitary to be found and is thus a systematic improvement for finding the optimal *global* disentangler, it comes at the cost of a scaling of required computational resources which is exponential in the number of included sites. In practice, we limited ourselves to optimizing at most four sites at once.

As an alternative for the global disentangling, we tried a method along the lines of Ref. [295]. Here, the idea is to identify pairs of sites with maximal mutual information as candidates for disentangling. Using swap gates (commonly used for TEBD with longer-range interactions [140]), we bring the two sites next to each other and disentangle them with a two-site disentangler as described above for the real-time evolution. Yet, we find that this approach is very limited by the fact that the purification can not be disentangled completely (except for $\beta \to \infty$), such that we fail at some point to identify the next candidate pair to be disentangled.

5.3 Benchmarks

5.3.1 Finite temperatures

To benchmark our algorithm, we study a concrete example, the generalized transverse field Ising model

$$\hat{H} = -J^x \sum_n \hat{\sigma}_n^x \hat{\sigma}_{n+1}^x - J^z \sum_n \hat{\sigma}_n^z \hat{\sigma}_{n+1}^z - h^z \sum_n \hat{\sigma}_n^z. \tag{5.11}$$

For $J^z = 0$, the model maps onto free fermions and exhibits a quantum phase transition at $h_c^z = J^x$. The term proportional to J^z introduces interactions and breaks integrability.

Figure 5.3 compares the entanglement of the optimized purification with the entanglement of the TFD state obtained by imaginary time evolution without disentangling, i.e., $\hat{U}_{\text{anc}} = \hat{\mathbb{1}}$. The infinite temperature state $|\psi_0\rangle$ has maximal entanglement between the physical and auxiliary DoF on each site, but no correlations between different sites, hence $S_{LL'} = 0$. For small β, the imaginary time evolution starts to build up correlations between neighboring sites, but it is not immediately possible to disentangle the state with a rotation in $\mathcal{H}^A$. For example, a non-trivial unitary acting on j_n^A and j_{n+1}^A would lead to a strong correlation between j_n^P and j_{n+1}^A, and thus larger entanglement for a cut between sites n and $n+1$. However, due to the monogamy of entanglement, the build-up of quantum correlations between different sites ensures the reduction of the entanglement between the physical and auxiliary spaces. Consequently, the disentangler can reduce the entanglement at larger β. This is most evident in the limit of large β in which $e^{-\frac{\beta}{2}\hat{H}}$ becomes a projector $|\text{gs}\rangle\langle\text{gs}|$ onto the ground state $|\text{gs}\rangle$. In this limit, the TFD purification ends up with two copies $|\text{gs}\rangle_P \otimes |\text{gs}\rangle_A$ of the ground state in $\mathcal{H}^P$ and $\mathcal{H}^A$. In contrast, a perfect disentangling algorithm should be able to rotate $|\text{gs}\rangle_A$ into an unentangled product state $|1\rangle_A$, ending up with the state $|\text{gs}\rangle_P \otimes |1\rangle_A$ which has only half as much entanglement as the TFD. The fact that we find a purification with an entanglement close to that of the ground state shows that our algorithm can indeed find the minimum, i.e., it finds E_p.

Notably, we also find a maximum at intermediate β (although our algorithm suffers from numerical instabilities in this region). This can be understood from the fact that the entanglement

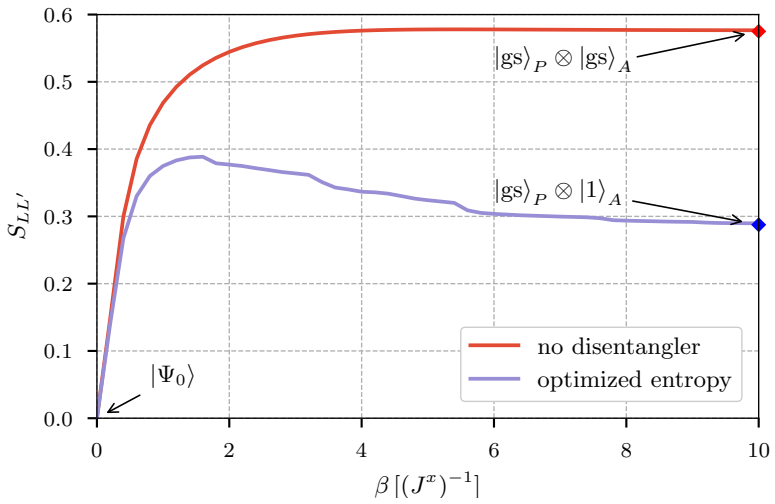

Figure 5.3 Half-chain entanglement entropy of the finite-temperature purification $|\psi_\beta\rangle \propto e^{-\frac{\beta}{2}\hat{H}}\,|\psi_0\rangle$ in the generalized Ising model (5.11) with $N = 50$ sites, for the TFD state ($\hat{U}_{\mathrm{anc}} = \hat{\mathbb{1}}$, upper line) and when disentangling up to four sites at once (lower line). The parameters $J^x = h^z = 1$ and $J^z = 0.1$ are chosen to be in the vicinity of the quantum phase transition. The diamonds on the right axis indicate the half-chain entanglement S_{gs} (blue) and $2S_{\mathrm{gs}}$ (red) of the ground state $|\mathrm{gs}\rangle$ obtained from DMRG.

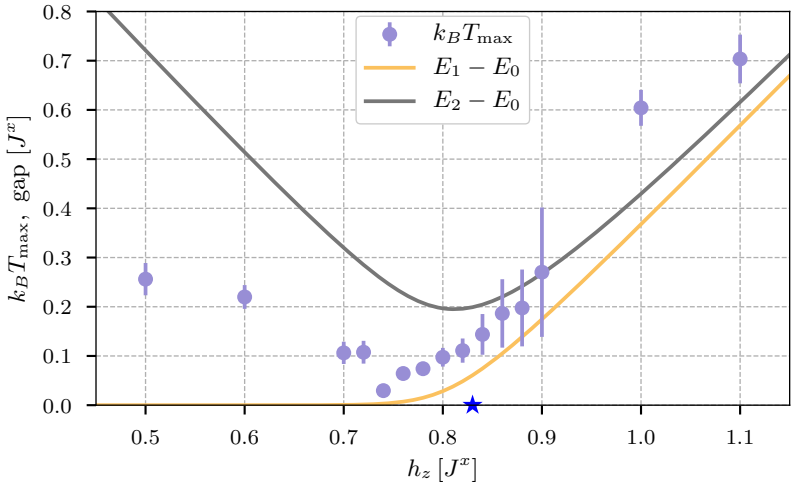

Figure 5.4 Behavior of the position of the maximum $k_B T_{\max} = (\beta_{\max})^{-1}$ in Fig. 5.3 with the parameter h^z, for $N = 50$ sites and $J^z = 0.1J^x$. Error bars indicate uncertainties in extracting $\beta_{\max}$ stemming from a limited resolution in β and numerical instabilities of the algorithm. For comparison, the energy gaps of the first and second states above the ground state (extracted with DMRG) are also shown. The critical h^z/J^x in the thermodynamic limit is indicated by the blue star on the x axis.

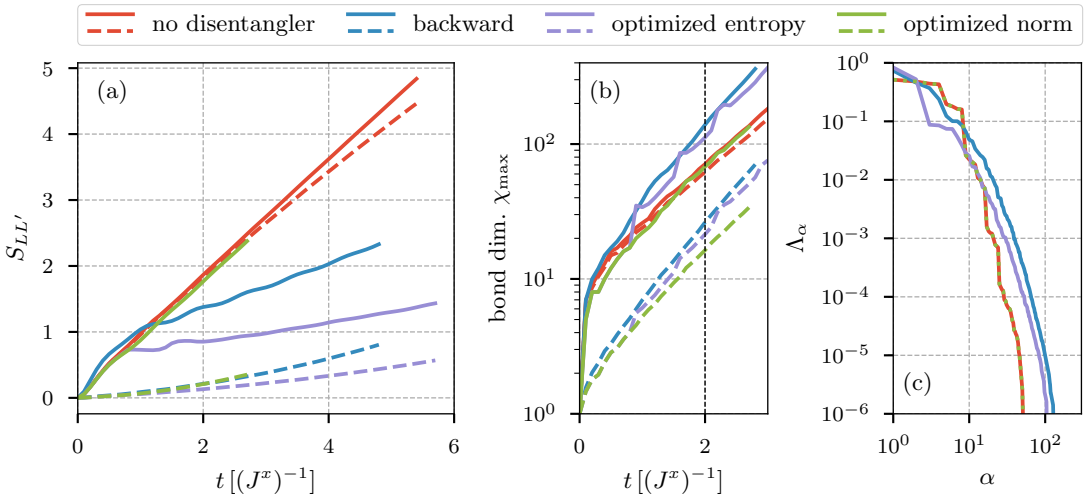

Figure 5.5 (a) Comparison of the entanglement in the purification state $|S^+_{N/2}(t,\beta=0)\rangle = e^{-it\hat{H}} S^+_{N/2}|\psi_0\rangle$ for the Ising chain (5.11) with $N = 40$ sites, $J^x = h^z = 1, J^z = 0.1$. (b) MPS bond dimension when the truncation error is kept below 10^{-6} in each step. (c) Decay of the Schmidt values s_i on the central bond at time $tJ^x = 2$. In all panels, different colors compare different disentanglers $\hat{U}_{\text{anc}}$, and solid lines (dashed lines) show the maximum (mean) over different bonds.

of purification has contributions from both quantum fluctuations and thermal fluctuations, and the latter vanish for $\beta \to \infty$. A similar maximum is also present in the holographic prescription for the entanglement of purification [296, 297]. Figure 5.4 shows that the maximum moves to larger β when tuning h^z towards the phase transition. We attribute this increase of $\beta_{\max}$ to the closing energy gap which induces thermal fluctuations at smaller temperatures (and thus additional entanglement entropy in the purified state on top of the ground-state entropy reached in the limit $\beta \to \infty$). In the symmetry-broken phase for $h^z \lesssim 0.75$, the ground state is (for the finite system almost) two-fold degenerate, and $S_{LL'}(\beta \to \infty)$ is increased by log(2) on top of the ground-state entanglement entropy. We still observe a maximum of $S_{LL'}$ at finite β in this phase, yet less pronounced than in the paramagnetic phase.

5.3.2 Real time evolution at infinite temperature

Next, we consider the time evolution of a local operator applied to the infinite-temperature purification $|S^+_{N/2}(t,\beta=0)\rangle = e^{-it\hat{H}} \hat{S}^+_{N/2}|\psi_0\rangle$, where $\hat{S}^+_n = \hat{S}^x_n + i\hat{S}^y_n$. Figure 5.5(a) compares the resulting entanglement for no disentangling ($\hat{U}_{\text{anc}} = \hat{\mathbb{1}}$), backward time evolution ($\hat{U}_{\text{anc}} = e^{it\hat{H}}$), and the optimized disentangler ($\hat{U}_{\text{anc}} = \hat{U}_{\text{disent}}$) using the two-site disentanglers described in Sec. 5.2.1 and Sec. 5.2.2. Note that for $\beta = 0$ backward time evolution is equivalent to the Heisenberg evolution of $S^+_{N/2}$. The maximum of the entropy over different bonds (solid lines) grows roughly linear in all three cases, yet with very different prefactors. While the growth is spatially almost uniform in the case $\hat{U}_{\text{anc}} = \hat{\mathbb{1}}$, both the backward time evolution and our optimized algorithm develop entropy only within a causal "light-cone," which leads to a significant reduction when the mean over different bonds is taken (dashed lines). Figure 5.5(b) compares the growth of the required MPS bond dimension when the truncation error is kept fixed. Both backward time evolution and the optimized disentangler minimizing the entropy require a slightly higher maximal bond dimension close to where $\hat{S}^+_{N/2}$ was applied. This apparent contradiction of a larger bond dimension despite a lower entropy can be understood from the fact

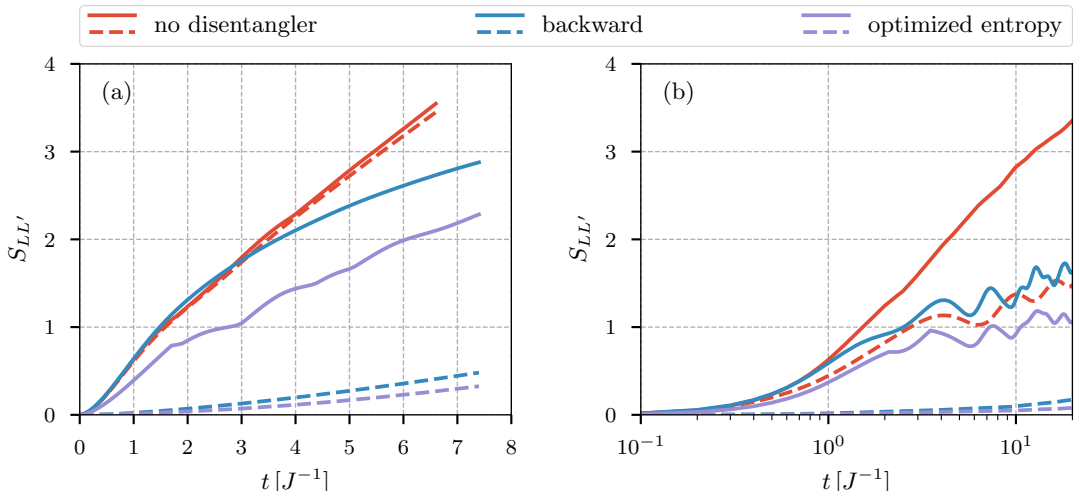

Figure 5.6 Comparison of the entanglement in the purification state $|S^+_{N/2}(t, \beta = 0)\rangle = e^{-it\hat{H}} S^+_{N/2} |\psi_0\rangle$ for the Heisenberg chain (5.12) with $N = 80$ sites without disorder ($W = 0$) (a) and for a single disorder realization with $W = 5J$ (b). In both panels, different colors compare different disentanglers $\hat{U}_{\text{anc}}$, and solid lines (dashed lines) show the maximum (mean) over different bonds,

that the entropy has large weight on the largest Schmidt values, but the required bond dimension is determined by the decay of Schmidt values in the tail. Indeed, we show in Fig. 5.5(c) that the optimization of the entropy leads to a reduction in the first few Schmidt values accompanied by a slightly longer tail of small Schmidt values compared to $\hat{U}_{\text{anc}} = \hat{\mathbb{1}}$. Nevertheless, the tail decays faster than with backward time evolution. In contrast, when the two-site disentangler described in Sec. 5.2.2 is used, we can indeed slightly reduce the required maximal bond dimension as a proof of principle, even though in practice performing the optimization itself is computationally more expensive than the speed-up gained by the reduced bond dimension. In this case, the disentangler acts almost trivially in the region where $S^+_{N/2}$ was applied, such that a larger tail of the singular values is avoided. While this optimization reduced the bond dimension during the real-time evolution, in the case of imaginary-time evolution we were not able to reduce the bond dimension with the same method.

As a second example, we consider the $S = 1/2$ Heisenberg chain with disordered z-directed field,

$$\hat{H} = J \sum_n \hat{\vec{S}}_n \cdot \hat{\vec{S}}_{n+1} - \sum_n h^z_n \hat{S}^z_n, \tag{5.12}$$

where h^z_n is chosen uniformly in the interval $[-W, W]$. This model has been established as a standard model in the study of MBL [22, 23, 27] in one dimension. Numerically, a localization transition was found to occur at $W_c \approx 3.5J$ [24, 33]. Figure 5.6(a) again compares the entanglement growth of $|S^+_{N/2}(t, \beta = 0)\rangle$ for the three choices of $\hat{U}_{\text{anc}}$ in the clean Heisenberg chain, $W = 0$. While the entropy grows linearly when no disentangler is used, the integrability of the Heisenberg chain and the presence of S^z conservation restricts the entanglement of time-evolved local operators in the Heisenberg picture (here the "backward" evolution) to $S(t) \propto \log(t)$ [298]. Our results are compatible with the same $S(t) \propto \log(t)$ scaling when optimized, again with a smaller prefactor. In the MBL phase [Fig. 5.6(b)], even $\hat{U}_{\text{anc}} = \hat{\mathbb{1}}$ displays only a logarithmic entanglement growth, which is a characteristic feature of the MBL phase [28–30, 299].

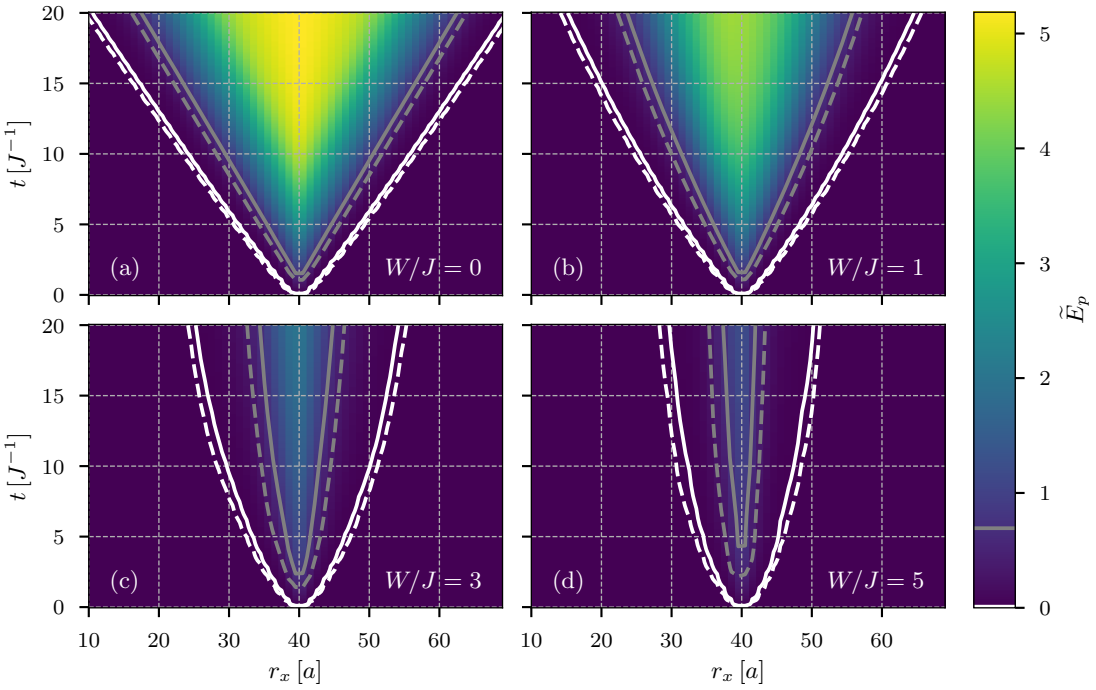

Figure 5.7 Optimized entanglement entropy $\widetilde{E}_p$ in the state $e^{-\mathrm{i}t\hat{H}}\hat{S}^+_{N/2}\,|\psi_0\rangle$ for the Heisenberg model (5.12) with disorder strength (a) $W = 0$, (b) $W = J$, (c) $W = 3J$, and (d) $W = 5J$, each averaged over 30 disorder realizations. The white and gray solid lines show the contour for the onset of finite values at a threshold of 0.01 and log(2). The dashed lines shows contours for the same threshold when backward time evolution is used.

Next, we focus on the spatial spread of the entanglement in $\hat{S}^{+}_{N/2}|\psi_0\rangle$ when using the optimized disentangler, tracking $S_{LL'}$ as a function of time t, and bipartition bond x, shown in Fig. 5.7. In the thermalizing regime, at small W [Figs. 5.7(a) and (b)], we observe the expected linear light-cone spreading [300]. Deep in the MBL phase [Fig. 5.7(d)] we find a qualitatively different spreading which is compatible with a logarithmic light cone. This is as expected from a generalized Lieb-Robinson bound $\mathbb{E}\|[\hat{A}_{r_x}(t), \hat{B}_{r'_x}]\| \leq c\, t e^{\frac{|r_x - r'_x|}{2\xi}}$, where ξ is the localization length and $c > 0$ some constant [301, 302]. At intermediate disorder, near the MBL transition, we observe a sub-linear spreading of the entanglement. Although there are extended eigenstates in this region, the system is expected to be subdiffusive and exhibits only slow transport on very long time scales (inaccessible to our numerical simulations) [35, 38, 247, 266, 303, 304]. Since the backward time evolution already reduces $S_{LL'}$ to a zero (up to exponentially small corrections) outside of the light cone, it is not surprising that the contours of the onset are nearly unchanged compared to our optimized case.

5.4 Conclusion

In this chapter, we introduced an MPS-based method to find a unitary $\hat{U}_{\text{anc}}$ acting on the ancilla DoFs of a purification state, which reduces the entanglement both in equilibrium and during real-time evolution, at a similar cost to the TEBD algorithm. At low temperatures, the optimized entanglement entropy $\widetilde{E}_p$ is half as large as in the TFD state, providing evidence that the algorithm actually finds the entanglement of purification E_p. We find a maximum of $\widetilde{E}_p$ at intermediate β, the location of which diverges to $\beta_{\max} \to \infty$ as the gap closes. During real-time evolution, the entanglement is significantly reduced both compared to $\hat{U}_{\text{anc}} = \hat{\mathbb{1}}$ and backward time evolution. In the clean Heisenberg chain, $\widetilde{E}_p$ shows a linear light-cone structure, which turns to a logarithmic spreading in the MBL phase (at large disorder). The minimization of the entanglement is, however, not directly accompanied by a reduction of the required bond dimensions, as it leads to a larger tail of small Schmidt values. This limitation might be overcome by another choice of local disentanglers.

6 Conclusion

The non-equilibrium physics of quantum many-body systems is an exciting research area with many interesting aspects. For example, the MBL phase challenges the whole framework of thermal equilibrium in closed quantum systems. Analytical calculations are often intractable due to the necessity to consider a time evolution in a large Hilbert space. Large-scale numerical simulations with tensor network techniques can aid us to explore new phenomena and gain a better understanding of quantum many-body systems far out of equilibrium.

In this thesis, we focused on quenches, which are of relevance in experiments with ultra-cold atoms in optical lattices. Motivated by recent experiments, we studied the 1D-to-2D crossover in the sudden expansion of a cloud of strongly interacting bosons. We then analyzed the domain-wall melting of fermions in the presence of disorder inducing a transition to an MBL phase. Finally, we developed of a new method to find purifications with minimal entanglement.

Before we focused on physical systems, we gave a pedagogical introduction to efficient simulations with tensor networks, in particular MPS. We explained the TEBD and DMRG algorithms in finite and infinite systems, provided a practical guide how abelian symmetries can be used to make the simulations more efficient, and discussed how one can find MPO representations for general models, in particular also when mapping a 2D system to 1D. Moreover, we presented a flexible program library called TeNPy.

We then turned to the sudden expansion of a cloud of strongly interacting bosons. We simulated the expansion of up to 4×4 hard-core bosons on a square lattice. We found a bunching in the momentum distribution function at quasimomenta compatible with energy conservation. This could signal a dynamical condensation at finite quasimomenta. However, we cannot ultimately clarify this, since it could also stem from surface effects and our simulations in the fully 2D lattice are limited to short times due to the fast buildup of entanglement. We studied the 1D-to-2D crossover further by considering long cylinders and ladders. We identified different time regimes: the expansion of a block is equivalent to a domain-wall melting, until the first holes in reach the center of the block at a time t_2 proportional to the block width. Moreover, there is an initial regime where the expansion in x-direction is independent of the hopping strength J_y in y-direction. On the two-leg ladder, the melting of domain-walls becomes weakly time-dependent and almost stationary, reflected in vanishing core velocities similar as in the experiments in 2D [178, 180]. Yet, we found significantly faster expansions for cylinders and ladders with $L_y = 3, 4$. We explained this observation by an analysis of possible propagation modes in terms of the eigenstates on a single ring of a cylinder or rung of a ladder. In agreement with this, we found bunching at preferred momenta $k_y = \pm\frac{\pi}{2a}$ and $k_y = \pm\frac{\pi}{2a}$.

Motivated by another experiment with ultracold atoms [45], we studied the effects of disorder on the expansion of fermions from a domain-wall initial state. We first summarized the phenomenology of MBL. Then, we analyzed noninteracting fermions and showed that the single-particle localization length can be extracted from the density profile at long times, and that the localization-delocalization transition in the Aubry-André model can be identified from the time-dependence of several quantities accessible to the experiment, such as the number of propagating particles. In the interacting case, the transition between the ergodic and the MBL phase can be located in a similar way. Hence, our work justifies the setup of the experiment

in Ref. [45]. The density profile still shows exponential tails, which allows to give a straightforward definition of a localization length in the MBL phase. However, care must be taken since the dynamics on the ergodic side of the transition becomes very slow.

Finally, we presented the development of a new, numerical method, which allows to find purifications with minimal entanglement. The main idea is to find a disentangling unitary acting on the ancilla DoFs of the purification state. At intermediate temperatures, we find a maximum in the optimized entanglement entropy $\widetilde{E}_p$, which diverges to $\beta_{\max} \to \infty$ as the gap closes. In the presence of a gap, $\widetilde{E}_p$ is half as large as the entanglement entropy of the TFD state at low temperatures, as expected for the entanglement of purification E_p. During a real-time evolution, we were able to significantly reduce the entanglement both compared to $\hat{U}_{\text{anc}} = \hat{\mathbb{1}}$ and backward time evolution. In the clean Heisenberg chain, $\widetilde{E}_p$ shows the expected linear light-cone structure after a local quench, which turns to a logarithmic spreading in the MBL phase at large disorder strength. The ability to obtain a well-defined entanglement entropy of an *infinite* temperature ensemble provides a new perspective on the MBL phase from a quantum information theory viewpoint.

Altogether, the results of this thesis demonstrate once more that numerical simulations based on tensor networks are a powerful and essential tool for the study of quantum many-body systems. Despite the challenge in the dynamical growth of entanglement, one can extract many quantities of physical interest from such simulations. The direct solution of the Schrödinger equation allows to perform clean "numerical experiments" on a computer, which often allow for a direct comparison with "analog quantum simulations" of ultracold atoms in optical lattices. The presented TeNPy program library simplifies the setup of simulations based on tensor networks, and we hope that it will find use in many future studies.

Simulations of 2D non-equilibrium quantum dynamics have the potential to uncover new, exciting physics. For the sudden expansion of hard-core bosons, we had to leave the question of a dynamical condensation at finite momenta open. The MBL phase challenges the established framework of statistical mechanics and calls for a deeper understanding of thermalization in closed quantum systems. In particular the existence of MBL in higher dimensions and the nature of the phase transition are still under debate. Our method for finding purifications with minimal entanglement did not lead to a reduction in the required MPS bond dimensions, hence we were not able to simulate significantly longer times with our method. However, this could potentially be overcome by another choice of local disentanglers.

Acknowledgments

First of all, I would like to thank Frank Pollmann — for the opportunity to do my doctoral studies under your supervision and for your continuous support over the past five years. Thank you for guiding my research with a lot of interesting projects, for enlightening discussions, and for helpful advice in all situations. I have learned a lot from you and cannot thank you enough for everything. It was a great experience to join your group back in Dresden and take part in the establishment of a new group in Garching, I enjoyed it all along.

I also want to thank Michael Knap, for agreeing to co-examine my thesis as well as for many interesting conversations – be it over lunch or during the hikes with the whole group, which Frank and you initiated. It's awesome to have group leaders like you both!

The work presented in this thesis would not have been possible without fruitful discussions and collaborations with many more researchers, for which I am very grateful. Notably, I want to thank Fabian Heidrich-Meisner, who taught me proper research during my bachelor and master studies, brought me in touch with Frank, and kept collaborating with me even after I left Munich. For the project on purifications, I acknowledge my coauthors Eyal Leviatan, Jens H. Bardarson, Ehud Altman and Michael P. Zaletel. I am especially grateful to the latter for his hospitality during my visit to Berkeley and the offer to join his group in the future, to which I am very much looking forward! Moreover, I thank Anushia Chandran for hosting me during my fascinating visit of the Perimeter Institute for Theoretical Physics.

Although the TeNPy library was rewritten from scratch, it builds on an earlier version developed mainly by Frank Pollmann, Michael P. Zaletel and Roger Mong, and I am thankful that they provided it to me – it really helped to get started. I hope that the current version can be as useful to many others, and I am glad that TeNPy found already so many users, who gave overwhelmingly positive and encouraging feedback. Some of the users started contributing on their own, which requires special acknowledgment. Here, I want to name Leon Schoonderwoerd, Kévin Héméry, Maximilian Schulz, Jakob Unfried. and thank them and all the other contributors; be assured that your work is appreciated. Bart Andrews invited me to Zurich for a presentation of TeNPy and organized a very pleasent trip, which I enjoyed a lot.

I would like to extend my gratitude to all group members and colleagues both at the Max-Planck Institute for the Physics of Complex systems and the Technical University of Munich. Thank you, Jan, Thalía, Omar, Matthias, Johannes, Maxi, Younes, and many more, for making me feel welcome in Dresden. Our late-night beach volleyball sessions are legendary! Tibor and Ruben, it was very nice to have you as colleagues and friends at both places! David, Julian, Kevin, Pablo, Elisabeth, Ananda and all you others, thank you for making the daily routine in Garching much more pleasant!

I also want to thank our secretaries, especially Claudine Voelcker: You made me enjoy administrative issues, thank you for shielding paperwork from me as far as possible! Further, I appreciate the help of our IT admins, most notably Hubert Scherrer-Paulus at MPIPKS and Stefan Recksiegel at TUM; thank you for setting up and maintaining the clusters. Special thanks also go to the organizers and speakers of our journal club, blackboard- and group seminars; I've learned a lot from them.

Last but not least, I would like to thank Maike, my family, and all my friends (you know who you are). You showed me that there is much more to life than just work, and yet encouraged me to go on with it by your unquestionable confidence that I can make it. Thank you for distracting me from the world of physics, with all the games we've played, all the deep conversations we made, and all the fun we had. You're great!

List of Figures

List of Algorithms

Acronyms

1D one dimensional 4, 5, 6, 7, 8, 9, 10, 22, 34, 35, 40, 42, 43, 44, 45, 46, 47, 48, 49, 51, 53, 56, 58, 60, 62, 63, 64, 65, 66, 68, 69, 73, 75, 89, 93

2D two dimensional 3, 4, 5, 6, 22, 34, 35, 42, 43, 44, 45, 46, 47, 48, 49, 51, 52, 57, 58, 59, 58, 60, 63, 64, 65, 72, 73, 89, 90, 93

AKLT Affleck, Kennedy, Lieb, and Tasaki 11, 12, 22

DMRG density matrix renormalization group 4, 5, 7, 15, 18, 19, 20, 22, 25, 26, 30, 31, 40, 41, 42, 44, 66, 75, 77, 78, 81, 82, 89

DoF degree of freedom 75, 77, 81, 82, 87, 90

ED exact diagonalization 4, 5, 66, 67

ETH eigenstate thermalization hypothesis 3, 66

GOE Gaussian orthogonal ensemble 66

iDMRG infinite density matrix renormalization group 25, 26, 41, 42, 93, 95

iMPS infinite matrix product state 22, 24, 25

iTEBD infinite time evolving block decimation 24, 25

MBL many body localization 3, 4, 5, 6, 65, 66, 67, 70, 71, 73, 85, 87, 89, 90, 93

MERA multi-scale entanglement renormalization ansatz 79, 80

METTS minimally entangled typical thermal states 75, 78

MPO matrix product operator 5, 7, 18, 19, 20, 19, 25, 28, 31, 33, 34, 35, 38, 40, 48, 75, 77, 78, 80, 89, 95

MPS matrix product state 4, 5, 6, 7, 10, 11, 12, 11, 12, 13, 14, 15, 16, 17, 18, 19, 20, 19, 22, 24, 25, 26, 27, 28, 34, 35, 38, 40, 42, 44, 48, 52, 66, 75, 77, 78, 79, 84, 87, 89, 90, 93, 95

OBC open boundary conditions 46

PBC periodic boundary conditions 46

PEPS projected entangled pair states 7, 34, 42, 75, 93

SVD singular value decomposition 5, 17, 19, 20, 26, 29, 30, 80, 81

TEBD time evolving block decimation 5, 7, 15, 17, 19, 20, 24, 26, 40, 41, 42, 48, 78, 79, 82, 87, 89, 93, 95

TeNPy Tensor Network Python 5, 7, 31, 36, 38, 40, 41, 42, 89, 90, 91, 93

TFD thermofield double 75, 77, 78, 82, 87, 90, 94

Bibliography

Refs. [1–5] can be found in the List of Publications.

[6] J. G. Bednorz and K. A. Müller. "Possible high T_c superconductivity in the Ba-La-Cu-O system." *Zeitschrift für Phys. B Condens. Matter* **64**, p. 189, 1986. doi:10.1007/BF01303701.

[7] P. W. Anderson. "The resonating valence bond state in La2CuO4 and superconductivity." *Science* **235**, p. 1196, 1987. doi:10.1126/science.235.4793.1196.

[8] P. Anderson. "Resonating valence bonds: A new kind of insulator?" *Mater. Res. Bull.* **8**, p. 153, 1973. doi:10.1016/0025-5408(73)90167-0.

[9] M. P. Shores, E. A. Nytko, B. M. Bartlett, and D. G. Nocera. "A Structurally Perfect $S = 1/2$ Kagomé Antiferromagnet." *J. Am. Chem. Soc.* **127**, p. 13462, 2005. doi:10.1021/ja053891p.

[10] M. R. Norman. "Colloquium : Herbertsmithite and the search for the quantum spin liquid." *Rev. Mod. Phys.* **88**, p. 041002, 2016. doi:10.1103/RevModPhys.88.041002.

[11] X.-G. Wen. "Quantum orders and symmetric spin liquids." *Phys. Rev. B* **65**, p. 165113, 2002. doi:10.1103/PhysRevB.65.165113. arXiv:cond-mat/0107071.

[12] L. Balents. "Spin liquids in frustrated magnets." *Nature* **464**, p. 199, 2010. doi:10.1038/nature08917.

[13] F. D. M. Haldane. "Continuum dynamics of the 1-D Heisenberg antiferromagnet: Identification with the O(3) nonlinear sigma model." *Phys. Lett. A* **93**, p. 464, 1983. doi:10.1016/0375-9601(83)90631-X.

[14] F. D. M. Haldane. "Nonlinear Field Theory of Large-Spin Heisenberg Antiferromagnets: Semiclassically Quantized Solitons of the One-Dimensional Easy-Axis Néel State." *Phys. Rev. Lett.* **50**, p. 1153, 1983. doi:10.1103/PhysRevLett.50.1153.

[15] D. C. Tsui, H. L. Stormer, and A. C. Gossard. "Two-dimensional magnetotransport in the extreme quantum limit." *Phys. Rev. Lett.* **48**, p. 1559, 1982. doi:10.1103/PhysRevLett.48.1559. arXiv:1011.1669.

[16] R. B. Laughlin. "Anomalous quantum Hall effect: An incompressible quantum fluid with fractionally charged excitations." *Phys. Rev. Lett.* **50**, p. 1395, 1983. doi:10.1103/PhysRevLett.50.1395. arXiv:1111.4781.

[17] J. M. Deutsch. "Quantum statistical mechanics in a closed system." *Phys. Rev. A* **43**, p. 2046, 1991. doi:10.1103/PhysRevA.43.2046.

[18] M. Srednicki. "Chaos and quantum thermalization." *Phys. Rev. E* **50**, p. 888, 1994. doi:10.1103/PhysRevE.50.888. arXiv:cond-mat/9403051.

[19] M. Rigol, V. Dunjko, and M. Olshanii. "Thermalization and its mechanism for generic isolated quantum systems." *Nature* **452**, p. 854, 2008. doi:10.1038/nature06838. arXiv:0708.1324.

[20] J. M. Deutsch. "Eigenstate thermalization hypothesis." *Reports Prog. Phys.* **81**, p. 082001, 2018. doi:10.1088/1361-6633/aac9f1. arXiv:1805.01616.

[21] H. Bethe. "Zur Theorie der Metalle." *Zeitschrift für Phys.* **71**, p. 205, 1931. doi:10.1007/BF01341708.

[22] D. M. Basko, I. L. Aleiner, and B. L. Altshuler. "Metal-insulator transition in a weakly interacting many-electron system with localized single-particle states." *Ann. Phys. (N.Y.)* **321**, p. 1126, 2006. doi:10.1016/j.aop.2005.11.014. arXiv:cond-mat/0506617.

[23] I. V. Gornyi, A. D. Mirlin, and D. G. Polyakov. "Interacting electrons in disordered wires: Anderson localization and low-T transport." *Phys. Rev. Lett.* **95**, p. 206603, 2005. doi:10.1103/PhysRevLett.95.206603. arXiv:cond-mat/0506411.

[24] A. Pal and D. A. Huse. "Many-body localization phase transition." *Phys. Rev. B* **82**, p. 174411, 2010. doi:10.1103/PhysRevB.82.174411. arXiv:1010.1992.

[25] R. Nandkishore and D. A. Huse. "Many-Body Localization and Thermalization in Quantum Statistical Mechanics." *Annu. Rev. Condens. Matter Phys.* **6**, p. 15, 2015. doi:10.1146/annurev-conmatphys-031214-014726. arXiv:1404.0686.

[26] E. Altman and R. Vosk. "Universal Dynamics and Renormalization in Many-Body-Localized Systems." *Annu. Rev. Condens. Matter Phys.* **6**, p. 383, 2015. doi:10.1146/annurev-conmatphys-031214-014701. arXiv:1408.2834.

[27] D. A. Abanin and Z. Papić. "Recent progress in many-body localization." *Ann. Phys. (Berl.)* **529**, p. 1700169, 2017. doi:10.1002/andp.201700169. arXiv:1705.09103.

[28] J. H. Bardarson, F. Pollmann, and J. E. Moore. "Unbounded Growth of Entanglement in Models of Many-Body Localization." *Phys. Rev. Lett.* **109**, p. 017202, 2012. doi:10.1103/PhysRevLett.109.017202. arXiv:1202.5532.

[29] M. Žnidarič, T. Prosen, and P. Prelovšek. "Many-body localization in the Heisenberg XXZ magnet in a random field." *Phys. Rev. B* **77**, p. 064426, 2008. doi:10.1103/PhysRevB.77.064426. arXiv:0706.2539.

[30] M. Serbyn, Z. Papić, and D. A. Abanin. "Universal Slow Growth of Entanglement in Interacting Strongly Disordered Systems." *Phys. Rev. Lett.* **110**, p. 260601, 2013. doi:10.1103/PhysRevLett.110.260601. arXiv:1304.4605.

[31] B. Bauer and C. Nayak. "Area laws in a many-body localized state and its implications for topological order." *J. Stat. Mech. Theory Exp.* **2013**, p. P09005, 2013. doi:10.1088/1742-5468/2013/09/P09005. arXiv:1306.5753.

[32] J. A. Kjäll, J. H. Bardarson, and F. Pollmann. "Many-body localization in a disordered quantum ising chain." *Phys. Rev. Lett.* **113**, p. 107204, 2014. doi:10.1103/PhysRevLett.113.107204. arXiv:1403.1568.

[33] D. J. Luitz, N. Laflorencie, and F. Alet. "Many-body localization edge in the random-field Heisenberg chain." *Phys. Rev. B* **91**, p. 081103, 2015. doi:10.1103/PhysRevB.91.081103. arXiv:1411.0660.

[34] W. De Roeck, F. Huveneers, M. Müller, and M. Schiulaz. "Absence of many-body mobility edges." *Phys. Rev. B* **93**, p. 014203, 2016. doi:10.1103/PhysRevB.93.014203. arXiv:1506.01505.

[35] A. Chandran, A. Pal, C. R. Laumann, and A. Scardicchio. "Many-body localization beyond eigenstates in all dimensions." *Phys. Rev. B* **94**, p. 144203, 2016. doi:10.1103/PhysRevB.94.144203. arXiv:1605.00655.

[36] W. De Roeck and F. Huveneers. "Stability and instability towards delocalization in many-body localization systems." *Phys. Rev. B* **95**, p. 155129, 2017. doi:10.1103/PhysRevB.95.155129. arXiv:1608.01815.

[37] A. C. Potter, R. Vasseur, and S. A. Parameswaran. "Universal Properties of Many-Body Delocalization Transitions." *Phys. Rev. X* **5**, p. 031033, 2015. doi:10.1103/PhysRevX.5.031033. arXiv:1501.03501.

[38] D. J. Luitz, N. Laflorencie, and F. Alet. "Extended slow dynamical regime close to the many-body localization transition." *Phys. Rev. B* **93**, p. 060201, 2016. doi:10.1103/PhysRevB.93.060201. arXiv:1511.05141.

[39] M. Serbyn, Z. Papić, and D. A. Abanin. "Thouless energy and multifractality across the many-body localization transition." *Phys. Rev. B* **96**, p. 104201, 2017. doi:10.1103/PhysRevB.96.104201. arXiv:1610.02389.

[40] A. Goremykina, R. Vasseur, and M. Serbyn. "Analytically Solvable Renormalization Group for the Many-Body Localization Transition." *Phys. Rev. Lett.* **122**, p. 040601, 2019. doi:10.1103/PhysRevLett.122.040601. arXiv:1807.04285.

[41] P. T. Dumitrescu, A. Goremykina, S. A. Parameswaran, M. Serbyn, and R. Vasseur. "Kosterlitz-Thouless scaling at many-body localization phase transitions." *Phys. Rev. B* **99**, p. 094205, 2019. doi:10.1103/PhysRevB.99.094205. arXiv:1811.03103.

[42] S. Roy, J. T. Chalker, and D. E. Logan. "Percolation in Fock space as a proxy for many-body localization." *Phys. Rev. B* **99**, p. 104206, 2019. doi:10.1103/PhysRevB.99.104206. arXiv:1812.06101.

[43] M. Schreiber, S. S. Hodgman, P. Bordia, H. P. Luschen, M. H. Fischer, R. Vosk, E. Altman, U. Schneider, and I. Bloch. "Observation of many-body localization of interacting fermions in a quasirandom optical lattice." *Science* **349**, p. 842, 2015. doi:10.1126/science.aaa7432. arXiv:1407.4127.

[44] P. Bordia, H. P. Lüschen, S. S. Hodgman, M. Schreiber, I. Bloch, and U. Schneider. "Coupling Identical one-dimensional Many-Body Localized Systems." *Phys. Rev. Lett.* **116**, p. 140401, 2016. doi:10.1103/PhysRevLett.116.140401. arXiv:1509.00478.

[45] J.-y. Choi, S. Hild, J. Zeiher, P. Schauss, A. Rubio-Abadal, T. Yefsah, V. Khemani, D. A. Huse, I. Bloch, and C. Gross. "Exploring the many-body localization transition in two dimensions." *Science* **352**, p. 1547, 2016. doi:10.1126/science.aaf8834. arXiv:1604.04178.

[46] V. Khemani, F. Pollmann, and S. L. Sondhi. "Obtaining Highly Excited Eigenstates of Many-Body Localized Hamiltonians by the Density Matrix Renormalization Group Approach." *Phys. Rev. Lett.* **116**, p. 247204, 2016. doi:10.1103/PhysRevLett.116.247204. arXiv:1509.00483.

[47] D. V. Else, B. Bauer, and C. Nayak. "Floquet Time Crystals." *Phys. Rev. Lett.* **117**, p. 090402, 2016. doi:10.1103/PhysRevLett.117.090402. arXiv:1603.08001.

[48] C. W. von Keyserlingk and S. L. Sondhi. "Phase structure of one-dimensional interacting Floquet systems. I. Abelian symmetry-protected topological phases." *Phys. Rev. B* **93**, p. 245145, 2016. doi:10.1103/PhysRevB.93.245145. arXiv:1602.02157.

[49] C. W. von Keyserlingk and S. L. Sondhi. "Phase structure of one-dimensional interacting Floquet systems. II. Symmetry-broken phases." *Phys. Rev. B* **93**, p. 245146, 2016. doi:10.1103/PhysRevB.93.245146. arXiv:1602.06949.

[50] T. Oka and S. Kitamura. "Floquet Engineering of Quantum Materials." *Annu. Rev. Condens. Matter Phys.* **10**, p. 387, 2019. doi:10.1146/annurev-conmatphys-031218-013423. arXiv:1804.03212.

[51] F. Wilczek. "Quantum Time Crystals." *Phys. Rev. Lett.* **109**, p. 160401, 2012. doi:10.1103/PhysRevLett.109.160401. arXiv:1202.2539.

[52] N. Y. Yao, A. C. Potter, I.-D. Potirniche, and A. Vishwanath. "Discrete Time Crystals: Rigidity, Criticality, and Realizations." *Phys. Rev. Lett.* **118**, p. 030401, 2017. doi:10.1103/PhysRevLett.118.030401. arXiv:1608.02589.

[53] T. Langen, R. Geiger, and J. Schmiedmayer. "Ultracold atoms out of equilibrium." *Annu. Rev. Condens. Matter Phys.* **6**, p. 201, 2014. doi:10.1146/annurev-conmatphys-031214-014548. arXiv:1408.6377.

[54] C. Gogolin and J. Eisert. "Equilibration, thermalisation, and the emergence of statistical mechanics in closed quantum systems." *Reports Prog. Phys.* **79**, p. 056001, 2016. doi:10.1088/0034-4885/79/5/056001. arXiv:1503.07538.

[55] J. Eisert, M. Friesdorf, and C. Gogolin. "Quantum many-body systems out of equilibrium." *Nat. Phys.* **11**, p. 124, 2015. doi:10.1038/nphys3215. arXiv:1408.5148.

[56] I. Bloch, J. Dalibard, and W. Zwerger. "Many-body physics with ultracold gases." *Rev. Mod. Phys.* **80**, p. 885, 2008. doi:10.1103/RevModPhys.80.885. arXiv:0704.3011.

[57] J. F. Sherson, C. Weitenberg, M. Endres, M. Cheneau, I. Bloch, and S. Kuhr. "Single-atom-resolved fluorescence imaging of an atomic Mott insulator." *Nature* **467**, p. 68, 2010. doi:10.1038/nature09378. arXiv:1006.3799.

[58] T. Fukuhara, A. Kantian, M. Endres, M. Cheneau, P. Schauß, S. Hild, D. Bellem, U. Schollwöck, T. Giamarchi, C. Gross, I. Bloch, and S. Kuhr. "Quantum dynamics of a mobile spin impurity." *Nat. Phys.* **9**, p. 235, 2013. doi:10.1038/nphys2561. arXiv:1209.6468.

[59] P. M. Preiss, R. Ma, M. E. Tai, A. Lukin, M. Rispoli, P. Zupancic, Y. Lahini, R. Islam, and M. Greiner. "Strongly correlated quantum walks in optical lattices." *Science* **347**, p. 1229, 2015. doi:10.1126/science.1260364. arXiv:1409.3100.

[60] R. Feynman. "There's Plenty of Room at the Bottom." *Caltech Eng. Sci.* **23**, p. 5, 1959.

[61] R. P. Feynman. "Simulating physics with computers." *Int. J. Theor. Phys.* **21**, p. 467, 1982. doi:10.1007/BF02650179.

[62] L. M. K. Vandersypen, M. Steffen, G. Breyta, C. S. Yannoni, M. H. Sherwood, and I. L. Chuang. "Experimental realization of Shor's quantum factoring algorithm using nuclear magnetic resonance." *Nature* **414**, p. 883, 2001. doi:10.1038/414883a. arXiv:quant-ph/0112176.

[63] M. W. Johnson, M. H. S. Amin, S. Gildert, T. Lanting, F. Hamze, N. Dickson, R. Harris, A. J. Berkley, J. Johansson, P. Bunyk, E. M. Chapple, C. Enderud, J. P. Hilton, K. Karimi, E. Ladizinsky, N. Ladizinsky, T. Oh, I. Perminov, C. Rich, M. C. Thom, E. Tolkacheva, C. J. S. Truncik, S. Uchaikin, J. Wang, B. Wilson, and G. Rose. "Quantum annealing with manufactured spins." *Nature* **473**, p. 194, 2011. doi:10.1038/nature10012.

[64] G. Wendin. "Quantum information processing with superconducting circuits: a review." *Reports Prog. Phys.* **80**, p. 106001, 2017. doi:10.1088/1361-6633/aa7e1a. arXiv:1610.02208.

[65] A. Smith, M. S. Kim, F. Pollmann, and J. Knolle. "Simulating quantum many-body dynamics on a current digital quantum computer." 2019. arXiv:1906.06343.

[66] A. M. Läuchli, J. Sudan, and R. Moessner. "The $S = 1/2$ Kagome Heisenberg Antiferromagnet Revisited." 2016. arXiv:1611.06990.

[67] M. Troyer and U.-J. Wiese. "Computational Complexity and Fundamental Limitations to Fermionic Quantum Monte Carlo Simulations." *Phys. Rev. Lett.* **94**, p. 170201, 2005. doi:10.1103/PhysRevLett.94.170201. arXiv:cond-mat/0408370.

[68] S. R. White. "Density matrix formulation for quantum renormalization groups." *Phys. Rev. Lett.* **69**, p. 2863, 1992. doi:10.1103/PhysRevLett.69.2863.

[69] S. R. White. "Density-matrix algorithms for quantum renormalization groups." *Phys. Rev. B* **48**, p. 10345, 1993. doi:10.1103/PhysRevB.48.10345.

[70] M. Fannes, B. Nachtergaele, and R. F. Werner. "Finitely correlated states on quantum spin chains." *Commun. Math. Phys.* **144**, p. 443, 1992. doi:10.1007/BF02099178.

[71] S. Stlund and S. Rommer. "Thermodynamic limit of density matrix renormalization." *Phys. Rev. Lett.* **75**, p. 3537, 1995. doi:10.1103/PhysRevLett.75.3537.

[72] J. Dukelsky, M. A. Martín-Delgado, T. Nishino, and G. Sierra. "Equivalence of the variational matrix product method and the density matrix renormalization group applied to spin chains." *Europhys. Lett.* **43**, p. 457, 1998. doi:10.1209/epl/i1998-00381-x.

[73] U. Schollwöck. "The density-matrix renormalization group in the age of matrix product states." *Ann. Phys. (N.Y.)* **326**, p. 96, 2011. doi:10.1016/j.aop.2010.09.012. arXiv:1008.3477.

[74] M. B. Hastings. "Solving gapped Hamiltonians locally." *Phys. Rev. B* **73**, p. 085115, 2006. doi:10.1103/PhysRevB.73.085115. arXiv:cond-mat/0508554.

[75] M. B. Hastings. "An Area Law for One Dimensional Quantum Systems." *J. Stat. Mech. Theory Exp.* **2007**, p. P08024, 2007. doi:10.1088/1742-5468/2007/08/P08024. arXiv:0705.2024.

[76] G. Vidal. "Efficient simulation of one-dimensional quantum many-body systems." *Phys. Rev. Lett.* **93**, p. 040502, 2003. doi:10.1103/PhysRevLett.93.040502. arXiv:quant-ph/0310089.

[77] I. Hen and M. Rigol. "Strongly interacting atom lasers in three-dimensional optical lattices." *Phys. Rev. Lett.* **105**, p. 180401, 2010. doi:10.1103/PhysRevLett.105.180401. arXiv:1010.5553.

[78] M. Jreissaty, J. Carrasquilla, F. A. Wolf, and M. Rigol. "Expansion of Bose-Hubbard Mott insulators in optical lattices." *Phys. Rev. A* **84**, p. 043610, 2011. doi:10.1103/PhysRevA.84.043610. arXiv:1108.1192.

[79] A. Jreissaty, J. Carrasquilla, and M. Rigol. "Self-trapping in the two-dimensional Bose-Hubbard model." *Phys. Rev. A* **88**, p. 031606, 2013. doi:10.1103/PhysRevA.88.031606. arXiv:1307.0821.

[80] M. Rigol and A. Muramatsu. "Emergence of Quasicondensates of Hard-Core Bosons at Finite Momentum." *Phys. Rev. Lett.* **93**, p. 230404, 2004. doi:10.1103/PhysRevLett.93.230404. arXiv:cond-mat/0403387.

[81] M. Rigol and A. Muramatsu. "Free expansion of impenetrable bosons on one-dimensional optical lattices." *Mod. Phys. Lett. B* **19**, p. 861, 2005. doi:10.1142/S0217984905008876. arXiv:cond-mat/0507351.

[82] J. Lancaster and A. Mitra. "Quantum quenches in an XXZ spin chain from a spatially inhomogeneous initial state." *Phys. Rev. E* **81**, p. 61134, 2010. doi:10.1103/PhysRevE.81.061134. arXiv:1002.4446.

[83] A. Micheli, A. J. Daley, D. Jaksch, and P. Zoller. "Single Atom Transistor in a 1D Optical Lattice." *Phys. Rev. Lett.* **93**, p. 140408, 2004. doi:10.1103/PhysRevLett.93.140408. arXiv:quant-ph/0406020.

[84] A. J. Daley, S. R. Clark, D. Jaksch, and P. Zoller. "Numerical analysis of coherent many-body currents in a single atom transistor." *Phys. Rev. A* **72**, p. 043618, 2005. doi:10.1103/PhysRevA.72.043618. arXiv:quant-ph/0506256.

[85] K. Rodriguez, S. R. Manmana, M. Rigol, R. M. Noack, and A. Muramatsu. "Coherent matter waves emerging from Mott-insulators." *New J. Phys.* **8**, p. 169, 2006. doi:10.1088/1367-2630/8/8/169. arXiv:cond-mat/0606155.

[86] L. Vidmar, S. Langer, I. P. McCulloch, U. Schneider, U. Schollwöck, and F. Heidrich-Meisner. "Sudden expansion of Mott insulators in one dimension." *Phys. Rev. B* **88**, p. 235117, 2013. doi:10.1103/PhysRevB.88.235117. arXiv:1305.5496.

[87] L. Vidmar, J. P. Ronzheimer, M. Schreiber, S. Braun, S. S. Hodgman, S. Langer, F. Heidrich-Meisner, I. Bloch, and U. Schneider. "Dynamical Quasicondensation of Hard-Core Bosons at Finite Momenta." *Phys. Rev. Lett.* **115**, p. 175301, 2015. doi:10.1103/PhysRevLett.115.175301. arXiv:1505.05150.

[88] M. Rigol and A. Muramatsu. "Fermionization in an Expanding 1D Gas of Hard-Core Bosons." *Phys. Rev. Lett.* **94**, p. 240403, 2005. doi:10.1103/PhysRevLett.94.240403. arXiv:cond-mat/0410683.

[89] A. Minguzzi and D. M. Gangardt. "Exact Coherent States of a Harmonically Confined Tonks-Girardeau Gas." *Phys. Rev. Lett.* **94**, p. 240404, 2005. doi:10.1103/PhysRevLett.94.240404. arXiv:cond-mat/0504024.

[90] P. W. Anderson. "Absence of Diffusion in Certain Random Lattices." *Phys. Rev.* **109**, p. 1492, 1958. doi:10.1103/PhysRev.109.1492.

[91] B. Kramer and A. MacKinnon. "Localization: theory and experiment." *Reports Prog. Phys.* **56**, p. 1469, 1993. doi:10.1088/0034-4885/56/12/001.

[92] F. Evers and A. D. Mirlin. "Anderson transitions." *Rev. Mod. Phys.* **80**, p. 1355, 2008. doi:10.1103/RevModPhys.80.1355. arXiv:0707.4378.

[93] F. Verstraete, J. J. García-Ripoll, and J. I. Cirac. "Matrix Product Density Operators: Simulation of Finite-Temperature and Dissipative Systems." *Phys. Rev. Lett.* **93**, p. 207204, 2004. doi:10.1103/PhysRevLett.93.207204. arXiv:cond-mat/0406426.

[94] T. Barthel, U. Schollwöck, and S. R. White. "Spectral functions in one-dimensional quantum systems at finite temperature using the density matrix renormalization group." *Phys. Rev. B* **79**, p. 245101, 2009. doi:10.1103/PhysRevB.79.245101. arXiv:0901.2342.

[95] B. M. Terhal, M. Horodecki, D. W. Leung, and D. P. DiVincenzo. "The entanglement of purification." *J. Math. Phys.* **43**, p. 4286, 2002. doi:10.1063/1.1498001. arXiv:quant-ph/0202044.

[96] I. P. McCulloch and M. Gulácsi. "The non-Abelian density matrix renormalization group algorithm." *Europhys. Lett.* **57**, p. 852, 2002. doi:10.1209/epl/i2002-00393-0. arXiv:cond-mat/0012319.

[97] S. Singh, R. N. C. Pfeifer, and G. Vidal. "Tensor network decompositions in the presence of a global symmetry." *Phys. Rev. A* **82**, p. 050301, 2010. doi:10.1103/PhysRevA.82.050301. arXiv:0907.2994.

[98] S. Singh, R. N. C. Pfeifer, and G. Vidal. "Tensor network states and algorithms in the presence of a global U(1) symmetry." *Phys. Rev. B* **83**, p. 115125, 2011. doi:10.1103/PhysRevB.83.115125. arXiv:1008.4774.

[99] S. Singh and G. Vidal. "Tensor network states and algorithms in the presence of a global SU(2) symmetry." *Phys. Rev. B* **86**, p. 195114, 2012. doi:10.1103/PhysRevB.86.195114. arXiv:1208.3919.

[100] A. Weichselbaum. "Non-abelian symmetries in tensor networks: A quantum symmetry space approach." *Ann. Phys. (N.Y.)* **327**, p. 2972, 2012. doi:10.1016/j.aop.2012.07.009. arXiv:1202.5664.

[101] S. R. White. "Density matrix renormalization group algorithms with a single center site." *Phys. Rev. B* **72**, p. 180403, 2005. doi:10.1103/PhysRevB.72.180403. arXiv:cond-mat/0508709.

[102] C. Hubig, I. P. McCulloch, U. Schollwöck, and F. A. Wolf. "Strictly single-site DMRG algorithm with subspace expansion." *Phys. Rev. B* **91**, p. 155115, 2015. doi:10.1103/PhysRevB.91.155115. arXiv:1501.05504.

[103] J. Motruk, M. P. Zaletel, R. S. Mong, and F. Pollmann. "Density matrix renormalization group on a cylinder in mixed real and momentum space." *Phys. Rev. B* **93**, p. 155139, 2016. doi:10.1103/PhysRevB.93.155139. arXiv:1512.03318.

[104] G. Ehlers, S. R. White, and R. M. Noack. "Hybrid-space density matrix renormalization group study of the doped two-dimensional Hubbard model." *Phys. Rev. B* **95**, 2017. doi:10.1103/PhysRevB.95.125125. arXiv:1701.03690.

[105] E. M. Stoudenmire and S. R. White. "Real-space parallel density matrix renormalization group." *Phys. Rev. B* **87**, p. 155137, 2013. doi:10.1103/PhysRevB.87.155137. arXiv:1301.3494.

[106] I. P. McCulloch. "Infinite size density matrix renormalization group, revisited." 2008. arXiv:0804.2509.

[107] A. J. Daley, C. Kollath, U. Schollwöck, and G. Vidal. "Time-dependent density-matrix renormalization-group using adaptive effective Hilbert spaces." *J. Stat. Mech. Theory Exp.* **2004**, p. P04005, 2004. doi:10.1088/1742-5468/2004/04/P04005. arXiv:cond-mat/0403313.

[108] S. R. White and A. E. Feiguin. "Real time evolution using the density matrix renormalization group." *Phys. Rev. Lett.* **93**, p. 076401, 2004. doi:10.1103/PhysRevLett.93.076401. arXiv:cond-mat/0403310.

[109] M. P. Zaletel, R. S. Mong, C. Karrasch, J. E. Moore, and F. Pollmann. "Time-evolving a matrix product state with long-ranged interactions." *Phys. Rev. B* **91**, p. 165112, 2015. doi:10.1103/PhysRevB.91.165112. arXiv:1407.1832.

[110] J. Haegeman, J. I. Cirac, T. J. Osborne, I. PiÅorn, H. Verschelde, and F. Verstraete. "Time-dependent variational principle for quantum lattices." *Phys. Rev. Lett.* **107**, p. 070601, 2011. doi:10.1103/PhysRevLett.107.070601. arXiv:1103.0936.

[111] J. Haegeman, C. Lubich, I. Oseledets, B. Vandereycken, and F. Verstraete. "Unifying time evolution and optimization with matrix product states." *Phys. Rev. B* **94**, p. 165116, 2016. doi:10.1103/PhysRevB.94.165116. arXiv:1408.5056.

[112] P. Calabrese and J. Cardy. "Evolution of entanglement entropy in one-dimensional systems." *J. Stat. Mech. Theory Exp.* **2005**, p. P04010, 2005. doi:10.1088/1742-5468/2005/04/P04010. arXiv:cond-mat/0503393.

[113] Y. Nishio, N. Maeshima, A. Gendiar, and T. Nishino. "Tensor Product Variational Formulation for Quantum Systems." 2004. arXiv:cond-mat/0401115.

[114] F. Verstraete and J. I. Cirac. "Renormalization algorithms for Quantum-Many Body Systems in two and higher dimensions." 2004. arXiv:cond-mat/0407066.

[115] T. Nishino and K. Okunishi. "Corner Transfer Matrix Renormalization Group Method." *J. Phys. Soc. Japan* **65**, p. 891, 1996. doi:10.1143/JPSJ.65.891. arXiv:cond-mat/9507087.

[116] M. Levin and C. P. Nave. "Tensor renormalization group approach to two-dimensional classical lattice models." *Phys. Rev. Lett.* **99**, 2007. doi:10.1103/PhysRevLett.99.120601. arXiv:cond-mat/0611687.

[117] G. Evenbly and G. Vidal. "Tensor Network Renormalization." *Phys. Rev. Lett.* **115**, p. 180405, 2015. doi:10.1103/PhysRevLett.115.180405. arXiv:1412.0732.

[118] S. Yang, Z. C. Gu, and X. G. Wen. "Loop Optimization for Tensor Network Renormalization." *Phys. Rev. Lett.* **118**, 2017. doi:10.1103/PhysRevLett.118.110504. arXiv:1512.04938.

[119] R. Orús. "A practical introduction to tensor networks: Matrix product states and projected entangled pair states." *Ann. Phys. (N.Y.)* **349**, p. 117, 2014. doi:10.1016/j.aop.2014.06.013. arXiv:1306.2164.

[120] G. K.-L. Chan and S. Sharma. "The Density Matrix Renormalization Group in Quantum Chemistry." *Annu. Rev. Phys. Chem.* **62**, p. 465, 2011. doi:10.1146/annurev-physchem-032210-103338.

[121] U. Schollwöck. "The density-matrix renormalization group." *Rev. Mod. Phys.* **77**, p. 259, 2005. doi:10.1103/RevModPhys.77.259. arXiv:cond-mat/0409292.

[122] S. Paeckel, T. Köhler, A. Swoboda, S. R. Manmana, U. Schollwöck, and C. Hubig. "Time-evolution methods for matrix-product states." 2019. arXiv:1901.05824.

[123] P. Calabrese and J. Cardy. "Entanglement entropy and quantum field theory." *J. Stat. Mech. Theory Exp.* **2004**, p. P06002, 2004. doi:10.1088/1742-5468/2004/06/P06002. arXiv:hep-th/0405152.

[124] L. Tagliacozzo, T. R. De Oliveira, S. Iblisdir, and J. I. Latorre. "Scaling of entanglement support for matrix product states." *Phys. Rev. B* **78**, p. 024410, 2008. doi:10.1103/PhysRevB.78.024410. arXiv:0712.1976.

[125] P. Calabrese and A. Lefevre. "Entanglement spectrum in one-dimensional systems." *Phys. Rev. A* **78**, p. 032329, 2008. doi:10.1103/PhysRevA.78.032329. arXiv:0806.3059.

[126] F. Pollmann, S. Mukerjee, A. M. Turner, and J. E. Moore. "Theory of finite-entanglement scaling at one-dimensional quantum critical points." *Phys. Rev. Lett.* **102**, p. 255701, 2009. doi:10.1103/PhysRevLett.102.255701. arXiv:0812.2903.

[127] M. Levin and X. G. Wen. "Detecting topological order in a ground state wave function." *Phys. Rev. Lett.* **96**, p. 110405, 2006. doi:10.1103/PhysRevLett.96.110405. arXiv:cond-mat/0510613.

[128] A. Kitaev and J. Preskill. "Topological Entanglement Entropy." *Phys. Rev. Lett.* **96**, p. 110404, 2006. doi:10.1103/PhysRevLett.96.110404. arXiv:hep-th/0510092.

[129] F. Verstraete, V. Murg, and J. I. Cirac. "Matrix product states, projected entangled pair states, and variational renormalization group methods for quantum spin systems." *Adv. Phys.* **57**, p. 143, 2008. doi:10.1080/14789940801912366. arXiv:0907.2796.

[130] H. Li and F. D. Haldane. "Entanglement spectrum as a generalization of entanglement entropy: Identification of topological order in non-Abelian fractional quantum hall effect states." *Phys. Rev. Lett.* **101**, p. 010504, 2008. doi:10.1103/PhysRevLett.101.010504. arXiv:0805.0332.

[131] D. N. Page. "Average entropy of a subsystem." *Phys. Rev. Lett.* **71**, p. 1291, 1993. doi:10.1103/PhysRevLett.71.1291.

[132] J. Eisert, M. Cramer, and M. B. Plenio. "Colloquium: Area laws for the entanglement entropy." *Rev. Mod. Phys.* **82**, p. 277, 2010. doi:10.1103/RevModPhys.82.277. arXiv:0808.3773.

[133] S. Rommer and S. Ostlund. "A class of ansatz wave functions for 1D spin systems and their relation to DMRG." *Phys. Rev. B* **55**, p. 2164, 1996. doi:10.1103/PhysRevB.55.2164. arXiv:cond-mat/9606213.

[134] I. Affleck, T. Kennedy, E. H. Lieb, and H. Tasaki. "Rigorous results on valence-bond ground states in antiferromagnets." *Phys. Rev. Lett.* **59**, p. 799, 1987. doi:10.1103/PhysRevLett.59.799.

[135] D. Gottesman and M. B. Hastings. "Entanglement versus gap for one-dimensional spin systems." *New J. Phys.* **12**, p. 025002, 2010. doi:10.1088/1367-2630/12/2/025002. arXiv:0901.1108.

[136] N. Schuch, M. M. Wolf, F. Verstraete, and J. I. Cirac. "Entropy scaling and simulability by matrix product states." *Phys. Rev. Lett.* **100**, p. 030504, 2008. doi:10.1103/PhysRevLett.100.030504. arXiv:0705.0292.

[137] G. Vidal, J. I. Latorre, E. Rico, and A. Kitaev. "Entanglement in quantum critical phenomena." *Phys. Rev. Lett.* **90**, p. 227902, 2003. doi:10.1103/PhysRevLett.90.227902. arXiv:quant-ph/0211074.

[138] G. Vidal. "Classical simulation of infinite-size quantum lattice systems in one spatial dimension." *Phys. Rev. Lett.* **98**, p. 070201, 2006. doi:10.1103/PhysRevLett.98.070201. arXiv:cond-mat/0605597.

[139] M. Suzuki. "General theory of fractal path integrals with applications to many-body theories and statistical physics." *J. Math. Phys.* **32**, p. 400, 1991. doi:10.1063/1.529425.

[140] E. M. Stoudenmire and S. R. White. "Minimally entangled typical thermal state algorithms." *New J. Phys.* **12**, p. 055026, 2010. doi:10.1088/1367-2630/12/5/055026. arXiv:1002.1305.

[141] M. B. Hastings. "Light-cone matrix product." *J. Math. Phys.* **50**, p. 095207, 2009. doi:10.1063/1.3149556. arXiv:0903.3253.

[142] I. P. McCulloch. "From density-matrix renormalization group to matrix product states." *J. Stat. Mech. Theory Exp.* **2007**, p. P10014, 2007. doi:10.1088/1742-5468/2007/10/P10014. arXiv:cond-mat/0701428.

[143] R. Orús and G. Vidal. "Infinite time-evolving block decimation algorithm beyond unitary evolution." *Phys. Rev. B* **78**, p. 155117, 2008. doi:10.1103/PhysRevB.78.155117. arXiv:0711.3960.

[144] G. Evenbly. "Gauge fixing, canonical forms, and optimal truncations in tensor networks with closed loops." *Phys. Rev. B* **98**, 2018. doi:10.1103/PhysRevB.98.085155. arXiv:1801.05390.

[145] V. Zauner-Stauber, L. Vanderstraeten, M. T. Fishman, F. Verstraete, and J. Haegeman. "Variational optimization algorithms for uniform matrix product states." *Phys. Rev. B* **97**, p. 045145, 2018. doi:10.1103/PhysRevB.97.045145. arXiv:1701.07035.

[146] C. Hubig. *Symmetry-Protected Tensor Networks*. Ph.D. thesis, Ludwig-Maximilians-Universität München, 2017. URL https://edoc.ub.uni-muenchen.de/21348/.

[147] T. E. Oliphant. "Python for scientific computing.", 2007. doi:10.1109/MCSE.2007.58. The NumPy and SciPy libraries can be found at https://www.scipy.org/.

[148] G. M. Crosswhite and D. Bacon. "Finite automata for caching in matrix product algorithms." *Phys. Rev. A* **78**, p. 012356, 2007. doi:10.1103/PhysRevA.78.012356. arXiv:0708.1221.

[149] S. Paeckel, T. Köhler, and S. R. Manmana. "Automated construction of $U(1)$-invariant matrix-product operators from graph representations." *SciPost Phys.* **3**, 2017. doi:10.21468/SciPostPhys.3.5.035. arXiv:1706.05338.

[150] G. M. Crosswhite, A. C. Doherty, and G. Vidal. "Applying matrix product operators to model systems with long-range interactions." *Phys. Rev. B* **78**, p. 035116, 2008. doi:10.1103/PhysRevB.78.035116. arXiv:0804.2504.

[151] B. Pirvu, V. Murg, J. I. Cirac, and F. Verstraete. "Matrix product operator representations." *New J. Phys.* **12**, p. 025012, 2010. doi:10.1088/1367-2630/12/2/025012. arXiv:0804.3976.

[152] J. Jordan, R. Orús, G. Vidal, F. Verstraete, and J. I. Cirac. "Classical Simulation of Infinite-Size Quantum Lattice Systems in Two Spatial Dimensions." *Phys. Rev. Lett.* **101**, p. 250602, 2008. doi:10.1103/PhysRevLett.101.250602. arXiv:cond-mat/0703788.

[153] P. Corboz, S. R. White, G. Vidal, and M. Troyer. "Stripes in the two-dimensional t-J model with infinite projected entangled-pair states." *Phys. Rev. B* **84**, p. 041108, 2011. doi:10.1103/PhysRevB.84.041108. arXiv:1104.5463.

[154] N. Schuch, M. M. Wolf, F. Verstraete, and J. I. Cirac. "Computational Complexity of Projected Entangled Pair States." *Phys. Rev. Lett.* **98**, p. 140506, 2007. doi:10.1103/PhysRevLett.98.140506. arXiv:quant-ph/0611050.

[155] M. P. Zaletel and F. Pollmann. "Isometric Tensor Network States in Two Dimensions." 2019. arXiv:1902.05100.

[156] S. Liang and H. Pang. "Approximate diagonalization using the density matrix renormalization-group method: A two-dimensional-systems perspective." *Phys. Rev. B* **49**, p. 9214, 1994. doi:10.1103/PhysRevB.49.9214.

[157] E. Stoudenmire and S. R. White. "Studying Two-Dimensional Systems with the Density Matrix Renormalization Group." *Annu. Rev. Condens. Matter Phys.* **3**, p. 111, 2012. doi:10.1146/annurev-conmatphys-020911-125018. arXiv:1105.1374.

[158] A. Kantian, M. Dolfi, M. Troyer, and T. Giamarchi. "Understanding repulsively mediated superconductivity of correlated electrons via massively parallel density matrix renormalization group." *Phys. Rev. B* **100**, p. 075138, 2019. doi:10.1103/PhysRevB.100.075138. arXiv:1903.12184.

[159] S.-S. Gong, W. Zhu, and D. N. Sheng. "Emergent Chiral Spin Liquid: Fractional Quantum Hall Effect in a Kagome Heisenberg Model." *Sci. Rep.* **4**, p. 6317, 2014. doi:10.1038/srep06317. arXiv:1312.4519.

[160] M. P. Zaletel, R. S. K. Mong, and F. Pollmann. "Flux insertion, entanglement, and quantized responses." *J. Stat. Mech. Theory Exp.* **2014**, p. P10007, 2014. doi:10.1088/1742-5468/2014/10/P10007. arXiv:1405.6028.

[161] A. G. Grushin, J. Motruk, M. P. Zaletel, and F. Pollmann. "Characterization and stability of a fermionic ν=1/3 fractional Chern insulator." *Phys. Rev. B* **91**, p. 035136, 2015. doi:10.1103/PhysRevB.91.035136. arXiv:1407.6985.

[162] Y.-C. He, M. P. Zaletel, M. Oshikawa, and F. Pollmann. "Signatures of Dirac Cones in a DMRG Study of the Kagome Heisenberg Model." *Phys. Rev. X* **7**, p. 031020, 2017. doi:10.1103/PhysRevX.7.031020. arXiv:1611.06238.

[163] P. Jordan and E. Wigner. "Über das Paulische Äquivalenzverbot." *Zeitschrift für Phys.* **47**, p. 631, 1928. doi:10.1007/BF01331938.

[164] S. Yan, D. A. Huse, and S. R. White. "Spin-Liquid Ground State of the $S = 1/2$ Kagome Heisenberg Antiferromagnet." *Science* **332**, p. 1173, 2011. doi:10.1126/science.1201080. arXiv:1011.6114.

[165] S. Depenbrock, I. P. McCulloch, and U. Schollwöck. "Nature of the spin-liquid ground state of the S=1/2 Heisenberg model on the kagome lattice." *Phys. Rev. Lett.* **109**, p. 067201, 2012. doi:10.1103/PhysRevLett.109.067201. arXiv:1409.5870.

[166] M. Fu, T. Imai, T.-H. Han, and Y. S. Lee. "Evidence for a gapped spin-liquid ground state in a kagome Heisenberg antiferromagnet." *Science* **350**, p. 655, 2015. doi:10.1126/science.aab2120. arXiv:1511.02174.

[167] M. Greiner, O. Mandel, T. W. Hänsch, and I. Bloch. "Collapse and revival of the matter wave field of a Bose–Einstein condensate." *Nature* **419**, p. 51, 2002. doi:10.1038/nature00968. arXiv:cond-mat/0207196.

[168] T. Kinoshita, T. Wenger, and D. S. Weiss. "A quantum Newton's cradle." *Nature* **440**, p. 900, 2006. doi:10.1038/nature04693.

[169] S. Hofferberth, I. Lesanovsky, B. Fischer, T. Schumm, and J. Schmiedmayer. "Non-equilibrium coherence dynamics in one-dimensional Bose gases." *Nature* **449**, p. 324, 2007. doi:10.1038/nature06149. arXiv:0706.2259.

[170] S. Trotzky, Y.-A. Chen, A. Flesch, I. P. McCulloch, U. Schollwöck, J. Eisert, and I. Bloch. "Probing the relaxation towards equilibrium in an isolated strongly correlated one-dimensional Bose gas." *Nat. Phys.* **8**, p. 325, 2012. doi:10.1038/nphys2232. arXiv:1101.2659.

[171] M. Gring, M. Kuhnert, T. Langen, T. Kitagawa, B. Rauer, M. Schreitl, I. Mazets, D. A. Smith, E. Demler, and J. Schmiedmayer. "Relaxation and Prethermalization in an Isolated Quantum System." *Science* **337**, p. 1318, 2012. doi:10.1126/science.1224953. arXiv:1112.0013.

[172] M. Cheneau, P. Barmettler, D. Poletti, M. Endres, P. Schauß, T. Fukuhara, C. Gross, I. Bloch, C. Kollath, and S. Kuhr. "Light-cone-like spreading of correlations in a quantum many-body system." *Nature* **481**, p. 484, 2012. doi:10.1038/nature10748. arXiv:1111.0776.

[173] D. Pertot, A. Sheikhan, E. Cocchi, L. A. Miller, J. E. Bohn, M. Koschorreck, M. Köhl, and C. Kollath. "Relaxation Dynamics of a Fermi Gas in an Optical Superlattice." *Phys. Rev. Lett.* **113**, p. 170403, 2014. doi:10.1103/PhysRevLett.113.170403. arXiv:1407.6037.

[174] S. Will, D. Iyer, and M. Rigol. "Observation of coherent quench dynamics in a metallic many-body state of fermionic atoms." *Nat. Commun.* **6**, p. 6009, 2015. doi:10.1038/ncomms7009. arXiv:1406.2669.

[175] S. Braun, M. Friesdorf, S. S. Hodgman, M. Schreiber, J. P. Ronzheimer, A. Riera, M. del Rey, I. Bloch, J. Eisert, and U. Schneider. "Emergence of coherence and the dynamics of quantum phase transitions." *Proc. Natl. Acad. Sci.* **112**, p. 201408861, 2015. doi:10.1073/pnas.1408861112. arXiv:1403.7199.

[176] T. Langen, S. Erne, R. Geiger, B. Rauer, T. Schweigler, M. Kuhnert, W. Rohringer, I. E. Mazets, T. Gasenzer, and J. Schmiedmayer. "Experimental observation of a generalized Gibbs ensemble." *Science* **348**, p. 207, 2015. doi:10.1126/science.1257026. arXiv:1411.7185.

[177] L. Xia, L. A. Zundel, J. Carrasquilla, A. Reinhard, J. M. Wilson, M. Rigol, and D. S. Weiss. "Quantum distillation and confinement of vacancies in a doublon sea." *Nat. Phys.* **11**, p. 316, 2015. doi:10.1038/nphys3244. arXiv:1409.2882.

[178] U. Schneider, L. Hackermüller, J. P. Ronzheimer, S. Will, S. Braun, T. Best, I. Bloch, E. Demler, S. Mandt, D. Rasch, and A. Rosch. "Fermionic transport and out-of-equilibrium dynamics in a homogeneous Hubbard model with ultracold atoms." *Nat. Phys.* **8**, p. 213, 2012. doi:10.1038/nphys2205. arXiv:1005.3545.

[179] A. Reinhard, J. F. Riou, L. A. Zundel, D. S. Weiss, S. Li, A. M. Rey, and R. Hipolito. "Self-trapping in an array of coupled 1D Bose gases." *Phys. Rev. Lett.* **110**, p. 033001, 2013. doi:10.1103/PhysRevLett.110.033001. arXiv:1207.4231.

[180] J. P. Ronzheimer, M. Schreiber, S. Braun, S. S. Hodgman, S. Langer, I. P. McCulloch, F. Heidrich-Meisner, I. Bloch, and U. Schneider. "Expansion Dynamics of Interacting Bosons in Homogeneous Lattices in One and Two Dimensions." *Phys. Rev. Lett.* **110**, p. 205301, 2013. doi:10.1103/PhysRevLett.110.205301. arXiv:1301.5329.

[181] S. Hild, T. Fukuhara, P. Schauß, J. Zeiher, M. Knap, E. Demler, I. Bloch, and C. Gross. "Far-from-Equilibrium Spin Transport in Heisenberg Quantum Magnets." *Phys. Rev. Lett.* **113**, p. 147205, 2014. doi:10.1103/PhysRevLett.113.147205. arXiv:1407.6934.

[182] T. Giamarchi. *Quantum Physics in One Dimension*. Oxford University Press, Oxford, 2003. ISBN 9780198525004.

[183] F. H. L. Essler, H. Frahm, F. Göhmann, A. Klümper, and V. E. Korepin. *The one-dimensional Hubbard model*. Cambridge University Press, Cambridge, 2005. ISBN 9780521802628.

[184] M. Mierzejewski, L. Vidmar, J. Bonča, and P. Prelovšek. "Nonequilibrium Quantum Dynamics of a Charge Carrier Doped into a Mott Insulator." *Phys. Rev. Lett.* **106**, p. 196401, 2011. doi:10.1103/PhysRevLett.106.196401. arXiv:1103.2018.

[185] J. Bonča, M. Mierzejewski, and L. Vidmar. "Nonequilibrium Propagation and Decay of a Bound Pair in Driven t-J Models." *Phys. Rev. Lett.* **109**, p. 156404, 2012. doi:10.1103/PhysRevLett.109.156404. arXiv:1207.5913.

[186] G. S. Uhrig. "Interaction quenches of Fermi gases." *Phys. Rev. A* **80**, p. 061602, 2009. doi:10.1103/PhysRevA.80.061602. arXiv:0909.1553.

[187] S. A. Hamerla and G. S. Uhrig. "Interaction quenches in the two-dimensional fermionic Hubbard model." *Phys. Rev. B* **89**, p. 104301, 2014. doi:10.1103/PhysRevB.89.104301. arXiv:1307.3438.

[188] F. Goth and F. F. Assaad. "Time and spatially resolved quench of the fermionic Hubbard model showing restricted equilibration." *Phys. Rev. B* **85**, p. 085129, 2012. doi:10.1103/PhysRevB.85.085129. arXiv:1108.2703.

[189] G. Carleo, F. Becca, M. Schiró, and M. Fabrizio. "Localization and Glassy Dynamics Of Many-Body Quantum Systems." *Sci. Rep.* **2**, p. 243, 2012. doi:10.1038/srep00243. arXiv:1109.2516.

[190] G. Carleo, F. Becca, L. Sanchez-Palencia, S. Sorella, and M. Fabrizio. "Light-cone effect and supersonic correlations in one- and two-dimensional bosonic superfluids." *Phys. Rev. A* **89**, p. 031602, 2014. doi:10.1103/PhysRevA.89.031602. arXiv:1310.2246.

[191] E. Gull, A. J. Millis, A. I. Lichtenstein, A. N. Rubtsov, M. Troyer, and P. Werner. "Continuous-time Monte Carlo methods for quantum impurity models." *Rev. Mod. Phys.* **83**, p. 349, 2011. doi:10.1103/RevModPhys.83.349. arXiv:1012.4474.

[192] M. Eckstein, A. Hackl, S. Kehrein, M. Kollar, M. Moeckel, P. Werner, and F. Wolf. "New theoretical approaches for correlated systems in nonequilibrium." *Eur. Phys. J. Spec. Top.* **180**, p. 217, 2009. doi:10.1140/epjst/e2010-01219-x. arXiv:1005.5097.

[193] M. Moeckel and S. Kehrein. "Interaction Quench in the Hubbard Model." *Phys. Rev. Lett.* **100**, p. 175702, 2008. doi:10.1103/PhysRevLett.100.175702. arXiv:0802.3202.

[194] F. Queisser, K. V. Krutitsky, P. Navez, and R. Schützhold. "Equilibration and prethermalization in the Bose-Hubbard and Fermi-Hubbard models." *Phys. Rev. A* **89**, p. 033616, 2014. doi:10.1103/PhysRevA.89.033616. arXiv:1311.2212.

[195] J. Lux, J. Müller, A. Mitra, and A. Rosch. "Hydrodynamic long-time tails after a quantum quench." *Phys. Rev. A* **89**, p. 053608, 2014. doi:10.1103/PhysRevA.89.053608. arXiv:1311.7644.

[196] J. Lux and A. Rosch. "Quench dynamics and statistics of measurements for a line of quantum spins in two dimensions." *Phys. Rev. A* **91**, p. 023617, 2015. doi:10.1103/PhysRevA.91.023617. arXiv:1408.6743.

[197] R. Schützhold, M. Uhlmann, Y. Xu, and U. R. Fischer. "Sweeping from the superfluid to the mott phase in the Bose-Hubbard model." *Phys. Rev. Lett.* **97**, p. 200601, 2006. doi:10.1103/PhysRevLett.97.200601. arXiv:cond-mat/0605121.

[198] M. Schiró and M. Fabrizio. "Time-Dependent Mean Field Theory for Quench Dynamics in Correlated Electron Systems." *Phys. Rev. Lett.* **105**, p. 076401, 2010. doi:10.1103/PhysRevLett.105.076401. arXiv:1005.0992.

[199] M. Schiró and M. Fabrizio. "Quantum quenches in the Hubbard model: Time-dependent mean-field theory and the role of quantum fluctuations." *Phys. Rev. B* **83**, p. 165105, 2011. doi:10.1103/PhysRevB.83.165105. arXiv:1102.1658.

[200] N. Schlünzen, S. Hermanns, M. Bonitz, and C. Verdozzi. "Dynamics of strongly correlated fermions: Ab initio results for two and three dimensions." *Phys. Rev. B* **93**, p. 035107, 2016. doi:10.1103/PhysRevB.93.035107. arXiv:1508.02947.

[201] J. J. Dorando, J. Hachmann, and G. K.-L. Chan. "Analytic response theory for the density matrix renormalization group." *J. Chem. Phys.* **130**, p. 184111, 2009. doi:10.1063/1.3121422. arXiv:0901.3166.

[202] M. Lubasch, V. Murg, U. Schneider, J. I. Cirac, and M.-C. Bañuls. "Adiabatic Preparation of a Heisenberg Antiferromagnet Using an Optical Superlattice." *Phys. Rev. Lett.* **107**, p. 165301, 2011. doi:10.1103/PhysRevLett.107.165301.

[203] A. J. A. James and R. M. Konik. "Quantum quenches in two spatial dimensions using chain array matrix product states." *Phys. Rev. B* **92**, p. 161111, 2015. doi:10.1103/PhysRevB.92.161111. arXiv:1504.00237.

[204] R. C. Brown, R. Wyllie, S. B. Koller, E. A. Goldschmidt, M. Foss-Feig, and J. V. Porto. "Two-dimensional superexchange-mediated magnetization dynamics in an optical lattice." *Science* **348**, p. 540, 2015. doi:10.1126/science.aaa1385. arXiv:1411.7036.

[205] T. Antal, Z. Rácz, A. Rákos, and G. M. Schütz. "Isotropic transverse XY chain with energy and magnetization currents." *Phys. Rev. E* **57**, p. 5184, 1998. doi:10.1103/PhysRevE.57.5184. arXiv:cond-mat/9711108.

[206] D. Gobert, C. Kollath, U. Schollwöck, and G. Schütz. "Real-time dynamics in spin-1/2 chains with adaptive time-dependent density matrix renormalization group." *Phys. Rev. E* **71**, p. 36102, 2005. doi:10.1103/PhysRevE.71.036102. arXiv:cond-mat/0409692.

[207] J.-S. Caux and J. Mossel. "Remarks on the notion of quantum integrability." *J. Stat. Mech. Theory Exp.* **2011**, p. P02023, 2011. doi:10.1088/1742-5468/2011/02/P02023. arXiv:1012.3587.

[208] L. F. Santos and A. Mitra. "Domain wall dynamics in integrable and chaotic spin-1/2 chains." *Phys. Rev. E* **84**, p. 016206, 2011. doi:10.1103/PhysRevE.84.016206. arXiv:1105.0925.

[209] T. Sabetta and G. Misguich. "Nonequilibrium steady states in the quantum XXZ spin chain." *Phys. Rev. B* **88**, p. 245114, 2013. doi:10.1103/PhysRevB.88.245114. arXiv:1308.4851.

[210] J. C. Halimeh, A. Wöllert, I. McCulloch, U. Schollwöck, and T. Barthel. "Domain-wall melting in ultracold-boson systems with hole and spin-flip defects." *Phys. Rev. A* **89**, p. 063603, 2014. doi:10.1103/PhysRevA.89.063603. arXiv:1307.0513.

[211] V. Alba and F. Heidrich-Meisner. "Entanglement spreading after a geometric quench in quantum spin chains." *Phys. Rev. B* **90**, p. 075144, 2014. doi:10.1103/PhysRevB.90.075144. arXiv:1402.2299.

[212] R. Steinigeweg, F. Heidrich-Meisner, J. Gemmer, K. Michielsen, and H. De Raedt. "Scaling of diffusion constants in the spin- 1/2 XX ladder." *Phys. Rev. B* **90**, p. 094417, 2014. doi:10.1103/PhysRevB.90.094417. arXiv:1406.2799.

[213] C. Karrasch, D. M. Kennes, and F. Heidrich-Meisner. "Spin and thermal conductivity of quantum spin chains and ladders." *Phys. Rev. B* **91**, p. 115130, 2015. doi:10.1103/PhysRevB.91.115130. arXiv:1412.6047.

[214] D. Muth, D. Petrosyan, and M. Fleischhauer. "Dynamics and evaporation of defects in Mott-insulating clusters of boson pairs." *Phys. Rev. A* **85**, p. 013615, 2012. doi:10.1103/PhysRevA.85.013615. arXiv:1111.1108.

[215] C. D. E. Boschi, E. Ercolessi, L. Ferrari, P. Naldesi, F. Ortolani, and L. Taddia. "Bound states and expansion dynamics of interacting bosons on a one-dimensional lattice." *Phys. Rev. A* **90**, p. 043606, 2014. doi:10.1103/PhysRevA.90.043606. arXiv:1407.2105.

[216] S. Sorg, L. Vidmar, L. Pollet, and F. Heidrich-Meisner. "Relaxation and thermalization in the one-dimensional Bose-Hubbard model: A case study for the interaction quantum quench from the atomic limit." *Phys. Rev. A* **90**, p. 033606, 2014. doi:10.1103/PhysRevA.90.033606. arXiv:1405.5404.

[217] F. Heidrich-Meisner, S. R. Manmana, M. Rigol, A. Muramatsu, A. E. Feiguin, and E. Dagotto. "Quantum distillation: Dynamical generation of low-entropy states of strongly correlated fermions in an optical lattice." *Phys. Rev. A* **80**, p. 041603, 2009. doi:10.1103/PhysRevA.80.041603. arXiv:0903.2017.

[218] J. Kajala, F. Massel, and P. Törmä. "Expansion Dynamics in the One-Dimensional Fermi-Hubbard Model." *Phys. Rev. Lett.* **106**, p. 206401, 2011. doi:10.1103/PhysRevLett.106.206401. arXiv:1101.6025.

[219] J. Schönmeier-Kromer and L. Pollet. "Ground-state phase diagram of the two-dimensional Bose-Hubbard model with anisotropic hopping." *Phys. Rev. A* **89**, p. 023605, 2014. doi:10.1103/PhysRevA.89.023605. arXiv:1308.2229.

[220] S. Fölling, S. Trotzky, P. Cheinet, M. Feld, R. Saers, A. Widera, T. Müller, and I. Bloch. "Direct observation of second-order atom tunnelling." *Nature* **448**, p. 1029, 2007. doi:10.1038/nature06112. arXiv:0707.3985.

[221] A. Celi, P. Massignan, J. Ruseckas, N. Goldman, I. B. Spielman, G. Juzeliūnas, and M. Lewenstein. "Synthetic Gauge Fields in Synthetic Dimensions." *Phys. Rev. Lett.* **112**, p. 043001, 2014. doi:10.1103/PhysRevLett.112.043001. arXiv:1307.8349.

[222] B. K. Stuhl, H.-I. Lu, L. M. Aycock, D. Genkina, and I. B. Spielman. "Visualizing edge states with an atomic Bose gas in the quantum Hall regime." *Science* **349**, p. 1514, 2015. doi:10.1126/science.aaa8515. arXiv:1502.02496.

[223] M. Mancini, G. Pagano, G. Cappellini, L. Livi, M. Rider, J. Catani, C. Sias, P. Zoller, M. Inguscio, M. Dalmonte, and L. Fallani. "Observation of chiral edge states with neutral fermions in synthetic Hall ribbons." *Science* **349**, p. 1510, 2015. doi:10.1126/science.aaa8736. arXiv:1502.02495.

[224] M. A. Cazalilla, R. Citro, T. Giamarchi, E. Orignac, and M. Rigol. "One dimensional bosons: From condensed matter systems to ultracold gases." *Rev. Mod. Phys.* **83**, p. 1405, 2011. doi:10.1103/RevModPhys.83.1405. arXiv:1101.5337.

[225] S. Langer, M. J. A. Schuetz, I. P. McCulloch, U. Schollwöck, and F. Heidrich-Meisner. "Expansion velocity of a one-dimensional, two-component Fermi gas during the sudden expansion in the ballistic regime." *Phys. Rev. A* **85**, p. 043618, 2012. doi:10.1103/PhysRevA.85.043618. arXiv:1109.4364.

[226] D. Jukić, B. Klajn, and H. Buljan. "Momentum distribution of a freely expanding Lieb-Liniger gas." *Phys. Rev. A* **79**, p. 033612, 2009. doi:10.1103/PhysRevA.79.033612. arXiv:0901.4437.

[227] Z. Mei, L. Vidmar, F. Heidrich-Meisner, and C. J. Bolech. "Unveiling hidden structure of many-body wave functions of integrable systems via sudden-expansion experiments." *Phys. Rev. A* **93**, p. 021607, 2016. doi:10.1103/PhysRevA.93.021607. arXiv:1509.00828.

[228] A. Trombettoni and A. Smerzi. "Discrete Solitons and Breathers with Dilute Bose-Einstein Condensates." *Phys. Rev. Lett.* **86**, p. 2353, 2001. doi:10.1103/PhysRevLett.86.2353. arXiv:cond-mat/0103368.

[229] H. Hennig, T. Neff, and R. Fleischmann. "Dynamical phase diagram of Gaussian wave packets in optical lattices." *Phys. Rev. E* **93**, p. 032219, 2016. doi:10.1103/PhysRevE.93.032219. arXiv:1309.7939.

[230] V. Hunyadi, Z. Rácz, and L. Sasvári. "Dynamic scaling of fronts in the quantum XX chain." *Phys. Rev. E* **69**, p. 066103, 2004. doi:10.1103/PhysRevE.69.066103. arXiv:cond-mat/0312250.

[231] V. Eisler and Z. Rácz. "Full Counting Statistics in a Propagating Quantum Front and Random Matrix Spectra." *Phys. Rev. Lett.* **110**, p. 060602, 2013. doi:10.1103/PhysRevLett.110.060602. arXiv:1211.2321.

[232] O. Penrose and L. Onsager. "Bose-Einstein Condensation and Liquid Helium." *Phys. Rev.* **104**, p. 576, 1956. doi:10.1103/PhysRev.104.576.

[233] T. Fukuhara, P. Schauß, M. Endres, S. Hild, M. Cheneau, I. Bloch, and C. Gross. "Microscopic observation of magnon bound states and their dynamics." *Nature* **502**, p. 76, 2013. doi:10.1038/nature12541. arXiv:1305.6598.

[234] R. Nandkishore, S. Gopalakrishnan, and D. A. Huse. "Spectral features of a many-body-localized system weakly coupled to a bath." *Phys. Rev. B* **90**, p. 064203, 2014. doi:10.1103/PhysRevB.90.064203. arXiv:1402.5971.

[235] S. Johri, R. Nandkishore, and R. N. Bhatt. "Many-Body Localization in Imperfectly Isolated Quantum Systems." *Phys. Rev. Lett.* **114**, p. 117401, 2015. doi:10.1103/PhysRevLett.114.117401. arXiv:1405.5515.

[236] J. Billy, V. Josse, Z. Zuo, A. Bernard, B. Hambrecht, P. Lugan, D. Clément, L. Sanchez-Palencia, P. Bouyer, and A. Aspect. "Direct observation of Anderson localization of matter waves in a controlled disorder." *Nature* **453**, p. 891, 2008. doi:10.1038/nature07000. arXiv:0804.1621.

[237] G. Roati, C. D'Errico, L. Fallani, M. Fattori, C. Fort, M. Zaccanti, G. Modugno, M. Modugno, and M. Inguscio. "Anderson localization of a non-interacting Bose–Einstein condensate." *Nature* **453**, p. 895, 2008. doi:10.1038/nature07071. arXiv:0804.2609.

[238] C. D'Errico, E. Lucioni, L. Tanzi, L. Gori, G. Roux, I. P. McCulloch, T. Giamarchi, M. Inguscio, and G. Modugno. "Observation of a Disordered Bosonic Insulator from Weak to Strong Interactions." *Phys. Rev. Lett.* **113**, p. 095301, 2014. doi:10.1103/PhysRevLett.113.095301. arXiv:1405.1210.

[239] J. Smith, A. Lee, P. Richerme, B. Neyenhuis, P. W. Hess, P. Hauke, M. Heyl, D. A. Huse, and C. Monroe. "Many-body localization in a quantum simulator with programmable random disorder." *Nat. Phys.* **12**, p. 907, 2016. doi:10.1038/nphys3783. arXiv:1508.07026.

[240] W. S. Bakr, J. I. Gillen, A. Peng, S. Fölling, and M. Greiner. "A quantum gas microscope for detecting single atoms in a Hubbard-regime optical lattice." *Nature* **462**, p. 74, 2009. doi:10.1038/nature08482. arXiv:0908.0174.

[241] T. Antal, Z. Rácz, A. Rákos, and G. M. Schütz. "Transport in the XX chain at zero temperature: Emergence of flat magnetization profiles." *Phys. Rev. E* **59**, p. 4912, 1999. doi:10.1103/PhysRevE.59.4912. arXiv:cond-mat/9812237.

[242] R. Steinigeweg, J. Gemmer, and M. Michel. "Normal-transport behavior in finite one-dimensional chaotic quantum systems." *Europhys. Lett.* **75**, p. 406, 2006. doi:10.1209/epl/i2006-10118-5. arXiv:cond-mat/0606083.

[243] L. F. Santos. "Transport control in low-dimensional spin- 1/2 Heisenberg systems." *Phys. Rev. E* **78**, p. 031125, 2008. doi:10.1103/PhysRevE.78.031125.

[244] G. Roux, T. Barthel, I. P. McCulloch, C. Kollath, U. Schollwöck, and T. Giamarchi. "Quasiperiodic Bose-Hubbard model and localization in one-dimensional cold atomic gases." *Phys. Rev. A* **78**, p. 023628, 2008. doi:10.1103/PhysRevA.78.023628. arXiv:0802.3774.

[245] P. Ribeiro, M. Haque, and A. Lazarides. "Strongly interacting bosons in multichromatic potentials supporting mobility edges: Localization, quasi-condensation, and expansion dynamics." *Phys. Rev. A* **87**, p. 043635, 2013. doi:10.1103/PhysRevA.87.043635. arXiv:1211.6012.

[246] V. Oganesyan and D. A. Huse. "Localization of interacting fermions at high temperature." *Phys. Rev. B* **75**, p. 155111, 2007. doi:10.1103/PhysRevB.75.155111. arXiv:cond-mat/0610854.

[247] Y. Bar Lev, G. Cohen, and D. R. Reichman. "Absence of Diffusion in an Interacting System of Spinless Fermions on a One-Dimensional Disordered Lattice." *Phys. Rev. Lett.* **114**, p. 100601, 2015. doi:10.1103/PhysRevLett.114.100601. arXiv:1407.7535.

[248] S. Bera, H. Schomerus, F. Heidrich-Meisner, and J. H. Bardarson. "Many-Body Localization Characterized from a One-Particle Perspective." *Phys. Rev. Lett.* **115**, p. 046603, 2015. doi:10.1103/PhysRevLett.115.046603. arXiv:1503.06147.

[249] T. Devakul and R. R. P. Singh. "Early Breakdown of Area-Law Entanglement at the Many-Body Delocalization Transition." *Phys. Rev. Lett.* **115**, p. 187201, 2015. doi:10.1103/PhysRevLett.115.187201. arXiv:1508.04813.

[250] E. Baygan, S. P. Lim, and D. N. Sheng. "Many-body localization and mobility edge in a disordered spin- 1/2 Heisenberg ladder." *Phys. Rev. B* **92**, p. 195153, 2015. doi:10.1103/PhysRevB.92.195153. arXiv:1509.06786.

[251] J. J. Sakurai and J. Napolitano. *Modern Quantum Mechanics*. Cambridge University Press, Cambridge, 2017. ISBN 9781108499996.

[252] D. M. Basko, I. L. Aleiner, and B. L. Altshuler. "On the problem of many-body localization." *Probl. Condens. Matter Phys. Quantum coherence Phenom. electron-hole coupled matter-light Syst.* p. 1, 2006. doi:10.1093/acprof:oso/9780199238873.003.0005. arXiv:cond-mat/0602510.

[253] S. Sachdev. *Quantum Phase Transitions*. Cambridge University Press, Cambridge, 2011. ISBN 9780511973765.

[254] D. A. Huse, R. Nandkishore, and V. Oganesyan. "Phenomenology of fully many-body-localized systems." *Phys. Rev. B* **90**, p. 174202, 2014. doi:10.1103/PhysRevB.90.174202. arXiv:1305.4915.

[255] A. Chandran, I. H. Kim, G. Vidal, and D. A. Abanin. "Constructing local integrals of motion in the many-body localized phase." *Phys. Rev. B* **91**, p. 085425, 2015. doi:10.1103/PhysRevB.91.085425. arXiv:1407.8480.

[256] L. Rademaker, M. Ortuño, and A. M. Somoza. "Many-body localization from the perspective of Integrals of Motion." *Ann. Phys. (Berl.)* **529**, p. 1600322, 2017. doi:10.1002/andp.201600322. arXiv:1610.06238.

[257] F. Pollmann, V. Khemani, J. I. Cirac, and S. L. Sondhi. "Efficient variational diagonalization of fully many-body localized Hamiltonians." *Phys. Rev. B* **94**, p. 041116, 2016. doi:10.1103/PhysRevB.94.041116. arXiv:1506.07179.

[258] X. Yu, D. Pekker, and B. K. Clark. "Finding Matrix Product State Representations of Highly Excited Eigenstates of Many-Body Localized Hamiltonians." *Phys. Rev. Lett.* **118**, p. 017201, 2017. doi:10.1103/PhysRevLett.118.017201. arXiv:1509.01244.

[259] A. Smith, J. Knolle, D. L. Kovrizhin, and R. Moessner. "Disorder-Free Localization." *Phys. Rev. Lett.* **118**, p. 266601, 2017. doi:10.1103/PhysRevLett.118.266601. arXiv:1701.04748.

[260] V. Khemani, S. P. Lim, D. N. Sheng, and D. A. Huse. "Critical Properties of the Many-Body Localization Transition." *Phys. Rev. X* **7**, p. 021013, 2017. doi:10.1103/PhysRevX.7.021013. arXiv:1607.05756.

[261] V. Khemani, D. N. Sheng, and D. A. Huse. "Two Universality Classes for the Many-Body Localization Transition." *Phys. Rev. Lett.* **119**, p. 075702, 2017. doi:10.1103/PhysRevLett.119.075702. arXiv:1702.03932.

[262] S. Gopalakrishnan and D. A. Huse. "Instability of many-body localized systems as a phase transition in a nonstandard thermodynamic limit." *Phys. Rev. B* **99**, p. 134305, 2019. doi:10.1103/PhysRevB.99.134305. arXiv:1901.04505.

[263] A. Morningstar and D. A. Huse. "Renormalization-group study of the many-body localization transition in one dimension." *Phys. Rev. B* **99**, p. 224205, 2019. doi:10.1103/PhysRevB.99.224205. arXiv:1903.02001.

[264] S. Roy, D. E. Logan, and J. T. Chalker. "Exact solution of a percolation analog for the many-body localization transition." *Phys. Rev. B* **99**, p. 220201, 2019. doi:10.1103/PhysRevB.99.220201. arXiv:1812.05115.

[265] S. Gopalakrishnan, K. Agarwal, E. A. Demler, D. A. Huse, and M. Knap. "Griffiths effects and slow dynamics in nearly many-body localized systems." *Phys. Rev. B* **93**, p. 134206, 2016. doi:10.1103/PhysRevB.93.134206. arXiv:1511.06389.

[266] D. J. Luitz and Y. B. Lev. "The ergodic side of the many-body localization transition." *Ann. Phys. (Berl.)* **529**, p. 1600350, 2017. doi:10.1002/andp.201600350. arXiv:1610.08993.

[267] J. Šuntajs, J. Bonča, T. Prosen, and L. Vidmar. "Quantum chaos challenges many-body localization." 2019. arXiv:1905.06345.

[268] S. Aubry and G. André. "Analyticity breaking and Anderson localization in incommensurate lattices." *Ann. Isr. Phys. Soc* **3**, p. 18, 1980.

[269] R. Vosk, D. A. Huse, and E. Altman. "Theory of the Many-Body Localization Transition in One-Dimensional Systems." *Phys. Rev. X* **5**, p. 031032, 2015. doi:10.1103/PhysRevX.5.031032. arXiv:1412.3117.

[270] J. Herbrych, P. Prelovšek, and X. Zotos. "Finite-temperature Drude weight within the anisotropic Heisenberg chain." *Phys. Rev. B* **84**, p. 155125, 2011. doi:10.1103/PhysRevB.84.155125. arXiv:1107.3027.

[271] S. Grossjohann and W. Brenig. "Hydrodynamic limit for the spin dynamics of the Heisenberg chain from quantum Monte Carlo calculations." *Phys. Rev. B* **81**, p. 012404, 2010. doi:10.1103/PhysRevB.81.012404. arXiv:0909.1972.

[272] M. Žnidarič. "Spin Transport in a One-Dimensional Anisotropic Heisenberg Model." *Phys. Rev. Lett.* **106**, p. 220601, 2011. doi:10.1103/PhysRevLett.106.220601. arXiv:1103.4094.

[273] C. Karrasch, J. H. Bardarson, and J. E. Moore. "Reducing the numerical effort of finite-temperature density matrix renormalization group calculations." *New J. Phys.* **15**, p. 083031, 2013. doi:10.1088/1367-2630/15/8/083031. arXiv:1303.3942.

[274] J. Sirker, R. G. Pereira, and I. Affleck. "Conservation laws, integrability, and transport in one-dimensional quantum systems." *Phys. Rev. B* **83**, p. 035115, 2011. doi:10.1103/PhysRevB.83.035115. arXiv:1011.1354.

[275] B. Bertini, M. Collura, J. De Nardis, and M. Fagotti. "Transport in out-of-equilibrium XXZ chains: Exact profiles of charges and currents." *Phys. Rev. Lett.* **117**, p. 207201, 2016. doi:10.1103/PhysRevLett.117.207201. arXiv:1605.09790.

[276] T. Prosen and E. Ilievski. "Families of Quasilocal Conservation Laws and Quantum Spin Transport." *Phys. Rev. Lett.* **111**, p. 057203, 2013. doi:10.1103/PhysRevLett.111.057203. arXiv:1306.4498.

[277] R. Steinigeweg, J. Gemmer, and W. Brenig. "Spin-Current Autocorrelations from Single Pure-State Propagation." *Phys. Rev. Lett.* **112**, p. 120601, 2014. doi:10.1103/PhysRevLett.112.120601. arXiv:1312.5319.

[278] C. Karrasch, J. E. Moore, and F. Heidrich-Meisner. "Real-time and real-space spin and energy dynamics in one-dimensional spin- 1 2 systems induced by local quantum quenches at finite temperatures." *Phys. Rev. B* **89**, p. 075139, 2014. doi:10.1103/PhysRevB.89.075139. arXiv:1312.2938.

[279] T. Barthel. "One-dimensional quantum systems at finite temperatures can be simulated efficiently on classical computers." 2017. arXiv:1708.09349.

[280] J. Dubail. "Entanglement scaling of operators: a conformal field theory approach, with a glimpse of simulability of long-time dynamics in 1 + 1d." *J. Phys. A Math. Theor.* **50**, p. 234001, 2017. doi:10.1088/1751-8121/aa6f38. arXiv:1612.08630.

[281] M. Zwolak and G. Vidal. "Mixed-State Dynamics in One-Dimensional Quantum Lattice Systems: A Time-Dependent Superoperator Renormalization Algorithm." *Phys. Rev. Lett.* **93**, p. 207205, 2004. doi:10.1103/PhysRevLett.93.207205. arXiv:cond-mat/0406440.

[282] S. R. White. "Minimally Entangled Typical Quantum States at Finite Temperature." *Phys. Rev. Lett.* **102**, p. 190601, 2009. doi:10.1103/PhysRevLett.102.190601. arXiv:0902.4475.

[283] M. Binder and T. Barthel. "Symmetric minimally entangled typical thermal states for canonical and grand-canonical ensembles." *Phys. Rev. B* **95**, p. 195148, 2017. doi:10.1103/PhysRevB.95.195148. arXiv:1701.03872.

[284] M. Berta, F. G. S. L. Brandão, J. Haegeman, V. B. Scholz, and F. Verstraete. "Thermal states as convex combinations of matrix product states." *Phys. Rev. B* **98**, p. 235154, 2018. doi:10.1103/PhysRevB.98.235154. arXiv:1709.07423.

[285] G. De las Cuevas, N. Schuch, D. Pérez-García, and J. Ignacio Cirac. "Purifications of multipartite states: limitations and constructive methods." *New J. Phys.* **15**, p. 123021, 2013. doi:10.1088/1367-2630/15/12/123021. arXiv:1308.1914.

[286] G. De las Cuevas, T. S. Cubitt, J. I. Cirac, M. M. Wolf, and D. Pérez-García. "Fundamental limitations in the purifications of tensor networks." *J. Math. Phys.* **57**, p. 071902, 2016. doi:10.1063/1.4954983. arXiv:1512.05709.

[287] C. Karrasch, J. H. Bardarson, and J. E. Moore. "Finite-temperature dynamical density matrix renormalization group and the Drude weight of spin-1/2 chains." *Phys. Rev. Lett.* **108**, p. 227206, 2012. doi:10.1103/PhysRevLett.108.227206. arXiv:1111.4508.

[288] T. Barthel. "Precise evaluation of thermal response functions by optimized density matrix renormalization group schemes." *New J. Phys.* **15**, p. 073010, 2013. doi:10.1088/1367-2630/15/7/073010. arXiv:1301.2246.

[289] E. Leviatan, F. Pollmann, J. H. Bardarson, D. A. Huse, and E. Altman. "Quantum thermalization dynamics with Matrix-Product States." *arXiv:1702.08894* 2017. arXiv:1702.08894.

[290] C. D. White, M. Zaletel, R. S. K. Mong, and G. Refael. "Quantum dynamics of thermalizing systems." *Phys. Rev. B* **97**, p. 035127, 2018. doi:10.1103/PhysRevB.97.035127. arXiv:1707.01506.

[291] M. Kliesch, D. Gross, and J. Eisert. "Matrix-Product Operators and States: NP-Hardness and Undecidability." *Phys. Rev. Lett.* **113**, p. 160503, 2014. doi:10.1103/PhysRevLett.113.160503. arXiv:1404.4466.

[292] G. Evenbly and G. Vidal. "Algorithms for Entanglement Renormalization: Boundaries, Impurities and Interfaces." *J. Stat. Phys.* **157**, p. 931, 2014. doi:10.1007/s10955-014-0983-1. arXiv:1312.0303.

[293] M. A. Nielsen and I. L. Chuang. *Quantum computation and quantum information*. Cambridge University Press, 2002. ISBN 9781107002173.

[294] K. Harada. "Entanglement branching operator." *Phys. Rev. B* **97**, p. 045124, 2018. doi:10.1103/PhysRevB.97.045124. arXiv:1710.01830.

[295] K. Hyatt, J. R. Garrison, and B. Bauer. "Extracting Entanglement Geometry from Quantum States." *Phys. Rev. Lett.* **119**, p. 140502, 2017. doi:10.1103/PhysRevLett.119.140502. arXiv:1704.01974.

[296] K. Umemoto and T. Takayanagi. "Entanglement of purification through holographic duality." *Nat. Phys.* **14**, p. 573, 2018. doi:10.1038/s41567-018-0075-2. arXiv:1708.09393.

[297] P. Nguyen, T. Devakul, M. G. Halbasch, M. P. Zaletel, and B. Swingle. "Entanglement of purification: from spin chains to holography." *J. High Energy Phys.* **2018**, p. 98, 2018. doi:10.1007/JHEP01(2018)098. arXiv:1709.07424.

[298] D. Muth, R. G. Unanyan, and M. Fleischhauer. "Dynamical Simulation of Integrable and Nonintegrable Models in the Heisenberg Picture." *Phys. Rev. Lett.* **106**, p. 077202, 2011. doi:10.1103/PhysRevLett.106.077202. arXiv:1009.4646.

[299] R. Vosk and E. Altman. "Many-Body Localization in One Dimension as a Dynamical Renormalization Group Fixed Point." *Phys. Rev. Lett.* **110**, p. 067204, 2013. doi:10.1103/PhysRevLett.110.067204. arXiv:1205.0026.

[300] H. Kim and D. A. Huse. "Ballistic spreading of entanglement in a diffusive nonintegrable system." *Phys. Rev. Lett.* **111**, p. 127205, 2013. doi:10.1103/PhysRevLett.111.127205. arXiv:1306.4306.

[301] I. H. Kim, A. Chandran, and D. A. Abanin. "Local integrals of motion and the logarithmic lightcone in many-body localized systems." 2014. arXiv:1412.3073.

[302] D.-L. Deng, X. Li, J. H. Pixley, Y.-L. Wu, and S. Das Sarma. "Logarithmic entanglement lightcone in many-body localized systems." *Phys. Rev. B* **95**, p. 024202, 2017. doi:10.1103/PhysRevB.95.024202. arXiv:1607.08611.

[303] K. Agarwal, S. Gopalakrishnan, M. Knap, M. Müller, and E. Demler. "Anomalous diffusion and Griffiths effects near the many-body localization transition." *Phys. Rev. Lett.* **114**, p. 160401, 2015. doi:10.1103/PhysRevLett.114.160401. arXiv:1408.3413.

[304] D. J. Luitz and Y. Bar Lev. "Information propagation in isolated quantum systems." *Phys. Rev. B* **96**, p. 020406, 2017. doi:10.1103/PhysRevB.96.020406. arXiv:1702.03929.